Master Thesis

Degree Project in Marine Geology 60 hp

Geophysical characterization of fluid flow and hydrocarbon migration features in the SW Loppa High area, Norwegian Barents Sea

Christoffer Bergstrand

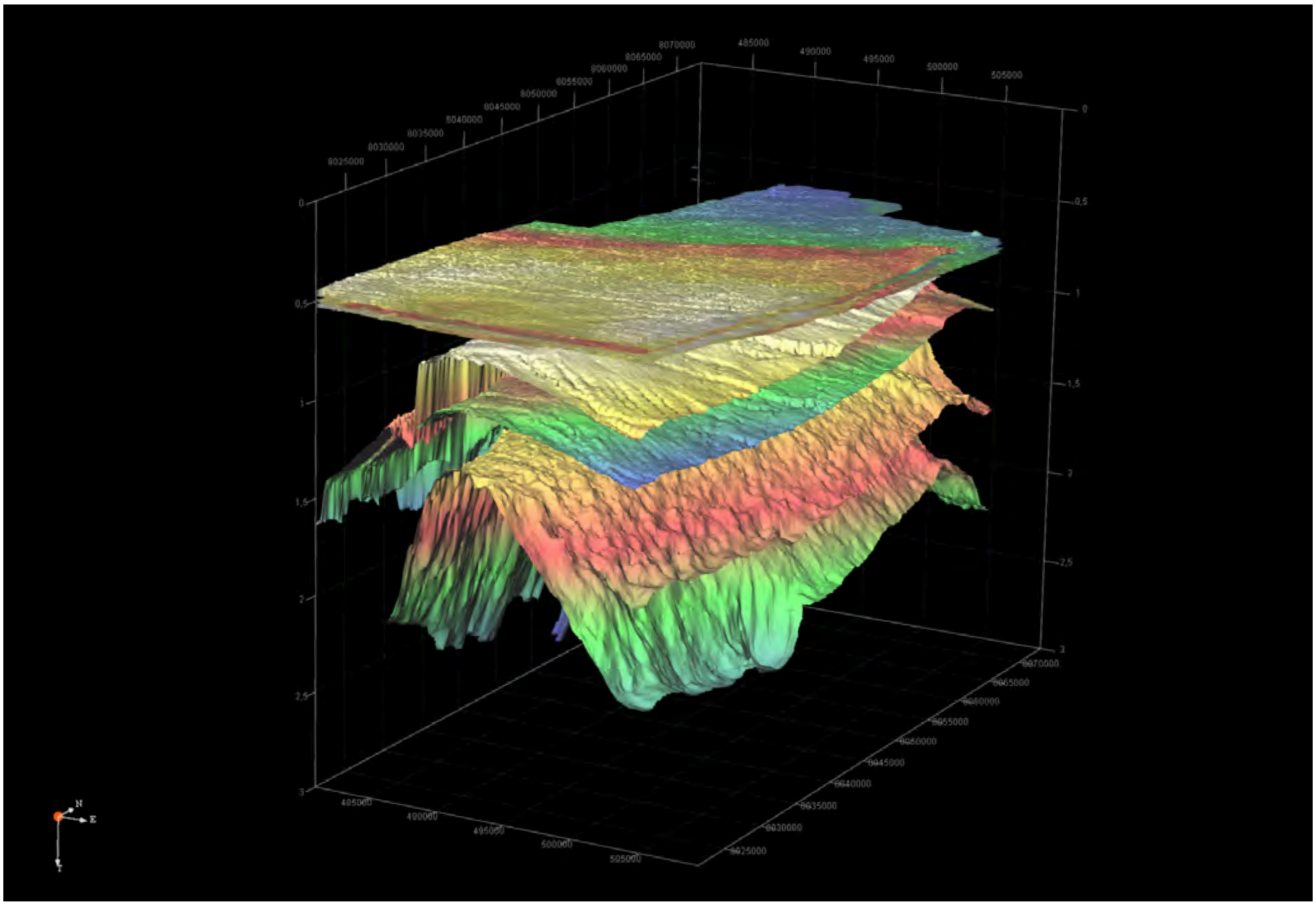

Stockholm 2015

Department of Geological Sciences
Stockholm University
SE-106 91 Stockholm
Sweden

Cover picture: 3D visualization of the main stratigraphic horizons in the Loppa High area, generated in IHS Kingdom from the interpreted layers of the LN12M01 data set.

Abstract

The objective of this master thesis is to establish a more detailed view of the geological features controlling fluid migration and accumulation in the Loppa High area, SW Barents Sea.

The Loppa High is a structural high formed through a series of tectonic activities ranging back to the Carboniferous. The structural high is surrounded by three major fault complexes and a number of deep sedimentary basins. Late Carboniferous to Triassic sediments as well as Quaternary successions in the upper parts are deposited on the Loppa High. The Polheim Sub-platform is a block-faulted structure of the Loppa High, formed in a series of tectonic events since the Early to Middle Triassic.

Processed data sets of 2D and 3D seismic surveys allowed for subsurface paleo-bathymetry mapping, followed by identification of fluid migration pathways and fluid accumulations within the southwest parts of the Loppa high and the adjacent Polheim Sub-platform, SW Barents Sea. Additional data from multibeam bathymetry and water column data gave a further understanding of the former and present sea floor activities.

Hydrocarbons originating from Triassic and Jurassic sandstone must migrate through thick deposits of glacial sediments before a sub-surface escape is possible. Fluid accumulations are identified in the Triassic and the Quaternary deposits; visible as strong amplitude reflections. Triassic deposits exhibited larger concentrations of fluids foremost in elevated areas, surrounded by faults. Fluid concentrations, located in the Quaternary strata, did not necessarily correspond to elevated areas. Thin stratum allowed for upward migration and focused movements were observed above an elongated depression located in the upper regional unconformity (URU). The presence of iceberg ploughmarks and pockmarks indicate a time of cold conditions where gas could escape first after glacial retreat.

An oil and gas pocket accumulated in Jurassic sandstone is located above the Polheim Sub-platform. Clusters of strong amplitude reflections observed in shallower deposits below the URU, indicate for an upward migration, either from this concentration or from deeper buried elements. The strata at these depths are tilted and deformed by fault movements, an ideal succession for fluid migration. Concentrations of strong amplitude reflections were also observed in the Triassic strata, deposited above the Loppa High next to the down-faulted structure. This is a tilted succession with faults leading up to the URU.

The Water column data was found to have registered three gas flares at the sea floor, one above the Polheim Sub-platform and two close by on top of the Loppa High, indicating hydrocarbon migration from within the sedimentary strata. The source of origin is difficult to determine but could be migrating up from the known source rock formations.

Keywords: Loppa High, Polheim Sub-platform, fluid migration, high amplitude

Sammanfattning

Syftet med detta examensarbete är att skapa en mer detaljerad bild av de geologiska särdrag som inverkar vid migration och ackumulering av fluider inom Loppa High-området, SV Barents hav.

Loppa High är en strukturell förhöjning som har bildats via en rad tektoniska händelser sedan Karbon. Den strukturella förhöjningen omges av tre större förkastningskomplex, samt ett antal djupa sedimentära bassänger. Sedimentära lagerföljder från sen Karbon till Trias, samt kvartära avsättningar, finns bevarade på Loppa High. Polheim Sub-platform är en block-förkastad struktur härrörande Loppa High, bildad via en serie av tektoniska händelser sedan tidiga till mellersta Trias.

Denna uppsats bygger på en paleo-batymetrisk kartläggning av sedimentära lager utifrån processade data från seismiska 2D- och 3D-undersökningar. Baserat på denna kartläggning har identifiering av migrationsvägar samt ansamling av fluider inom den sydvästra delen av Loppa High och den angränsande Polheim Sub-platform kunnat göras. Ytterligare data från multibeam batymetri och vattenkolumn-data gav en vidare insikt i de forna samt nuvarande processer vid havsbotten.

Olja och gas från sandsten tillhörande Trias och Jura måste migrera genom tjocka avsättningar av glaciala sediment innan de kan penetrera havsbotten. Fluidansamlingar har identifierats inom triassiska och kvartära avlagringar, synliga som reflektioner av stark amplitud. Sedimentära avsättningar från Trias uppvisar större koncentrationer av fluider främst i upphöjda områden, omgivna av förkastningar. Koncentrationer av fluider inom de kvartära skikten överensstämde dock inte alltid med upphöjda områden. Däremot möjliggör tunna lager en uppåtriktad migration, vilket främst observerades vid de koncentrerade fluidrörelser som förekom över den långsträckta fördjupning som tillhör den övre regionala diskordansen (URU). Isbergs-spår samt pockmarks identifierade på havsbotten berättar om en tid med kalla förhållanden där gas kunde lämna de sedimentära avlagringarna först efter en glacial tillbakadragning.

En olje- och gasficka i jurassisk sandsten är belägen ovanför Polheim Sub-platform. Grupperingar av reflektioner med stark amplitud kan observeras i de grundare avlagringarna under URU, vilket påvisar en uppåtriktad migration, antingen från olje- och gasfickan eller från djupare belägna avsättningar. Sedimentära lager på dessa djup är snedställda samt deformerade av förkastningsrörelser, vilket underlättar för migration av fluider. Ansamlingar av reflektioner med stark amplitud observerades också i trias-lagren inom Loppa High, bredvid den nedåt-förkastade strukturen. Trias utgörs här av en lutande lagerföljd med förkastningar som leder upp till URU.

Vattenkolumn-data visade spår av tre gasutsläpp från havsbotten, ett ovanför Polheim Sub-platform och två närliggande över Loppa High, vilket påvisar gas-migration från de sedimentära avsättningarna. Källa för dessa utsläpp är svår att fastställa men de kan ha migrerat upp från de tidigare kända olje- och gaskällorna.

Nyckelord: Loppa High, Polheim Sub-platform, vätskemigration, höga amplituder

Acknowledgments

I would like to express my gratitude to my supervisor Dr. Richard Gyllencreutz for helping me with guidance and constructive criticism during this master thesis project.

I am also thankful for all help and support provided by Lundin Norway AS, for all the data and softwares used in this project. I owe special thanks to Mats Andersson, Harald Brunstad and Dr. Jan Erik Lie for outstanding guidance and support when discussing the geological and geophysical problems encountered as well as all logistical difficulties.

I would like to acknowledge the Norwegian Petroleum Directorate (NPD) for providing me with litho-stratigrapic data and well data for this study.

I am deeply and forever indebted to Patricia Jusslin for her unremitting support and encouragement throughout this master thesis.

Table of contents

1. Introduction

The Barents Sea is an epi-continental sea situated between the Norwegian and Russian mainland in the south and the Franz Josef Land and Svalbard archipelago to the north (Fig. 1) (Dore, 1995; Smelror et al., 2009). The geological history of the Barents Shelf is long and complex, with numerous events of plate tectonic collisions and expansions related formations and deformations dating back to the Paleozoic and Early Ordovician (Gudlaugsson et al., 1998; Golonka et al., 2003; Pease et al., 2014). In the Mesozoic and Cenozoic time, continuing crustal extension led to repeating rifting, fault complex formation, subsidence, and uplift (Smelror et al., 2009). Structural highs and deep basins were formed throughout the western Barents Sea as a result of the recurrent tectonic movements, which had a large impact on the stratigraphy (Dore, 1995; Vadakkepuliyambatta et al., 2013). It has long been believed that the Barents Sea, containing tectonic-related faults and fractures and a great variety of structural traps and sealing mechanisms, is a promising shelf for oil and gas exploration (Gudlaugsson et al., 1998; Golonka et al., 2003; Faleide et al., 2010). Petroleum explorations of the southern Barents Sea began in 1980 and had its first discovery in 1981. Since then and up to 2010, about 25 discoveries were made on the Barents Shelf. Oil and gas reservoirs have mainly been found in Jurassic and Triassic sandstone, as well as in Carboniferous to Permian carbonates (Dore, 1995; Faleide et al., 2010; Hameed, 2012).

The aim of this master thesis is to develop a better understanding of the geological features controlling fluid migration and accumulation within the research area of the Loppa High, SW Barents Sea. Detailed 2D and 3D seismic interpretations is performed in order to analyze layer propagation, stratigraphic features and fault systems within the study area. Finally, to compile and visualize relevant data sets for characterization and mapping of major fluid flows and to locate hydrocarbon entrapments within the glacial deposits.

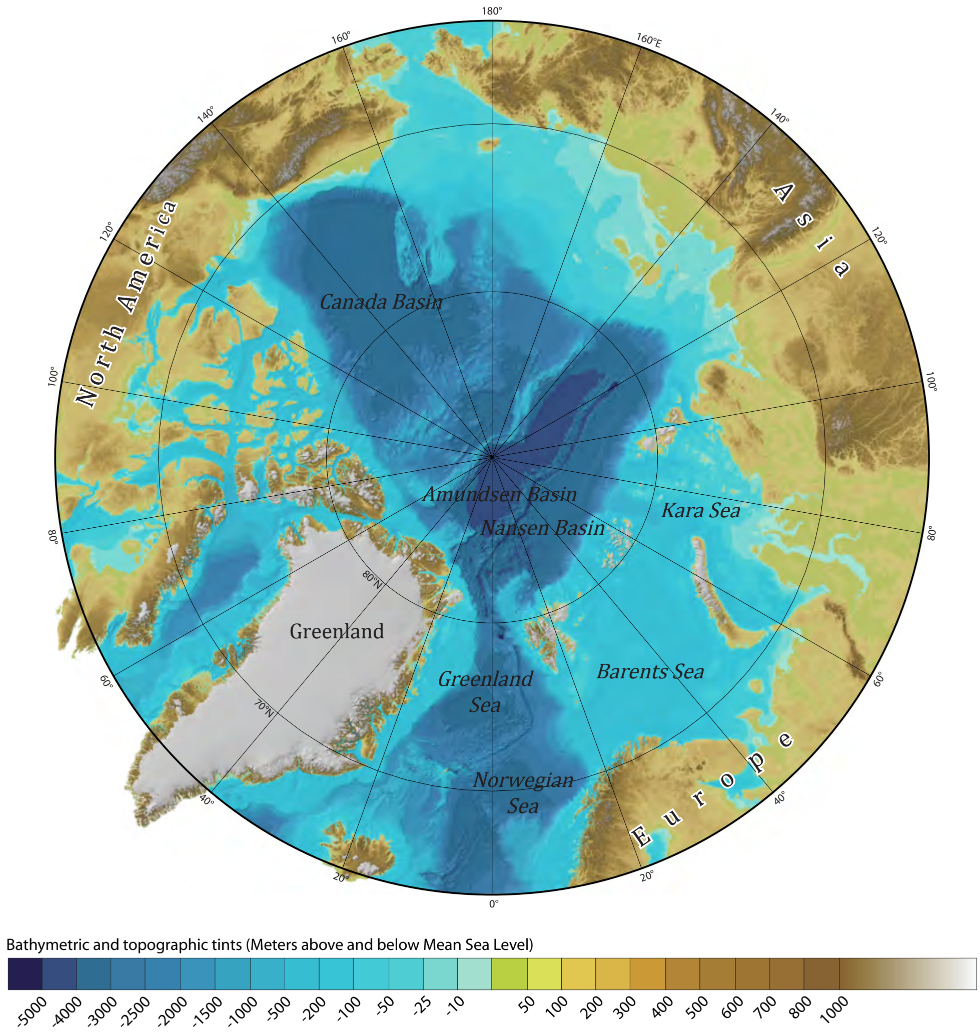

Figure 1: Map of the Arctic Ocean with surrounding seas, obtained from IBCAO (Jakobsson et al., 2012).

1.1 Geological framework of the Barents Sea

1.1.1 Study area

The Barents Sea is a 200 – 400 m deep epi-continental sea situated between the Franz Josef Land and Svalbard archipelagos in the North and the Norwegian and Russian mainland in the south. The island of Novaya Zemlya is located to the east of the Barents Sea and the eastern margin of the deep Atlantic Ocean to the west, connecting to the Greenland and Norwegian Seas (Dore, 1995; Pless, 2009; Smelror et al., 2009). The Barents Sea region has a long and complex geological history of plate tectonic collisions and expansions related formations and deformations. The region has throughout Paleozoic time experienced continental collision, back-arc extension and crustal extension with subsequent rifting as well as strike-slip faulting (Gudlaugsson et al., 1998; Golonka et al., 2003). In the Mesozoic and Cenozoic time, continuing crustal extension led to recurrent rifting, fault complex formation, subsidence, and uplift (Smelror et al., 2009). Major structural trends extend in ENE-WSW to NE-SW and NNE-SSW to NNW-SSE throughout the Barents Sea (Gabrielsen et al., 1990). The region is made up of a number of basins and structural highs, created by processes related to tectonic activities in the surrounding areas (Dore, 1995; Vadakkepuliyambatta et al., 2013). The region can be divided into an eastern and western part, as different areas of the Barents Sea were subjected differently by tectonic activities. In the east, the region consists primarily of two larger basins, the North Barents Basin and the South Barents Basin, separated by the structural high Ludlow Saddle (Gabrielsen et al., 1990; Smelror et al., 2009). Numerous smaller basins and structural highs make out the western Barents Sea (Fig. 2), e.g. Bjørnøya Basin, Harstad Basin, Hammerfest Basin and Nordkapp Basin, along with Loppa High, Stappen High and Veslemøy High (Gabrielsen et al., 1990; Smelror et al., 2009).

The Loppa High is a positive tectonic element located in the southwest Barents Sea, between 71°50´N, 20°E and 51°55´N, 22°40´E (Gabrielsen et al., 1990; Dore, 1995; Hameed, 2012). The Loppa High is situated north of the Hammerfest Basin, separated by the Asterias Fault Complex (Larssen et al., 2002).

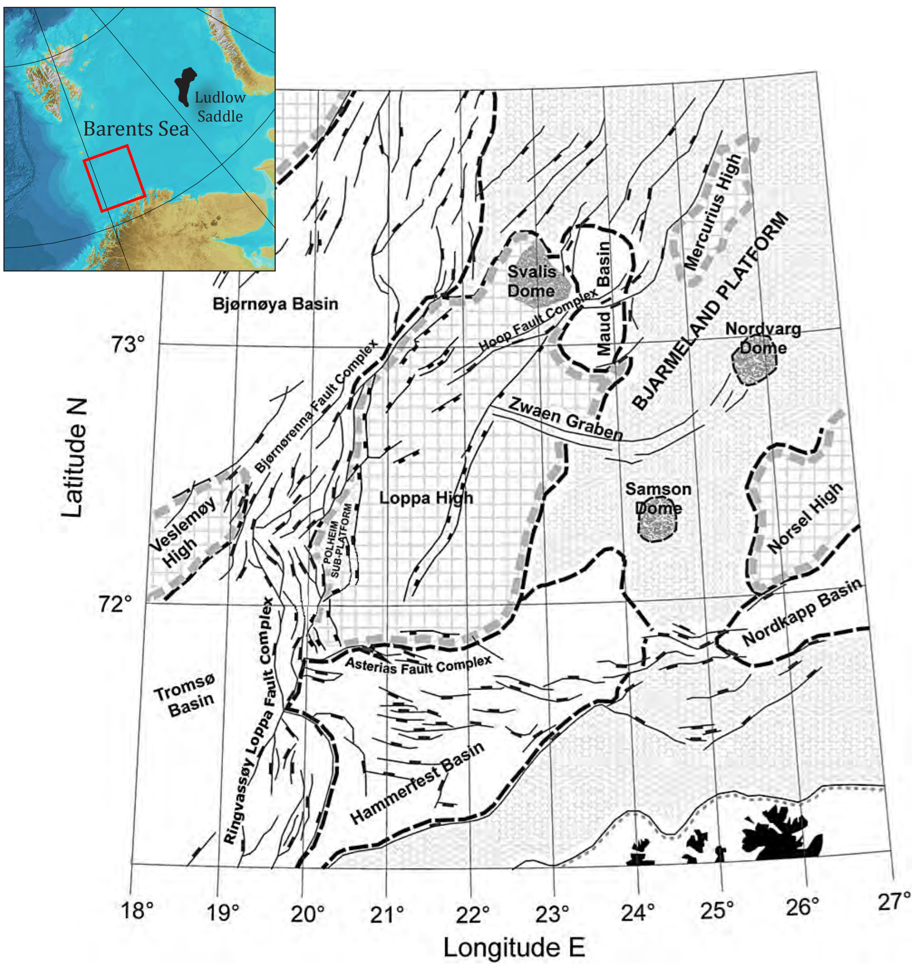

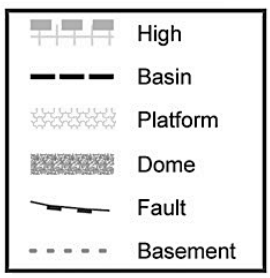

Figure 2: Tectonic framework of the southwestern Barents Sea. Illustrating the Loppa High with adjacent basins and fault complex. Modified after Gradstein et al. (2012). The reference map in the upper left corner are from IBCAO (Jakobsson et al., 2012), with the approximate location of the structural elements map marked in red and the location of Ludlow Saddle (Smelror et al., 2009).

The Bjørnøya Basin to the northwest and the Tromsø Basin is located to the southwest of the Loppa High, bounded by the Bjørnøyrenna Fault Complex and the Ringvassøy-Loppa Fault Complex (Larssen et al., 2002; Smelror et al., 2009). The structural high is a result of Carboniferous and Permian tectonic activity, Late Permian to Early Triassic normal faulting and footwall uplift (Dore, 1995; Gudlaugsson et al., 1998; Stemmerik et al., 1999), followed by Late Jurassic to Early Cretaceous rifting and subsidence (Dore, 1995; Stemmerik et al., 1999; Smelror et al., 2009). The Polheim Sub-platform is a down-faulted area located between the SW Loppa High, the Bjørnøyrenna- and the Ringvassøy-Loppa Fault Complex, situated between 72°N and 72°30´N, 20°E. The Sub-platform is a block-faulted element of the Loppa High, a result of Early to Middle Triassic tectonic activity followed by Jurassic movements to the west (Gabrielsen et al., 1990).

Lithostratigrapic strata of the Barents Sea region can be seen as a direct result of tectonic movements. While continental drift slowly transported the Barents Shelf northward and continental consolidation or break-up altered the sea floor to a more varied bathymetry, depositional environments came to reflect the changing climate with marine fauna and flora as well as supply of sedimentary material from surrounding denudation areas. Through time, the depositional strata were heavily affected by tectonic movements, where structural highs like Loppa High or Stappen High could have completely different environments in relation to surrounding basins. The uneven surface of the basement, brought on by rifting and tilted half-grabens, led to various depositional settings throughout the Loppa High (Stemmerik et al., 1999). An angular unconformity located on the northwestern parts is thought to be a result of Permian to Early Triassic extensional tectonism, followed by uplift and erosion (Gudlaugsson et al., 1998). A lithostratigrapic scheme gives an overview of the southwestern Barents Sea depositional environment (Fig. 3).

1.1.2 Geological history

The Barents Sea has a long and complex geological evolution that extends back to the Caledonian Orogeny, Early Ordovician to Early Devonian, and the Baltica and Laurentia plate consolidation (Smelror et al., 2009; Vernikovsky et al., 2013; Pease et al., 2014) , which lead to the creation of the Laurussian continent, at approximately 400 Ma (million years ago) (Dore, 1995). This is a well-documented mountain building era that resulted in the Greenland and Scandinavian Caledonides (Smelror et al., 2009). NE-SW striking bedrock is exposed on the Svalbard archipelago and the Norwegian mainland (Ritzmann and Faleide, 2009). In early Late Devonian time, the passive continental margin along the eastern Barents Sea region became active, resulting in subduction of the Uralian oceanic crust underneath the Baltica plate (Petrov et al., 2008). The westward dipping led to back-arc extension and rifting activities along the eastern Barents Sea region (Golonka et al., 2003; Ritzmann and Faleide, 2009; Smelror et al., 2009).

The Baltican and Laurentian plates began to break up again in the Late Devonian to Early Carboniferous, at the present-day Mid-Atlantic Ridge (MAR) (Golonka et al., 2003; Smelror et al., 2009). A fan-shaped rift zone was formed between the Barents Sea region and the northern Greenland as the rift extended up north (Stemmerik et al., 1999; Pless, 2009; Smelror et al., 2009). Numerous rift-grabens and structural highs were formed in the Barents Sea at this time (Golonka et al., 2003; Smelror et al., 2009), followed by a conjugate dextral strike-slip fault in the central region as well as sinistral strike-slip faulting in the western Barents Sea (Gudlaugsson et al., 1998; Golonka et al., 2003; Dengo and Røssland, 2013). The Bjørnøya-Maud- Nordkapp- Tromsø- and possibly also the Hammerfest Basin were formed in the SW Barents Sea along structural trends striking ENE-WSW (Gudlaugsson et al., 1998; Dengo and Røssland, 2013; Vadakkepuliyambatta et al., 2013). The Mercurius and Norsel highs were formed through fault complex developments related to the tectonic rifting of Early Carboniferous (Gabrielsen et al., 1990).

The Uralian Orogeny was the next great continental consolidation event of the Barents Sea region. Stretching from Early Carboniferous to Early Triassic time, it can be subdivided into two events based on the time and location of the tectonic activities (Smelror et al., 2009). During Early Carboniferous and Late Permian, approximately 350-250 Ma, an island arc next to the Novaya Zemlya marginal basin and the Yamal-Gydan plate (part of the Western Siberia) consolidated. This is evidenced by folding within the South Kara Basin (Golonka et al., 2003; Petrov et al., 2008; Smelror et al., 2009).

The later collisional event of the Uralian Orogeny occurred between Late Permian and Early Triassic time when the Baltican part of the Laurussian continent and Western Siberia consolidated, approximately 260-245 Ma (Dore, 1995; Golonka et al., 2003; Petrov et al., 2008). The Ural suture was created next to Novaya Zemlya, which became uplifted in the process, and in the northern Ural mountain chain, also known as the Pay-Khoy-Novaya Zemlya fold structure (Dore, 1995; Golonka et al., 2003; Ritzmann and Faleide, 2009). The North and South Barents Sea basins located on the eastern region were strongly influenced by the Triassic tectonic event, with rifting and following subsidence (Ritzmann and Faleide, 2009; Smelror et al., 2009). The formation of the Ludlow Saddle structural high has been shown to originate from this event (Lindquist, 1999). In Late Triassic, the eastern Barents Sea-Kara Sea region was uplifted by renewed tectonic activity of the Uralian Orogeny (Smelror et al., 2009).

Throughout the Middle and Late Carboniferous, only minor strike-slip movements were occurring in the western Barents Sea region. Incidents of passive regional subsidence followed along basin margins and lineaments as a result of unstable formations. (Pless, 2009; Smelror et al., 2009). In Permian and Early Triassic, recurrent tectonic plate separation and rifting between the Baltican and Laurentian plates led to tilted half grabens, uplifting and erosion in the western Barents Sea region (Gudlaugsson et al., 1998; Smelror et al., 2009). The Loppa High and Tromsø Basin were subjected to fault movements along the Ringvassøy-Loppa Fault Complex, orientated in an N-S structural trend. This resulted in uplift and tilting of the Loppa High, followed by sedimentary erosion (Gabrielsen et al., 1990; Gudlaugsson et al., 1998; Dengo and Røssland, 2013; Vadakkepuliyambatta et al., 2013).

Crustal extension of the Mid-Atlantic Ridge between Greenland and Norway intensified again in Late Jurassic to Early Cretaceous (Stemmerik et al., 1999; Dengo and Røssland, 2013; Vadakkepuliyambatta et al., 2013). Re-activation of old faults along with generation of new faults was occurring in the western parts of the Barents Sea (Pless, 2009). The Bjørnøyrenna Fault Complex, which runs with a NE-SW trend between the western limit of the Loppa High and the Bjørnøya Basin, was activated (Gabrielsen et al., 1990; Hameed, 2012). The Loppa High and Stappen High were uplifted in Late Jurassic, initiated by the Cimmerian movements (Smelror et al., 2009).

The north Barents Sea region was uplifted and tilted in the Early Cretaceous, as sea-floor spreading in the Arctic Ocean opened the Amerasian Basin (Brekke et al., 2001; Petrov et al., 2008; Smelror et al., 2009). In Late Cretaceous, renewed rifting phases with strike-slip movements and rapid subsidence led to formations of grabens and westward tilting in the southwestern Barents Sea shelf (Pless, 2009; Smelror et al., 2009). Major deep basins are formed in the Bjørnøya, Harstad and Tromsø basins (Gabrielsen et al., 1990). The northern region along with Svalbard was also uplifted in Late Cretaceous, a result of tectonic reorganization in the Arctic region (Brekke et al., 2001; Golonka et al., 2003).

During Paleogene and Neogene, mature sea floor spreading in the Arctic and Northern Atlantic continued, followed by numerous uplift, subsidence and erosional events throughout the entire Barents Sea region (Golonka et al., 2003; Pless, 2009). The Greenland-Norwegian Sea breakup began at around 55-54 Ma and the Greenland and Svalbard separation at 28 Ma as well as the volcanic platform formation of Iceland, in Neogene time (Brekke et al., 2001; Golonka et al., 2003; Smelror et al., 2009).

1.1.3 Lithostratigraphy of the Barents Sea

Depositional settings throughout the Barents Sea region have been strongly influenced by surrounding tectonic activities, resulting in sea floor alterations via features such as fault complexes, uplift and subsidence. Due to continental drift, the Barents Sea region moved from a paleo-latitude of 20°N in Early Carboniferous to its present location of approximately 75°N, leading to a slow but continuous alteration in the depositional environments (Dore, 1995; Stemmerik et al., 1999). In Devonian time, areas of the western Barents Sea region were highlands or denudation areas with fluvial plains and lacustrine basins (Smelror et al., 2009). Continental clastic sediments eroded from the Caledonian Orogeny were also deposited here, known as the Old Red Sandstone (Dengo and Røssland, 2013). In Early Devonian, coastal areas with a shallow water shelf covered the eastern parts of the Barents Sea region (Smelror et al., 2009). In Late Devonian, the region had shifted into a deep-water shelf area as subduction and rifting proceeded. Marine deposits of biogenic carbonates, limestone and organic-rich black shale continued throughout the Devonian period (Petrov et al., 2008).

The sedimentary accumulations proceeded until Late Carboniferous when the Barents Shelf reached 25°N (Stemmerik et al., 1999; Smelror et al., 2009). As the climate shifted into warm but arid regimes, most of the region remained under water as coastal or shelf areas (Dore, 1995; Worsley, 2008). Together with regional transgressions, the depositional environments were altered from continental to marine siliclastic accumulations, followed by widespread carbonate depositions (Worsley, 2008; Smelror et al., 2009; Dengo and Røssland, 2013). Salt mineral deposits of evaporite and halite occurred in deeper basins of the western Barents Sea region, such as the Nordkapp and Tromsø basins (Smelror et al., 2009; Dengo and Røssland, 2013), while structural highs like Loppa High had siliclastic and carbonate mixed cycles (Stemmerik et al., 1999). Clayey material containing silty and sandy sediments from the Uralian tectonic belt were accumulated in depressions along the eastern region (Dore, 1995; Petrov et al., 2008; Smelror et al., 2009).

During Early Permian, narrow straits and shallow coastal areas in the west strained the water exchange in the Barents Sea (Smelror et al., 2009). Glaciations in the southern hemisphere gave eustatic sea-level fluctuations, and with climatic ice-house conditions, warm-water carbonates, evaporites and local siliclastic sediments were deposited throughout the Barents Shelf (Stemmerik et al., 1999; Golonka et al., 2003; Ritzmann and Faleide, 2009). The entire shelf was flooded during periods with high sea-level fluctuations, which enabled thick carbonate build-ups to accumulate on structural highs like Loppa and Stappen (Smelror et al., 2009). Periods with low sea-level stands in the region resulted in dominated anhydrite and halite basinal deposits (Stemmerik et al., 1999). The deeper basins in the eastern Barents Sea were also subjected to carbonate mudstones and shale accumulations (Smelror et al., 2009). In Late Permian, the Barents Shelf had drifted to 40°N (Stemmerik et al., 1999; Worsley, 2008). The climate reached temperate conditions, and with regional transgression, the marine depositional environment shifted from carbonate deposits to an overall siliclastic regime (Smelror et al., 2009). Siliclastic sediments along with cherty limestones and shales were deposited in the western region while more clastic sediments from the Uralian event accumulated in the eastern Barents Sea (Gudlaugsson et al., 1998; Golonka et al., 2003; Ritzmann and Faleide, 2009).

In Early Triassic, depositional environments of the eastern Barents Sea region underwent a change as tectonic movements closed of the marine connection to the southeast (Worsley, 2008). Continental siliclastic sediments from the Fennoscandian Shield and the Uralian highlands were transported out and deposited throughout most of the shelf areas (Brekke et al., 2001; Smelror et al., 2009; Glørstad-Clark et al., 2010). The marine link between the Atlantic Ocean and the southwestern Barents Sea became more and more restrained during Middle and Late Triassic (Worsley, 2008). Organic-rich mudstone was deposited in the Middle Triassic, when anoxic conditions prevailed in basins along the western region (Smelror et al., 2009). In the Late Triassic, the Barents Shelf had drifted to 55 °N and experienced humid conditions (Bergan and Knarud, 1993; Worsley, 2008). Continued erosion and deposit of terrestrial clastic material from the east and south, as well as from elevated areas in the north, led to westward coastal progradation with regional deltaic and flood-plain developments (Dore, 1995; Worsley, 2008; Glørstad-Clark et al., 2010). The western parts of the Barents Sea remained as a marine environment, now with accumulation of sandstone and inter-bedded estuarine mudrocks, overlaid by coal-bearing coastal-plain sediments (Smelror et al., 2009). Large deposits of sandstone occurred throughout most of the region (Brekke et al., 2001; Smelror et al., 2009).

Erosional denudation of the uplifted eastern hinterlands continued into the Early Jurassic, with continental clastic deposits in the eastern Barents basins (Brekke et al., 2001; Golonka et al., 2003). By the late Early Jurassic, low-lying peneplains are thought to have covered large areas of the Barents Shelf (Brekke et al., 2001; Smelror et al., 2009). A transgressional phase with coastal progradation, known as the Stø Formation, took place in the west, with sandstone, siltstone and minor shale deposits in shallow-marine environments (Smelror et al., 2009). In Late Jurassic, the regional transgression reached its maximum, with all of the Barents Shelf submerged (Brekke et al., 2001; Petrov et al., 2008; Worsley, 2008). Shallow-shelf to deep-marine depositional environments now stretched over the region, with organic-rich black shale and mudstone deposits (Golonka et al., 2003; Worsley, 2008; Smelror et al., 2009). The Loppa High and Stappen High as well as elevated areas in the central Barents Sea had clastic deposits of sandstone, siltstone and clay (Smelror et al., 2009).

In the Early Cretaceous, terrigenous sediments were eroded from the uplifted northern Barents Sea region and transported south into deeper basins (Brekke et al., 2001; Petrov et al., 2008). Regional transgressions occurred prior to and after the uplift, evidenced by southwards-directed deltaic progradation and large-scale clinoforms (Brekke et al., 2001; Worsley, 2008). Fine-grained clastic sediments were predominant throughout the region, with large sandstone accumulations in the north (Golonka et al., 2003; Worsley, 2008; Smelror et al., 2009). The rising sea-level also gave open marine marl and shale deposits (Brekke et al., 2001). Arctic area tectonism related uplift and erosion of the northern Barents Sea region began in Late Cretaceous, where sediments in places were completely eroded down to top basement Devonian rocks (Golonka et al., 2003; Worsley, 2008). A regional transgression took place, followed by shallow shelf deposits of calcareous sandstones and mudstones (Brekke et al., 2001).

Regional uplift in Paleocene and Eocene resulted in extensive erosion of central and eastern Barents Sea, with clastic deposits in westerly subsided basins and deeper areas (Worsley, 2008; Smelror et al., 2009). Little is known about the eastern sedimentary deposits; the area is, due to uplift, believed to have had a very limited net accumulation or perhaps only large-scale erosion (Golonka et al., 2003; Smelror et al., 2009). In Late Paleocene, a transgressional phase occurred in the western Barents Sea, with sublittoral to deep-shelf deposits of foremost claystone (Brekke et al., 2001; Worsley, 2008). Tectonic plate movements during Neogene caused a regional uplift of the Barents Shelf, where all except the western region were elevated above sea-level (Pless, 2009; Smelror et al., 2009). Eroded sediments of up to and over 4000 m is thought to have occurred throughout the region, most of which were deposited in the western region or out over the shelf margin (Worsley, 2008). Northern hemisphere glaciations in Pliocene and Pleistocene had a heavy impact on the Barents Sea, as it initiated at approximately 3.6 Ma (Smelror et al., 2009). Subdivided into three phases of glacial growth, the Barents Sea was subjected to periods of glacially induced subsidence, erosion, isostatic uplift and glaciomarine deposits (Brekke et al., 2001; Smelror et al., 2009; Glørstad-Clark et al., 2010). An erosional surface between the pre-glacial strata and the Quaternary deposits marks the transition from glacial erosion to net accumulation, termed the Upper Regional Unconformity (URU). It is a relative thin fine-grained layer created through repeated glacial erosion (Solheim and Kristoffersen, 1984; Faleide et al., 1996; Pless, 2009).

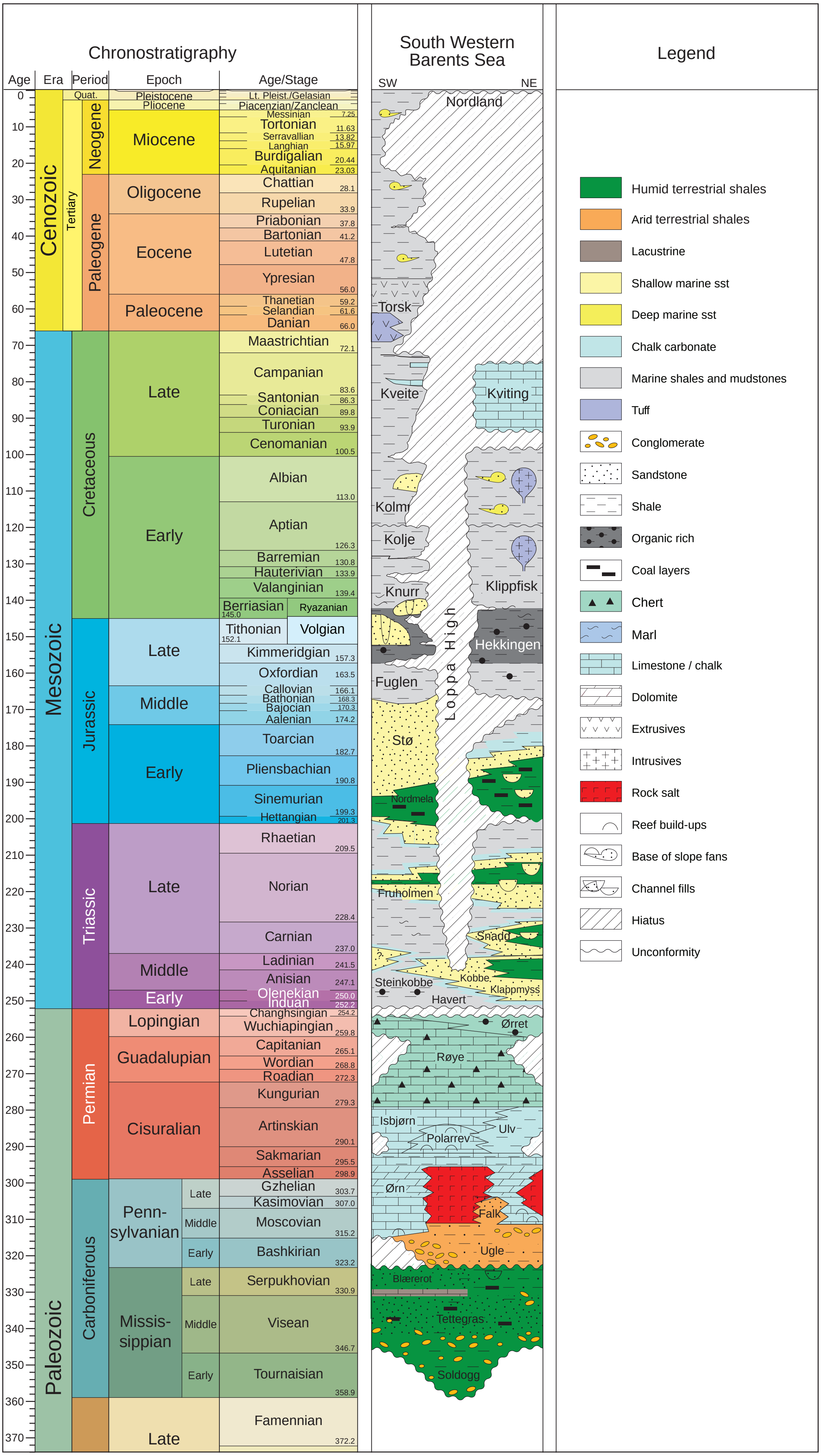

Figure 3: Lithostratigrapic scheme of the southwestern Barents Sea. Modified after Gradstein et al. (2012).

1.2 Fluids from fossil source

1.2.1 Hydrocarbon

Photosynthesis is the foundation of all marine life, and important in the carbon cycle since it is through this process atmospheric carbon dioxide is incorporated into the marine food chain. Most organisms end up eaten by predators, decomposed by microbiological processes or broken down by oxidation. Although some of the marine organic material, as well as imported terrestrial matter, will accumulate in anoxic environments where oxidation is inhibited (Dore, 1995). Fossil fluids are formed by natural processes where algae and other organic material is accumulated and buried by silt and sand below seabed. Over millions of years organic matter will be exposed to temperature and pressure as it is slowly transformed into hydrocarbons and other compounds (Bjørlykke, 2010).

Fluids may occur in three forms; as gas, oil or hydrate (gas trapped in frozen water molecules). Natural gas is a hydrocarbon-based fluid containing foremost methane (70-90 %), ethane, propane and butane (0-20 %) as well as carbon dioxide, nitrogen and hydrogen sulfide (Speight, 2010). Hydrocarbons can be produced below seabed via two different chemical processes; the biogenic and the thermogenic transformation (Fig. 4) (Schulz and Zabel, 2006). In oxic conditions, a single bacterium can degrade organic material into carbon dioxide. But as matter accumulates in anoxic conditions, a more complex interaction of microbial organisms is required. Positioned by the end of the chain, anaerobic Archaea utilizes substrate like acetate and H_2CO_2 to generate biogenic gas, a process generally known as methanogens (Wellsbury and Parkes, 2000; Schulz and Zabel, 2006). Archaea capable of methanogens have been found to exist in a wide range of temperatures. With surrounding pressure preventing water from boiling, they been found to grow at depths where temperatures reaches 110°C (Wellsbury and Parkes, 2000). A more detailed description of these organisms or the pathway involved in methanogenesis is given by Wellsbury and Parkes (2000).

Thermogenic fluids on the other hand in produced deep below seabed. With prolonged accumulation of sediment, organic matter is forced down as the sedimentary basin continues to subside. Due to the geothermal gradient at an average of 25 to 30°C, temperature and pressure will continue to increases with depth (Speight, 2012). Organic compounds are first reworked into kerogen by the increasing temperature and pressure (McCarthy et al., 2011). Referred to as a carbonaceous material, kerogen is an insoluble organic matter that can be divided into four types depending on the origin or composition of organisms (Speight, 2010). Oil will start to form as temperature reaches 80 to 90°C (Bjørlykke, 2010). Chemical bonds within the kerogen are slowly broken down (1-100 million years) by thermal alteration, a process known as catagenesis (Schulz and Zabel, 2006). In the higher temperature range of this process (170-180°C), kerogen and any present oil will start to crack, slowly transforming into gas (Bjørlykke, 2010; McCarthy et al., 2011). Metagenesis marks the last stage as temperature approaches 200°C (McCarthy et al., 2011). Any kerogen still present above 200°C will remain as no gas can be produced above these temperatures (Dore, 1995).

Biogenic gases consist primarily of methane while thermogenic gases, except for its high abundance of

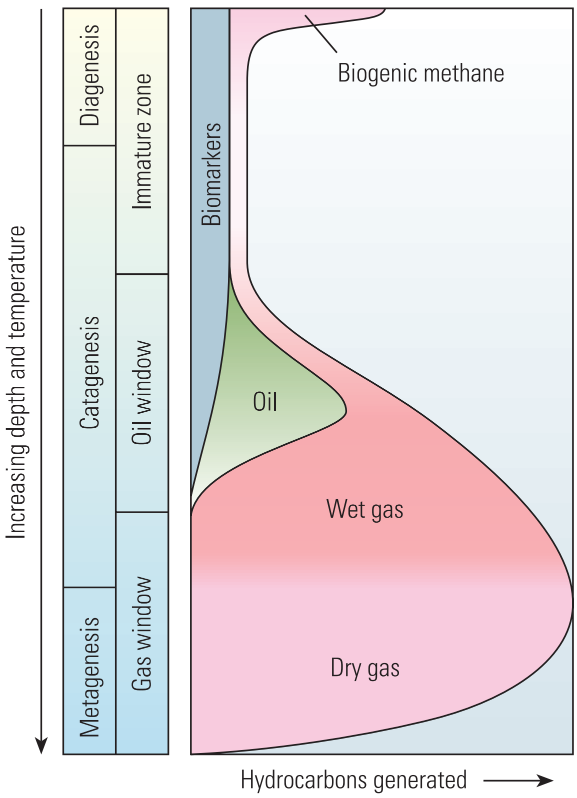

Figure 4: Thermal transformation of kerogen, a hydrocarbon generation diagram given from the seabed and down. Organic material is transformed either by methanogenesis into methane in the upper levels or via kerogen into oil and different forms of thermogenic gas during catagenesis and metagenesis processes as temperature rises. From McCarthy et al. (2011).

methane, also contain higher orders of hydrocarbons (Schulz and Zabel, 2006). Biogenic methane is, relative to thermogenic methane, depleted in ^{13}C as a result of H_2CO_2 driven methanogenesis (Wellsbury and Parkes, 2000). Differences in chemical and isotopic composition make it therefore possible to distinguish these two gases apart (Schulz and Zabel, 2006).

Natural gas can also occur in a crystalline solid state under the seabed. Depending on temperature and pressure (Fig. 5), gas hydrates are formed in pore spaces of sediments as water molecules are frozen around small molecules of hydrocarbons, with an ice ratio of 90 % to 10 % respectively (Abdel-Aal et al., 2003; Speight, 2010). The presence of higher order hydrocarbons or other gases like CO_2 and H_2S reduces the size of pressure needed for gas hydrates to form (Libes, 2011). Thermogenic gas may therefore form closer to the seabed then biogenic gas. Gas hydrates have been found in oceanic and inland sea sediments all over the world as well as in continental (permafrost) regions of the northern hemisphere (Kvenvolden, 2000). The worldwide amount of fossil fuel bound as gas hydrates are believed to exceed any other forms of carbon reservoir found on Earth, an average of estimates from the 80s and 90s are set to as high as $21*10^{15}$ m^3 of frozen gas (Kvenvolden, 2000; Speight, 2010).

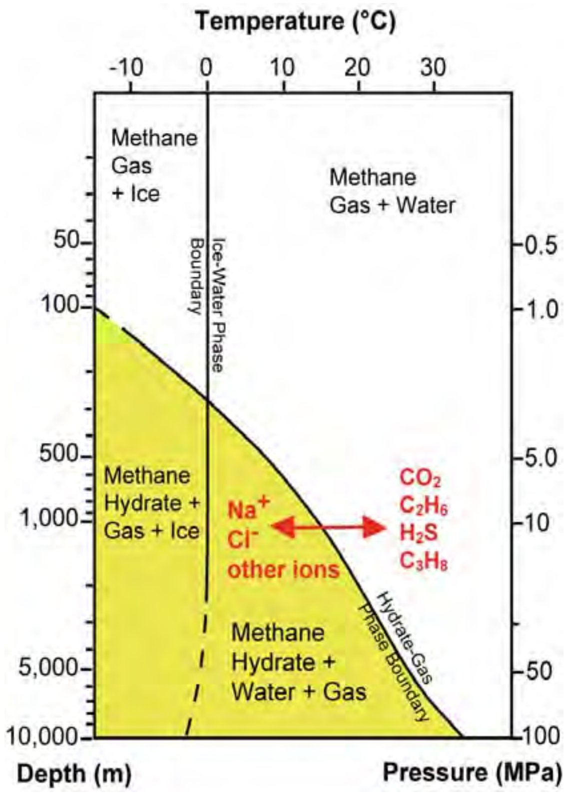

Figure 5: Gas hydrate phase diagram. The boundary between natural gas and gas hydrates are given by the phase line, referred to as the gas hydrate stability zone (GHSZ). A high enough pressure as well as a low temperature is required for gas hydrates to form. The composition of gas molecules affect the size of pressure needed. From Schulz and Zabel (2006).

1.2.2 Source rock

Sedimentary strata that have the potential to generate hydrocarbons are referred to as source rock, usually a limestone or organic-rich shale (Dore, 1995; Langrock and Stein, 2004; Libes, 2011). Geological and geophysical surveys as well as exploration drilling in the Barents Sea have shown that sedimentary strata of the Late Devonian, Late Permian, Early to Middle Triassic and Late Jurassic are capable of generating hydrocarbons (Lindquist, 1999; Abdel-Aal et al., 2003; Vigran et al., 2008; Smelror et al., 2009). But large areas in the Barents Sea region have yet to produce hydrocarbons to its full potential, with organic material buried to deep or to shallow, temperatures lies outside the oil and gas windows, referred to as immature source rock (Dore, 1995). Possible source rock formations in the southwestern Barents Sea are the Havert and Klappmyss Formation of Early Triassic, the Kobbe and Snadd Formation of Middle to Late Triassic, the Tubåen and Nordmela Formation of Early Jurassic and the Fuglen and Hekkingen Formation of Late Jurassic (Dore, 1995; Stemmerik et al., 1999; Pless, 2009; NPD, 2015). A source rock depends on several factors as it is evaluated for its quality, one of which is the total organic carbon (TOC) accumulated within the sediment. TOC levels of 2 to 5 % are according to McCarthy et al. (2011) a source rock of good quality.

1.2.3 Fluid migration

Migration is a slow process where hydrocarbons are transported from source rock and into reservoir rocks. Various models have been applied to understand the parameters working on the hydrocarbon migration (Clennell et al., 2000). This text will give a simplified overview of the major parameters involved in migration and how the driving and counteracting forces function within a fluid flow. A more comprehensive review is provided by Clennell et al. (2000). They underline the importance of porosity and permeability as a way to regulate the rates of transport.

Driving forces and issues associated with buoyancy, capillary theory, invasion percolation, multiphase flow and flow in faults and fractures are more thoroughly explained. The counteracting force that is the capillary pressure and how to calculate the pressure differences between two phases are also presented in detail by Dake (1998).

Porosity and permeability are two important factors when trying to determine a fluid´s possibility to pass through or within sedimentary strata. Porosity or void fractions refer to the empty space between rock grains in a matrix (Marshak and Prothero, 2008). The percentage of a material that is occupied by voids can thus be given by the void ratio:

$$V_r = \varphi_1/(1-\varphi_2) \qquad (1.1)$$

where porosity is displayed as a ratio between the volume of the void phase *(φ_1)* and the solid phase *(φ_2)* (Bjørlykke, 2010). The porosity of a material can vary depending on the depositional environment. Sediment transported a short distance from its source before deposit, i.e. stream gravel or glacial till, is known to be less mature due to the high content of various grain sizes. Sediment deposited in high energy areas, i.e. in strongly directed currents or by winnowing, is known to be well-sorted (Marshak and Prothero, 2008). Porosity is classified depending on its origin. Primary porosity is referred to the pore spaces present on formation, voids that are formed as grains are deposited or during rock formation. Secondary porosity is formed after rock formation, due to dissolution or fracturing of grains or by joints and faults (Marshak and Prothero, 2008; Bjørlykke, 2010).

Permeability refers to a fluid´s ability to flow through a matrix (Fig. 6) (Schulz and Zabel, 2006). The rate of which a gas or liquid will be transmitted depends upon several factors; the number of available conduits or interconnections between pore spaces, size of the conduits and straightness of the conduits (Bjørlykke, 2010). Permeability is not to be mixed up with porosity. A layer can have high porosity, but if the pore spaces are isolated due to cementing or recrystallization, the material becomes impermeable and fluid flow will be prevented (Marshak and Prothero, 2008).

Hydraulic gradient is another force controlling the rate of the transmission. Dependent on elevation or pressure differences, a fluid will flow faster through voids and conduits of a stratum if the hydraulic head is lower in the direction of the flow. The hydraulic gradient *(HG)* can be calculated with the formula:

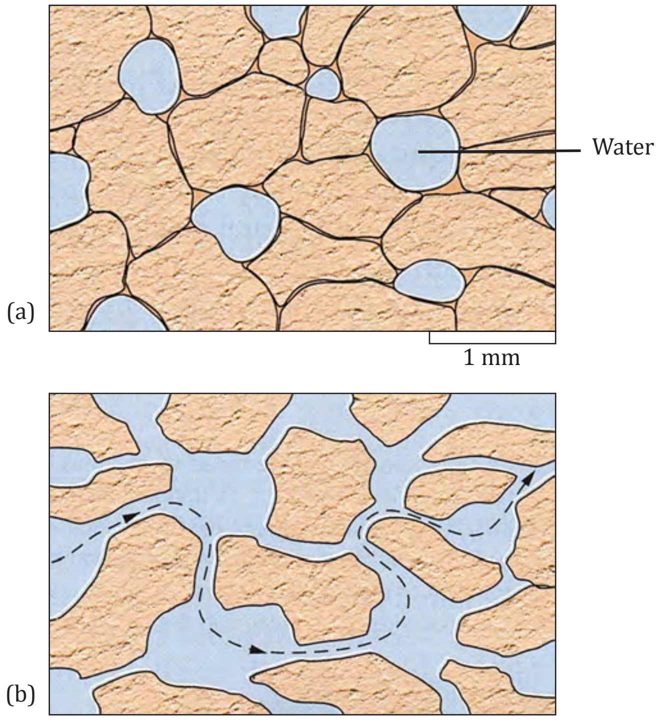

Figure 6a: Impermeable matrix with separated, non-connecting, voids. (b) Permeable matrix with voids interconnected by conduits. From Marshak and Prothero (2008).

$$HG = \Delta h/j \qquad (1.2)$$

where *(Δh)* gives the elevation difference between the two hydraulic heads and *(j)* is the distance between these two points (Marshak and Prothero, 2008).

The major driving force for migrating fluids, however, have long been unclear; how oil and gas have moved within voids and conduits, faults and fractures. Studies have shown that hydrocarbon fluids do not move together with pore water but as a separate phase (Bjørlykke, 2010). Driven by buoyancy, the fluid is forced upward due to density differences (Clennell et al., 2000). Buoyancy is an upward force exerted on an object (solid or liquid) within a fluid. Driven by the concept that an object of lower density, submerged in a fluid of higher density, will be forced upward because the volume of fluid that the object pushes aside weighs more than the object itself (Marshak and Prothero, 2008). In relation to hydrocarbon migration, the buoyancy force *(F_1)* can be given as:

$$F_1 = (\rho_w - \rho_o)H \quad (1.3)$$

where (ρ_w) and (ρ_o) are the density values for water and oil/gas. *(H)* gives the height of the coherent fossil fluid column (Bjørlykke, 2010).

The migration of fossil fluids is not without resistance. A hydrocarbon fluid cannot enter or transport within porous structures of a sedimentary rock if the fluid pressure doesn't overcome the capillary pressure resisting migration (Dake, 1998). Referred to as a threshold force, the capillary entry pressure is the pressure difference between two immiscible fluid phases working in between the conduits of two grains (Clennell et al., 2000; Bjørlykke, 2010). A contact angle (θ) is created when two immiscible fluids are interacting, caused by the relative attraction between the fluids and the solids (pore walls) (Dake, 1998). Referred to as the wetting angle, it reflects the degree by which the capillary pressure is influenced by the surface tension (γ), an attraction force between the fluids and the rock (Clennell et al., 2000; Golsanami et al., 2015). The pressure is also dependent on the size of the throat between two grains, given by the radius (r) (Clennell et al., 2000; Bjørlykke, 2010). The capillary pressure (P_c) between two fluids and their attraction to the pore wall is thus given by the equation:

$$P_c = (2\gamma \cos\theta)/r \quad (1.4)$$

(Bjørlykke, 2010). If the hydrocarbon fluid is gas trying to migrate through oil or water, the contact angle will be close to zero and the equation will instead look like:

$$P_c = \gamma/r \quad \text{respectively} \quad P_c = 2\gamma/r \quad (1.5 \;\&\; 1.6)$$

Depending on whether the void is a slit or a cylindrical pore (Clennell et al., 2000)

Gas molecules can bypass the counteracting capillary pressure (Fig. 7). By being fully saturated into a liquid, at depth where pressure is high enough, gas can move freely in between voids by bulk motion of the pore water. This is known as advection (Clennell et al., 2000; Marshak and Prothero, 2008). But as soon as hydraulic pressure drops, due to uplift or levels of less pressure is reached, the gas will exsolve and become trapped again.

Hydrocarbon migration can be divided into two separate phases (Bjørlykke, 2010; Libes, 2011). Primary migration is fluid movements within the source rock as hydrocarbons are migrating into adjacent rock. Secondary migration is the later fluid transport where hydrocarbons migrate through different strata before ending up in a reservoir or finds its way to the surface.

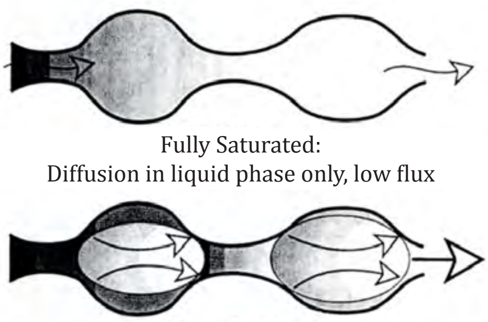

Figure 7: Void ratio during gas migration is also dependent on the degree of saturation within a fluid. Gas bubbles in an unsaturated fluid have to overcome the capillary pressure in order to migrate. From Clennell et al. (2000).

1.2.3.1 Primary migration

Generated from organic matter, the kerogen is a solid compound formed in source rock (Speight, 2012). Over millions of years, the kerogen is broken down to generate hydrocarbons (Schulz and Zabel, 2006). The oil and gas retains a lighter molecular weight than the large polymers (molecules composed of many repeated subunits) of kerogen (Bjørlykke, 2010). The density difference between the primary kerogen and the lighter oil and gas as well as the remaining kerogen creates a volume expansion as it matures (Libes, 2011). This can led to a pressure buildup if the surrounding source rock lacks permeability (Schulz and Zabel, 2006). Kerogen located in a fine-grained matrix, i.e. a clay-rich deposit, will allow fluids to migrate less freely (Bjørlykke, 2010). Limited by low permeability and narrow conduits, the void ratio decreases (Marshak and Prothero, 2008). The pressure created when buoyancy tries to force the fluids up towards lower pressurized areas has to overcome the strong threshold force that is the capillary pressure, for migration to occur (Dake, 1998; Bjørlykke, 2010). For sedimentary strata containing minimal permeability, i.e. a shale matrix, a pressure buildup cannot force hydrocarbons to migrate through pore spaces if the conduits are to narrow or not at all (Marshak and Prothero, 2008).

Pressure increases with the growing number of molecules within the fluid phase until fracture pressure is reached (Bjørlykke, 2010). Fracture pressure is the pressure in a source rock at which a layer will crack (Clennell et al., 2000). Controlled by vertical stress (σ_v) and horizontal stress (σ_h), a hydrofracture is more likely to occur vertical as the horizontal stress is exceeded before the vertical stress is reached, or parallel to the direction of maximum stress (Clennell et al., 2000; Bjørlykke, 2010). The Fracture stays open as long as the phase pressure is high enough. Once hydrocarbons start to pass through, pressure declines and the fracture can close up again (Libes, 2011). A clay or mud layer previously exposed to stress will be relative brittle, causing a new pressure phase to fracture the layer using less tensile stress (Clennell et al., 2000).

1.2.3.2 Secondary migration

Secondary migration means that fossil fluids have left the source rock and continue to migrate through strata. In this stage, the fluids move separately as gas of lower density travel out ahead (Libes, 2011). The volume of oil or gas saturated in pore water is an important part as fluids tries to migrate. Low fluid concentrations cannot generate a high enough buoyancy to overcome the capillary pressure, the water will instead flow past the hydrocarbon droplets (Clennell et al., 2000; Bjørlykke, 2010). Seal bypass systems are geological features located within impermeable strata, where fluids can bypass an otherwise enclosed sequences (Pless, 2009). Faults and fractures located in the migration path can increase the flow rate as long as they remain open. High permeability and low capillary pressure within the crack, together with density differences between the fluid and the surrounding saturated matrix, generates a buoyancy upthrust (Clennell et al., 2000; Schulz and Zabel, 2006). But not all faults and fractures will support a migration. Materials located in the other end of a crack may clog the opening, thus resulting in a trap or fault seal (Bjørlykke, 2010). Faults once opened can close or get sealed off due to new stress releases, when the direction of stress changes (Clennell et al., 2000; Marshak and Prothero, 2008). A fault will only serve as a migration path as long as the phase pressure doesn't rise too close to the fracture pressure, or rock matrix will fracture causing hydrocarbons to leak out elsewhere (Bjørlykke, 2010). A fracture can stay open even as pressure decreases. If asperities (uneven surface of the crack) or adjacent material like sand ends up in the fracture, the pathway remains open due to the permeability it creates (Clennell et al., 2000; Marshak and Prothero, 2008). Chemical reactions, such as cementation, pressure dissolution or recrystallization can over time alter permeability, thus affecting the migration pathway (Schulz and Zabel, 2006). Strata of higher permeability, i.e. sandstone, will allow hydrocarbons to migrate more efficiently. Reflected by the depositional environment, changes in current or a sudden debris flow will accumulate graded beddings. This causes the permeability within the strata to vary (Fig. 8) (Marshak and Prothero, 2008). A fining-upwards sandstone with smaller voids at the top will trap more hydrocarbons during migration (migration loss) due to buoyancy, than a coarsening-upwards sandstone (Bjørlykke, 2010).

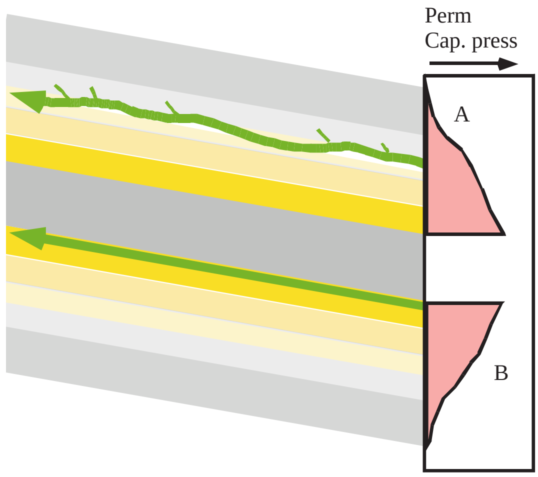

Figure 8a: Hydrocarbon migration through a fining-upward sandstone. (b) Hydrocarbon migration through a coarsening-upward sandstone. From Gradstein et al. (2012).

1.2.4 Hydrocarbon entrapment

Fossil fluids will continue to migrate as long as the buoyancy is strong enough, until it reaches the surface or is blocked by impermeable strata. A reservoir rock is a sedimentary layer of high porosity where oil or gas can accumulate in large quantities (Libes, 2011). But fluids need to be trapped within the reservoir rock for a reserve to form, or fluids will just continue to migrate (Marshak and Prothero, 2008). Impermeable layers and structural formations that inhibit further movements will form a trap. Called a cap rock or seal rock, it is the limited permeability or strong enough capillarity force that traps the hydrocarbon fluid within the reservoir rock (Abdel-Aal et al., 2003; Bjørlykke, 2010). Matrix known to have low permeability are evaporite, shale and unfractured limestone, while the most efficient seal rock is formed by gas hydrates (Libes, 2011). Siltstone, sandstone, limestone (with solution cavities), fractured shale and conglomerate all have a relative high porosity, thus have good potentials to become a reservoir rock (Marshak and Prothero, 2008). Entrapment of a reservoir will look different depending on the geological settings (Fig. 9). Stratigraphic traps are formed by sedimentary processes absent of any tectonic deformation (Lyons and Plisga, 1996). *Pinch out traps* can arise in a tilted reservoir rock as a layer ends, “pinches out”, between two impermeable strata (Marshak and Prothero, 2008). *Unconformity traps* are the result of changes in depositional patterns; the surface of tilted or sloping sediments are eroded and covered by a new layer. This strata can work as a seal rock trapping the hydrocarbons (Libes, 2011). *Sand body traps* refers to sand bodies, i.e. beaches, deltas and river bars, which are covered by shale-forming deposits (Lyons and Plisga, 1996; Abdel-Aal et al., 2003). Structural traps can occur in deformed strata, usually as a consequence of fault or folding (Marshak and Prothero, 2008). *Anticline traps* are formed when layers are folded into an arch-like shape. Covered by a seal rock, migrating hydrocarbons will be trapped within the reservoir rock (Lyons and Plisga, 1996). *Fault traps* can occur when there has been a sliding between two rock bodies (Abdel-Aal et al., 2003). Oil and gas will accumulate in the connecting reservoir rock if adjacent rocks are impermeable and/or clogging material, i.e. clay, collects in the end of the fault, referred to as smearing (Marshak and Prothero, 2008; Bjørlykke, 2010). *Salt-dome traps* are the result of plastic salt formations. Buoyancy will drive a thick salt layer up through overlying strata due to the density differences between the various strata. An impenetrable dome is formed that together with adjacent layers can trap the migrating hydrocarbons (Lyons and Plisga, 1996; Abdel-Aal et al., 2003).

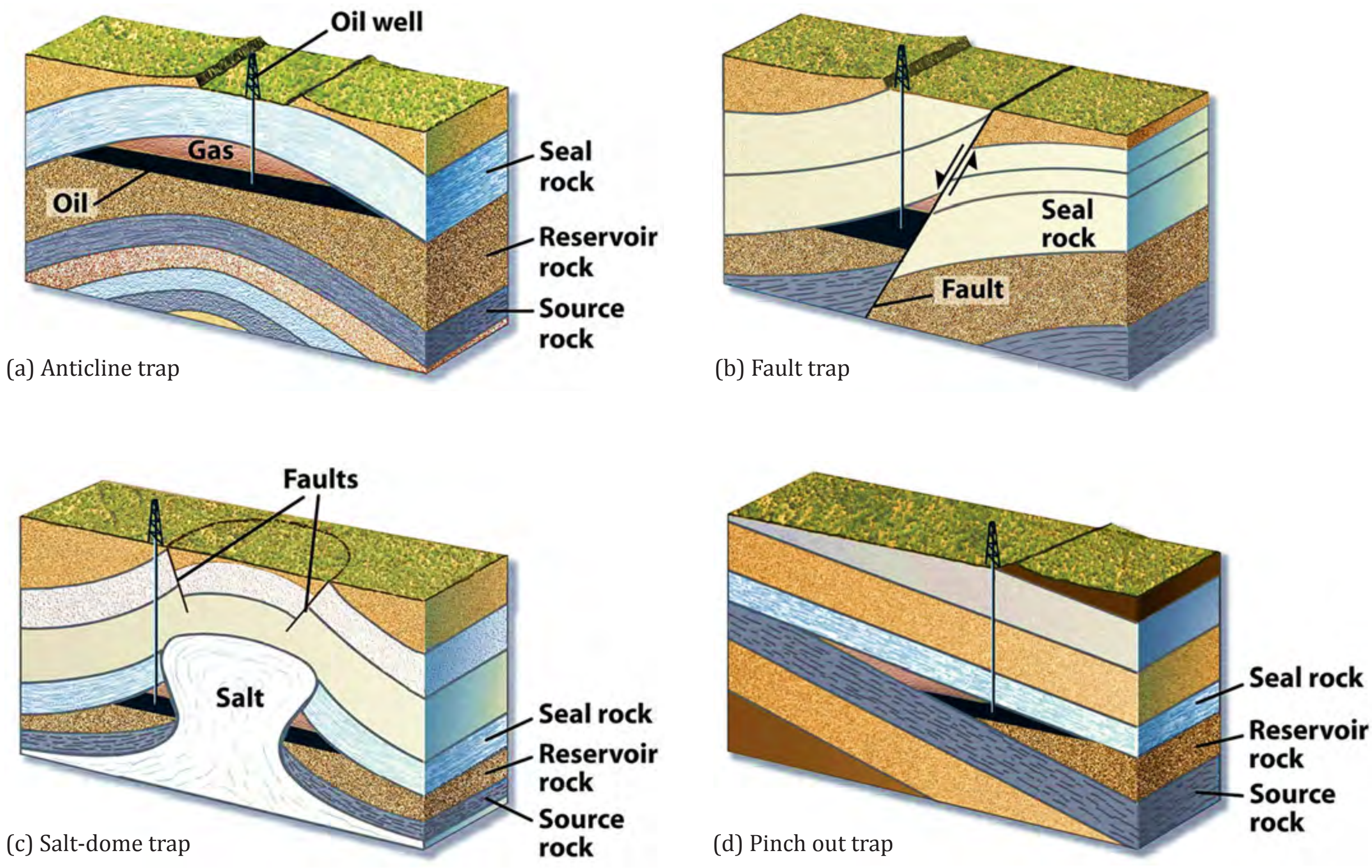

(a) Anticline trap

(b) Fault trap

(c) Salt-dome trap

(d) Pinch out trap

Figure 9a: Anticline trap. Buoyancy forces oil and gas to the top of the dome. (b) Fault trap. Fault movement cuts of the migration pathway. (c) Salt-dome trap. Oil and gas accumulates between the salt body and the tilted strata. (d) Pinch out trap. Hydrocarbons are trapped as the permeable layer pinches out. From Marshak and Prothero (2008).

1.3 Marine geophysics

1.3.1 Geophysical exploration

Geophysics is the discipline of geoscience that, instead of being defined as an observational science, deals with physical applications to study the earth's surface and internal structure (Aminzadeh and Dasgupta, 2013). Over time, the range of application expanded as new techniques with more accurate and high resolution geophysical instruments were developed. Seismic reflection measurements are a powerful geophysical application in geological surveys. It is used extensively in commercial exploration, for example petroleum industries that utilizes this technology to locate hydrocarbon-bearing reservoirs (Kearey et al., 2002). Seismic signal propagation beneath the surface is a complex journey. Authors as Jones (1999) and Kearey et al. (2002) gives a thorough description of how seismic wave propagation works with a theoretical background followed by seismic data acquisition at sea. Presented here is a brief description of how a seismic wave will respond to the geological and physical settings within a layer.

A seismic survey is based on the concept that rock properties can be measured through their response to elastic disturbances (Onajite, 2013). By transmitting seismic (elastic) waves into the ground, the acoustic impedance (AI), i.e. compressional velocity and density of a rock unit, will affect the emitted wave velocity, thus altering the travel time (Aminzadeh and Dasgupta, 2013). There are two high frequency waves to be considered in seismic exploration: compressional waves and shear waves. Grouped as body waves, they utilize the elastic character of a rock to propagate within the internal volume (Jones, 1999; Aminzadeh and Dasgupta, 2013). Compressional waves or P-waves moves through a medium by applying compressional and extensional strain in the direction of an emitted wave pulse, whereas the velocity of a P-wave will be restrained by particle motion within the rock (Kearey et al., 2002). According to Jones (1999) and Onajite (2013), the velocity (V_p) can be determined by knowing the bulk modulus (K), density (ρ) and the shear modulus (μ) of a medium:

$$V_p = \sqrt{\frac{K + {}^4\!/_3\,\mu}{\rho}} \tag{1.7}$$

Shear waves or S-waves will propagate perpendicular to the direction of a generated force and particle motion will bend like a sinusoidal waveform upon shear force, while containing no pressure disturbance (Kearey et al., 2002; Onajite, 2013). The S-wave velocity (V_s) containing a pure shear strain, is given by:

$$V_s = \sqrt{\frac{\mu}{\rho}} \tag{1.8}$$

S-waves, however, cannot propagate in water due to the inability of shear stress and strain to occur in liquids (Aminzadeh and Dasgupta, 2013). This makes P-waves a far more preferred waveform in seismic surveys.

A transmitted seismic signal will generate an echo for every sedimentary body it passes through, as long as the impedance contrast is large enough (difference in density and velocity between the sedimentary units). A reflected wave will contain the acoustic impedance given by the physical properties of the rock. Each reflection will produce a unique seismic trace, recorded by the receiver (Aminzadeh and Dasgupta, 2013). A signal´s two way travel time (TWTT) for the n:th layer (t_n) is shown by:

$$t_n = \frac{(x^2 + 4z^2)^{1/2}}{V_{rms}} \tag{1.9}$$

as long as (x<<z). The offset (x) is the distance between the transmitter and the receiver and (z) is the depth beneath surface. The root-mean-square velocity (V_{rms}) is given as an average travel time for the above positioned layers (Fig. 10) (Kearey et al., 2002).

But the TWTT will vary if several transmitters and receivers are used simultaneously to measure at one point of the reflector. The Normal moveout (NMO) refers to the difference in travel time (ΔT) from (t_0) to (t_x), given by the change in distance (x) to a receiver located on either side of the transmitter (Fig. 11a) (Jones, 1999).

In the presence of a dipping reflector, the emitted signal's path of motion will differ in time between the two receivers of which the transmitter is positioned (Kearey et al., 2002). By knowing the dipping angle (θ) of a reflector and the velocity (V) within, a TWTT of the dipping reflector can be given as:

$$t = \frac{(x^2 + 4z^2 + 4xz\sin\theta)^{1/2}}{V} \qquad (1.10)$$

Regarding the time-distance curve in figure 11b, a dipping reflector will offset the travel time by *(ΔT_d)*, known as the dip moveout (DMO) (Jones, 1999). The opposite paths of the reflected signal will differ in travel times *(t_x)* and *(t_{-x})*, shown by:

$$\Delta T_d = t_x - t_{-x} \qquad (1.11)$$

towards the two receivers of equal distance *(x)* and *(-x)* (Kearey et al., 2002).

A signal transmitted into the ground will not reflect of a layer or object as long as the acoustic impedance doesn't change. The transition of a signal into a layer of different density and velocity will produce an echo containing the reflected amplitude sampled by the receiver. The reflected amplitude is defined as the difference between the two acoustic impedances of each layer. A reflection coefficient of the same transition can be given as a ratio by dividing the reflected amplitude to the sum of the two acoustic impedances of each layer, shown by:

$$R = \frac{v_2\rho_2 - v_1\rho_1}{v_2\rho_2 + v_1\rho_1} \qquad (1.12)$$

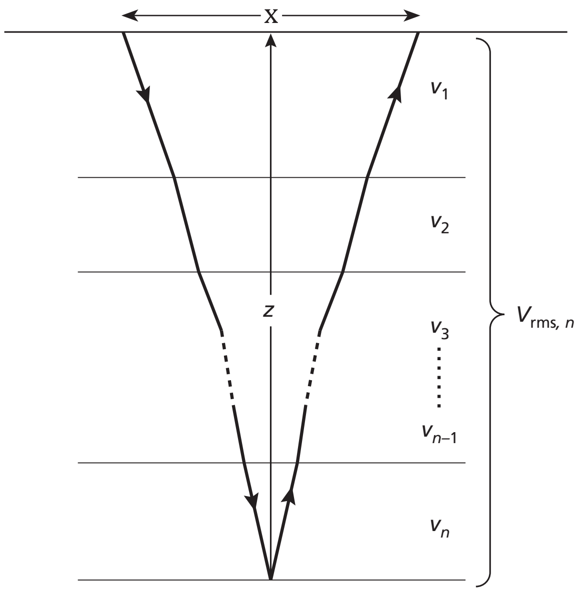

Figure 10: A reflected signal is traveling through a multi-layered ground, given by the depth (z) and distance (x) between a transmitter and receiver. Refraction of the signal will occur at layer boundaries. From Kearey et al. (2002).

where *(V_1 ρ_1)* and *(V_2 ρ_2)* are acoustic impedances of the two sides of a transition, viewed from above (Aminzadeh and Dasgupta, 2013; Onajite, 2013). Figure 12 shows the convolutional model of a reflectivity trace. The input pulse (source wave) is multiplied with the amplitude value given in the reflectivity function to generate the seismic trace (Kearey et al., 2002).

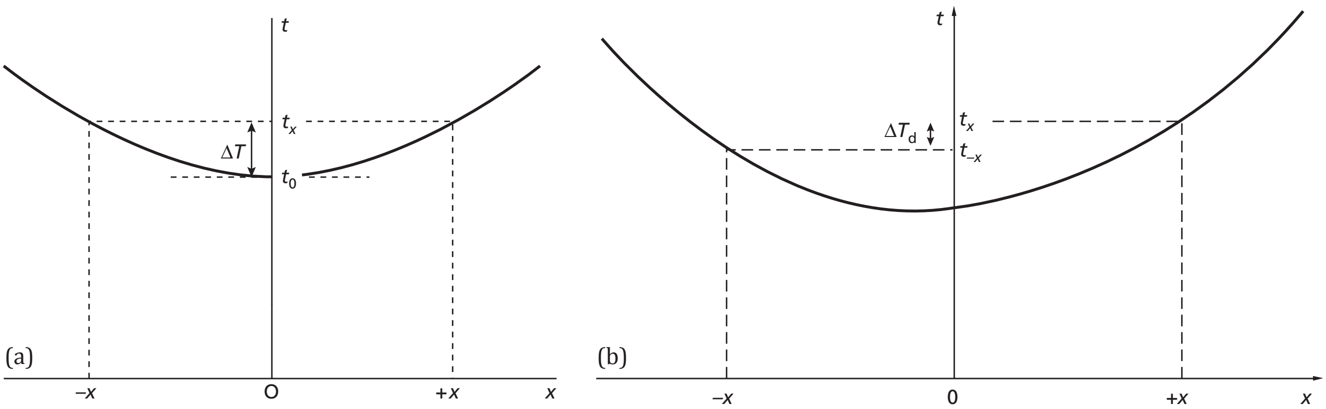

Figure 11a: A time-distance curve showing the difference in travel time from a transmitter positioned on either side of the receiver, reflected of a horizontal reflector. (b) A time-distance curve given of a dipping reflector. From Kearey et al. (2002).

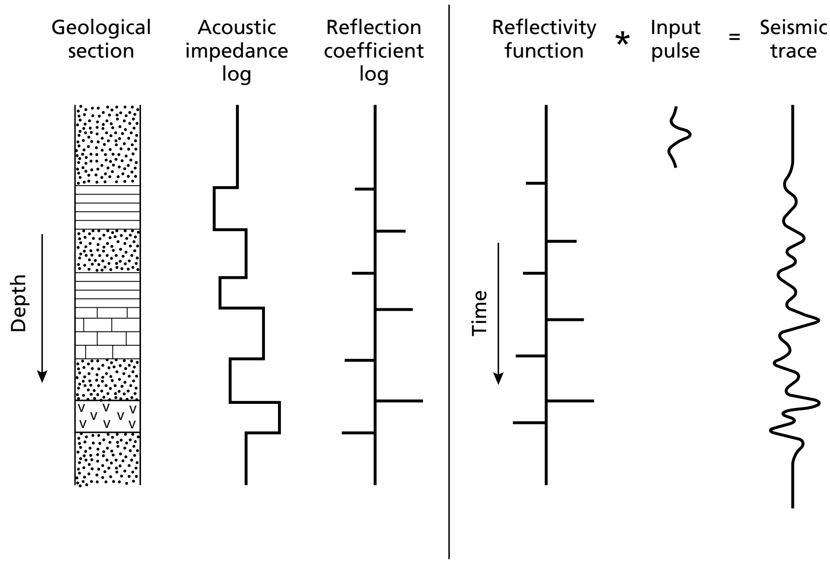

Figure 12: The convolutional model show how a reflection coefficient, given in time, is transformed into the seismic trace used for interpretation. The relationship between geological features and the physical properties registered is also illustrated. From Kearey et al. (2002).

1.3.2 Marine seismic survey

Seismic surveys are a preferred technique for both offshore and onshore operations, with a variety of instruments to be used depending on the research area and expected outcomes. Groundwater reservoirs, location of ore bodies or deposits of coal are all subjects of interest while conducting a seismic survey. The foundation of a building or road has to be evaluated using seismic signals before construction can begin. But one of the most common applications for seismic surveys is through the exploration and development of oil and gas (IOGP and IAGC, 2011) Large interest from petroleum industries has driven the development of this technique, with a wider application area as well as new improved instruments. The search for hydrocarbon-bearing rock is a time consuming operation that is taking place over large regions of the earth, both on land and water. In marine seismic surveys there are foremost three application techniques for retrieving geological information. Ocean bottom seismic (OBS) is a fixed survey technique carried out through a stationary installation positioned on the seabed, capable of measuring S-waves and time-lapse recordings of high quality (Jones, 1999). Vertical seismic profiling (VSP) is a different seismic reflection technique design to utilize boreholes. A number of receivers are lowered into a borehole at known depth to detect reflected sound waves transmitted from the surface (Kearey et al., 2002). Towed streamer seismic is a mobile survey method that is carried out behind a vessel, with a single cable or set of cables towed at a fixed depth. This technique is able to cover any large scaled area (IOGP and IAGC, 2011). A single transmitter or a number of transmitters is positioned behind the survey vessel to generate a sound wave. The most common instrument today is the airgun, where a sealed chamber compressed with air is opened to generate a high-energy pulse. Surrounding water-pressure then interacts with the air bubbles, causing them to oscillate and generate subsequent pulses on their way to the water surface (Jones, 1999; Onajite, 2013). Hydrophone receivers are positioned on the cable towed behind a survey vessel to record the reflected pulses. Encased in a streamer equipped with a GPS, this marine recording equipment uses pressure sensors to detect incoming energy (Aminzadeh and Dasgupta, 2013). The number of airguns and streamers used on a seismic survey may depend on the size of the data acquisition.

For a two-dimensional (2D) seismic survey (Fig. 13), only one seismic cable containing a number of hydrophones is towed behind the vessel. The use of one sound source will give off enough reflections from the subsurface to generate a 2D image directly below the course of the vessel (IOGP and IAGC, 2011). However, since this method only gives a general understanding of the geological structure, it is often used mainly in an early stage of a hydrocarbon reservoir search. A three-dimensional (3D) seismic survey can be conducted after a 2D survey if a more detailed picture of the geological structure below is of interest (Fig. 14). Airguns and a number of seismic cables are towed behind the vessel forming closely spaced 2D lines. Reflected signals generated are recorded by the many hydrophones and later interpolated to create a 3D cube (Kearey et al., 2002; Onajite, 2013). P-cable is a fairly new high resolution way of towed streamer 3D acquisition (Fig. 15) (Petersen et al., 2010). The streamers are instead aligned parallel along a cable towed perpendicular to the ship, forming an arcuate shape. The airgun is positioned right behind the survey vessel.

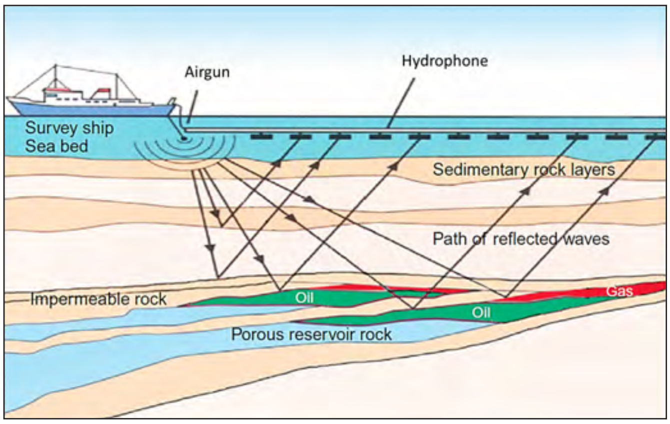

Figure 13: Marine seismic 2D data acquisition using a single airgun and multiple hydrophones. From Aminzadeh and Dasgupta (2013).

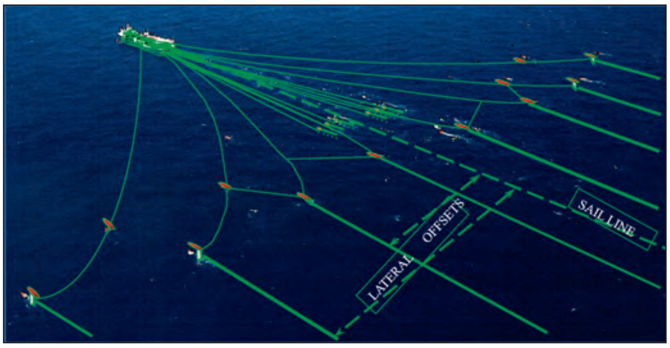

Figure 14: Marine seismic 3D data acquisition. A number of airguns are positioned right behind the survey vessel, and multiple seismic cables, containing hydrophones, are towed parallel with a lateral offset to each other. From Onajite (2013).

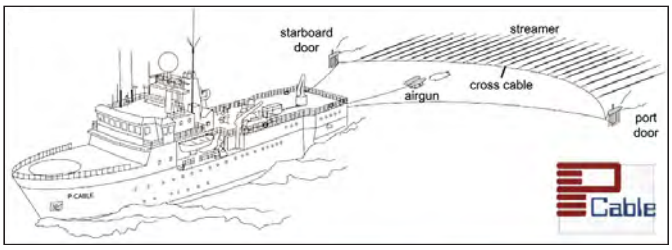

Figure 15: Marine seismic 3D data acquisition using a P-cable. Airguns are positioned behind the survey vessel, and multiple seismic cables, containing hydrophones, are towed parallel along the cross cable. From Petersen et al. (2010).

1.3.3 Direct hydrocarbon indicators

Seismic data sampled at sea are later analyzed using state of the art geological and geophysical interpretation software. By utilizing changes in acoustic impedance (AI), the software is able to display seismic signals as subsurface images (Pless, 2009). An amplitude scale is added to give each value (sample) a distinct colour. Representing the rock and fluid properties of a specific sample, the software is able to display large features as a combination of color tones (Aminzadeh and Dasgupta, 2013).

The presence of fluids in a sedimentary layer will be reflected by the seismic signal as P-wave velocity is drastically reduced due to density differences within the layer (Fig. 16), known as a direct hydrocarbon indicator (DHI) (Kearey et al., 2002; Pless, 2009). A *bright spot* is displayed by an area of higher amplitude reflections than surrounding data, known as an amplitude anomaly. Bright spots may occur at the top and bottom of a hydrocarbon reservoir (e.g. gas-filled sand) (Kearey et al., 2002; Løseth et al., 2009). A *dim spot* can also be the result of a reservoir present. If a porous material, containing water, is overlaid by a layer of lower acoustic impedance, the replacement of water into hydrocarbons would lower the reflection coefficient and thus create a dimmed area (Pless, 2009). A *flat spot* is a horizontal or near horizontal seismic reflection induced by a fluid interface, preferentially a gas-water or oil-water contact (Kearey et al., 2002). *Phase reversal* can occur within a layer when pore water is replaced by hydrocarbons. The significant decrease in acoustic impedance, caused by the replacement, will be displayed as a change in reflection polarity from a positive to negative phase (Løseth et al., 2009; Pless, 2009).

The physical properties of hydrocarbons may also cause acoustic energy to be absorbed or scattered. (Kjerkreit, 2014). *Acoustic masking* is referred to an area of faint or absent seismic reflectors, caused by the attenuation in acoustic energy. Amplitude shadow, low frequency shadow and vertical structures, known as seismic chimney/pipe, are recorded as acoustic masking (Pless, 2009). Hydrocarbons are also known to reduce the P-wave velocity of the returning signal, with reflector displacement created by the longer two-way travel time (Løseth et al., 2009). *Pull-down* or *push-down* is an effect caused by velocity sag, where an area containing hydrocarbons are recorded as deeper located then its surrounding layer,

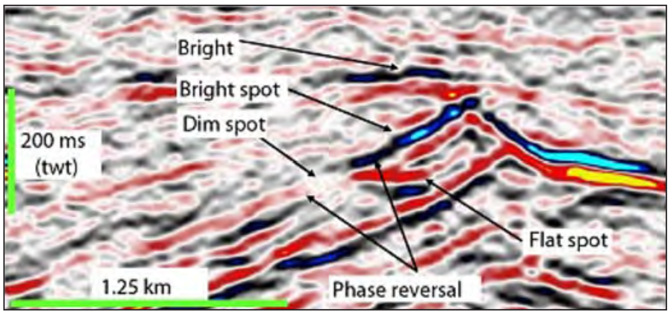

Figure 16: Seismic indicators of hydrocarbons present within a reservoir. From Løseth et al. (2009).

due to the slower P-wave velocity reflected (Hustoft et al., 2007; Kjerkreit, 2014). *Pull-up* will instead occur where there is a zone of high velocity, e.g. a salt dome (Pless, 2009). Bottom-simulating reflectors (BSR) are high amplitude reflectors, often found as parallel or near parallel to the sea floor. A BSR can originate from a diagenesis transformation of siliceous-rich sediments or work as an indicator for the base of a gas hydrate stability zone (GHSZ). This is the transition zone where current temperature and pressure no longer can support gas as a fluid state but entraps them into gas hydrate formations (Hustoft et al., 2007; Kjerkreit, 2014).

Seismic data can be analyzed in a number of different ways depending on what sort of questions is attempted to answer. A seismic attribute may extract or derive anomalies by applying a mathematical analysis method on the original seismic data, in order to highlight lithological, physical or reservoir properties (Aminzadeh and Dasgupta, 2013). These properties of a seismic wave are analyzed for its geological signature, to provide specific quantities of dynamic, geometric, kinematic and statistical characteristics hidden within the seismic data (Kearey et al., 2002; Li and Zhao, 2014). There are a number of seismic attributes to be applied while extracting specific features. Amplitude changes are an interesting attribute when interpreting lithological settings and reservoir capacity (Li and Zhao, 2014). A reflected wave illustrates the reflected coefficient of an interface, given by the physical properties within the formation. The appearance of an amplitude anomaly (e.g. bright spot or flat spot) along this seismic line could indicate a change in porosity or pore fluid (Kearey et al., 2002; Aminzadeh and Dasgupta, 2013). Root-mean-square (rms) amplitude is a statistical function used to isolate specific geological features from surrounding background features. It is the amplitude anomalies within a layer that contain the most interesting information. A layer previously defined can be analyzed using the rms method. A sampling interval (Δt) within the layer, (t_1) and (t_2), is set to define the analysis time window. Every amplitude (A) within this window will be sampled and recalculated into a rms amplitude value (A_{rms}), given by:

$$A_{rms} = \sqrt{\frac{\Delta t}{t_2 - t_1} \sum_{t_1}^{t_2} A^2(t)} \qquad (1.13)$$

Amplitude anomalies within this layer will then be more clearly distinguished on a map, making the location and quality of possible hydrocarbon reservoirs easier to interpret (Pless, 2009; Haavik and Landrø, 2014; Li and Zhao, 2014).

1.4 Well data

Major petroleum companies such as A/S Norske Shell, Lundin Norway AS, Norsk Hydro Produksjon AS and Statoil Petroleum AS have all drilled on Loppa High and the adjacent basins (NPD, 2015). A well is drilled due to a number of reasons; it could be to obtain improved stratigraphical control in an area or to identify the physical and chemical properties of a sedimentary body. Another reason is the presence of oil and gas, how high the total organic carbon (TOC) concentration is within sedimentary strata and if the seismic data were accurate (McCarthy et al., 2011; NPD, 2015). A large number of wells are located along the Bjørnøyrenna- and the Ringvassøy-Loppa Fault Complex, Barents Sea, due to the highly altered geological structure and the hydrocarbon related features that this may generate (Bjørlykke, 2010; NPD, 2015). Two of these drilled wells are the well 7220/5-1, located on the Bjørnøyrenna Fault Complex, and the well 7220/6-1, located to the ENE along the west of Loppa High, Barents Sea (Fig. 17). The sedimentary strata penetrated by these two wells were identified as six lithostratigrapic units formed during different geological periods.

1.4.1 Nordland Group

The Nordland Group is a Quaternary unit accumulated in a bathyal to glacial marine depositional environment. The lithology consist of clay and sand (coarsening upwards) that grade into claystone and sandstone. Cobbles and boulders are present with clay in the upper strata. The Nordland Group is also present in the Norwegian- and North Sea, where it's been dated back to Early and Middle Miocene (Ryseth et al., 2003; NPD, 2015).

1.4.2 Sotbakken Group

The Sotbakken Group was formed in Thanetian (Late Paleocene) to Lutetian (Middle Eocene), with minor Oligocene sequences present in the western parts of the Barents Sea. The Shelf was subjected to a transgressional phase in the mid-Paleocene, which brought with it sublittoral to deep shelf claystone to mudrock accumulations; containing minor siltstone and carbonate horizons. Large quantities of the Sotbakken Group have been eroded throughout the Barents Shelf, but younger sequences are found to be preserved in the Tromsø Basin and the Ringvassøy-Loppa Fault Complex. The Torsk formation is a sedimentary subunit of the Sotbakken group that ranges from Late Paleocene to Oligocene (Ryseth et al., 2003; NPD, 2015).

1.4.3 Adventdalen Group

Adventdalen Group is a Late Jurassic to Early Cretaceous unit composed of sandstone, siltstone and shale. It is further divided into six formations: the Fuglen, Hekkingen, Klippfisk, Knurr, Kolje and Kolmule formations. The Fuglen and Hekkingen formations are important hydrocarbon source rocks from the Upper Jurassic succession. The group has been identified on Svalbard and throughout the Barents Shelf (NPD, 2015).

1.4.4 Kapp Toscana Group

The Kapp Toscana Group is the result of Ladinian (Middle Triassic) to Bathonian (Middle Jurassic) sedimentary deposits in a near-shore, deltaic environment, with shallow marine to coastal reworking. A sedimentary composition of sandstone, siltstone and shale dominate in the Group. Five formations are recognized on the Barents Shelf: the Snadd, Fruholmen, Tubåen, Nordmela and Stø formations. The Snadd Formation consists of shales with siltstone and sandstone interbedded, where limestone and calcareous interbeds occur in the lower to middle parts of the formation. It was formed in Ladinian to early Norian (Late Triassic) as relatively distal marine deposits (NPD, 2015).

1.4.5 Gipsdalen Group

Gipsdalen Group is a Serpukhovian (Early Carboniferous) to Sakmarian (Early Permian) unit that was formed in stages by terrestrial and marine depositional environments. The non-marine stage between Serpukhovian and Bashkirian (Late Carboniferous) was formed as alluvial fan and braided river deposits; composed of red bed sandstone, siltstone and conglomerate. The marine stage is a Bashkirian to Sakmarian formation of mixed carbonates and siliclastic deposits; containing conglomerate, sandstone and shale. Three formations present: the Ugle, Falk and Ørn formations. The Ugle formation belongs to the terrestrial stage while the Falk and Ørn formations were deposited during the marine stage (Larssen et al., 2002; NPD, 2015).

1.4.6 Basement

The basement consists of low- to high metamorphic graded rocks, including metamorphosed igneous rocks. Samples gathered from drilled wells have been dated using K/Ar, Ar/Ar and Rb/Sr isochron dating and results indicated the top basement to originate from pre-Devonian rocks (NPD, 2015).

1.4.7 Well 7220/5-1

The well is located at 72°31’ 0.67”N 20°20’ 29.15”E of the Bjørnøyrenna Fault Complex, neighboring the northern Polheim Sub-platform, Barents Sea. It was drilled by Statoil Petroleum AS in January to Mars 2012 in order to obtain evidence of oil and gas volumes in the Skrugard middle segment, an operation that generated good results (NPD, 2015). A gas-oil contact and a oil-water contact were discovered in Jurassic sandstone (Skjelle et al., 2012). The drill went 1740 m down before stopping in the Kapp Toscana Group; penetrating the seabed at 428 m. Nordland Group was reached at 428 m, Sotbakken Group at 478 m and the Adventdalen Group at 1035 m. The Kapp Toscana Group was first penetrated at 1337 m below the ocean surface. Depth indications given in the well data are measured depth from the elevation of the rotary kelly bushing (MD RKB), 40 m for well 7220/5-1 and 25 m for well 7220/6-1 (NPD, 2015).

1.4.8 Well 7220/6-1

The well is located at 72°33’ 12.56”N 20°59’ 26.86”E of the western Loppa High, Barents Sea. It was drilled by Norsk Hydro Produksjon AS in January to Mars 2005 to test reservoir properties and hydrocarbon migration in the Permian and Carboniferous strata. The seabed was reached at 394 m and drilled down to 1540 m. Three sedimentary groups were penetrated before reaching top basement at 1483 m; Nordland Group at 394; Kapp Toscana Group at 476 m; Gipsdalen Group at 1138 m (NPD, 2015).

Age		Group/Formation	7220/5-1	7220/6-1
Sub-Era	Period		Top Depth (m)	Top Depth (m)
Cenozoic	Neogene - Quaternary	**Nordland Group**	428	394
	Paleogene	**Sotbakken Group**	478	Missing
		Torsk Formation	478	
Mesozoic	Cretaceous	**Adventdalen Group**	1035	
		Kolmule Formation	1035	
		Kolje Formation	Missing	
		Knurr Formation	1238	
		Klippfisk Formation	Missing	
	Jurassic	Hekkingen Formation	1296	
		Fuglen Formation	1312	
		Kapp Toscana Group	1337	476
		Stø Formation	1337	Missing
		Nordmela Formation	1415	
	Triassic	Tubåen Formation	1578	
		Fruholmen Formation	1695	
		Snadd Formation		476
Paleozoic	Permian	**Gipsdalen Group**		1138
		Ørn Formation		1138
	Carbon-iferous	Falk Formation		1436
		Ugle Formation		Missing
	Pre-Devonian	Basement		1483

Figure 17: Well data for 7220/5-1 and 7220/6-1 with lithostratigrapic units identified from a given depth (m MD RKB). Data obtained from NPD (2015), but are not rendered to illustrate its representative epoch.

2. Material and methods

Marine geophysical data covering large areas of the Loppa High with surroundings were provided by Lundin Norway AS. An outline for the area of interest had to be defined since some of the datasets covers a too large area to be analyzed, considering the time-span of this project. The study area represents a 2054 km^2 rectangular surface area located along the west part of central Loppa High, including the northern half of the Polheim Sub-platform as well as parts of the Bjørnøyrenna Fault Complex. The study area is 51*40 km long and extends in a NNE-SSW direction. The database consists of well data, seismic reflection 2D and 3D data sets (Fig. 18) as well as multibeam echosounder data (Fig. 19) and water column data. The coordinate system used in this project is the European Datum 1950 (ED50) UTM Zone 34N. All data used for this project are listed in Table 1, Appendix D.

2.1 Well data

Well data were added to the study in order to obtain an overview of the depositional environments and lithology of the area. Two wells were selected within the study area; well 7220/5-1, located central along the western edge (Fig. A5); and well 7220/6-1 (Fig. 21), drilled in the northern region of the area. These two wells were selected due to their geological locations and because both penetrate sedimentary formations known to host source rocks. The names given to the interpreted seismic layers were deduced from the known age of a sedimentary unit, with the corresponding sedimentary formation, penetrated by the wells. The five different lithostratigrapic units and the basement referred to in this study exhibits different depositional patterns and could be named via an exclusion method, also the Kingdom software used for interpretation had sedimentary formations highlighted along the well 7220/6-1.

2.2 Seismic survey

Two sets of 2D seismic reflection lines (NBRD07-234838 and NBR10-338364) were analyzed. They are 61.1 km and 36.8 km long, extending NNW-SSE and WNW-ESE respectively across the study area (Fig. 18). The NBRD07 and the NBR10 survey lines were collected in 2007 and 2010 respectively. There are three survey areas containing 3D reflection data: the LN12M01, NH0372 and Pcable area B PL609 data sets (Fig. 18). The survey area of the LN12M01 is 1513.4 km^2 and the largest of the three datasets, covering most of the study area. The LN12M01 data set consist of two separate events of data acquisition; the first survey taking place between June and August 1998 on board the vessel M/V Seisranger; and the second survey occurring between September and October 2011, on board the vessel M/V Artemis Arctic (Barrie et al., 1998; Billard, 2011). The second 3D reflection survey, NH0372, is a high resolution cube acquired in July 2013 on board the vessel M/V Sea Explorer. Located in the upper right region of the study area, it covers 22.4 km^2. The third 3D reflection dataset, Pcable area B PL609, cover a 10.2 km^2 rectangular shaped area located to the west of NH0372. The seismic survey was carried out 2012 on board the vessel FF Helmer Hanssen, using a P-cable instrument for data acquisition.

Seismic 2D profiles were constructed in each of the three 3D data sets; one line striking N-S (Fig. A2) and three lines striking W-E (Fig. A3-A5) in the LN12M01 data set; one line WNW-ESE for the NH0372 data set (Fig. B1); and one line striking WNW-ESE for the Pcable area B PL609 data set (Fig. C1). These 2D seismic profiles were generated to displays reflected layers and depositional features registered in the surveys.

Individual layers were identified and mapped using the seismic and geological interpretational software IHS Kingdom vers. 8.8. Each layer obtained from the three different 3D datasets was interpolated to create bathymetry maps showing the sedimentary layers distribution. Volume attribute layers were generated using the statistical function "VATrms" in order to obtain color-coded amplitude illustrations of the three data sets. The interpolated seismic layers were also used to create isopach layers; a time-difference interval obtained by subtracting the seismic signals travel time between two layers. Geological fault layers were created for the heavily deformed and tilted layers; using "Polygon Autopicking" and the digitizing tool "3D Hunt". Time slice layers were generated separately for the three 3D seismic cubes, with a slice interval ranging between 20 and 100 ms.

The bathymetry, amplitude and isopach layers as well as the generated time slices created in IHS Kingdom were exported into the geographic information system (GIS) and its module ArcMap 10.2.1 for further map developments and exportation options. Polylines were added to the autopicking and time slice layers in order to highlight the faults visible in each layer. The faults were color-coded according to their orientation; NNW-SSE and NNE-SSW are red; NNW-SSE and WNW-ESE are yellow; WNW-ESE and ENE-WSW are blue; NNE-SSW and ENE-WSW are green. Main structural elements of the SW Barents Sea and well data used in ArcMap were obtained from the Norwegian Petroleum Directorate (NPD) (NPD, 2015). The location of bacterial mats and carbonate crusts discovered within the study area were obtained from the Lundin Norway AS.

2.3 Multibeam echosounder survey

Additional datasets containing multibeam bathymetry and water column data were offered by Lundin Norway AS to help with the seismic reflection-data research. The multibeam bathymetry data consists of five previously interpolated files with a cell resolution of 1-3 m (Fig. 19). The bathymetry surveys do only cover parts of the study area and were thus of limited use. The water column data consists of 29 lines, located foremost around the Pcable survey area (Fig. 18). The data was analyzed using the module FMMidwater of the geo-spatial processing and analysis software suite Fledermaus, vers. 7.4.0.C.

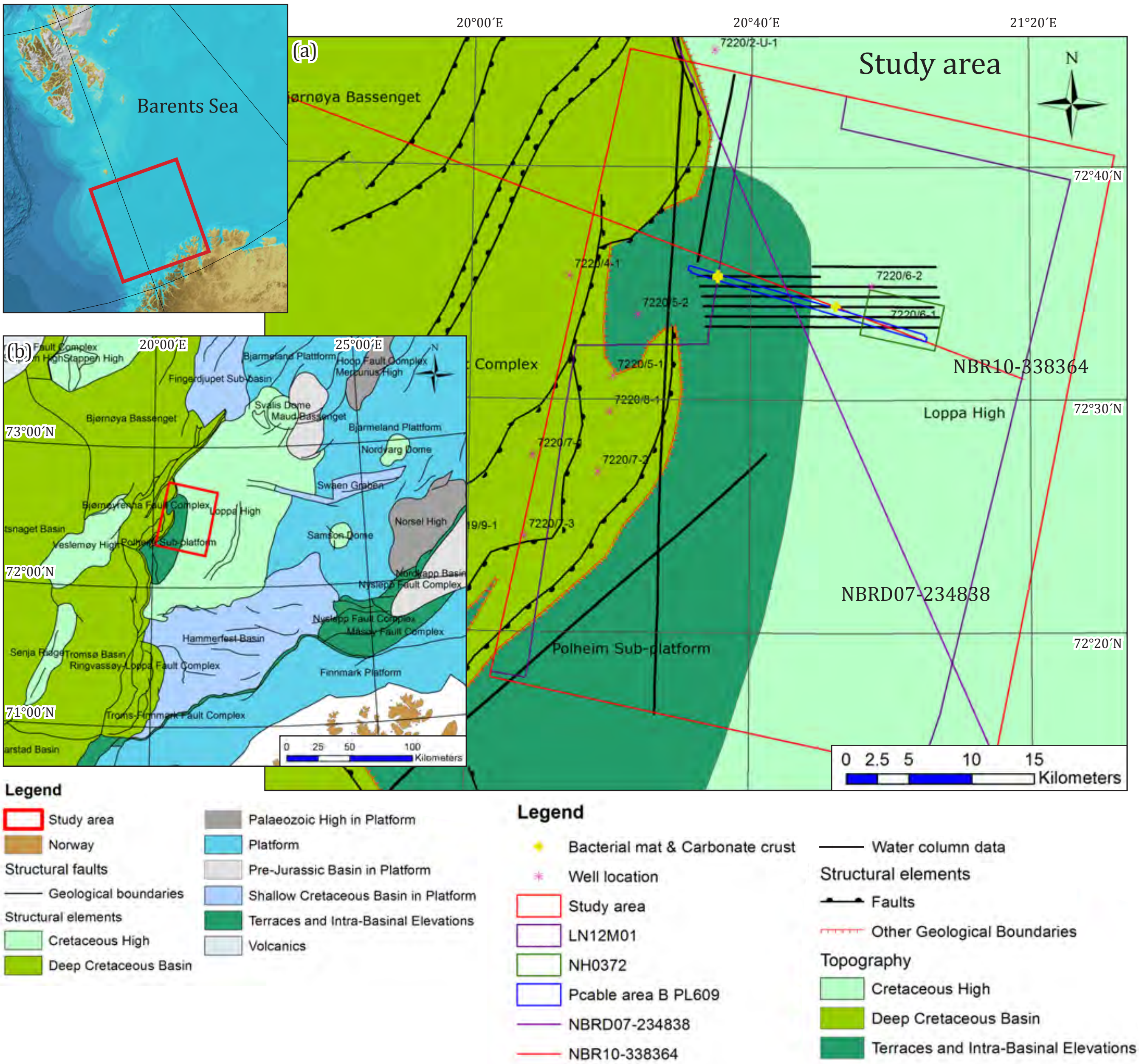

Figure 18a: Map showing the three survey areas located within the study area, together with alignments of the two survey lines. Wells drilled in the area is given as well as the location of previously known bacterial mats and carbonate crusts (courtesy by the Lundin Norway AS). The water column data used in this study are marked as black lines. (b) The structural elements map in the lower left corner displays structural elements and fault movements of the SW Barents Sea. Based on the NPD (2015). The reference map in the upper left corner are from IBCAO (Jakobsson et al., 2012), with the approximate location of the structural elements map marked in red.

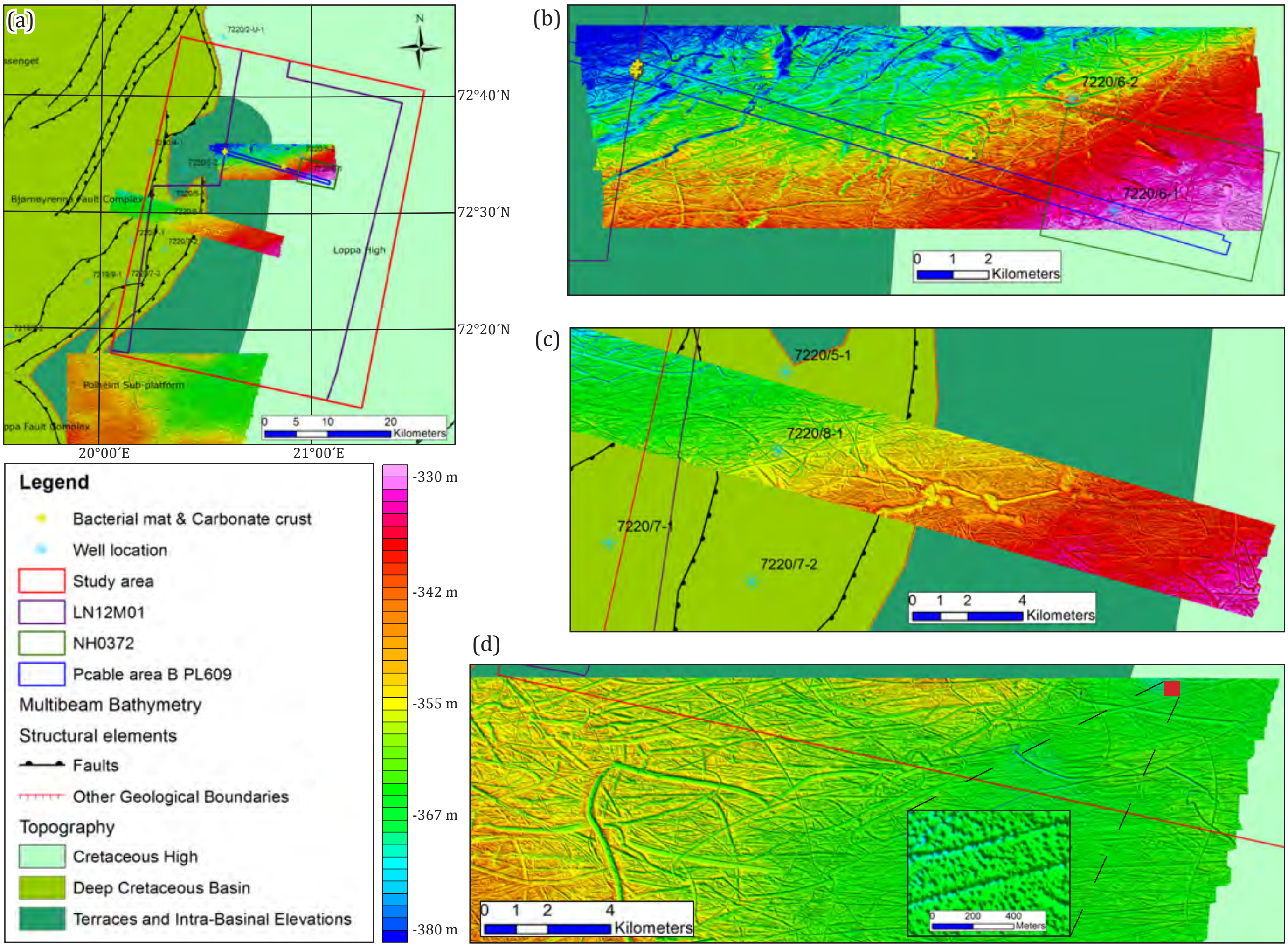

Figure 19a: Map showing the three survey areas located within the study area, together with three areas of multibeam bathymetry areas. Wells drilled in the area as well as the location of previously known bacterial mats and carbonate crusts. (b-d) The three bathymetry layers are illustrated separately to the right. The location of the zoomed in area positioned in the left corner of the lower bathymetry layer are marked with a red box. The color ramp gives the approximate depth (m) below seabed for the multibeam bathymetry interpolations.

3. Results

Seismic interpretations were carried out on 2D and 3D marine reflection data sets, comprised of two seismic lines and three seismic cubes. The individual layers were then correlated with previous results from well data drilled in the area. Multibeam data and water column data were also used to visualize previous and ongoing gas emissions at the sea floor.

3.1 2D seismic profiles

The two survey lines, NBRD07-234838 and NBR10-338364 (Fig. 20 & 21), were analyzed in order to obtain an understanding of the sedimentary strata located within the study area. Data from well 7220/5-1 (Fig. A5) and 7220/6-1 (Fig. 21) were correlated with the six layers mapped within the 2D seismic profiles. These layers were selected for their characteristic features and named accordingly: seabed, URU, Triassic reflector 2, Triassic reflector 1, Late Carboniferous and top basement (pre-Devonian). Deposited reflections above URU were found to belong to the Nordland Group (Quaternary) and the two Triassic reflectors highlighted below URU, seen in the area of well 7220/6-1, were interpreted to belong to the Kapp Toscana Group (Triassic). Underneath follows the Gipsdalen Group (Late Carboniferous) before reaching top basement somewhere at pre-Devonian time. The Gipsdalen Group is according to the NPD (2015) deposited between Early Carboniferous and Early Permian time, but will here be referred to as Late Carboniferous age. The low frequency 2D seismic profiles do not fully reflect the top strata, leaving the interpretation above URU to be carried out in the 3D seismic data. The strata of URU, Late Carboniferous and top basement were identified as impenetrable, non-permeable materials (positive values) while the layers marked as Triassic reflectors 1 & 2 both contain permeable materials capable of transporting fluids (negative values). The sedimentary strata of Triassic age and Late Carboniferous, as well as the top basement, exhibits a sloping structure towards W-SW, coated with faults. Faults are visible on both the 2D seismic profiles, marked by black lines. Strata located on the west side of this fault have undergone deformations of heavy faulting, causing this region to be difficult to interpret. The contacts of gas-oil and oil-water is visible in the WNW of the NBR10-338364 seismic profile, at 1460 ms respective 1540 ms (Fig. 21).

3.2 3D seismic profiles

The layers identified in the 2D seismic lines were correlated to the 3D data sets. Eight additional layers were mapped above URU, referred to as Lower Pleistocene 0-7. The Pleistocene layers were all selected for their soft sediment features of high permeability (negative values), layers of low permeability located in between were ignored as they do only limit the fluid migration. The layer of Lower Pleistocene 0 was first located in the end of this study, in survey area NH0372, and came to be named thereafter. Every layer tracked in Kingdom where interpolated to create paleo-bathymetry maps and isopach maps. Layers containing permeable materials were also processed to generate amplitude maps (RMS). Time slices where constructed throughout each of the three 3D cubes to help determine fluid migration pathways.

3.2.1 Survey area LN12M01

The paleo-bathymetry maps reflect form and features of the sedimentary layers mapped inside survey area LN12M01. The seabed is located at 431-587 ms below the sea level and with a downhill slope towards north (Fig. A6). The irregularly oriented linear patterns visible are iceberg ploughmarks (Haavik and Landrø, 2014). Seven layers of Pleistocene deposits were registered beneath the seabed (Fig. A7-A13), where the Lower Pleistocene 1 was the only actual layer found to cover most of the survey area (Fig. A13). The Pleistocene layers have an S-N sloping bathymetry with many of the elevated areas located in the SW or SE corner. The Lower Pleistocene 7 is a replica of the seabed, located only 14.6 ms deeper, created to identify amplitude anomalies as shallow as possible (Fig. A7). The low permeability layer of the URU has a sloping pattern to the north (Fig. 22), with a curved depression located in the bottom half of the map. A feature also seen in the Lower Pleistocene 1. Layers located below URU have a W-SW tilted structure that is cut off by a major N-S extending fault. The Triassic reflector 2 has several sharp elevation changes identified along the west side of the N-S striking fault and a gap located in the upper half of the map (Fig. A15); eroded and replaced by URU. None of the layers; Triassic reflector 1 (Fig. A16); Late Carboniferous (Fig. A17) or top basement (Fig. A18) could be mapped on the west side of the N-S extending fault. Elongated features were detected in the SW corner

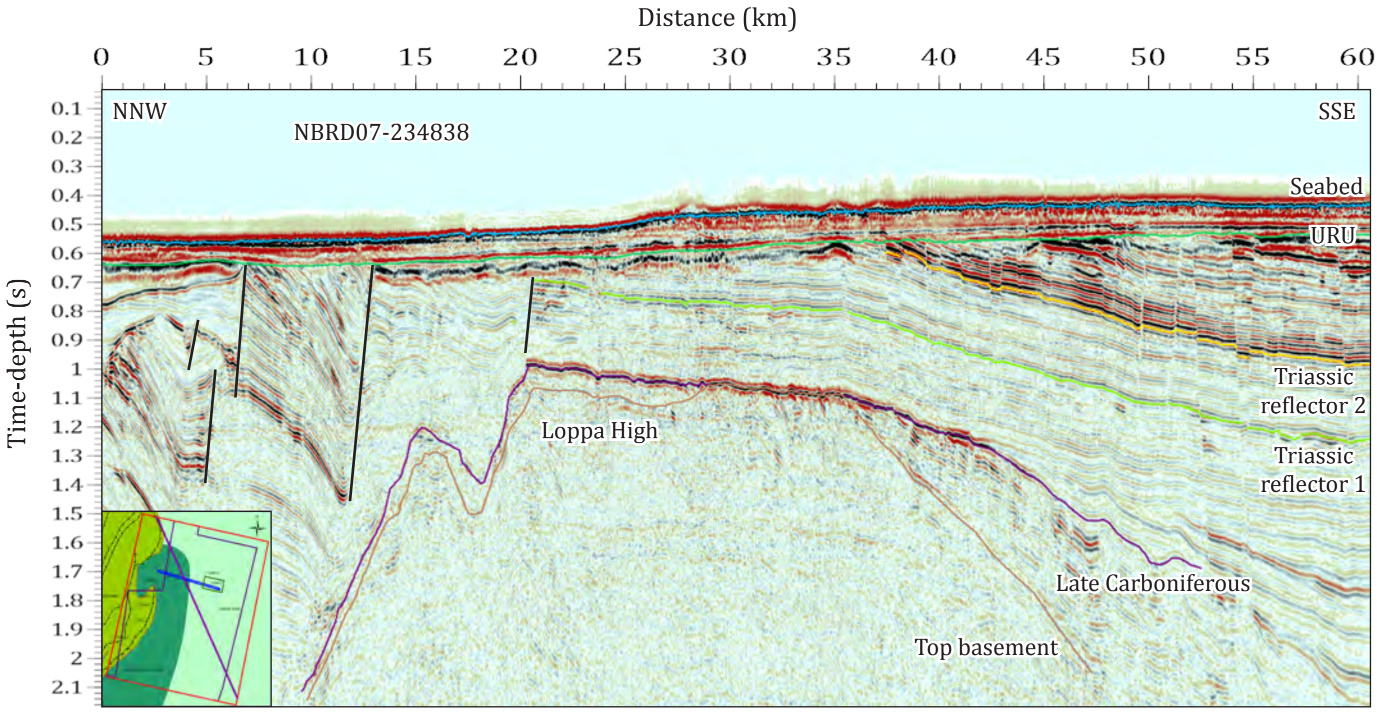

Figure 20: Seismic profile of the NBRD07-234838 survey line, located within the study area, strikes NNW-SSE. Six layers are highlighted: the seabed (blue); URU (green); Triassic reflector 2 (yellow); Triassic reflector 1 (neon green); Late Carboniferous (purple) and top basement (brown). Major faults are highlighted in the NNW area by black lines. The map in the lower left corner displays an overview of the study area and the LN12M01 study areas (Fig. 18), with the orientation of the 2D seismic profile (purple line).

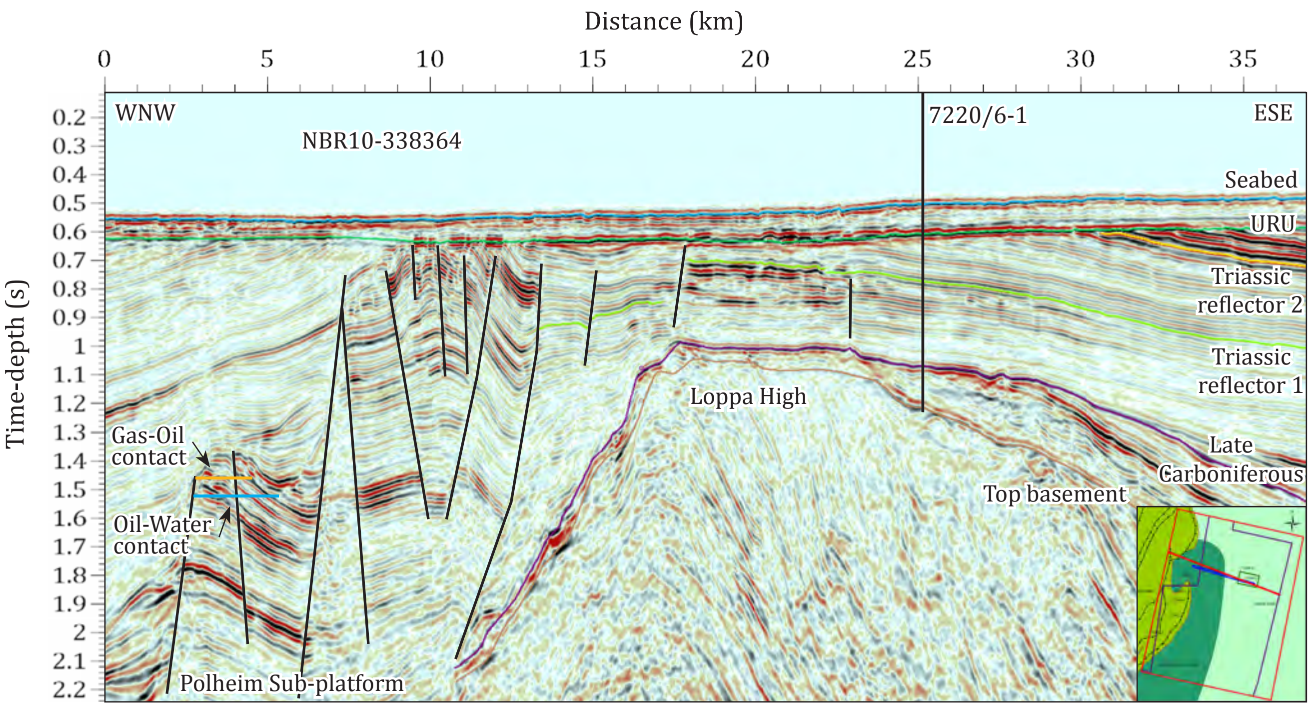

Figure 21: Seismic profile of the NBR10-338364 survey line, located within the study area, strikes WNW-ESE. Six layers are highlighted: the seabed (blue); URU (green); Triassic reflector 2 (yellow); Triassic reflector 1 (neon green); Late Carboniferous (purple) and top basement (brown). Major faults are highlighted in the WNW area by black lines. The well 7220/6-1, with drilling depth, is illustrated in the seismic profile. A gas-oil contact (orange) and an oil-water contact (blue) are illustrated in the WNW region. The map in the lower right corner displays an overview of the study area and the LN12M01 study areas (Fig. 18), with the orientation of the 2D seismic profile (red line).

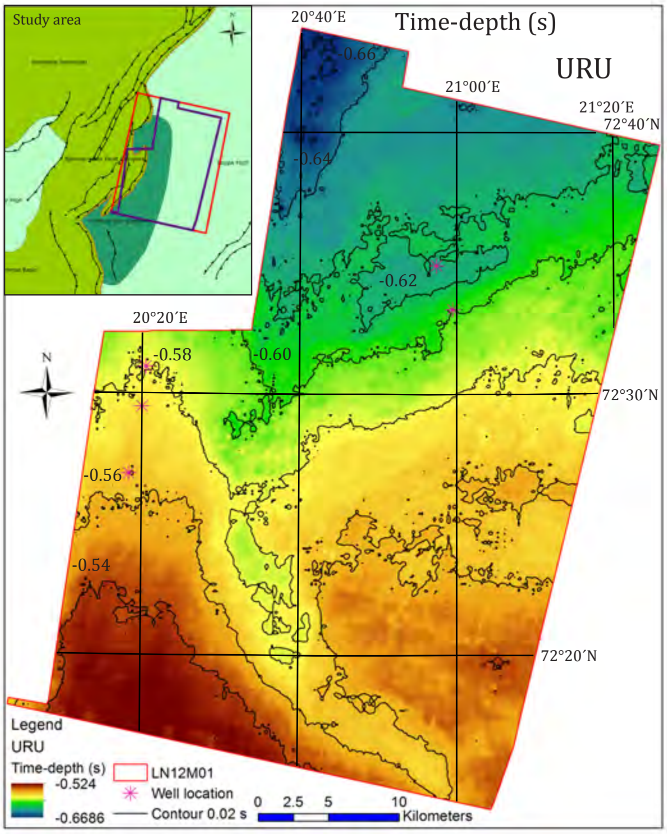

Figure 22: Paleo-bathymetry map of the UR, generated from the LN12M01 survey area. The depth is presented in seconds and the contour lines illustrate elevation changes for every 0.02 s. Pink dots mark the location of drilled wells. See also figure A14. The map in the upper left corner displays an overview of the study area (Fig. 18).

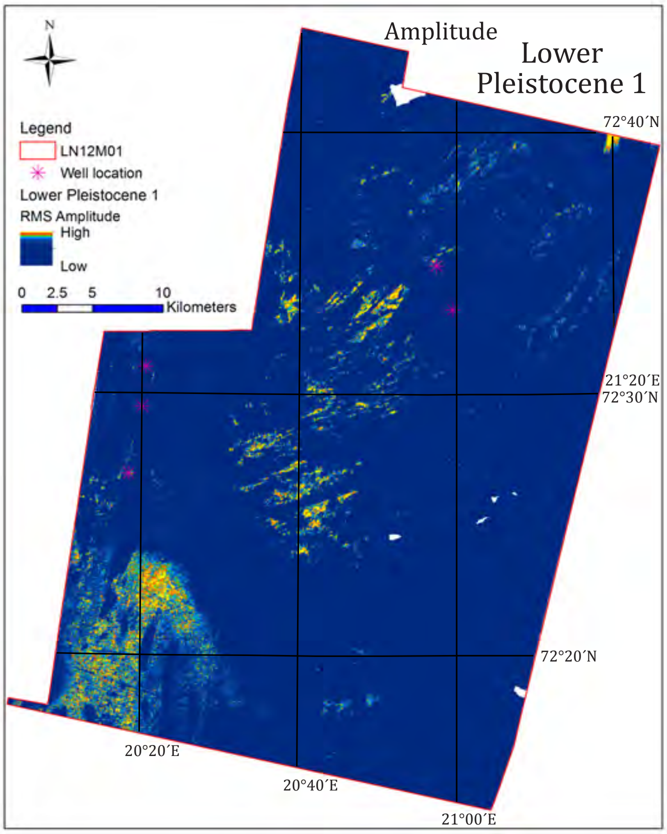

Figure 23: Amplitude map (RMS) of the Lower Pleistocene 1, generated from the LN12M01 survey area. Amplitude anomalies are illustrated in red to yellow colors. Pink dots mark the location of drilled wells. See also figure A26.

of the LN12M01 survey area, extending N-S between 608 and 833 ms. As these features cannot be correlated to any well units or seismic reflectors, they will be referred to as gas hydrates (Fig. A19).

There are nine amplitude maps generated for the LN12M01 survey area, seven above the URU and two below. In the Lower Pleistocene 7 these anomalies are more focused on the western half as well as some minor areas along the northern edge (Fig. A20). The Lower Pleistocene 6 has these anomalies more evenly spread over the layer, with one more concentrated area located in the SE region (Fig. A21). Yellow linear features are present in the southern half, bearing W-E. The Lower Pleistocene 5 (Fig. A22) has areas of higher amplitudes in the SW regions while the Lower Pleistocene 4 (Fig. A23) has most of these areas in the northern parts. The majority of anomalies identified in the Lower Pleistocene 3 (Fig. A24) are of the northern and southern regions while the Lower Pleistocene 2 (Fig. A25) has these areas more centrally located. In the Lower Pleistocene 1 was high amplitudes found in the SW corner, in centrally spread areas as well as in one area of the NE corner (Fig. 23). The Triassic reflector 2 has high concentrations of high-amplitude reflections along the elevated edge to the URU (Fig. A27), where the Triassic reflector 1 has three larger areas located in the central to northern parts not far from the N-S striking fault (Fig. A28).

Fault charts were generated for the Triassic reflectors 1 & 2 to display movements present within each layer (Fig. A29 & A30). The Triassic reflector 2 has N-S and NE-SW striking faults located west of the major N-S fault, intersected by minor NW-SE and W-E striking faults. On the east side there are NE-SW and W-E striking faults present, as well as NW-SE striking thrust faults located in the SE region. The Triassic reflector 1 was found to contain NE-SW and W-E striking faults east of the N-S striking fault, with NW-SE striking thrust faults located in the SE region. However, on the west side, the layering was too faulted and badly reflected to be mapped. No faults were found in the Lower Pleistocene deposits using this color ramp.

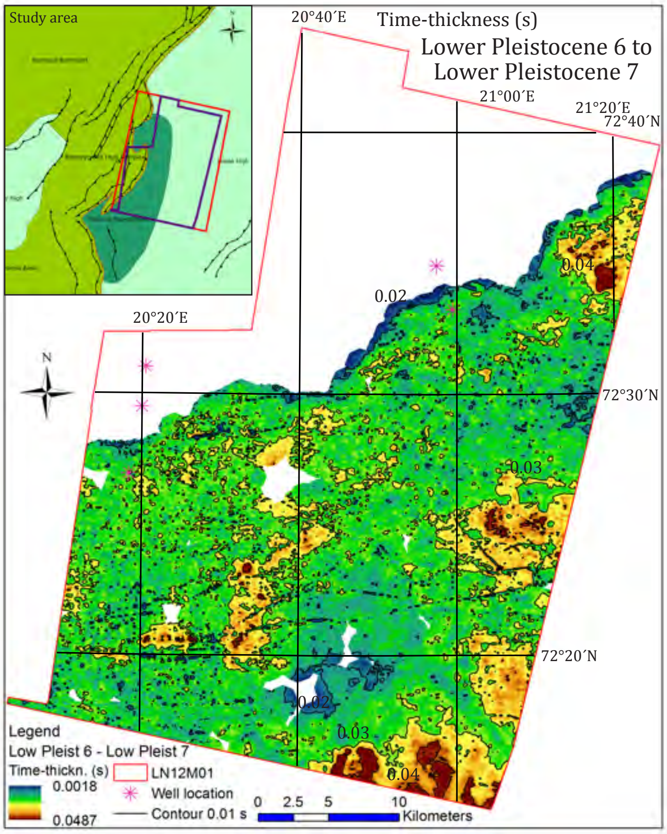

Figure 24: Isopach maps showing the time-depth differences between the Lower Pleistocene 6-7, generated from the LN12M01 survey area. The thickness is presented in seconds and the contour lines illustrate elevation changes for every 0.01 s. Pink dots mark the location of wells. See also figure A31. The reference map displays an overview of the study area (Fig. 18), with the LN12M01 survey area (purple).

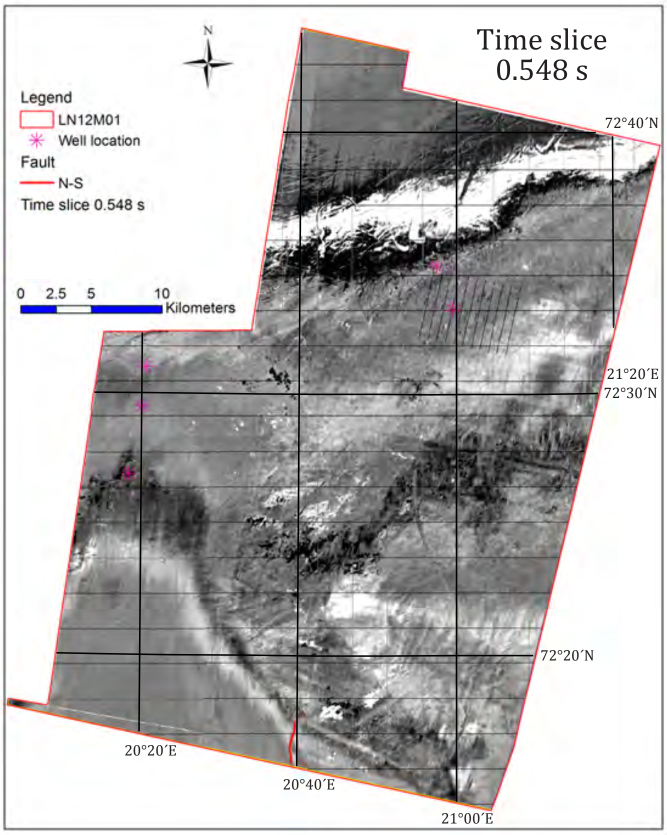

Figure 25: Time slice velocity maps cutting the LN12M01 survey area horizontally at 0.548 s. Black color reflect areas of high permeability and white areas of low permeability. The fault is highlighted using a color coded orientation. Pink dots mark the location of drilled wells. See also figure A47.

Isopach maps generated between the seabed, the Lower Pleistocene layers and the URU have a thickness variations of up to 48.7 ms (Fig. A31-A42). The thickest areas may vary between layer to layer but are in general thicker in central to NW or NE regions, except for the Lower Pleistocene 6-7 that exhibit elevated areas in the central regions as well as along the eastern edge of the survey area (Fig. 24). The sedimentary thickness between the seabed and the URU is low (up to 80 ms) along the western edge and SW corner as well as in the northern regions (Fig. A38). Thick areas, 120-148.8 ms, occur in the central to eastern regions with four pronounced areas rendering 110 ms. The isopach map of The Triassic reflector 2 to the URU has low sedimentary levels in the center and increases towards both sides, east and west (Fig. A39), while the sedimentary thickness between the Triassic reflector 1 & 2 have a volume increase from east to west (Fig. A40). The Late Carboniferous to the Triassic reflector 1 has an N-S striking central sedimentary depletion where thickness increases towards west and east (Fig. A41). The isopach map of the top basement to the Late Carboniferous has a sedimentary increase towards west (Fig. A42), with the thickest areas located in the north and southwest regions of the LN12M01 survey area.

Time slice velocity maps were generated to help identify faults and possible fluid migration pathways. Each map consist of two separate parts (print screened from Kingdom) that are geotagged together using ArcMap, which caused the shading to differ some. Figure A43 display a seismic profile of the LN12M01 survey area, striking center W-E. Red lines mark the horizontal depth for the generated time slices. The quantities of fourteen time slices were generated between 472-1100 ms (Fig. A44-A57), where identified faults were highlighted and color-coded to their orientation. The occurrence of a fault is visible as sedimentary displacements along a line, here highlighted in various colors. One single fault was first identified at 548 ms (Fig. 25), central along the south side striking N-S. The number of faults then quickly increased, N-S striking faults occurred along the center of the time slices and with NW-SE, W-E and NE-SW orientated fault located on both sides. Faults in the northern region were first identified at 652 ms (Fig. A51), foremost N-S and NE-SW striking. Faults were identified down to 1100 ms (Fig. A57), located foremost at center to west regions. The white elongated feature stretching NE-SW in the northern half of the study area, across the 472 ms, 500 ms and 524 ms time slices, is the seabed reflection (Fig. A46 - A48). The transition to the URU is visible between 652 ms and 576 ms (Fig. A48-A51), presented in bright white color as it reflects the low permeability properties of its material. The bright white areas visible in the center of the 1100 ms and 1000 ms time slices are the outer reflector of the Late Carboniferous deposits and the tilted stratification to the east are of Triassic origin (Fig. A56 & A57).

The 2D seismic profiles generated from the LN12M01 survey area exhibits a depression feature in the SW region of the URU (Fig. A2-A4). Fault movements was found above the Polheim Sub-Platform, below URU (Fig. A5).

3.2.2 Survey area NH0372

The paleo-bathymetry maps of survey area NH0372 consists of eight layers. The seabed is located 479-533 ms below the sea level; sloping NW with visible iceberg ploughmarks (Fig. B2). There are four Pleistocene layers identified, one of which did not occur on the LN12M01 data set. The Lower Pleistocene 4 (Fig. B3) has a north downward inclination while the Lower Pleistocene 0, 1 & 3 (Fig. B4-B6) all slopes toward the NW. The sedimentary layer of URU (Fig. B7) has a NW downward inclination whiles the Triassic reflector 1 (Fig. 26) and the Late Carboniferous (Fig. B9) layers slopes to the W-SW, both exhibiting a 140 ms drop-off.

Amplitude maps of the Lower Pleistocene 0, 1, 3 & 4 (Fig. B10-B13) as well as the Triassic reflector 1 (Fig. 27) was generated within the survey area. The Lower Pleistocene 3 and 4 have anomalies N-S centrally occurring, followed by areas in the NW and NE regions. The Lower Pleistocene 0 and 1 have several high amplitude areas in the NW corners, although the Lower Pleistocene 0 has a more disperse area. The Triassic reflector 1 exhibits a wide area of amplitude anomalies south of the NW corner.

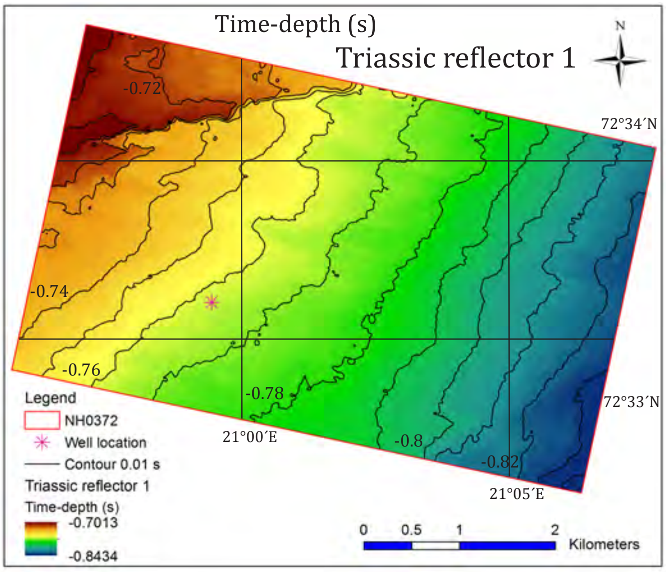

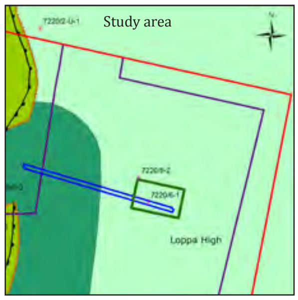

Figure 26: Paleo-bathymetry maps of the Triassic reflector 1, generated from the NH0372 survey area. The depth is presented in seconds and the contour lines illustrate elevation changes for every 0.01 s. See also figure B8. The pink dot mark the location of the well 7220/6-1. The reference map to the right displays an overview of the NH0372 survey area (green box). See figure 18 for the entire study area.

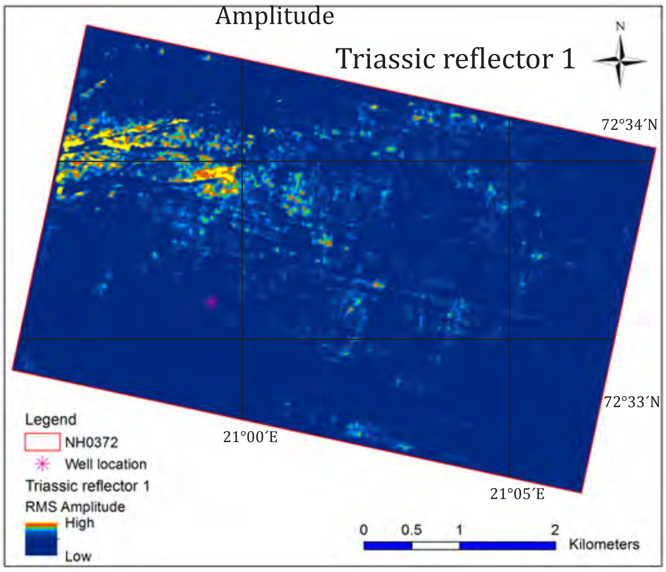

Figure 27: Amplitude maps (RMS) of the Triassic reflector 1, generated from the NH0372 survey area. Amplitude anomalies are illustrated in red to yellow colors. The pink dot mark the location of the well 7220/6-1. See also figure B14.

A fault chart was generated for the Triassic reflector 1 (Fig. B15), to display movements present within the layer. The Triassic reflector 1 has W-E, NE-SW and one N-S striking fault located south of the NW corner. No faults were found in the Lower Pleistocene deposits using this color ramp.

Isopach maps of the NH0372 survey area have a shifting thickness orientation; the Lower Pleistocene 4 to seabed (Fig. B16) has a NW-SE thickening, while the four remaining isopach maps down to the URU (Fig. B17-B20) all exhibits a SE-NW sedimentary increase. The thickness variations between the URU and the seabed are 84.5-117.6 ms (Fig. B21), increasing from both sides to peak in an N-SW orientated elevation. The Triassic reflector 1 up to URU exhibits a NW-SE thickening (Fig. B22), a result of the tilted strata. Steep elevation changes are observed in the NW regions. The isopach map of the Late Carboniferous to the Triassic reflector 1 has an altering sediment thickness with denser areas along the east side and both the west corners (Fig. 28). Thin areas do occur in two regions; as an elongated strip stretching north central to west central and one small area in the SE region.

Time slice velocity maps containing 12 horizontal slides were created between 500 ms and 1070 ms (Fig. B25-B36). Black reflect areas of low permeability and red areas of high permeability, a different color ramp of that used in the LN12M01 survey area. Figure B24 display a seismic profile of the NH0372 survey area, striking center W-E. Red lines mark the horizontal depth for the generated time slices. No faults were observed down to 580 ms (Fig. B28) but appeared as W-E striking movements at 600 ms (Fig. B29) in the SE corner. The faults continued down to 950 ms (Fig. B35), experiencing both NE-SW and NW-SE orientations. Faults were also detected central at 620 ms (Fig. B30) and in the NW corner at 650 ms (Fig. 29), striking foremost in a NW-SE and W-E direction continuing down to 1070 ms (Fig. B36). The Triassic reflector 1 can be seen as a red reflector in the center of the 764 ms time slice (Fig. B35), exhibiting a NE-SW orientated strike as well as cut by W-E and NW-SE striking faults.

The 2D seismic profile generated for the NH0372 survey area was found to contain one fault movement below URU in ESE area (Fig. B1).

3.2.3 Survey area Pcable area B PL609

The paleo-bathymetry maps of the Pcable survey

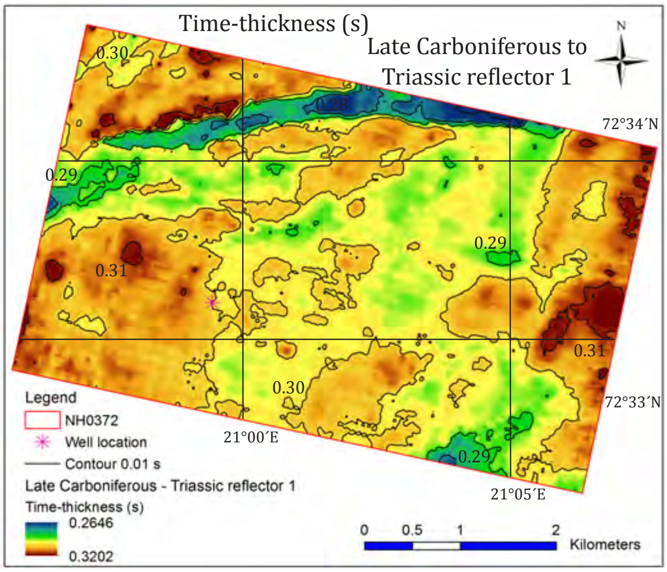

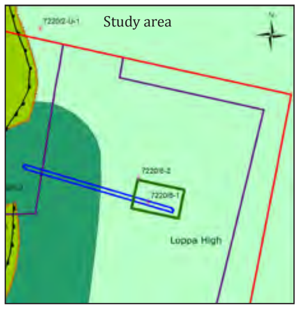

Figure 28: Isopach maps showing the time-depth differences between the Late Carboniferous to the Triassic reflector 1, generated from the NH0372 survey area. The thickness is presented in seconds and the contour lines illustrate elevation changes for every 0.01 s. The pink dot mark the location of the well 7220/6-1. See also figure B23. The reference map to the right displays an overview of the NH0372 survey area (green box). See figure 18 for the entire study area.

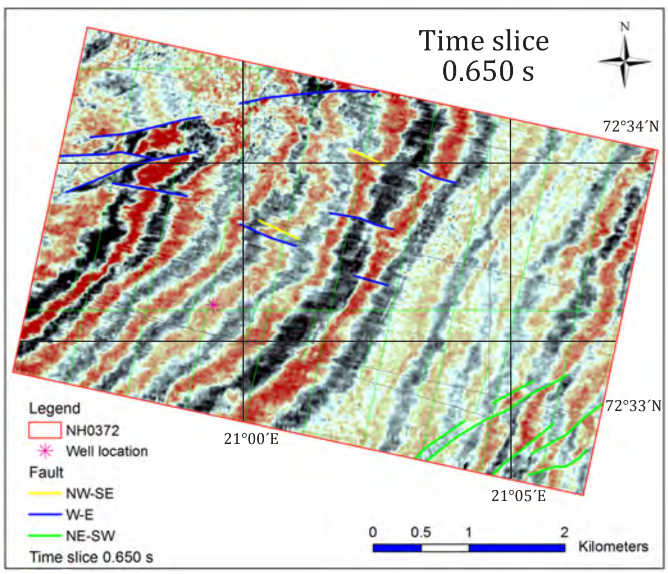

Figure 29: Time slice velocity maps cutting the NH0372 survey area horizontally at 0.650 s. Red color reflect areas of high permeability and black areas of low permeability. The pink dot mark the location of the well 7220/6-1. Faults are highlighted using color coded orientations. See also figure B31.

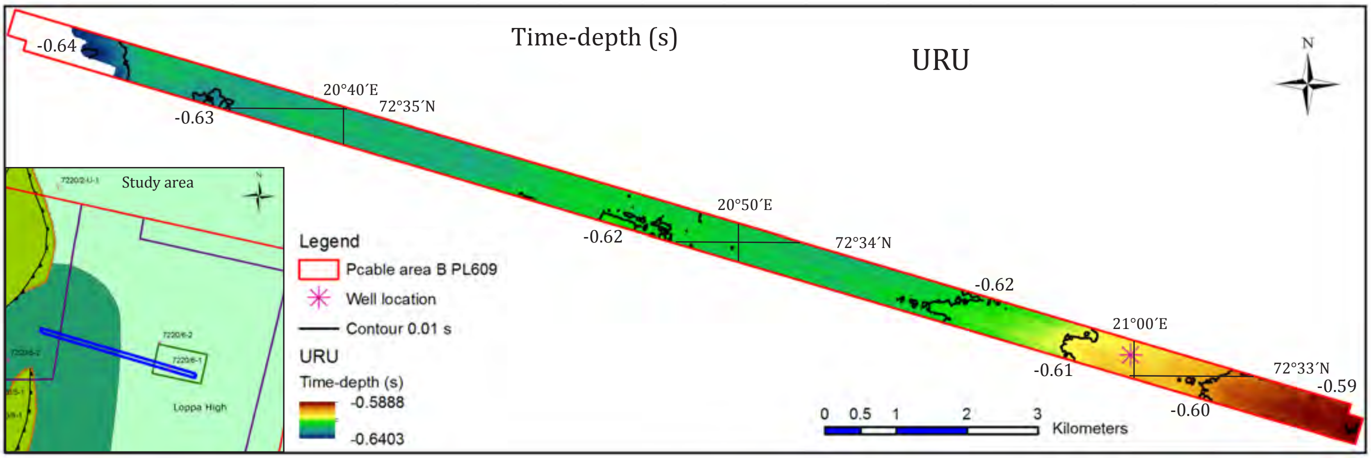

Figure 30: Paleo-bathymetry maps of the URU, generated from the Pcable area B PL609 survey area. The depth is given in seconds and the contour lines illustrate elevation changes for every 0.01 s. See also figure C8. The pink dot mark the location of the well 7220/6-1. The reference map in the left corner displays an overview of the Pcable survey area (blue outline). See figure 18 for the entire study area.

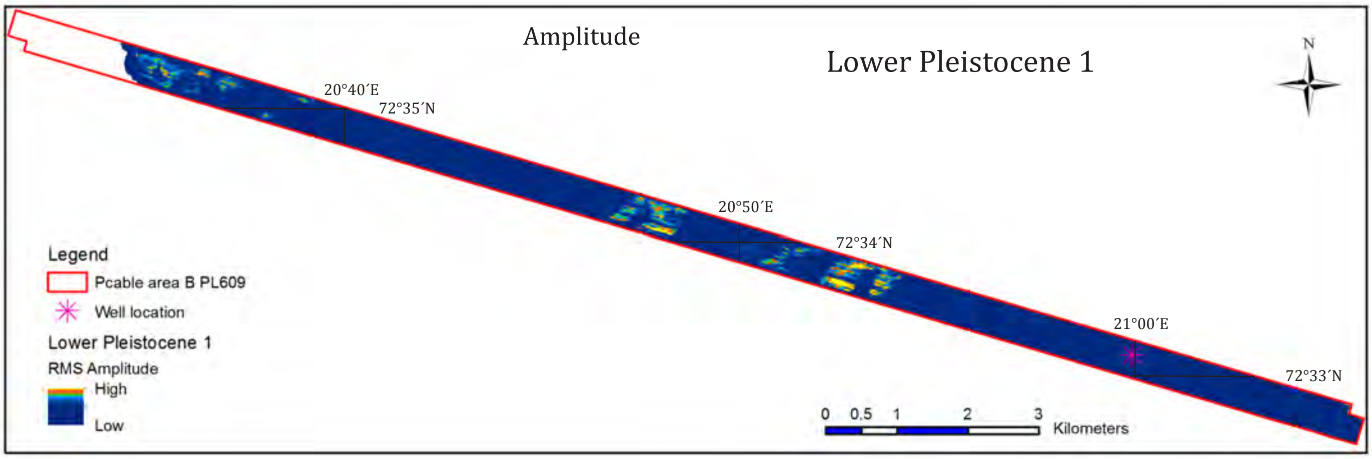

Figure 31: Amplitude maps (RMS) of the Lower Pleistocene 1, generated from the Pcable area B PL609 survey area. Amplitude anomalies are illustrated in red to yellow colors. The pink dot mark the location of the well 7220/6-1. See also figure C14.

area consists of eight layers. The seabed is a 486-562 ms deep sedimentary surface sloping NW (Fig. C2). The Lower Pleistocene 1-5 do also exhibit a NW sloping bathymetry (Fig. C3-C7), although only the Lower Pleistocene 3 (Fig. C5) is completely covering the survey area. The same layer has a small elevation again in the western half, a feature not seen on the other Pleistocene layers. The URU exhibits similar trends as the Lower Pleistocene 3, but could not be fully mapped in the NW corner (Fig. 30). The Triassic reflector 1 was only identified in the east half of the Pcable area, sloping SE (Fig. C9).

Fault charts were generated for the Triassic reflector 1 and the Lower Pleistocene deposits to display movements present within each layer. But no maps will be presented here as no faults were identified within these amplitude maps (RMS), using the relevant color ramp.

Amplitude maps showing areas of high permeability were generated on six layers; Lower Pleistocene 1-5 (Fig. C10-C14) and the Triassic reflector 1 (Fig. C15). The Lower Pleistocene 5 contain only minor areas along the southern edge (Fig. C10). The Lower Pleistocene 4 has areas of amplitude anomalies in the center (Fig. C11), while the Lower Pleistocene 3 has areas located in the NW corner of the Pcable survey area (Fig. C12). The Lower Pleistocene 2 contains five minor areas of high amplitudes located west of center (Fig. C13), while the Lower Pleistocene 1 display large anomaly areas in the center and in the west region (Fig. 31). The Triassic reflector 1 exhibit high amplitudes east of center.

Isopach maps of the Pcable area B PL609 survey area are limited due to the identified extent of each

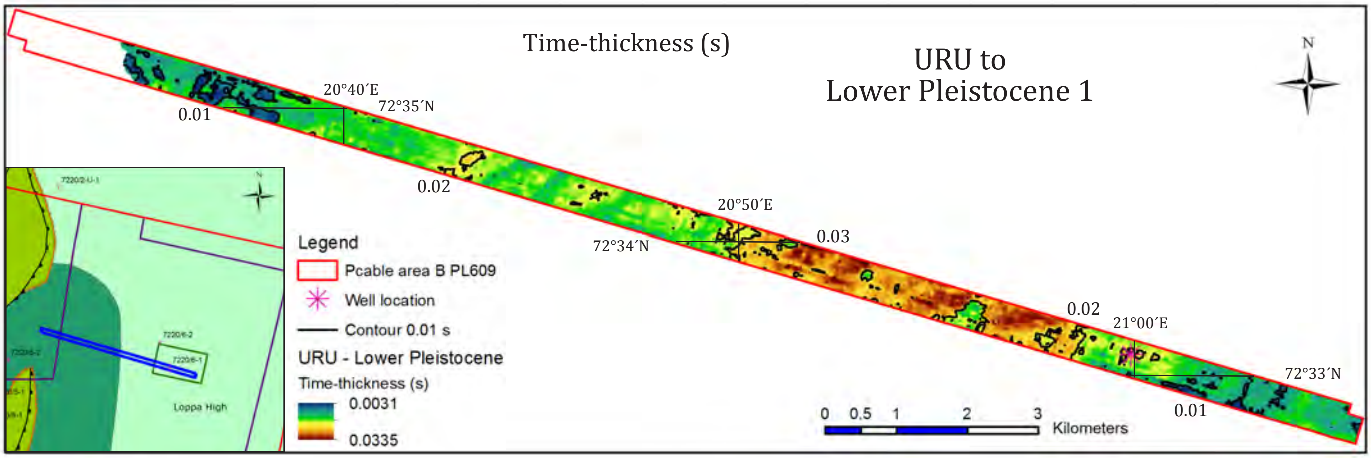

Figure 32: Isopach maps showing the time-depth differences between the URU and the Lower Pleistocene 1, generated from the Pcable area B PL609 survey area. The thickness is presented in seconds and the contour lines illustrate elevation changes for every 0.01 s. The pink dot mark the location of the well 7220/6-1. See also figure C21. The reference map in the left corner displays an overview of the Pcable survey area (blue outline). See figure 18 for the entire study area.

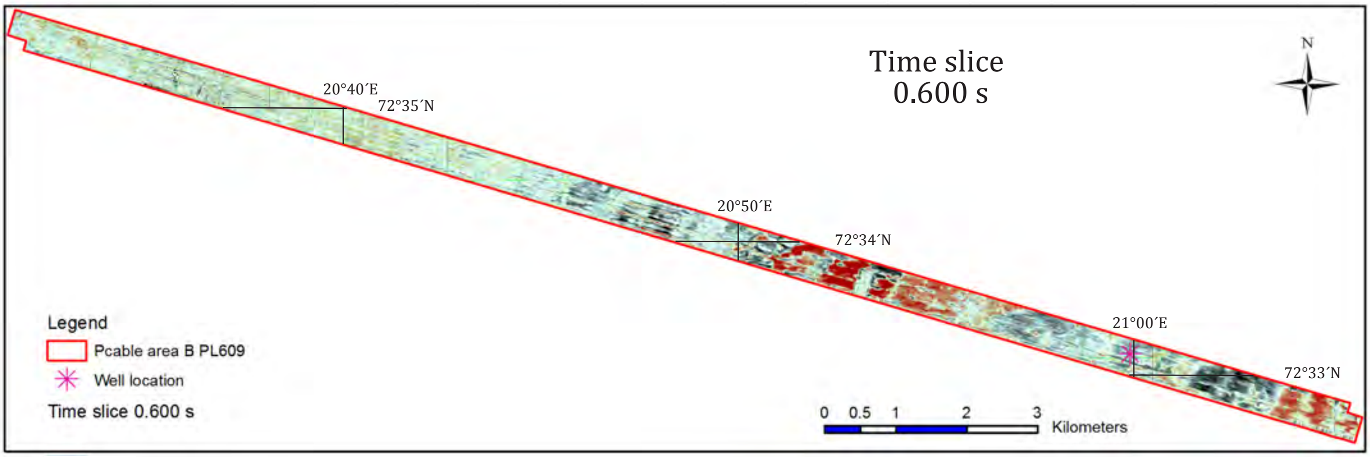

Figure 33: Time slice velocity maps cutting the Pcable area B PL609 survey area horizontally at 0.600 s. Red color reflect areas of high permeability and black areas of low permeability. The pink dot mark the location of the well 7220/6-1. See also figure C30.

layer, barely covering half the Pcable survey area. The Lower Pleistocene 5-seabed (Fig. C16) and the Lower Pleistocene 3-4 (Fig. C18) indicates thickness increase towards SE, while the Lower Pleistocene 4-5 (Fig. C17) exhibit an uneven shape with high and low concentrations spread over the area. Isopach maps of the Lower Pleistocene 2-3 (Fig. C19) and 1-2 (Fig. C20) have a thickness increase towards NW. The isopach map of the URU to the Lower Pleistocene 1 cover most of the survey area (Fig. 32); thin areas on either side with the thicker sedimentary cover located east of center. The URU-seabed (Fig. C22) and The Triassic reflector 1-URU (Fig. C23) both exhibits an SE thickening, where the URU-seabed sedimentary thickness peaks shortly before the SE corner.

Time slice velocity maps were produced for the Pcable survey area; ten horizontal slides ranging from 500-800 ms (Fig. C25-C34). Black reflect areas of low permeability and red areas of high permeability. Figure C24 display a seismic profile of the NH0372 survey area, striking center W-E. Red lines mark the horizontal depth for the generated time slices. The 600 ms time slice exhibits strong red reflections in the center of the survey area (Fig. 33). Faults were identified in the NW region at 700 ms (Fig. C32) and 801 ms (Fig. C34), striking in an N-S, W-E and NE-SW orientation. The time slice velocity maps consist of three separate parts (print screened) that are geotagged together using ArcMap, which caused the shading to differ some.

The 2D seismic profile generated for the Pcable area B PL609 was found to contain fault movements at the end of the Triassic reflector 1; at 700 ms; and further in at 725 ms (Fig. C1).

3.3 Multibeam backscatter

The three processed bathymetry surveys are spread out over the study area (Fig. 19). The northern located one is in the regions of the NH0372 and the Pcable area B PL609 survey areas, exhibiting a surface filled with iceberg ploughmarks. The second area are orientated in a WNW-ESE direction located below the well 7220/5-1, also covered with iceberg ploughmarks. The third bathymetry area is located in the southern region of the study area, filled with foremost ploughmarks. In the NE corner are small circular features, known as pockmarks (Chand et al., 2012), also visible.

3.4 Water column data

The water column data were analyzed in Fledermaus FMMidwater and with the result of three positive areas located along the survey area Pcable area B PL609. Two areas of potential gas flares were identified along the "0005 20120426 123817 sverdrup R1 CH1" survey line at time 12:47:33 - 12:47:47 and 12:47:50 - 12:47:56 (Fig. 35a & 35b). The third area was located 9.7 km further to the SE along the survey line "0016 20120426 175525 sverdrup R1 CH1" at time 18:43:25 – 18:43:39 (Fig. 35c). A single water column survey line with gas flares are illustrated in figure 35d, which is composed of several time slides.

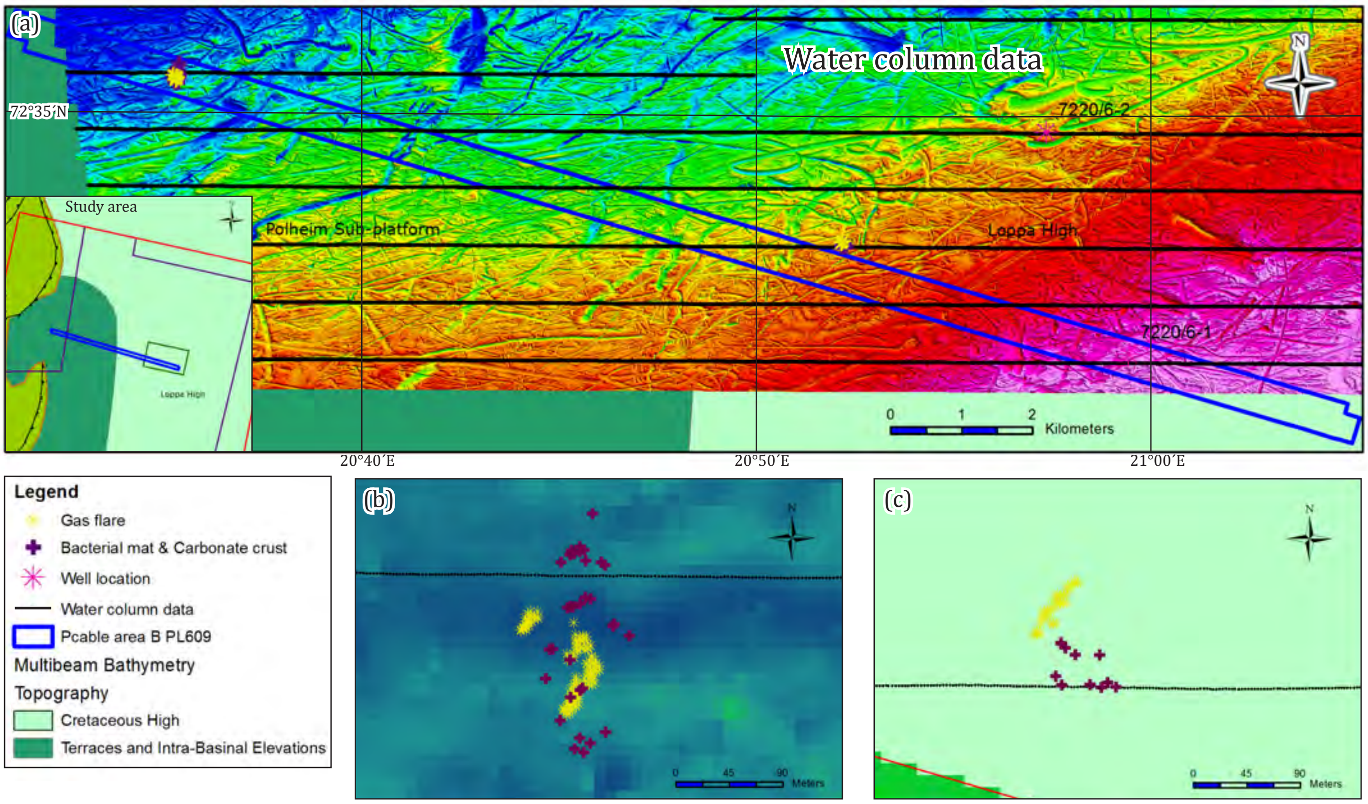

Figure 34a: Multibeam bathymetry map generated from the corresponding water column data survey (Fig. 19b), surrounded by a structural elements sheet. The pink dot mark the location of drilled wells. The reference map in the lower left corner displays an overview of the Pcable survey area (blue outline) (Fig. 18). Previously discovered bacterial mats and carbonate crusts are displayed as purple cross. The location of identified gas flares are marked as yellow areas. (b & c) Zoomed in areas of the identified gas flares, with close by bacterial mats and carbonate crusts.

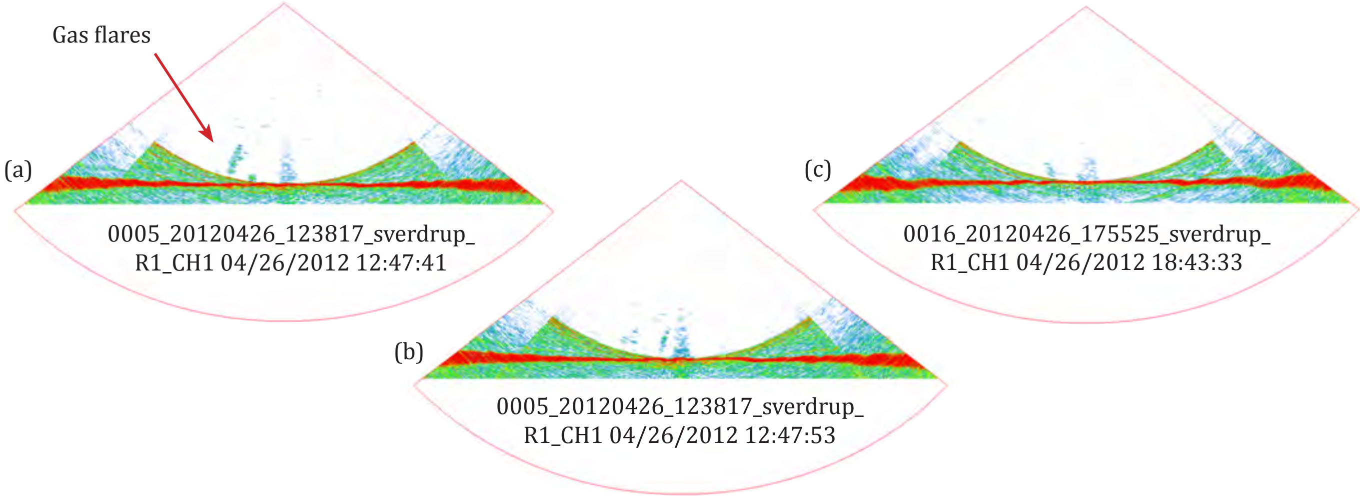

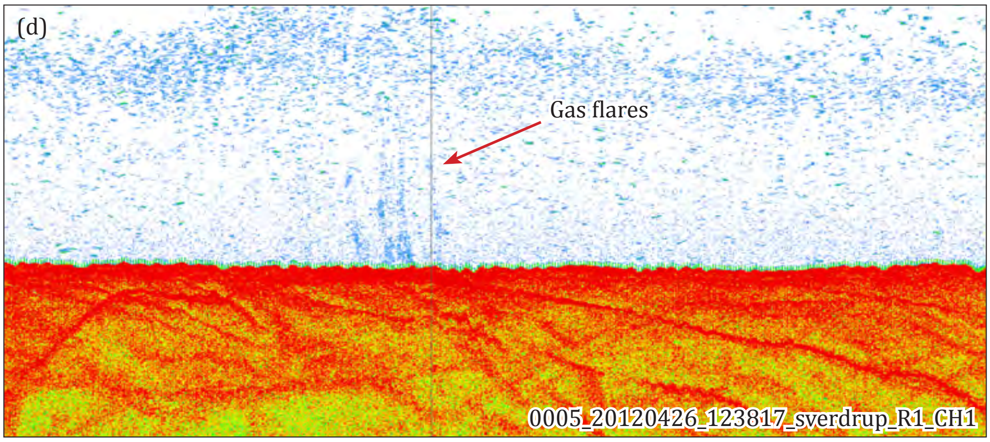

Figure 35a-c: Water column data showing gas flares recorded on the sea floor. (d) A single water column data survey line with visible gas flares (red arrow).

4. Discussion

As previously mentioned in the introduction, the objective of this master thesis was to better understand fluid migrations and to track these movements in between sedimentary strata deposited in the SW parts of the Loppa High, SW Barents Sea. This is carried out by interpretation of seismic data, both depositional patterns and sedimentary movements, to identify possible shallow hydrocarbon cap rocks. The analyzed data are from two 2D seismic reflection survey lines and three 3D survey cubes located in the SW of Loppa High, Barents Sea. Multibeam backscatter, water column data and well data were mainly used to supplement the seismic surveys.

4.1 A summary of the SW Barents Sea's geological history

The geological history of Loppa High do only reflect a small part of what the Barents Sea has endured since the formation of the Caledonian Orogeny, approximately 400 Ma (million years ago) (Dore, 1995; Smelror et al., 2009; Pease et al., 2014). Large sea floor alterations took place in the western parts of the Barents Sea region, between Late Devonian to Early Carboniferous, as the Baltican and Laurentian plates began to break up (Golonka et al., 2003; Smelror et al., 2009). Numerous rift-grabens and structural highs were formed, followed by sinistral strike-slip faulting in the western Barents Sea (Gudlaugsson et al., 1998; Golonka et al., 2003; Smelror et al., 2009; Dengo and Røssland, 2013). Basins like the Bjørnøya, Maud, Nordkapp and Tromsø Basin were formed along structural trends striking ENE-WSW (Gudlaugsson et al., 1998; Dengo and Røssland, 2013). Mercurius and Norsel highs located east of the Loppa High were a result of fault complex developments related to the tectonic rifting of Early Carboniferous (Gabrielsen et al., 1990). The Loppa High is believed to initially originate from Carboniferous and Permian tectonic activities (Gudlaugsson et al., 1998) and maybe the breakup into present-day Mid-Atlantic Ridge (MAR) can be the cause of this structural high.

During Late Carboniferous, the climate of the Barents Sea shifted into warm but arid regimes, followed by altered depositional environments from continental to marine siliclastic and carbonate accumulations (Dore, 1995; Worsley, 2008; Smelror et al., 2009; Dengo and Røssland, 2013). Structural highs such as Loppa High had siliclastic and carbonate mixed depositional cycles (Stemmerik et al., 1999). In Permian and Early Triassic, recurrent tectonic plate separation and rifting between the Baltican and Laurentian plates led to tilted half grabens, uplifting and erosion in the western Barents Shelf (Gudlaugsson et al., 1998; Smelror et al., 2009). The Loppa High was subjected to footwall uplift along the Ringvassøy-Loppa Fault Complex, next to the Tromsø Basin (Gabrielsen et al., 1990; Gudlaugsson et al., 1998; Stemmerik et al., 1999; Dengo and Røssland, 2013). The Polheim Sub-platform, a block-faulted area, was down-faulted from Loppa High in Early to Middle Triassic. A result of the unstable conditions brought on by the uplifting event (Gabrielsen et al., 1990). Re-activation of old faults along with generation of new faults was occurring in the western parts of the Barents Sea as crustal extensions between Greenland and Norway intensified again in late Jurassic to Early Cretaceous (Stemmerik et al., 1999; Pless, 2009; Dengo and Røssland, 2013). The Bjørnøyrenna Fault Complex was activated between the SW of Loppa High and the Bjørnøya Basin, at the same time as the Loppa High was subjected to uplift, rifting and subduction (Gabrielsen et al., 1990; Smelror et al., 2009). The Polheim Sub-platform was in Jurassic subjected to westward movements, brought on by the activation of the Bjørnøyrenna Fault Complex (Gabrielsen et al., 1990).

In late Early Jurassic, low-lying peneplains are thought to have covered large areas of the Barents Shelf (Brekke et al., 2001; Golonka et al., 2003; Smelror et al., 2009). A transgressional phase with coastal progradation took place in the west and by Late Jurassic this phase had reached its maximum, with all of the Barents Shelf submerged (Brekke et al., 2001; Petrov et al., 2008; Worsley, 2008; Smelror et al., 2009). The Loppa High and Stappen High experienced clastic deposits of sandstone, siltstone and clay. (Smelror et al., 2009). Northern hemisphere glaciations in Pliocene and Pleistocene had a heavy impact on the Barents Sea, since subjected to periods of glacially induced subsidence, erosion, isostatic uplift and glaciomarine deposits (Brekke et al., 2001; Smelror et al., 2009; Glørstad-Clark et al., 2010). The upper regional unconformity (URU), created by the last glaciation, is present in the sedimentary strata of Loppa High and reflected in the seismic data (Pless, 2009).

4.2 Hydrocarbon migration

Fossil fluids generated within a source rock will either remain trapped or escape its area of origin and migrate towards the surface. The migration pathways are often a long and complex, where oil and gas have to find its way through 100's of millions years of accumulated sediments. Tilted strata, open faults and fractures as well as chimneys or pipes are known sedimentary features that may favor large scale migrations. Possible source rocks formations located within the study area and also identified in well 7220/5-1 or 7220/6-1 (Fig. 17) are the Snadd Formation of Middle to Late Triassic, the Tubåen- and Nordmela Formation of Early Jurassic and the Fuglen- and Hekkingen Formation of Late Jurassic (Dore, 1995; Stemmerik et al., 1999; Pless, 2009; NPD, 2015). Migrating fluids are driven foremost by buoyancy and the hydraulic gradient and will follow layers or features of higher permeability as long as the fluid concentrations are high enough to overcome the capillary pressure (Clennell et al., 2000; Marshak and Prothero, 2008). Oil and gas may on its way up encounter formations that will work as an entrapment; a sedimentary structure of low permeability that terminates or at least hampers the migration to the level that large amounts of fossil fluids can collect. Hydrocarbons will accumulate within these reservoir rocks until the rising pressure cracks the seal rock or the fossil fluids find an alternative route past the entrapment. Fluid accumulations, within a sedimentary layer, are illustrated in the amplitude maps as red to yellow colors. The higher concentration of fluids for one area are visualized as strong focused yellow fields (high amplitudes in higher concentrations for one area), also referred to as amplitude anomalies. Areas of more dispersed fluid concentrations are viewed as a mixture of blue to yellow spots (high amplitudes in lower concentrations for one area). A number of the Lower Pleistocene layers could not be reproduced to cover the entire study area, either due to the limitations of the data or too the fact that the individual layers don't extend further. Regardless, this constitutes a degree of uncertainty to the study.

4.2.1 Survey area LN12M01

Well 7220/5-1, located west of the Loppa High (Fig. A5), was found to contain the Tubåen, Nordmela, Fuglen and Hekkingen formations at depth of 1269 m (MD RKB) to 1695 m below the ocean surface (NPD, 2015). In time-depth (ms) these formations, known to be of source rock potential, occur at approximately 1200-1300 ms and continues down to the corresponding depth of 1695 m (approx. 1600 ms, see figure A5. The gas-oil and the oil-water boundaries, visible at 1460 ms respective 1540 ms to the WNW of the NBR10-338364 seismic profile (Fig. 36), are buried under Late Paleocene to Oligocene claystone deposits of the Torsk Formation (Ryseth et al., 2003; NPD, 2015). The fossil fluids originating from these source rocks will, if released, not migrate through the low permeability claystone but along the tilted strata to the east until it reaches an open fault and upward migration is possible. The N-S striking faults, located just west of the Loppa high and above the Polheim Sub-platform, may be a possible result of the Late Jurassic to Early Cretaceous Bjørnøyrenna Fault Complex related rifting and subsidence (Dore, 1995; Stemmerik et al., 1999; Smelror et al., 2009). The magnitude of these faults as well as the high frequency of minor faults in the area can be traced using the time slice velocity maps, ranging from 1100 ms and up to 548 ms (Fig. A47-A57). The N-S striking faults (red) marks the outer edge of the Loppa High and the down-faulted movements of the Polheim Sub-platform. The amplitude maps of the Triassic reflector 1 & 2 (Fig. A29 & A30), with highlighted faults, do also exhibit these movements, especially the second Triassic reflector with layer interpolations extending over the Polheim Sub-platform. The isopach map of the Triassic reflector 2 to the URU (Fig. 37) has a few major thickness variations in the western half of the LN12M01 survey area. The sedimentary volume increase to the west with sharp progressive transitions that indicate rifting in the region. The down-faulted deposits can also be viewed in the NBRD07-234838 and NBR10-338364 seismic profiles (Fig. 20 & 21) and in the seismic profile of well 7220/5-1 (Fig. A5). The brighter reflections located within these sedimentary rocks indicate the presence of fluids and possibly hydrocarbons (Kearey et al., 2002; Pless, 2009), outlined reflections to the left in figure 36. The upward migrating hydrocarbons will either encounter a cap rock or via tilted layers and numerous faults reach the low permeable layer of URU.

The Snadd Formation of the Kapp Toscana Group was identified in the well 7220/6-1, at 476 m and down to 1138 m (Fig. 36) (NPD, 2015). The cause of these shallow located deposits originates from the footwall uplift and tilting of the Loppa High, initiated by the Permian to Early Triassic fault movements along the Ringvassøy-Loppa Fault Complex (Gud-

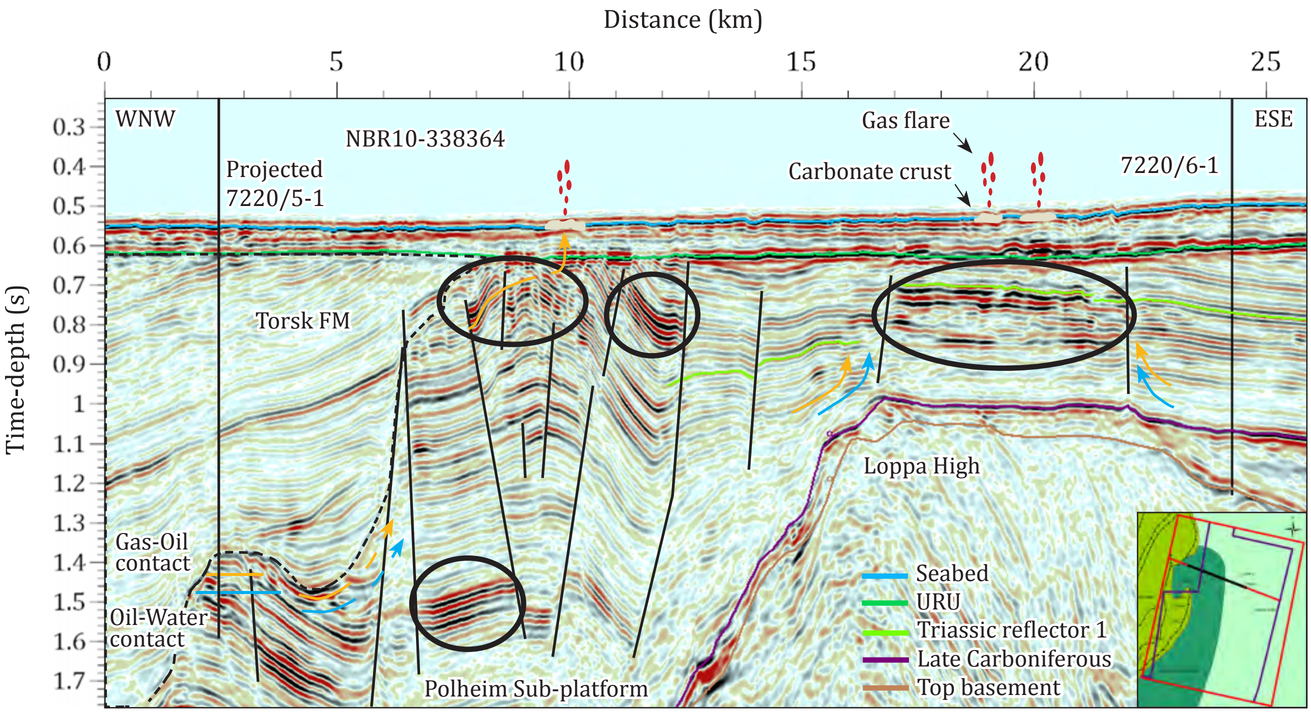

Figure 36: Seismic profile of the NBR10-338364 survey line occur in a WNW-ESE orientation. Black ellipses mark areas of fluid concentration, possibly hydrocarbons. Five layers are identified within this profile. Major faults are highlighted with black lines. The well 7220/6-1 and a projected drilling of well 7220/5-1 is displayed. A gas-oil (orange) and an oil-water (blue) contact are illustrated in the WNW region. Possible migration pathways are illustrated using color-coded arrows. The gas flares (red) displayed on the seabed do not mark the exact located of the three identified seeps, but illustrate probable seep occurrences. The map in the lower right corner displays an overview of the study area and the LN12M01 survey areas (Fig. 18), with the orientation of this section of the 2D seismic profile (black line). The seismic profile of the NBR10-338364 survey line, as it is displayed in figure 21, is marked with a red line behind the black line.

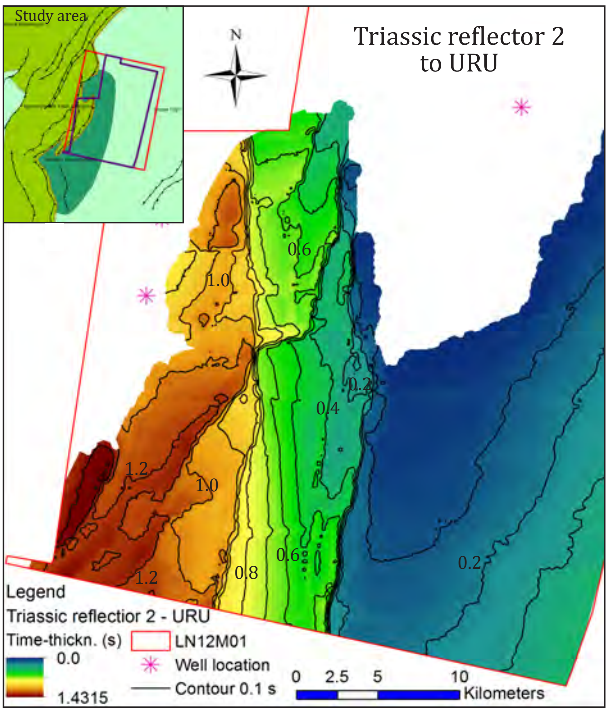

Figure 37: Isopach map showing the time-depth differences between the Triassic reflector 2 and the URU, generated from the LN12M01 survey area. The map in the upper left corner displays an overview of the study area (Fig. 18), with the LN12M01 survey area (purple outline). Pink dots mark the location of wells. See figure A39 for the complete map.

laugsson et al., 1998; Stemmerik et al., 1999; Smelror et al., 2009). The Snadd Formation occurring source rock of possible Loppa High origin or from more deeply buried source rocks will migrate westward along the tilted strata (Fig. A16) until it reaches the N-S striking faults, at the transit between Loppa High and the Polheim Sub-platform. Fluids may also find pathways through open minor faults located within the Triassic deposits of the Loppa High, leading up to the URU. The time slice velocity maps ranging from 1100 ms and up to 576 ms exhibits a high variety of orientated faults along the eastern half of the study area (Fig. A48-A57). The same is indicated by the fault charts of the Triassic reflector 1 & 2 (Fig. A29 & A30). The bright red reflectors, located in the higher elevated areas of the Loppa high (outlined area, Fig. 36), display indications of fluid accumulations (Kearey et al., 2002; Pless, 2009).

Concentrations of higher amplitudes in the Triassic reflector 1 can be subdivided into three larger areas (Fig. 38). The northern area of amplitude anomalies occur in the highest elevated area of the reflector (Fig. A16), on the border to the URU. Faults of foremost N-S

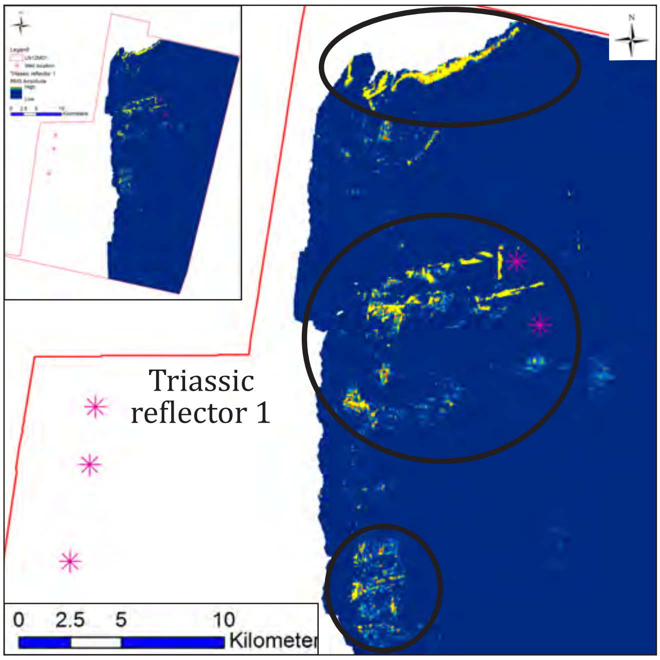

Figure 38: Amplitude map (RMS) of the Triassic reflector 1. Amplitude anomalies are illustrated in red to yellow colors. Three regions of higher amplitudes are outlined by black ellipses. The map in the upper left corner displays an overview of the layer, generated within the LN12M01 survey area (Fig. A28).

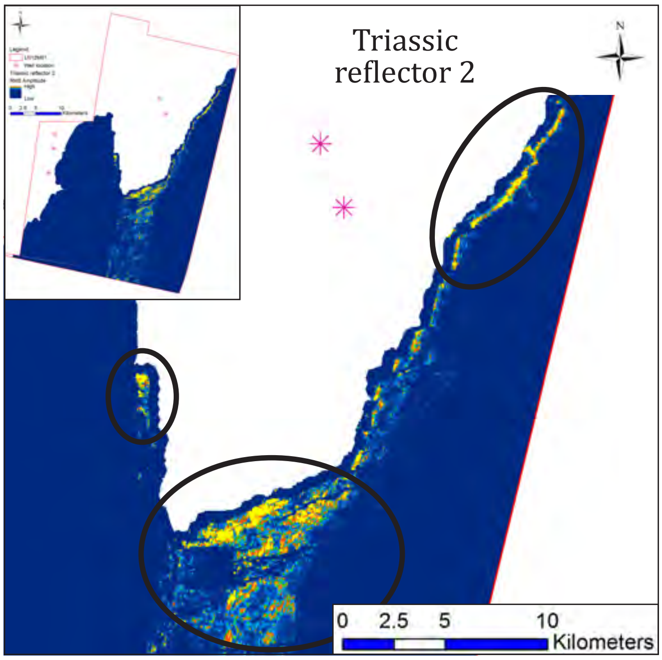

Figure 39: Amplitude map (RMS) of the Triassic reflector 2. Amplitude anomalies are illustrated in red to yellow colors. Three regions of higher amplitudes are outlined by black ellipses. The map in the upper left corner displays an overview of the layer, generated within the LN12M01 survey area (Fig. A27).

orientation are located to the west of these anomalies, as seen in figure A30 and in the 652 ms and 700 ms time slices (Fig. A51 & A52). Fluids may migrate within the tilted layer until it reaches higher elevations or move through open faults in the area. The middle area is located at the second highest peak of the Triassic reflector 1 (Fig. A16). A large number of faults have been identified in this area, both in the fault chart (Fig. A30) and in the time slices ranging from 752 ms and up to 652 ms (Fig. A51-A53). Black reflections of higher permeability can also be seen in the 700 ms and 752 ms time slices (Fig. A52 & A53). As for this accumulation, fluids seems to follow within the layer or via faults from deeper deposited layer. The souther area of higher amplitudes are in a N-S sloping region, surrounded by faults (Fig. A30). Maybe these represent fields of higher permeability sediments where fluids have collected.

The Triassic reflector 2 is eroded in the middle to northern regions by glacial movements and adjoins to the URU (Fig. A15). The amplitude map of the Triassic reflector 2 has higher amplitudes center, south to north, along the highest elevated areas and along the border to the URU (Fig. 39). Fluid migration appears to follow within the layer, migrating to higher elevations along the center and to the border of the URU. Possible fluid movements up through the faults identified in the faults chart of the Triassic reflector 2 will allow for further migrations within the layer (Fig. A29).

The Snadd Formation, consisting of tilted shale with interbedded siltstone and sandstone (NPD, 2015), may hamper a large scale horizontal migration underneath the URU. However, the curved elongated depression located center to southeast in the URU layer could have a positive effect on the migration (Fig. A14). The identified fault at 548 ms seems to cut the URU in the area of the depression and thus allowing fluids to migrate through (Fig. A47). The depression can also be seen in the two W-E orientated 2D seismic profiles (Fig. A3 & A4), where the reflection of URU is not rendered as completely intact.

The Lower Pleistocene 1 exhibit higher amplitudes on both sides of the depression (Fig. 40a & b) in higher elevated areas (Fig. A13), supporting the argument that the URU is not completely undisturbed. Two more fields of anomalies were located in the northern half of the survey area (Fig. 40c & d). They do not coincide with any peak elevated areas but occur in regions of thicker sedimentary deposits (Fig. A37). The coars-

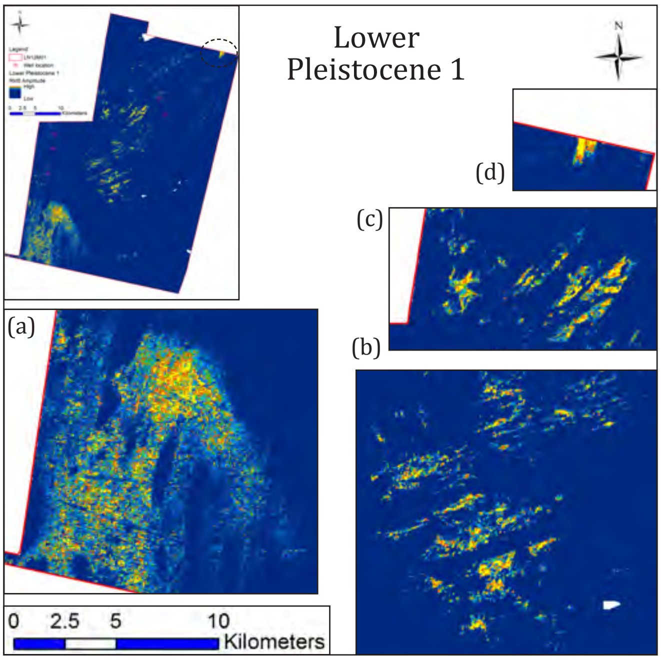

Figure 40a-d: Amplitude map (RMS) of the Lower Pleistocene 1. Amplitude anomalies are illustrated in red to yellow colors. Four regions of higher amplitudes were identified; (a & b) are located on either side of the depression; and (c & d) in the northern half of the survey area. The map in the upper left corner displays an overview of the layer, generated within the LN12M01 survey area (Fig. A26).

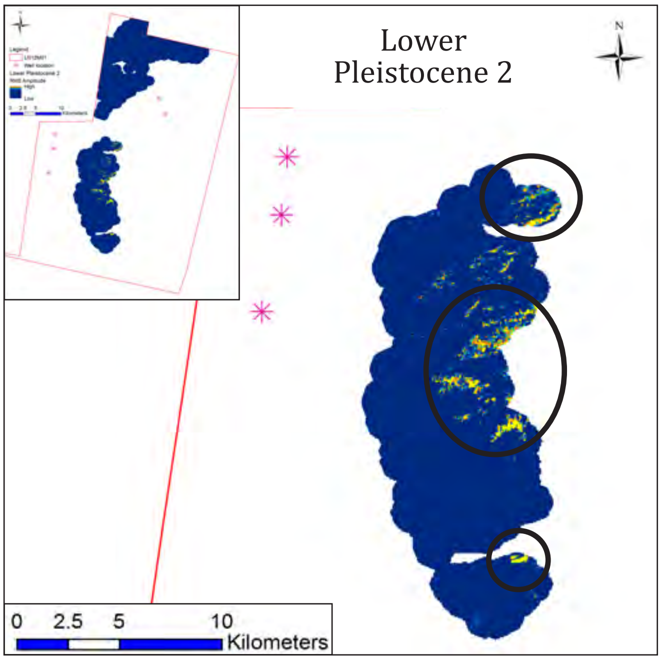

Figure 41: Amplitude map (RMS) of the Lower Pleistocene 2. Amplitude anomalies are illustrated in red to yellow colors. Three regions of higher amplitudes are outlined by black ellipses. The map in the upper left corner displays an overview of the layer, generated within the LN12M01 survey area (Fig. A25).

ening upwards deposits of the Nordland Group (NPD, 2015) could imply that these areas of thicker volumes are delimited fields of increased permeability, where hydrocarbons have accumulated.

The higher amplitudes of the Lower Pleistocene 2 are positioned above the URU depression (Fig. 41). The amplitude anomalies along this edge overlaps with higher amplitudes of the Lower Pleistocene 1 (Fig. 40b), thus indicating the possibility of an upward migration within the depression. Overlapping clear black reflections can also be seen in the 548 ms time slice (Fig. A47), indicating large high permeability bodies.

Amplitude anomalies above the major depression can also be seen in the Lower Pleistocene 3 (Fig. 42a). They are focused around a deeper elevation within the layer (Fig. A11), possibly working as migration pathways up to smaller sand bodies. The 548 ms time slice has minor areas of higher permeability (clear black reflections) that corresponds to the areas of higher amplitudes, even if the time slice is generated a few ms too deep (Fig. A47). The higher amplitudes in the NW region of the Lower Pleistocene 3 (Fig. 42b) occur in an area of elevation incline to the south (Fig. A11) and exhibit thin to thicker sedimentary deposit

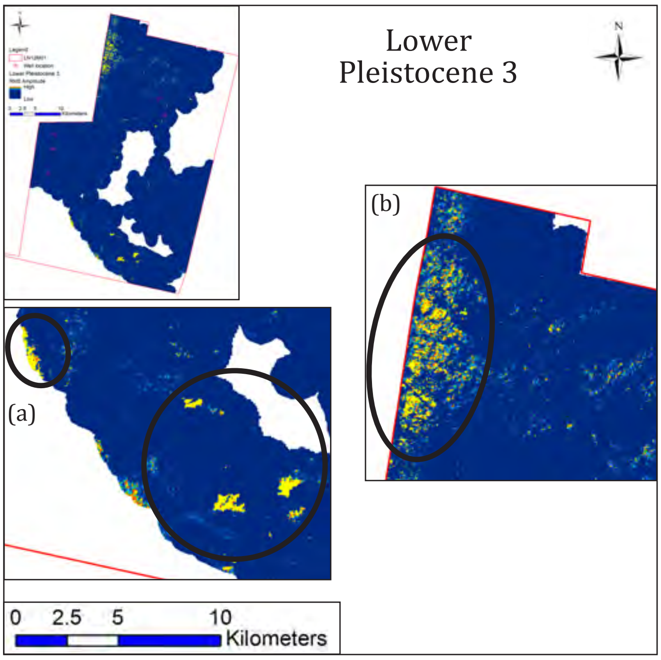

Figure 42a & b: Amplitude map (RMS) of the Lower Pleistocene 3. Amplitude anomalies are illustrated in red to yellow colors. Two regions of higher amplitudes were identified; (a) is located in the southern region; and (b) is located in the northern half of the survey area. The areas of larger amplitude concentrations are outlined by black ellipses. The map in the upper left corner displays an overview of the layer, generated within the LN12M01 area (Fig. A24).

in the area (Fig. A35). Fluids may have migrated in via lower elevated areas of the layer (outside the study area) and accumulated in the thicker deposits. But no indications for higher permeability deposits could be identified in the 600 ms or the 576 ms time slice (Fig. A48 & A49), which implies for a thinner sedimentary body capable of storing fluids.

The amplitude anomalies of the Lower Pleistocene 4 are along the NW border to the Lower Pleistocene 3 (Fig. 43a). Hydrocarbons can migrate in from the amplitude anomalies of the northern Lower Pleistocene 3 (Fig. 42b), located approximately 2 ms below, and accumulate in the thicker sedimentary deposits (Fig. A34). The absence of dark fields in the 576 ms and 548 ms time slices may indicate thinner bodies of higher permeability for the fluids to accumulate in (Fig. A47 & A48). The small concentration of higher amplitudes in the southern region of the Lower Pleistocene 4 is positioned above the large depression of the URU (Fig. 43b). The area is in an elevated parts of the layer (Fig. A10) with a low sedimentary thickness (Fig. A34), which would allow for fluid migration to occur up through the directly underlying fluid concentrations of the Lower Pleistocene 3.

The larger area of amplitude anomalies of the Lower Pleistocene 5 are positioned above the elongated depression of the URU (Fig. 44), located in deeper elevations and surrounded by more elevated areas. The second area, identified along the SW edge of the survey area, occur in the highest elevated region of the Lower Pleistocene 5 (Fig. A9). Fluids could have migrated up via the deeper occurring Lower Pleistocene layers until it reaches the Lower Pleistocene 5. Once here, fluids may have continued migrating up to the higher elevations where sediments of higher permeability could be deposited.

The Lower Pleistocene 6 exhibit fluids in low abundances spread out over most of the layer, especially in the NW and SE regions (Fig. A21). Small elongated features with higher amplitude levels are observed in the lower parts of the LN12M01 survey area, possible relics of old buried iceberg ploughmarks.

The Lower Pleistocene 7 is a copy of the seabed, generated 14.6 ms below the seabed to obtain any shallow occurring fluids registered by the seismic survey. The amplitude anomalies, that are spread out center along the western edge, can be divided into three fields of higher fluid concentrations (Fig. 45). These areas are surrounded by smaller abundances of

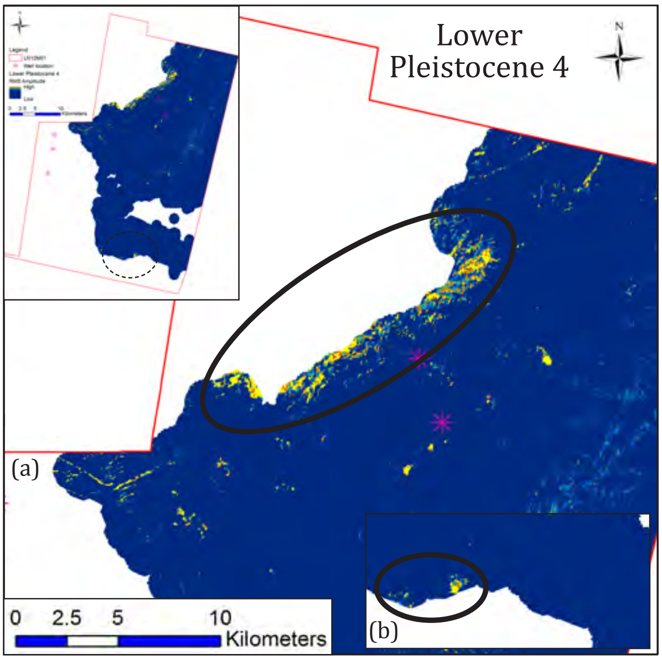

Figure 43a & b: Amplitude map (RMS) of the Lower Pleistocene 4. Amplitude anomalies are illustrated in red to yellow colors. Two regions of higher amplitudes were identified; (a) is located in the northern half of the survey area; and (b) is located in the southern region. The areas of larger amplitude concentrations are outlined by black ellipses. The map in the upper left corner displays an overview of the layer, generated within the LN12M01 survey area (Fig. A23).

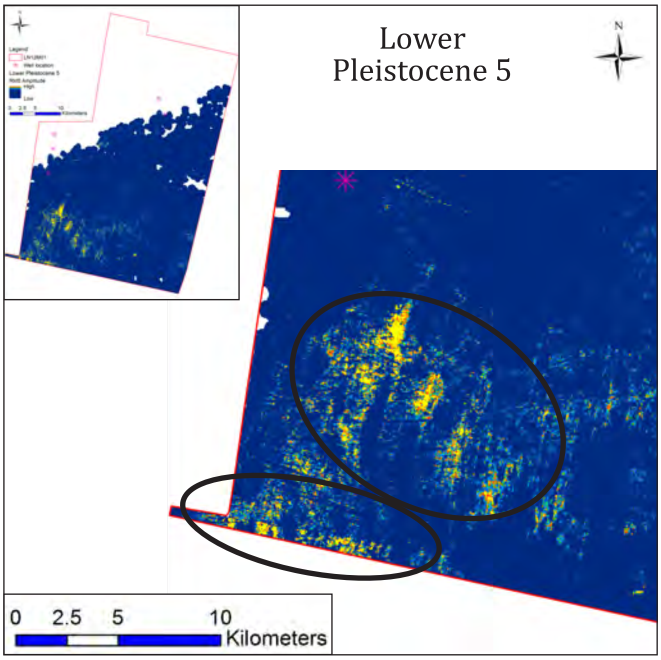

Figure 44: Amplitude map (RMS) of the Lower Pleistocene 5. Amplitude anomalies are illustrated in red to yellow colors. Two regions of higher amplitudes are outlined by black ellipses. The map in the upper left corner displays an overview of the layer, generated within the LN12M01 survey area (Fig. A22).

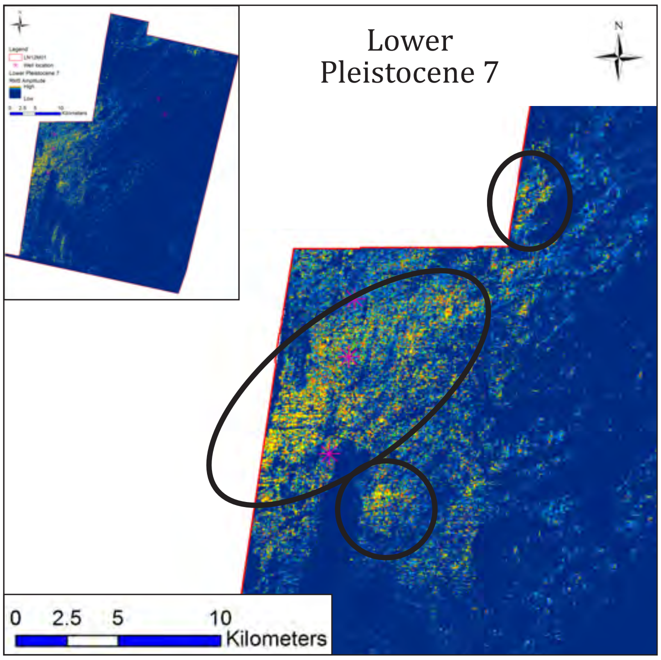

Figure 45: Amplitude map (RMS) of the Lower Pleistocene 7. Amplitude anomalies are illustrated in red to yellow colors. Three regions of higher amplitudes are outlined by black ellipses. The map in the upper left corner displays an overview of the layer, generated within the LN12M01 survey area (Fig. A20).

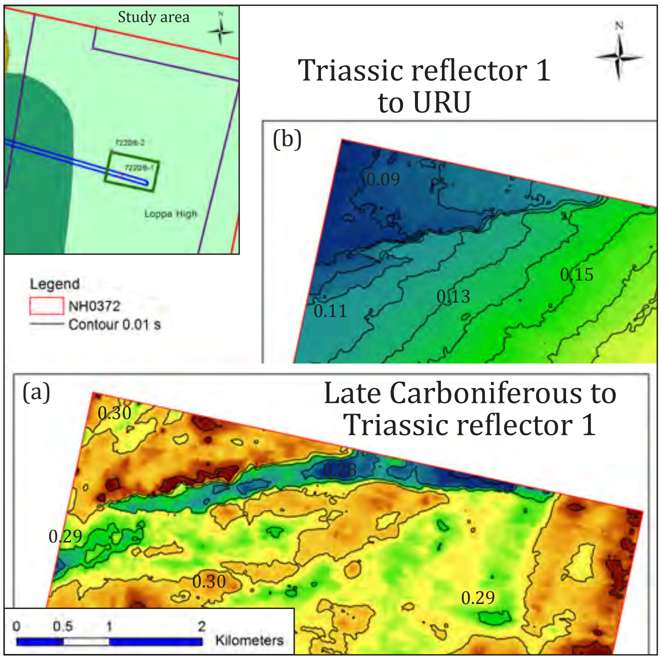

Figure 46a & b: Isopach maps showing the time-depth differences between two layers, generated from the NH0372 survey area. See figure B22 and B23 for the complete maps. The map in the upper left corner displays an overview of the study area (Fig. 18), with the NH0372 survey area (green box).

higher amplitudes, a mixture of blue to yellow spots, which indicates low concentrations of fluids spread out in the top strata.

The gas hydrate features identified in the SW regions of the LN12M01 survey area are formed in the Torsk Formation of Late Paleocene to Oligocene (NPD, 2015), at depth ranging from 608 and 833 ms (Fig. A19). The 652 ms to 800 ms time slices exhibit both black and white elongated features in the SW regions (Fig. A51-A54). The white reflections appears to occur above and on either side of the black areas as an low permeable layer, indicating that this may be a gas hydrate with possible hydrocarbons trapped beneath.

4.2.2 Survey area NH0372

The high resolution data set of survey area NH0372 cover a small region of the study area and will be displayed as a close up study to illustrate the hydrocarbon migrations not registered in the LN12M01 data set. It should be noted that, these two data sets were collected during different times and could thus be registering new migrations not previously occurred.

The Late Carboniferous layer is a low permeability stratum (black reflection, see figure B1) consisting of marine deposits with mixed carbonates and siliclastic sediments (NPD, 2015). A steep elevation change is visible along the northern edge (Fig. B9) and in the corresponding isopach map (Fig. 46a), as well as movements in the 1070 ms time slice (Fig. B36), which indicates the presence of a fault cutting the Late Carboniferous layer. Hydrocarbons trapped under the Late Carboniferous layer could thus migrate upwards via this fault, as long as it is open or kept open by the pressure build up generated from the migrating fluids (Clennell et al., 2000; Schulz and Zabel, 2006).

Time slices generated between the Late Carboniferous and the Triassic reflector 1 (Fig. B33-B35) have continuous faults in the western regions and in the SE corner, features created by the Late Jurassic to Early Cretaceous rifting and subsidence of the Loppa High (Dore, 1995; Stemmerik et al., 1999; Smelror et al., 2009). Fluids leaving the Carboniferous deposits or migration deep in the Triassic strata can move up through the Triassic faults. The higher amplitudes of the Triassic reflector 1 (Fig. 47) occur in an elevated part of the mapped layer (Fig. B8), where faults of foremost W-E orientation penetrating the reflected layer (Fig. B15). Deeper occurring hydrocarbon may have migrated in via surrounding faults, or moved within the layer, to concentrate in high permeability

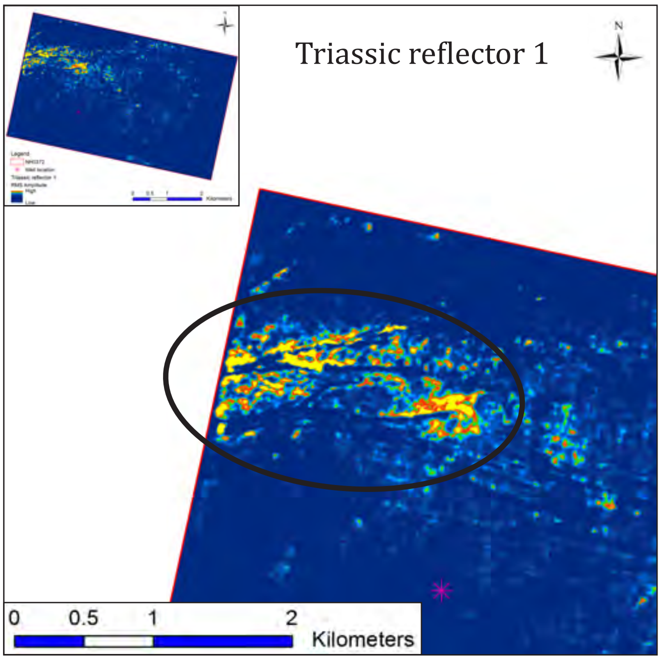

Figure 47: Amplitude map (RMS) of the Triassic reflector 1. Amplitude anomalies are illustrated in red to yellow colors. One major region of higher amplitudes are identified within this layer, outlined by a black ellipse. The map in the upper left corner displays an overview of the layer, generated within the NH0372 survey area (Fig. B14).

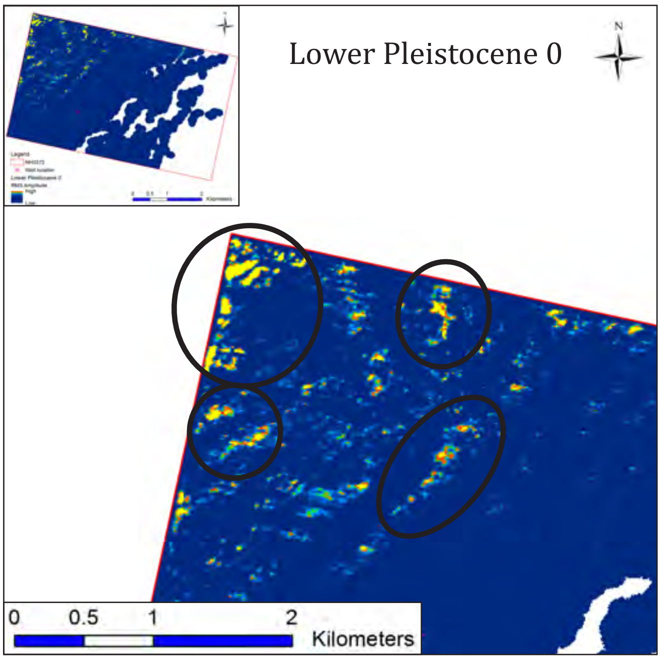

Figure 48: Amplitude map (RMS) of the Lower Pleistocene 0. Amplitude anomalies are illustrated in red to yellow colors. Four areas of higher amplitudes are identified within this layer, outlined by black ellipses. The map in the upper left corner displays an overview of the layer, generated within the NH0372 survey area (Fig. B13).

bodies of sandstone (NPD, 2015).

Time slices ranging from the Triassic reflector 1 (764 ms) and up to the URU at 620 ms exhibits fault movements in the western to NE regions (Fig. B30-B33), the same area as for the amplitude anomalies of the Triassic reflector 1. A major fault is also visible in the isopach map between the Triassic reflector 1 and the URU; where sedimentary thickness drastically changes (Fig. 46b). Fluids can, via these faults, continue to migration upwards towards the URU, as long as they remain open.

Four areas with amplitude anomalies of higher concentrations were outlined in the NW region of the Lower Pleistocene 0 (Fig. 48). This is in the lower elevated areas of the layer, at 620 ms (Fig. B6). The amplitude anomalies do not overlap with the thickest sedimentary deposits (Fig. B20), but occur around them. Although, the 620 ms time slice exhibit strong red reflections in the upper NW corner and can be correlated to fields of higher amplitudes (Fig. B30), indicating an area of higher permeability. Fluids do probably migrate along the layer, outside the NH0372 survey area, and accumulates here rather then moving through the URU as no faults could be identified in the area.

The Lower Pleistocene 1 do also exhibit larger concentrations of higher amplitudes in the NW corner (Fig. 49a), at an elevation of about 600 ms (Fig. B5). The 600 ms time slice has red fields in the NW corner (Fig. B29), indicating high permeability deposits where hydrocarbons may accumulate. Fluids could be migrating through the thin deposits of the Lower Pleistocene 1 or from migrations within the layer. The small area of higher amplitudes in the NE corner of the Lower Pleistocene 1 (Fig. 49b) is located in elevated areas (Fig. B5), indicating within layer migrations and probably the presence of a high permeability sand body.

The Lower Pleistocene 2 could not be identified within the NH0372 survey area due to the incoherent and badly reflected deposits between the Lower Pleistocene 1 and 3 (Fig. B1). The same goes for the Lower Pleistocene 5 & 6 of the LN12M01 survey area.

The Lower Pleistocene 3 has three larger regions of higher amplitudes located throughout the NH0372 survey area (Fig. 50). The anomalies located in the south center region (Fig. 50a) overlaps with higher elevations of the layer (Fig. B4). This may allow for migrations within the layer and possibly from the fluid concentrations in the NW corner of Lower Pleistocene 1 (Fig. 49a). The second area of higher amplitudes, located center to NE (Fig. 50b), do also occur in an elevated area (Fig. B4). Fluid migration may, as for the anomalies in the south center region, originate from the concentrations in the NW corner of the Lower Pleistocene 1. Fluid migration from the north is also a possibility. The higher amplitudes located in the NE corner of the Lower Pleistocene 3 (Fig. 50c) occur in a lower elevated area (Fig. B4), where the isopach between the Lower Pleistocene 1 and 3 exhibits thin sedimentary thickness (Fig. B18). These higher amplitudes are positioned on top of the amplitude anomalies discovered in the NE corner of the Lower Pleistocene 1, indicating possible upward migration of fluids.

The Lower Pleistocene 4 has four areas of higher amplitudes (Fig. 51), three of which are located in the northern half. The first area of anomalies is in the NW region (Fig. 51a), overlapping with thicker sedimentary deposits. This is in the deepest part of the layer, at 560 ms (Fig. B4). Small amplitude anomalies can be seen in the NW regions of the Lower Pleistocene 0, 1 & 3 as well, all in the deeper parts of their layers. This may be the result of a migration pathway through the four layers, made possible due to the thin deposits. The second area for higher amplitudes are located in the south center area (Fig. 51b), close to high elevated areas (Fig. B3). The sedimentary thickness is low (Fig. B17), but the 552 ms time slice exhibits strong red reflections for this location (Fig. B27). Higher amplitudes of the Lower Pleistocene 3 were also found in the same region (Fig. 50a), indicating an upward migration through the thinner deposits of the Lower Pleistocene 4 and accumulating in the high permeability deposits. The large concentration of higher amplitudes, located in the center to NE (Fig. 51c), occur in deeper deposits (Fig. B3). The sedimentary thickness in the area is low, but the 552 ms time slice exhibits strong red reflections that correspond to the same area as the amplitude anomalies (Fig. B27). These concentrations exhibits almost the same patterns as for the higher amplitudes located in the center to NE region of the Lower Pleistocene 3 (Fig. 50b). Fluids seems to migrate up through thin deposits of the Lower Pleistocene 4 to accumulate in high permeability bodies of the center to NE region. The higher amplitudes of the NE corner (Fig. 51d) occur in deeper regions that contains lower sedimentary deposits. The 552 ms time slice (Fig. B27) has small red reflections

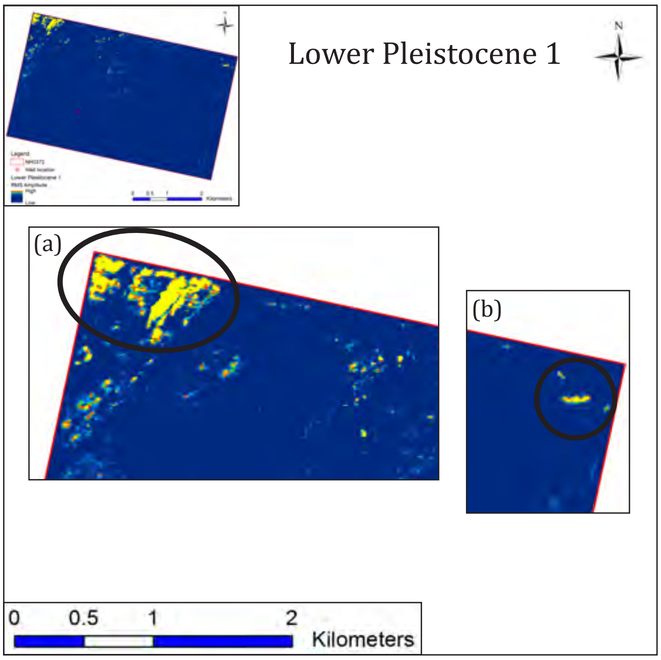

Figure 49a & b: Amplitude map (RMS) of the Lower Pleistocene 1. Amplitude anomalies are illustrated in red to yellow colors. Two regions of higher amplitudes are identified within this layer, outlined by black ellipses. The map in the upper left corner displays an overview of the layer, generated within the NH0372 survey area (Fig. B12).

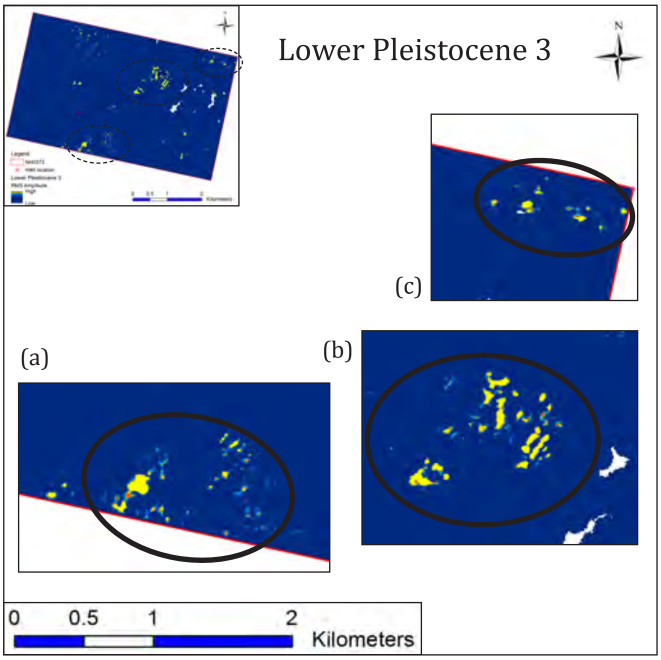

Figure 50a-c: Amplitude map (RMS) of the Lower Pleistocene 3. Amplitude anomalies are illustrated in red to yellow colors. Three regions of higher amplitudes are identified within this layer, outlined by black ellipses. The map in the upper left corner displays an overview of the layer, generated within the NH0372 survey area (Fig. B11).

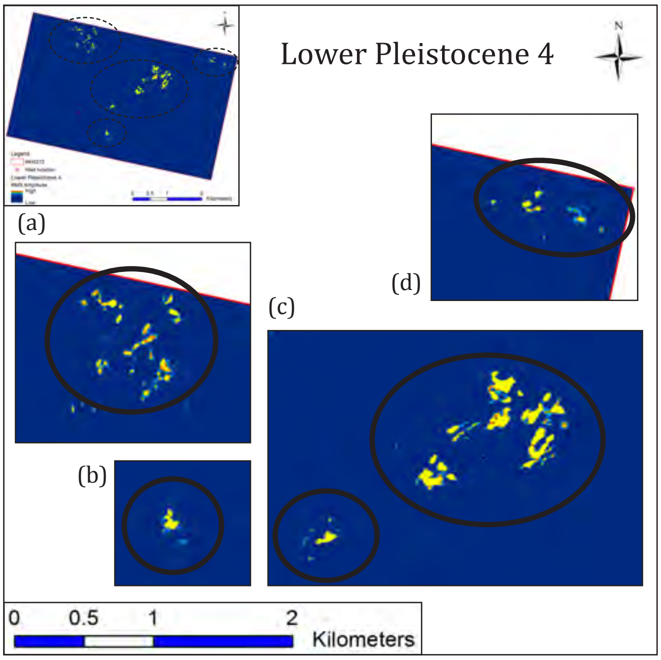

Figure 51a-d: Amplitude map (RMS) of the Lower Pleistocene 4. Amplitude anomalies are illustrated in red to yellow colors. Three areas of higher amplitudes are identified within this layer, outlined by black ellipses. The map in the upper left corner displays an overview of the layer, generated within the NH0372 survey area (Fig. B10).

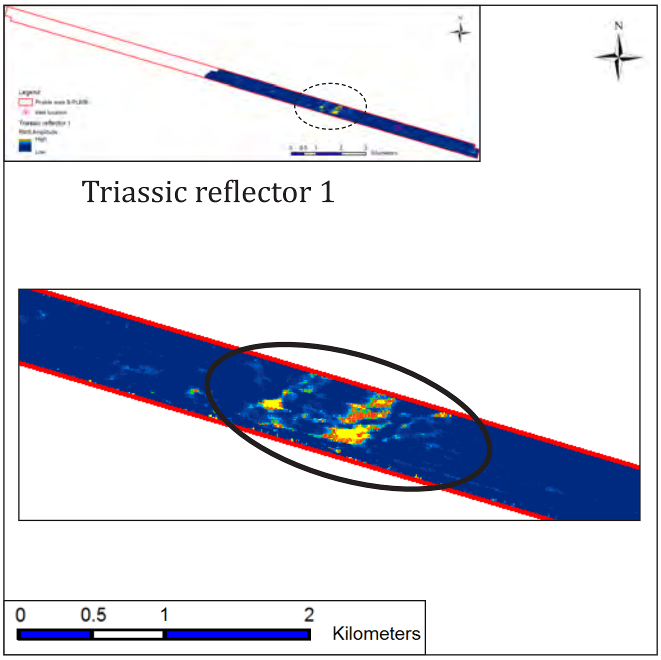

Figure 52: Amplitude map (RMS) of the Triassic reflector 1. Amplitude anomalies are illustrated in red to yellow colors. One areas of higher amplitudes is identified in the center, outlined by a black ellipse. The map in the upper left corner displays an overview of the layer, generated within the Pcable survey area (Fig. C15).

of higher permeability bodies that overlaps with the amplitude anomalies. Both the Lower Pleistocene 1 and 3 have higher amplitudes in the NE corner, which implies for an upward migration through the layers.

4.2.3 Study area Pcable area B PL609

The Pcable area B PL609 data set is a high resolution data set acquired by lining the streamers parallel along a cable towed perpendicular to the ship (Fig. 15) (Petersen et al., 2010), compared to the conventional method where streamers are towed parallel with a lateral offset to each other (Fig. 14) (Onajite, 2013). The Pcable data set do, as for the NH0372 data set, only cover a small part of the survey area and will thus be displayed as a close up study to illustrate the hydrocarbon migrations not registered in the LN12M01 data set. The Pcable overlaps with the NH0372 survey area in the SW region, but with no new amplitude anomalies that occur within the NH0372 survey area. It should be noted that, these three data sets were collected during different times and could thus be registering new migrations not previously occurred.

The Triassic reflector 1 is the deepest reflected layer mapped in the NH0372 survey area (Fig. C9). It is a tilted layer with top elevation in the center, cut off by the Bjørnøyrenna Fault Complex related rifting and subsidence in Late Jurassic to Early Cretaceous (Dore, 1995; Stemmerik et al., 1999; Smelror et al., 2009). Higher amplitudes can be seen in the center of the Triassic reflector 1 (Fig. 52), present at 720 ms and right above the fault located in the center (Fig. 53). Fluids have probably migrated in via the tilted layer and up the fault movement or migrated via the fault from older deposit. No visible red reflections were located in the 750 ms or the 700 ms time slices to verify the volume of the high permeability body (Fig. C32 & C33).

The time slices generated below the URU, from the LN12M01 data set, exhibited N-S striking faults crossing the center of the Pcable survey area (Fig. A51-A56). But only the 801 ms and 700 ms time slices generated from the Pcable data set were found to contain faults and they occur in the western region, above the Polheim Sub-platform. However, these faults form possible pathways for fluids to migrating within. Fluids may thus reach the URU, deriving either from the Triassic reflector 1 or from deeper buried fluids west of the Loppa High.

The Lower Pleistocene 1 has three areas of higher amplitudes, two located in the center and one in the NW region (Fig. 54). All three areas correspond to am-

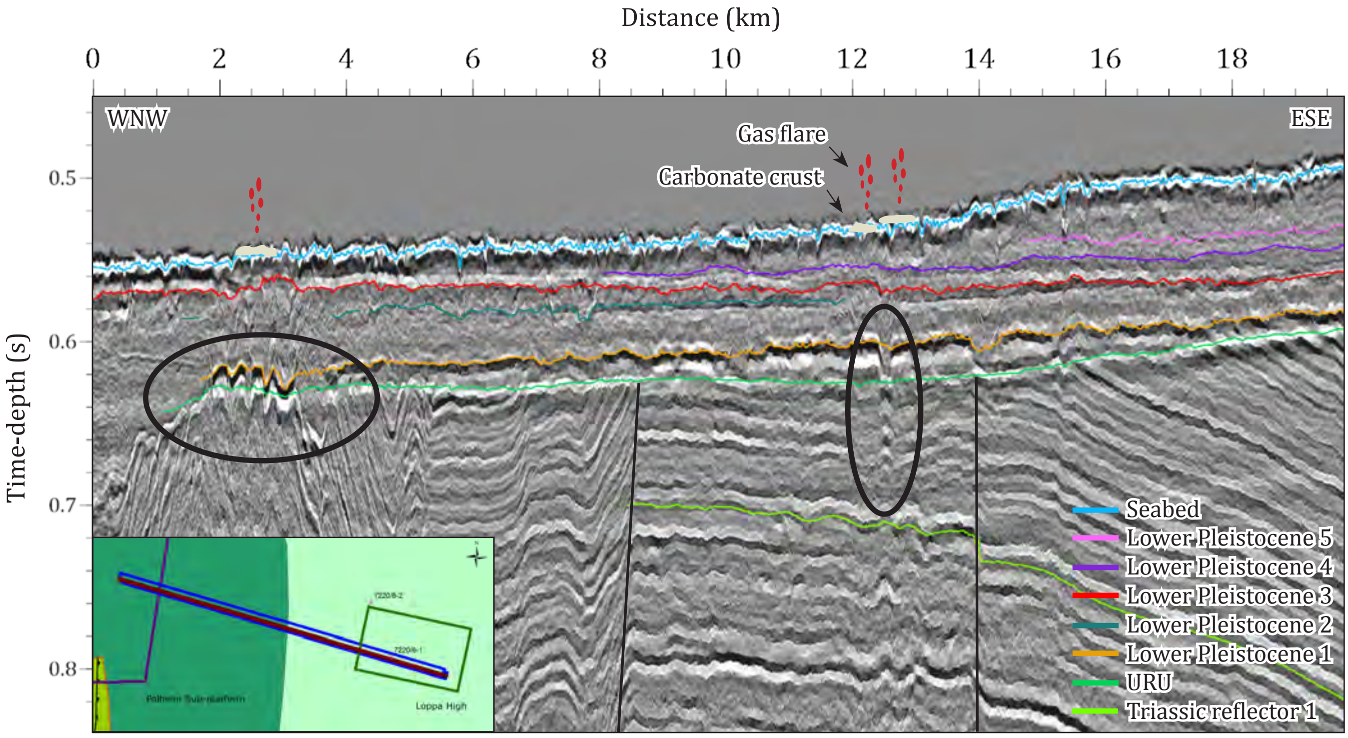

Figure 53: A seismic profile of the Pcable area B PL609 survey area, located center striking WNW-ESE. Eight layers are identified. Two major fault are highlighted in the center by black lines. The black ellipse in the WNW region marks an area of disturbed layering, preferentially the URU. The black ellipse in the center marks an acoustic masking. The gas flares (red) displayed on the seabed mark the approximate located of the three identified seeps. The map in the lower left corner displays an overview of the Pcable area B PL609 (blue outline) and NH0372 (green box) survey areas, with the orientation of the 2D seismic profile (dark red line). See figure A1 for the entire study area.

plitude anomalies exhibited in the Lower Pleistocene 1 of the LN12M01 survey area. The higher amplitudes in the NW region (Fig. 54a) occur in the deeper parts of the layer (Fig. C7). This is also in an area where the URU is disturbed and proved difficult to map, indicating for a fluid migration up through the URU and accumulating in the overlying deposits of the Lower Pleistocene 1 (Fig. 53). The second area is located higher up, at 605 ms, in the center of the Pcable survey area. Thicker sedimentary deposits in the area (Fig. 54b), but with no red reflections in the 600 ms time slice to support the presence of a larger high porosity body (Fig. C30). Fluids may have migrated along the layer, from NW, and accumulated here. The third area of higher amplitudes (Fig. 54c) overlaps with strong red reflections exhibited in the 600 ms time slice (Fig. C30). A vertical structure, known as an acoustic masking (Løseth et al., 2009; Pless, 2009), is present in the center to SE of the 2D seismic profile, between the Triassic reflector 1 and the Lower Pleistocene 1 (Fig. 53). Fluids may migrate up through the URU here and accumulate in the high permeability bodies. Migration along the Lower Pleistocene 1, in a NW-SE direction, is also possible due to the elevation incline (Fig. C7).

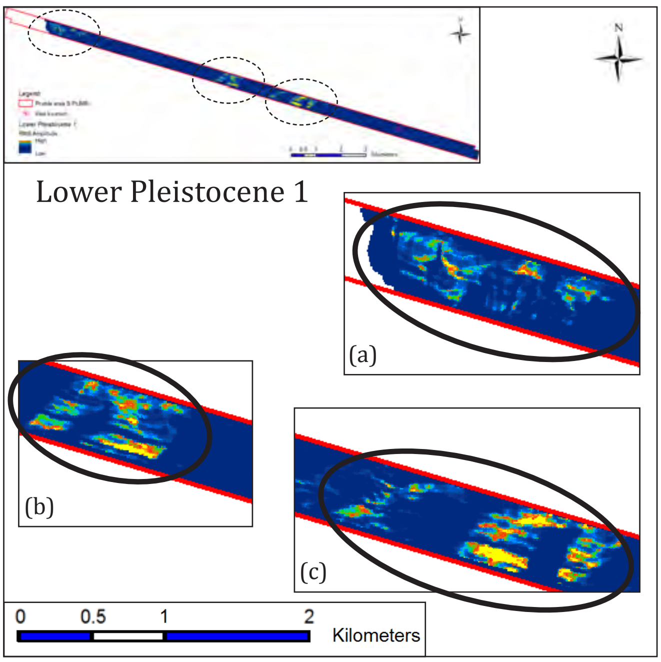

Figure 54a-c: Amplitude map (RMS) of the Lower Pleistocene 1. Amplitude anomalies are illustrated in red to yellow colors. Three areas of higher amplitudes are identified in the survey area, outlined by black ellipses. The three zoomed areas (a-c) are arranged as W-E. The map in the upper left corner displays an overview of the layer, generated within the Pcable survey area (Fig. C14).

No direct concentrations of higher amplitudes were identified in the Lower Pleistocene 2, only smaller anomalies in the center to NW region (Fig. C13).

The Lower Pleistocene 3 exhibits higher concentrations of amplitude anomalies in the NW corner of the survey area (Fig. 55). This is at the deeper parts of the layer, at 570 ms (Fig. C5). Fluids have probably migrated in from outside the Pcable survey area, from the west, and accumulated here.

The higher amplitudes of the Lower Pleistocene 4 occur in the center of the survey area (Fig. 56). This is in the deepest elevated region of the Lower Pleistocene 4 (Fig. C4), exhibiting thin sedimentary deposits (Fig. C18). Amplitude anomalies, of both high and low concentrations, can be traced up from the central parts of the Lower Pleistocene 1 (Fig. 54b). Occurring as smaller concentrations in the overlapping regions of the Lower Pleistocene 2 and 3 before reaching the higher amplitudes in the Lower Pleistocene 4. Fluids may have migrated upwards through these layers, but the more likely cause is lateral movements within each layer.

No major fluid accumulations could be located within the Lower Pleistocene 5 as no larger areas of higher amplitudes were identified, only smaller fluid concentrations spread out over the mapped layer (Fig. C10).

4.3 Water column data

Additional data set of water column data was examined over foremost the NH0372 and Pcable area B PL609 survey areas, with vicinity, to locate potential gas migrations leaving the sea floor. The three areas of gas flares identified were along the Pcable survey; two flares located on the Loppa High; and one gas flare to the NW above the Polheim Sub-platform. The fossil fluids seeping out from the seabed occur in an area covered with iceberg ploughmarks (Fig. 34). Hydrocarbons from the oil and gas discoveries in the well 7220/5-1, or from deeper deposits, could migrate up via the numerous faults in the area until it reaches the URU (Fig. 36). If the migration occurs in a NE direction, via the tilted layers below the URU, then the fluids will reach the Lower Pleistocene layers in the vicinity of the NW gas flare. A NE migration above the URU would be difficult since the Lower Pleistocene layers have a NW-SE inclination (Fig. A14). The two gas flares located above the Loppa High might originate from two sources; located close to the foot-

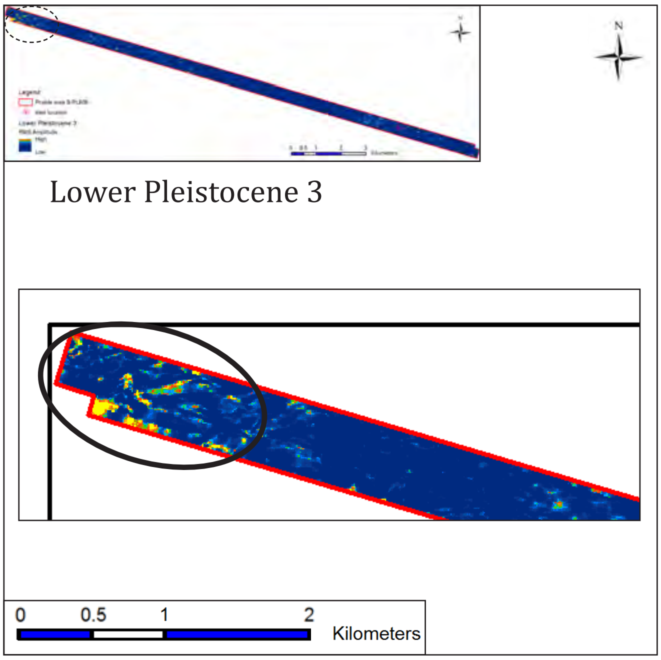

Figure 55: Amplitude map (RMS) of the Lower Pleistocene 3. Amplitude anomalies are illustrated in red to yellow colors. One areas of higher amplitudes is identified in the NW region, outlined by a black ellipse. The map in the upper left corner displays an overview of the layer, generated within the Pcable survey area (Fig. C13).

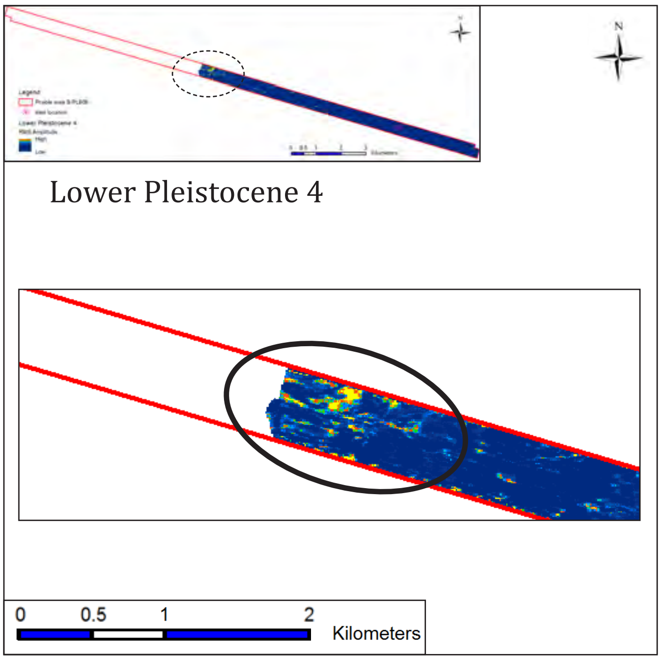

Figure 56: Amplitude map (RMS) of the Lower Pleistocene 4. Amplitude anomalies are illustrated in red to yellow colors. One areas of higher amplitudes is identified in the center, outlined by a black ellipse. The map in the upper left corner displays an overview of the layer, generated within the Pcable survey area (Fig. C12).

wall uplift, the hydrocarbons may migrate through the numerous faults in the area; or up via the tilted and faulted Triassic deposits before finding a pathway through the Lower Pleistocene deposits.

5. Conclusions

The gas-oil contact and the oil-water contact, visible at 1460 ms respective 1540 ms to the WNW of the NBR10-338364 seismic profile, were penetrated by well 7220/5-1 in 2012. The drilling results confirmed hydrocarbon concentrations in Jurassic sandstone. The migration of these fluids or from deeper buried hydrocarbons could be evidenced by the many strong reflections visible in the shallower, tilted and faulted strata located above the Polheim Sub-platform. Fluid concentrations were also identified in the Snadd Formation of Triassic deposits, as strong reflections visible above the Loppa High and next to the down-faulted structure. Amplitude maps of the Triassic reflector 1 and 2 as well as the many faults identified in the region did indicate for an upward migration towards URU.

The impermeable layer of URU were found to transmit hydrocarbons along a curved elongated depression located in the southern region of the LN12M01 survey area. Amplitude maps of the Lower Pleistocene 1 and up to the Lower Pleistocene 5 exhibits areas of larger fluid concentrations above the depression, indicating an upward migration in the southern region of the study area. The Lower Pleistocene 1 was found to contain large concentrated areas of fluids in the center to northern region, corresponding with thick sedimentary deposits. Amplitude anomalies of greater magnitudes were also located in the NW regions of the Lower Pleistocene 3 and 4, indicating a possible fluid migration in a SE direction between the two layers.

The stratigraphic layers generated from the NH0372 data set were found to contain fluid concentrations not registered in the LN12M01 data set. Faults were identified in the Late Carboniferous deposits and up to the URU, which would allow fluids to migrate upwards within the survey area. The Lower Pleistocene 0 and 1 exhibit similar concentrated patterns of fluids located in the NW corner. Minor fluid concentrations can also be seen in the NW regions of the Lower Pleistocene 3 and 4, indicating for an upward fluid migration in the area. The Lower Pleistocene 3 and 4 exhibit similar patterns of higher amplitudes in the center of the study area, indicating high permeability layers with focused upward migration between the two layers. Small fluid concentrations were also identified in the NE corner of the Lower Pleistocene 1 to 4, implying a concentrated fluid migration up through the thin sedimentary deposits.

The Pcable area B PL609 data set was sampled above the border to the Loppa High and the Polheim Sub-platform. N-S striking faults were found to cut the Triassic deposits and thus provide possible fluid migration pathways. The disturbance of the URU in the NW region and the presence of a vertical structure in the center to NE region has probably allowed for an upward migration through the URU. The Lower Pleistocene 1 was found to contain three areas of higher concentrations, all of which corresponds with findings in the LN12M01 data set. Fluid concentrations in the center of the Lower Pleistocene 1-4 indicated for an upward migration, but could just as easily be horizontal migrations within each layer as the inclination runs in a NW-SE orientation.

Three gas flares were identified, two on the Loppa High and one over the Polheim Sub-platform. The single gas flare to the NW may originate from the oil and gas findings of well 7220/5-1, but could as well be biogenic gas from much shallower origins. The two gas flares above the Loppa High may have migrated in from the Triassic deposits or via faults located along the footwall uplift, if not of biogenic origin.

Further research can be done in this area to improve my work. The absence of high resolution data sets over most of the study area limited the identification of smaller fluid concentrations, or even specific areas for upward migrations between layers. Data from sub bottom profiler (SBP) would be of great assistance in the top sedimentary deposits as a more detailed picture of fluid concentrations and migrations could be constructed. Another interesting area for further research is the biological response to hydrocarbon emissions from the seabed. Observations aboard the vessel M/V Stril Explorer shown indications of an interaction between the marine fauna and the sulfide consuming bacterial mats.

6. References

Abdel-Aal, H.K., Aggour, M.A., Fahim, M.A. (2003). Petroleum and gas field processing. CRC Press, pp. 357

Aminzadeh, F., Dasgupta, S.N. (2013). Geophysics for Petroleum Engineers. Developments in Petroleum Science. Elsevier, vol. 60, ch. 3, p. 37-92

Barrie, S., Clarke, G., Harrison, E., Hawes, N., Smith, N. (1998). 3D Survey Final Report for SAGA Petroleum ASA SG9810 NOCS, Barents Sea Loppa Vest. EPI Report no. 467, pp. 356

Bergan, M., Knarud, R. (1993). Apparent changes in clastic mineralogy of the Triassic-Jurassic succession, Norwegian Barents Sea: possible implications for palaeodrainage and subsidence. Arctic Geology and Petroleum Potential, Norwegian Petroleum Society (NPF), Special Publication, vol. 2, p. 481-493

Billard, M. (2011). Final Survey Report: 3003-ARC-Lundin Norway-LN11003 Survey 3D Project. Dolphin Geo Job no. 3002-ARC-LUNDIN, pp. 127

Bjørlykke, K. (2010). Petroleum geoscience: From sedimentary environments to rock physics. Springer Science & Business Media, pp. 518

Brekke, H., Sjulstad, H.I., Magnus, C., Williams, R.W. (2001). Sedimentary environments offshore Norway - an overview. Norwegian Petroleum Society Special Publications, vol. 10, p. 7-37

Chand, S., Thorsnes, T., Rise, L., Brunstad, H., Stoddart, D., Bøe, R., Lågstad, P., Svolsbru, T. (2012). Multiple episodes of fluid flow in the SW Barents Sea (Loppa High) evidenced by gas flares, pockmarks and gas hydrate accumulation. Earth and Planetary Science Letters, vol. 331-332, p. 305–314

Clennell, M.B., Judd, A., Hovland, M. (2000). Movement and accumulation of methane in marine sediments: relation to gas hydrate systems. Natural Gas Hydrate in Oceanic and Permafrost Environments. Kluwer Academic Publishers, vol. 5, ch. 9, p. 105-122

Dake, L.P. (1998). Fundamentals of reservoir engineering. Elsevier, vol. 17, ch. 3 & 10, p. 71-99 & 337-421

Dengo, C.A., Røssland, K.G. (2013). Extensional tectonic history of the western Barents Sea. Structural and tectonic modelling and its application to petroleum geology, Norwegian Petroleum Society (NPF), Special Publication, vol. 1, p. 91-107

Dore, A.G. (1995). Barents Sea Geology, Petroleum Resources and Commercial Potential. Arctic, vol. 48, no. 3, p. 207-221

Faleide, J.I., Bjørlykke, K., Gabrielsen, R.H. (2010). Geology of the Norwegian continental shelf. In Petroleum Geoscience. Springer Science & Business Media, p. 467-499

Faleide, J.I., Solheim, A., Fiedler, A., Hjelstuen, B.O., Andersen, E.S., Vanneste, K. (1996). Late Cenozoic evolution of the western Barents Sea-Svalbard continental margin. Global and Planetary Change, vol. 12 no. 1, p. 53-74

Gabrielsen, R.H., Færseth, R.B., Jensen, L.N., Kalheim, J.E. Riis, F. (1990). Structural elements of the Norwegian continental shelf, Part I: The Barents Sea Region. Norwegian Petroleum Directorate (NPD) Bulletin, no. 6 pp. 33

Glørstad-Clark, E., Faleide, J.I., Lundschien, B.A., Nystuen, J.P. (2010). Triassic seismic sequence stratigraphy and paleogeography of the western Barents Sea area. Marine and Petroleum Geology, vol. 27, no. 7, p. 1448-1475

Golonka, J., Bocharova, N.Y., Ford, D., Edrich, M.E., Bednarczyk, J., Wildharber, J. (2003). Paleogeographic reconstructions and basins development of the Arctic. Marine and Petroleum Geology, vol. 20, p. 211–248

Golsanami, N., Kadkhodaie-Ilkhchi, A., Erfani, A. (2015). Synthesis of capillary pressure curves from post-stack seismic data with the use of intelligent estimators: A case study from the Iranian part of the South Pars gas field, Persian Gulf Basin. Journal of Applied Geophysics, vol. 112, p. 215-225

Gradstein, F.M., Ogg, J.G., Schmitz, M., Ogg, G. (2012). The Geologic Time Scale 2012. Elsevier, vol. 2. Retrieved 13 November 2014 from https://engineering.purdue.edu/Stratigraphy/

Gudlaugsson, S.T., Faleide, J.I., Johansen, S.E., Breivik, A.J. (1998). Late Palaeozoic structural development of the South-western Barents Sea. Marine and Petroleum Geology, vol. 15, p. 73-102

Haavik, K.E., Landrø, M. (2014). Iceberg ploughmarks illuminated by shallow gas in the central North Sea. Quaternary Science Reviews, vol. 103, p. 34-50

Hameed, M.S. (2012). Detailed Structural Investigation of the Bjørnøyrenna Fault Complex. Department of Geoscience, University of Oslo, pp. 126

Hustoft, S., Mienert, J., Bünz, S., Nouzé, H. (2007). High-resolution 3D-seismic data indicate focused fluid migration pathways above polygonal fault systems of the mid-Norwegian margin. Marine Geology, vol. 245, no. 1, p. 89-106

IOGP, IAGC (2011). An overview of marine seismic operations. International Association of Oil & Gas Producers (IOGP), International Association of Geophysical Contractors(IAGC). Report no. 448, pp. 50

Jakobsson, M., Mayer, L., Coakley, B., Dowdeswell, J.A., Forbes, S., Fridman, B., Hodnesdal, H., Noormets, R., Pedersen, R., Rebesco, M., Werner Schenke, H., Zarayskaya, Y., Accettella, D., Armstrong, A., Anderson, R.M., Bienhoff, P., Camerlenghi, A., Church, I., Edwards, M., Gardner, J.V., Hall, J.K., Hell, B., Hestvik, O., Kristoffersen, Y., Marcussen, C., Mohammad, R., Mosher, D., Nghiem, S.V., Pedrosa, M.T., Travaglini, P.G., Weatherall, P. (2012). The international bathymetric chart of the Arctic Ocean (IBCAO) version 3.0. Geophysical Research Letters, vol. 39 no. 12. pp. 6. Retrieved 14 April 2015 from http://www.ngdc.noaa.gov/mgg/bathymetry/arctic/arctic.html

Jones, E.J.W. (1999). Marine geophysics. John Wiley & Sons, ch. 4 & 5, p. 61-130

Kearey, P., Brooks, M., Hill, I. (2002). An introduction to geophysical exploration. John Wiley & Sons, ch 3 & 4, p. 21-98

Kjerkreit, K. (2014). Origin and accumulation mechanism of shallow gas accumulations in the SW Barents Sea. Department of Geology, University of Tromsø, pp. 103

Kvenvolden, K.A. (2000). Natural gas hydrate: Background and history of discovery. Natural Gas Hydrate in Oceanic and Permafrost Environments. Kluwer Academic Publishers, vol. 5, ch. 2, p. 9-16

Langrock, U., Stein, R. (2004). Origin of marine petroleum source rocks from the Late Jurassic to Early Cretaceous Norwegian Greenland Seaway evidence for stagnation and upwelling. Marine and petroleum geology, vol. 21, no. 2, p. 157-176

Larssen, G.B., Elvebakk, G., Henriksen, L.B., Kristensen, S-E., Nilsson, I., Samuelsberg, T.J., Stemmerik, L., Worsley, D. (2002). Upper Palaeozoic lithostratigraphy of the Southern Norwegian Barents Sea. Norwegian Petroleum Directorate Bulletin, no. 9, pp. 76

Li. M., Zhao. Y. (2014). Geophysical Exploration Technology - Applications in Lithological and Stratigraphic Reservoirs. Elsevier, ch. 5, p. 103-131

Libes, S. (2011). Introduction to marine biogeochemistry. Academic Press, vol. 2, ch. 26, pp. 34

Lindquist, S.J. (1999). South and North Barents Triassic-Jurassic Total Petroleum System of the Russian Offshore Arctic. U. S. Geological Survey, Open File Report 99-50N, pp. 22

Løseth, H., Gading, M., Wensaas, L. (2009). Hydrocarbon leakage interpreted on seismic data. Marine and Petroleum Geology, vol. 26, no. 7, p. 1304-1319

Lyons, W.C., Plisga, G.J. (1996). Standard handbook of petroleum & natural gas engineering. Gulf Professional Publishing, vol. 2, ch. 2, p. 61-199

Marshak, S., Prothero, D.R. (2008). Earth: portrait of a planet. WW Norton & Company, vol. 3, pp. 880

McCarthy, K., Rojas, K., Niemann, M., Palmowski, D., Peters, K., Stankiewicz, A. (2011). Basic petroleum geochemistry for source rock evaluation. Oilfield Review, vol. 23 no. 2, p. 32-43

MMT (2014). Operational and Summary Report, Barents Sea Survey. Seabed Mapping and Inspection Barents Sea. Marin Mätteknik (MMT). Project 101722, doc. no. 101722-LUN-MMT-OPS-SUM-01, pp. 77

Nickel, J.C., di Primio, R., Mangelsdorf, K., Stoddart, D., Kallmeyer, J. (2012). Marine Geology, vol. 332–334, pp. 152–162

NPD (2015). Norwegian Petroleum Directorate Factpages (NPD). Retrieved 10 April 2015 from http://www.npd.no/en/

Onajite, E. (2013). Seismic Data Analysis Techniques in Hydrocarbon Exploration. Elsevier, ch. 2 & 3, p. 17-62

Pease, V., Drachev, S., Stephenson, R., Zhang, X. (2014). Arctic lithosphere - A review. Tectonophysics, vol. 628, p. 1-25

Petersen, C.J., Bünz, S., Hustoft, S., Mienert, J., Klaeschen, D. (2010). High-resolution P-Cable 3D seismic imaging of gas chimney structures in gas hydrated sediments of an Arctic sediment drift. Marine and Petroleum Geology, vol. 27, no. 9, p. 1981-1994

Petrov, O.V., Sobolev, N.N., Koren, T.N., Vasiliev, V.E., Petrov, E.O., Larssen, G.B., Smelror, M. (2008). Palaeozoic and Early Mesozoic evolution of the East Barents and Kara Seas sedimentary basins. Norwegian Journal of Geology, vol. 88, p. 227-234

Pless, G. (2009). Occurrence of free gas and focused fluid flow systems in the Veslemøy High area, SW Barents Sea. Department of Geology, University of Tromsø, pp. 137

Ritzmann, O., Faleide, J.I. (2009). The crust and mantle lithosphere in the Barents Sea/Kara Sea region. Tectonophysics, vol. 470, p. 89–104

Ryseth, A., Augustson, J.H., Charnock, M., Haugerud, O., Knutsen, S-M., Midbøe, P.S., Opsal, J.G., Sundsbø, G. (2003). Cenozoic stratigraphy and evolution of the Sørvestsnaget Basin, southwestern Barents Sea. Norwegian Journal of Geology, vol. 83, no. 2, p. 107-130

Schulz, H.D., Zabel, M. (2006). Marine geochemistry. Springer-Verlag Berlin Heidelberg, vol. 2, pp. 582

Skjelle, H., Grønås, T., Dunn, M., Salman, A., Taghiyev, F., Andersen, Ø. (2012). Final Well Report, Appraisal Well 7220/5-1. Doc. no. EPDS-7220/5-1-00003, pp. 248

Smelror, M., Petrov, O., Larssen G.B., Werner, S. (2009). ATLAS - Geological history of the Barents Sea. Geological Survey of Norway (NGU), pp. 138

Solheim, A., Kristoffersen, Y. (1984). The physical environment in the Western Barents Sea, 1:5,000,000. Sediments above the upper regional unconformity: thickness, seismic stratigraphy and outline of the glacial history. Norsk Polarinstitutt, Skrifter 179B, pp. 26

Speight, J.G. (2010). Handbook of industrial hydrocarbon processes. Gulf Professional Publishing, ch. 2, p. 43-83

Speight, J.G. (2012). Shale Oil Production Processes. Gulf Professional Publisher, vol. 1, ch. 1 & 3, p. 1-33 & 75-92

Stemmerik, L., Elvebakk, G., Worsley, D. (1999). Upper Palaeozoic carbonate reservoirs on the Norwegian arctic shelf: delineation of reservoir models with application to the Loppa High. Petroleum Geoscience, vol. 5, p. 173-187

Vadakkepuliyambatta, S., Bünz, S., Mienert, J., Chand. S. (2013). Distribution of subsurface fluid-flow systems in the SW Barents Sea. Marine and Petroleum Geology, vol. 43, p. 208-221

Vernikovsky, V.A., Dobretsov, N.L., Metelkin, D.V., Matushkin, N.Y., Koulakov, I.Y. (2013). Concerning tectonics and the tectonic evolution of the Arctic. Russian Geology and Geophysics, vol. 54, p. 838–858

Vigran, J.O., Mørk, A., Forsberg, A.W., Weiss, H.M., Weitschat, W. (2008). Tasmanites algae-contributors to the Middle Triassic hydrocarbon source rocks of Svalbard and the Barents Shelf. Polar Research, vol. 27 no. 3, p. 360-371

Wellsbury, P., Parkes, R.J. (2000). Deep biosphere: Source of methane for oceanic hydrate. Natural Gas Hydrate in Oceanic and Permafrost Environments. Kluwer Academic Publishers, vol. 5, ch. 8, p. 91-104

Worsley, D. (2008). The post-Caledonian development of Svalbard and the western Barents Sea. Polar Research, vol. 27, no. 3, p. 298-317

Appendix A - Survey area LN12M01

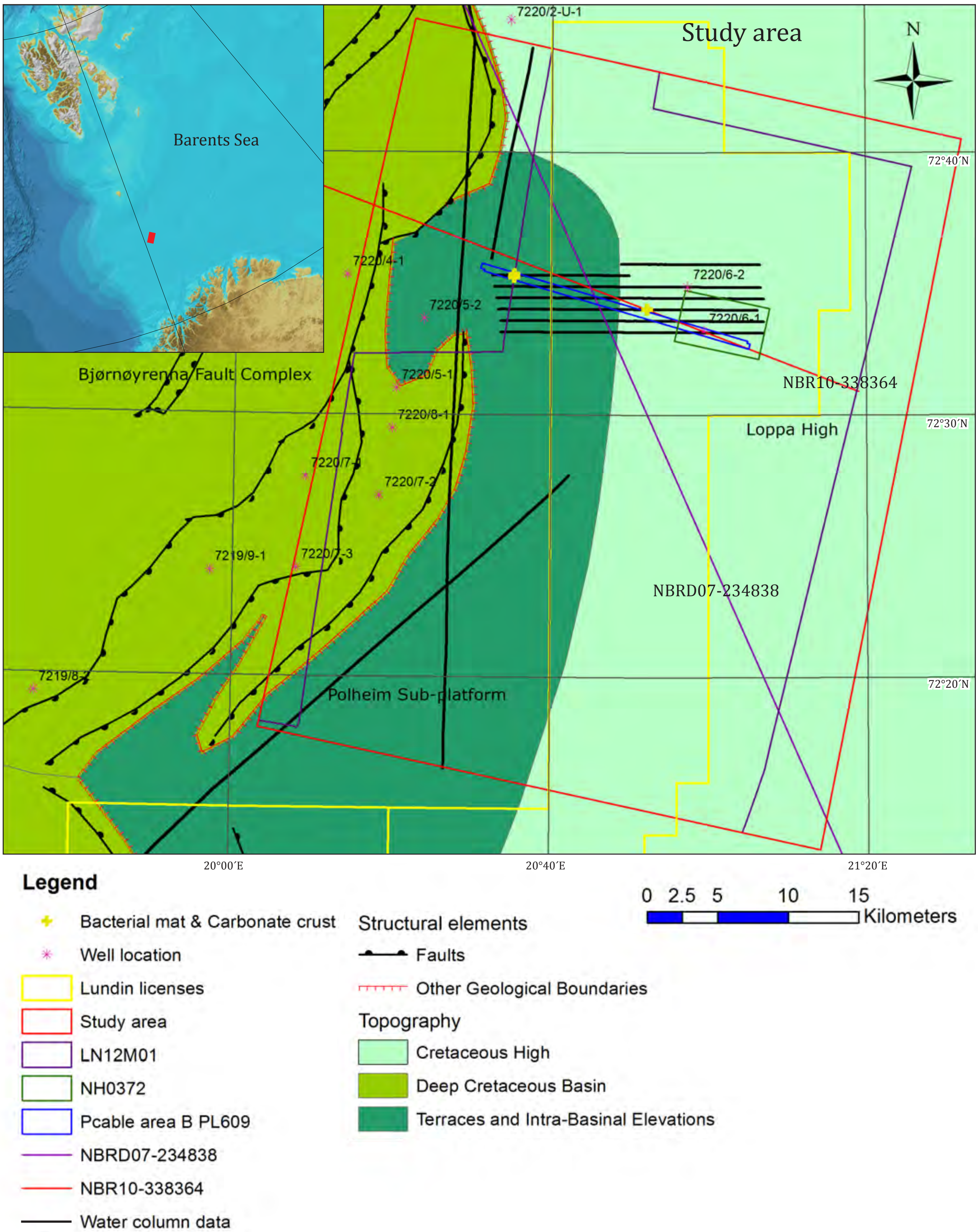

Figure A1: Map showing the three survey areas located within the study area, together with alignments of the two survey lines. Wells drilled in the area is given as well as the location of previously known bacterial mats and carbonate crusts. The water column data used in this study are marked as black lines. License areas belonging to Lundin Norway AS are outlined with yellow lines. The reference map in the left corner are from IBCAO (Jakobsson et al., 2012), with the approximate location of the study area marked in red.

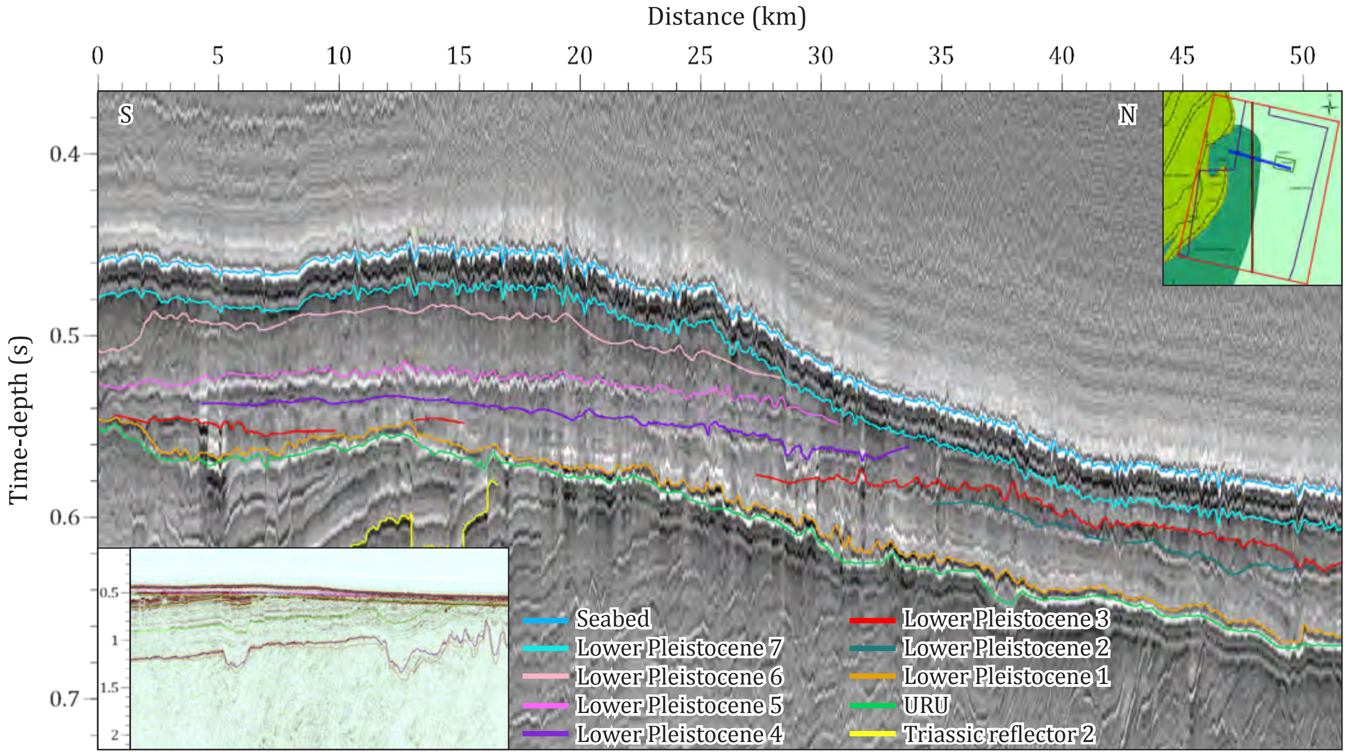

Figure A2: A seismic profile of the LN12M01 survey area, located center striking S-N. Ten layers are highlighted: the seabed (blue); Lower Pleistocene 7 (turquoise); Lower Pleistocene 6 (pale pink); Lower Pleistocene 5 (pink); Lower Pleistocene 4 (violet); Lower Pleistocene 3 (red); Lower Pleistocene 2 (dark green); Lower Pleistocene 1 (orange); URU (green); Triassic reflector 2 (yellow). Three additional layers are highlighted in the deeper deposits, lower left corner: Triassic reflector 1 (neon green); Late Carboniferous (purple) and top basement (brown). The map in the upper right corner displays an overview of the study area (Fig. A1) and the LN12M01 survey areas (purple outline), with the orientation of the 2D seismic profile (dark red line).

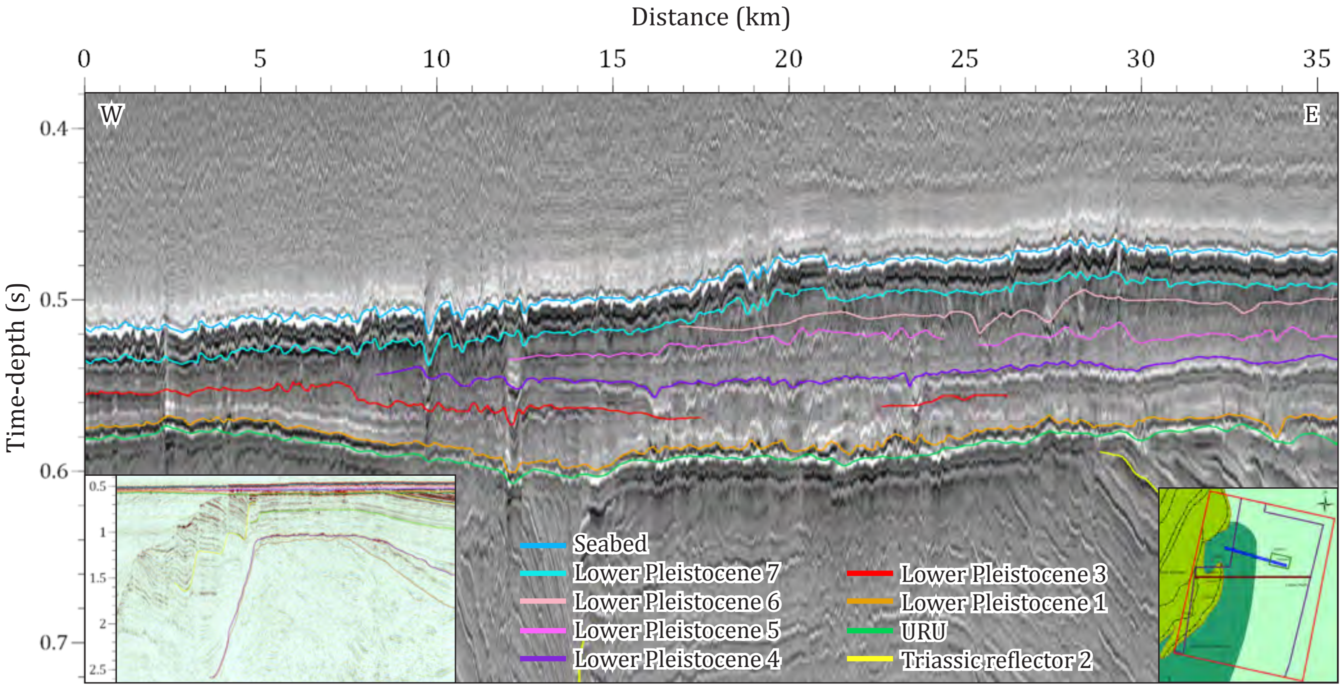

Figure A3: A seismic profile of the LN12M01 survey area, located center striking W-E. Ten layers are highlighted: the seabed (blue); Lower Pleistocene 7 (turquoise); Lower Pleistocene 6 (pale pink); Lower Pleistocene 5 (pink); Lower Pleistocene 4 (violet); Lower Pleistocene 3 (red); Lower Pleistocene 1 (orange); URU (green); Triassic reflector 2 (yellow). Three additional layers are highlighted in the deeper deposits, lower left corner: Triassic reflector 1 (neon green); Late Carboniferous (purple) and top basement (brown). The map in the lower right corner displays an overview of the study area (Fig. A1) and the LN12M01 survey areas (purple outline), with the orientation of the 2D seismic profile (dark red line).

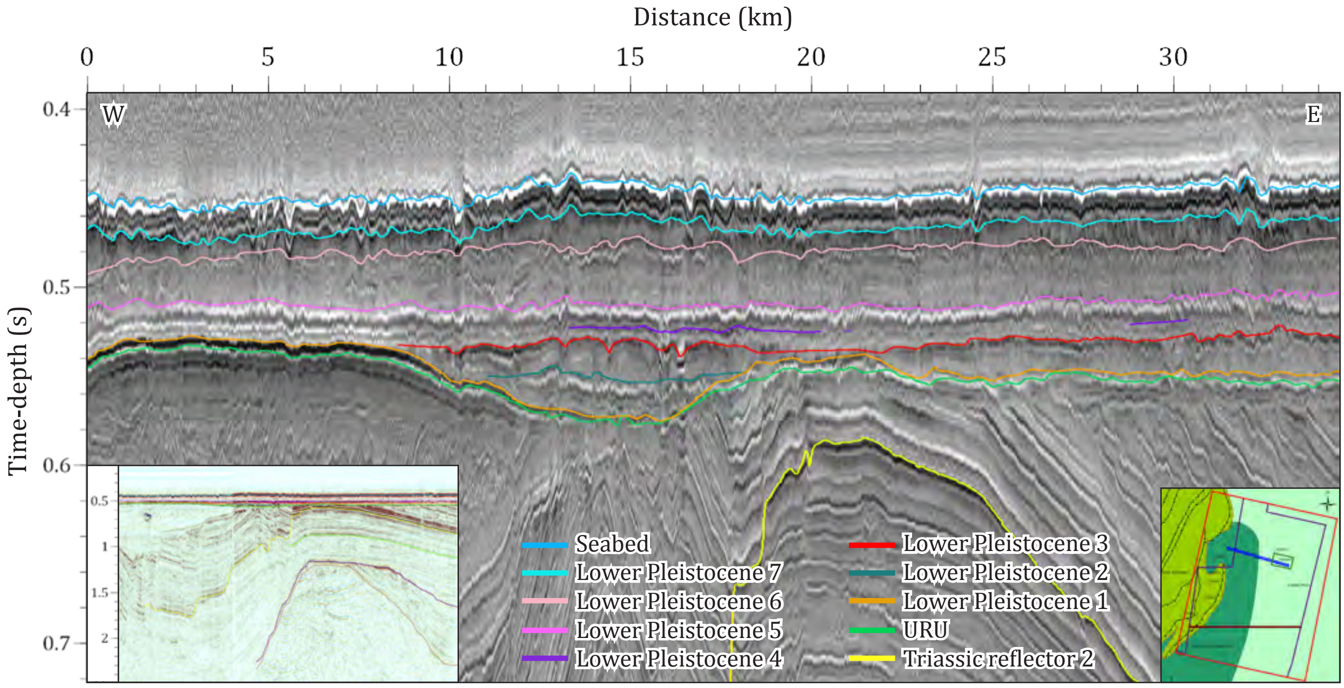

Figure A4: A seismic profile of the LN12M01 survey area, located in the southern half striking W-E. Ten layers are highlighted: the seabed (blue); Lower Pleistocene 7 (turquoise); Lower Pleistocene 6 (pale pink); Lower Pleistocene 5 (pink); Lower Pleistocene 4 (violet); Lower Pleistocene 3 (red); Lower Pleistocene 2 (dark green); Lower Pleistocene 1 (orange); URU (green); Triassic reflector 2 (yellow). Three additional layers are highlighted in the deeper deposits, lower left corner: Triassic reflector 1 (neon green); Late Carboniferous (purple) and top basement (brown). The map in the lower right corner displays an overview of the study area (Fig. A1) and the LN12M01 survey areas (purple outline), with the orientation of the 2D seismic profile (dark red line).

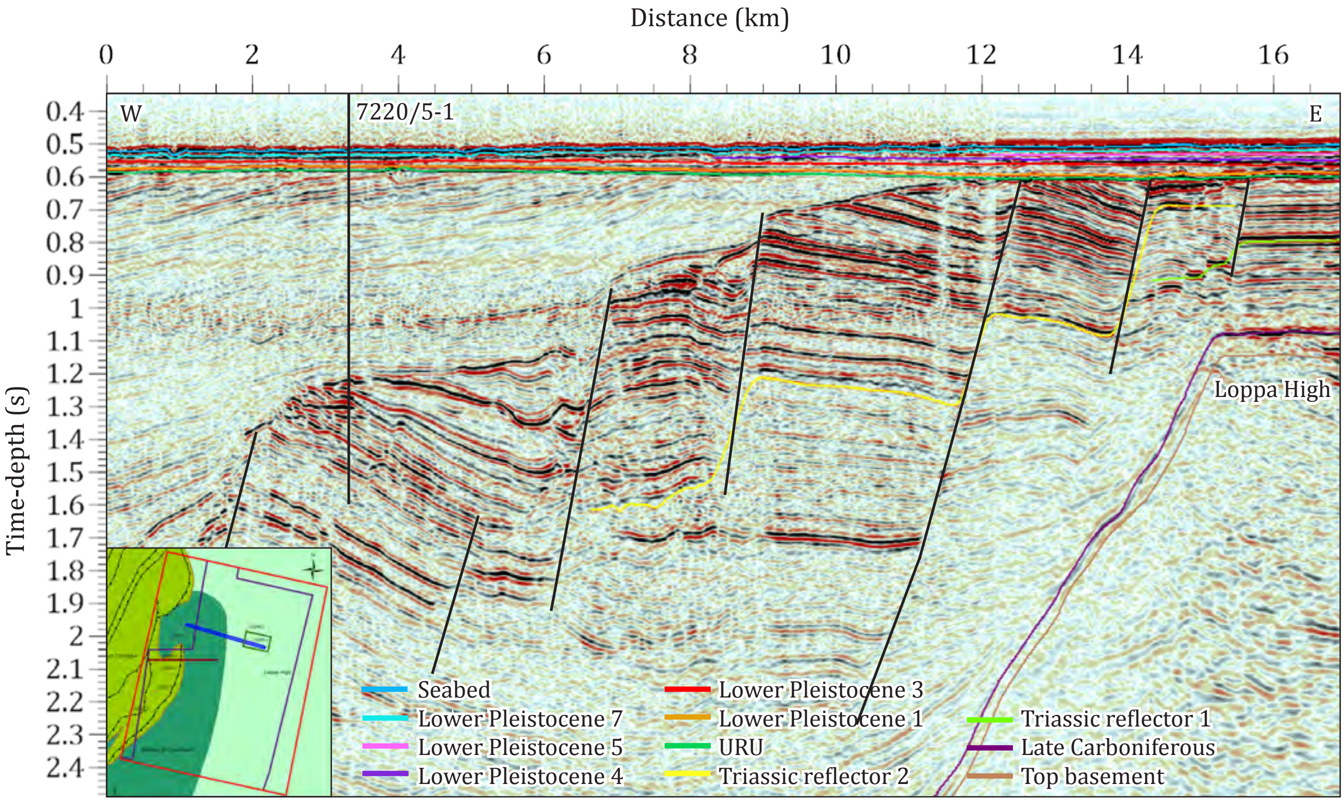

Figure A5: A seismic profile of the LN12M01 survey area, located center striking W-E. Eleven layers are highlighted: the seabed (light blue); Lower Pleistocene 7 (turquoise); Lower Pleistocene 5 (pink); Lower Pleistocene 4 (violet); Lower Pleistocene 3 (red); Lower Pleistocene 1 (orange); URU (green); Triassic reflector 2 (yellow); Triassic reflector 1 (neon green); Late Carboniferous (purple) and the top basement (brown). Major faults are highlighted with black lines. The well 7220/5-1, with drilling depth, is illustrated in the seismic profile (black line). The map in the lower left corner displays an overview of the study area (Fig. A1) and the LN12M01 survey area (purple outline), with the orientation of the 2D seismic profile (dark red line).

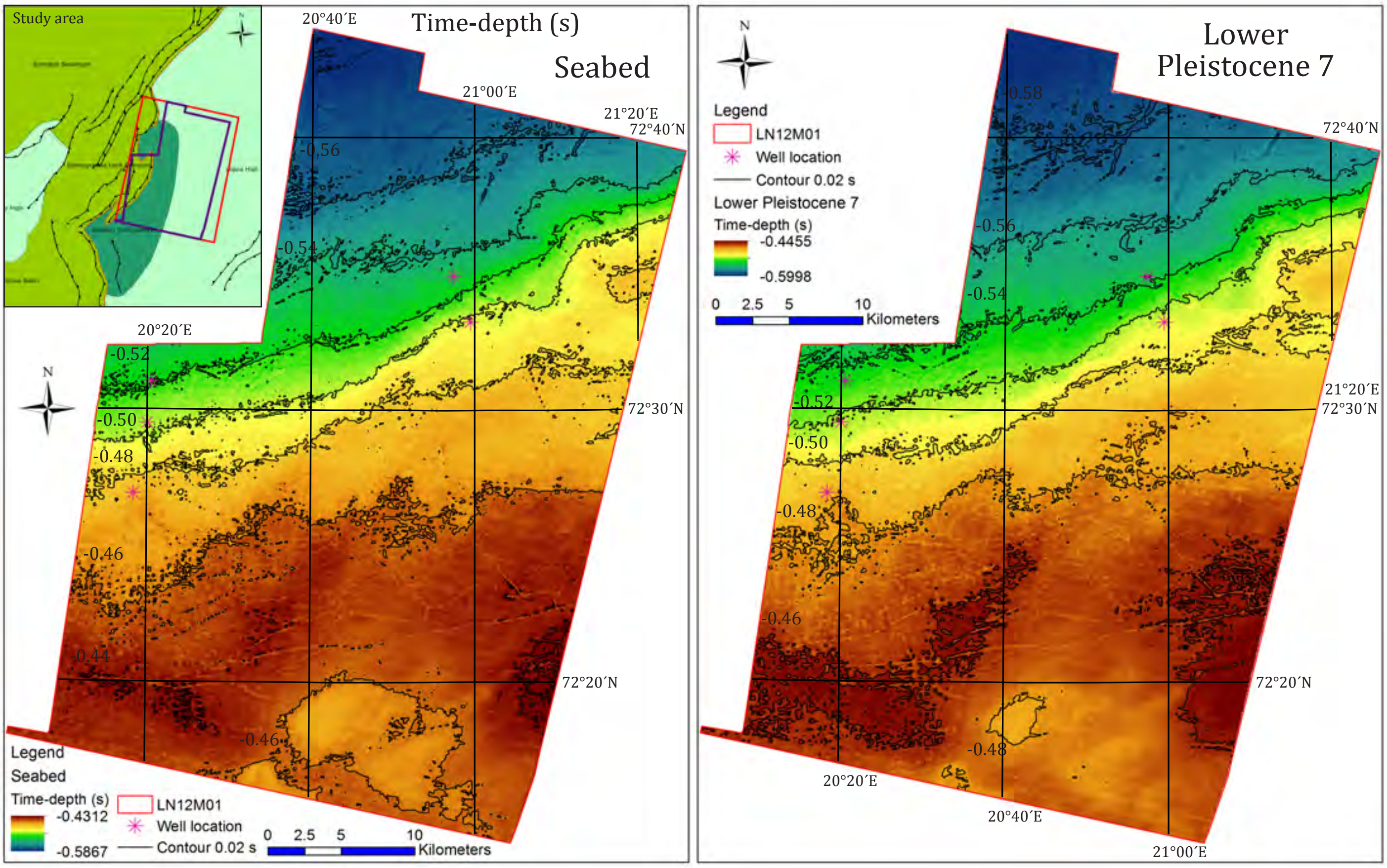

Figure A6 & A7: Paleo-bathymetry maps of the seabed and the Lower Pleistocene 7, generated from the LN12M01 survey area. The depth is presented in seconds and the contour lines in each map illustrate elevation changes for every 0.02 s. Pink dots mark the location of wells. The map in the upper left corner of the seabed displays an overview of the study area (Fig. A1), with the LN12M01 survey area (purple).

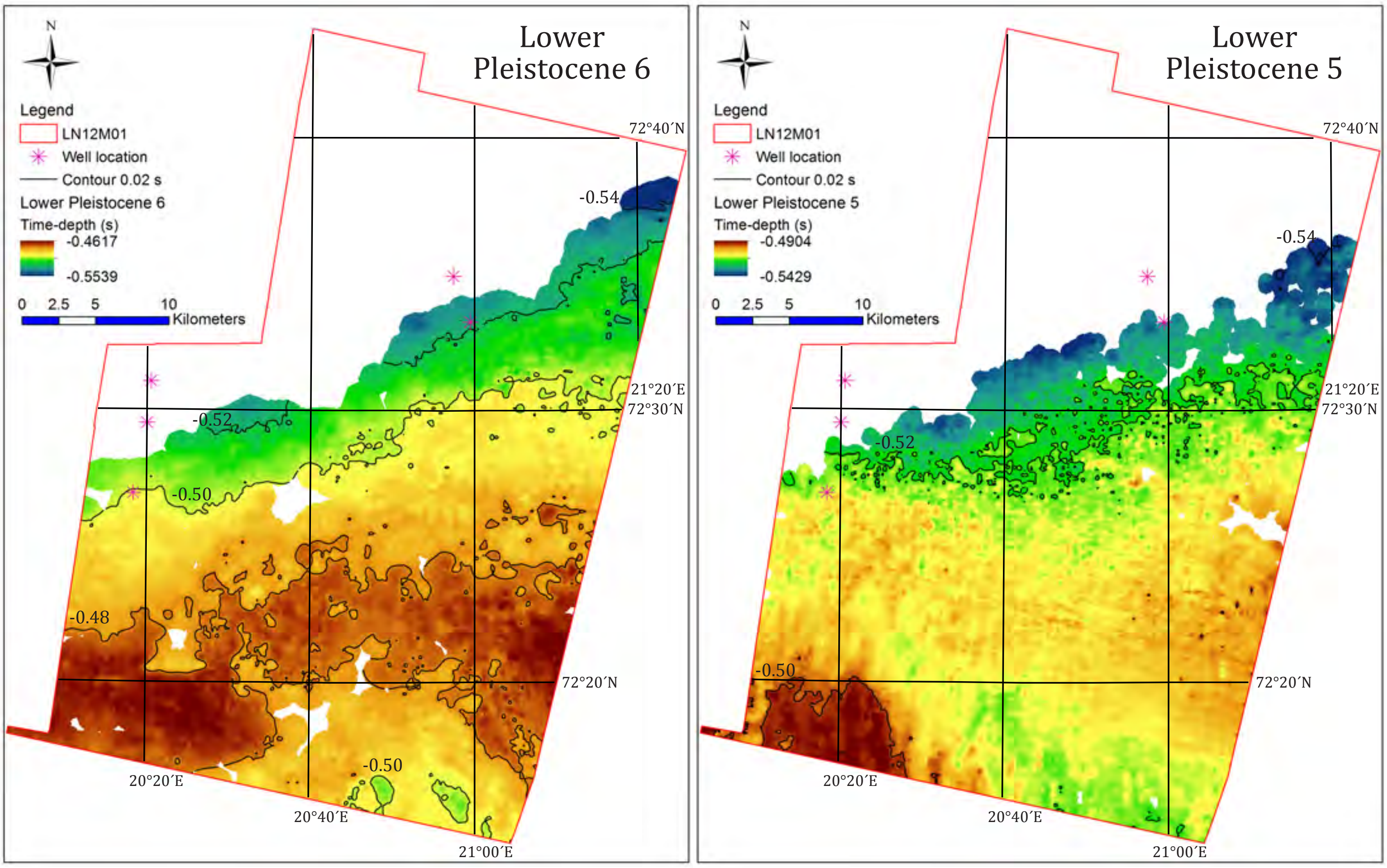

Figure A8 & A9: Paleo-bathymetry maps of the Lower Pleistocene 6 and the Lower Pleistocene 5, generated from the LN12M01 survey area. The depth is presented in seconds and the contour lines in each map illustrate elevation changes for every 0.02 s. Pink dots mark the location of drilled wells.

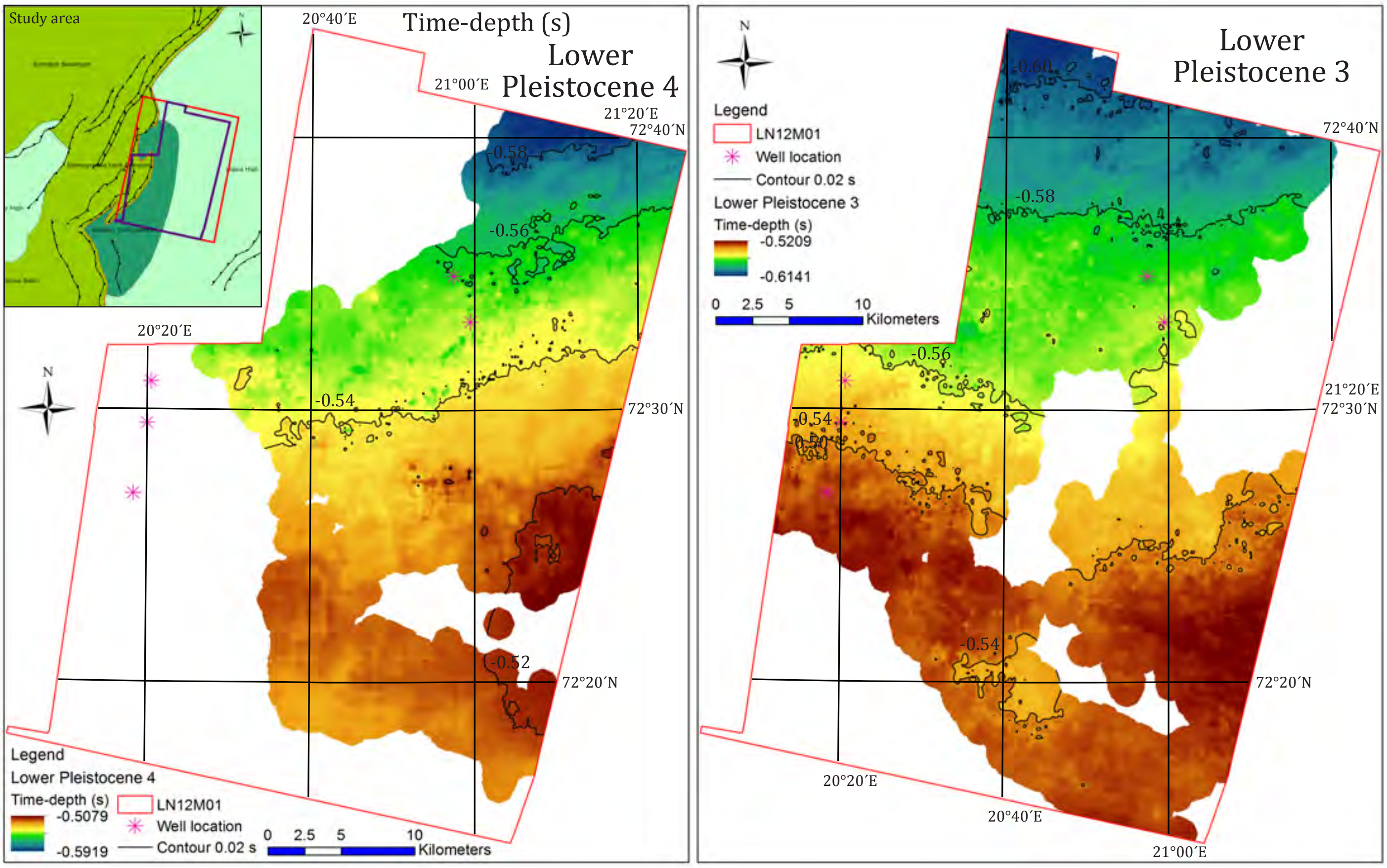

Figure A10 & A11: Paleo-bathymetry maps of the Lower Pleistocene 4 and the Lower Pleistocene 3, generated from the LN12M01 survey area. The depth is presented in seconds and the contour lines in each map illustrate elevation changes for every 0.02 s. Pink dots mark the location of drilled wells. The map in the upper left corner of the Lower Pleistocene 4 displays an overview of the study area (Fig. A1).

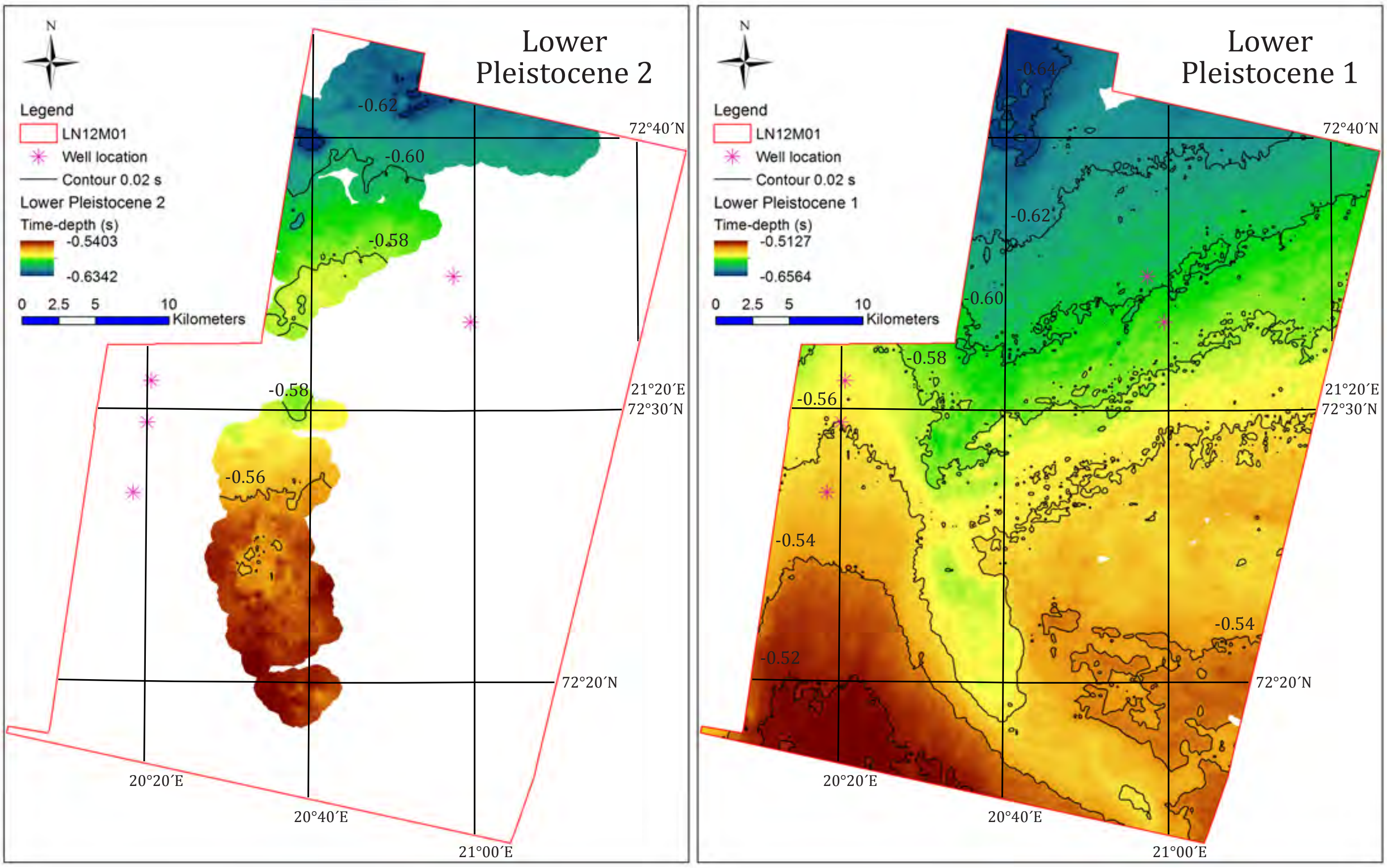

Figure A12 & A13: Paleo-bathymetry maps of the Lower Pleistocene 2 and the Lower Pleistocene 1, generated from the LN12M01 survey area. The depth is presented in seconds and the contour lines in each map illustrate elevation changes for every 0.02 s. Pink dots mark the location of drilled wells.

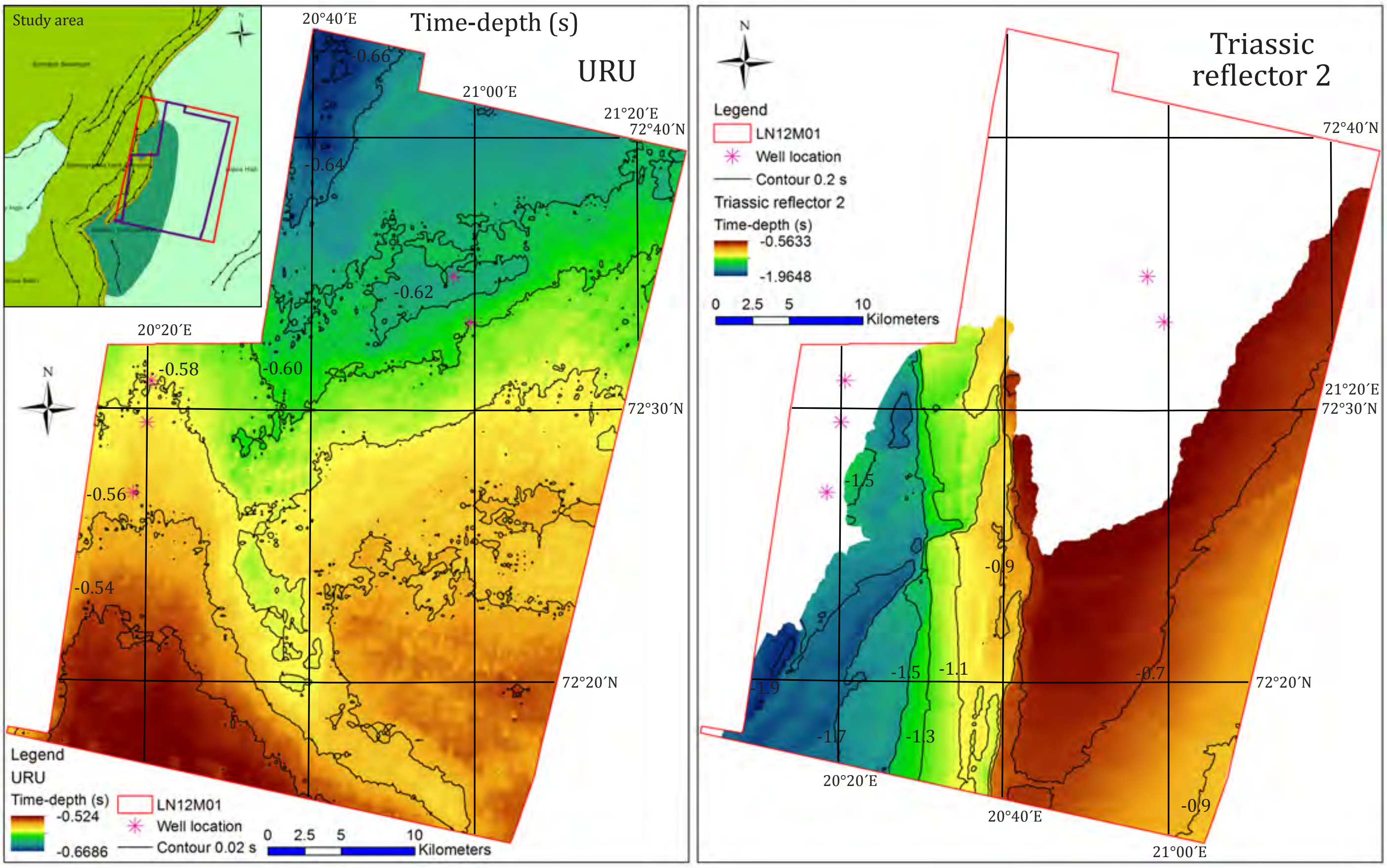

Figure A14 & A15: Paleo-bathymetry maps of the URU and the Triassic reflector 2, generated from the LN12M01 survey area. The depth is presented in seconds and the contour lines in each map illustrate elevation changes for every 0.02 s respective 0.2 s. Pink dots mark the location of drilled wells. The map in the upper left corner of the URU displays an overview of the study area (Fig. A1).

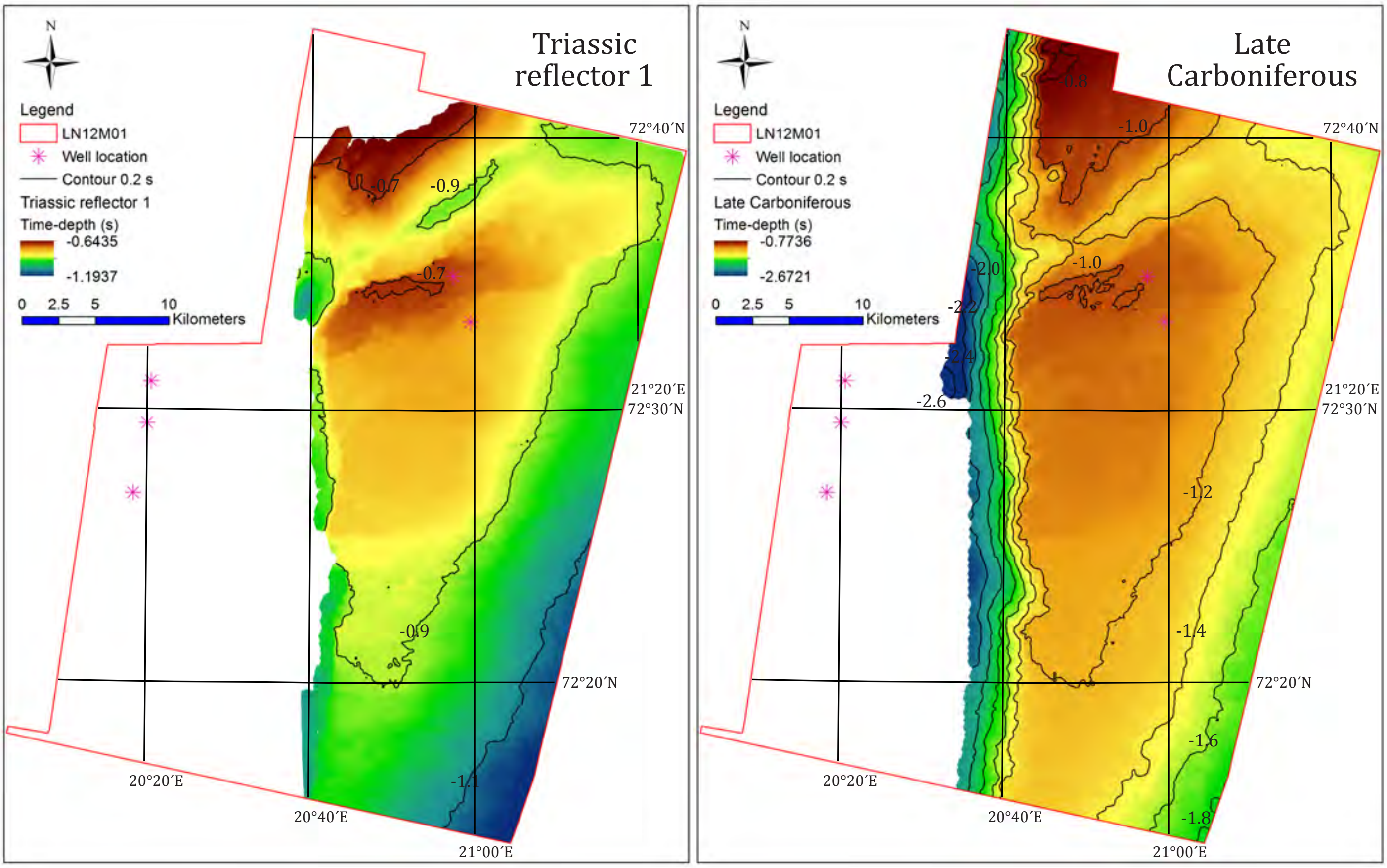

Figure A16 & A17: Paleo-bathymetry maps of the Triassic reflector 2 and the Late Carboniferous, generated from the LN12M01 survey area. The depth is presented in seconds and the contour lines in each map illustrate elevation changes for every 0.2 s. Pink dots mark the location of drilled wells.

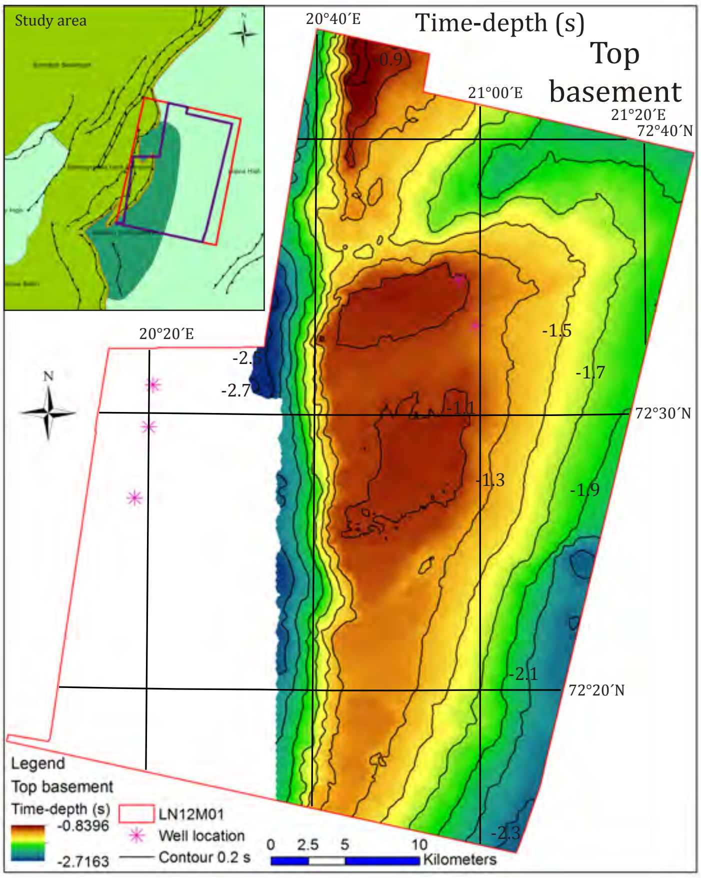

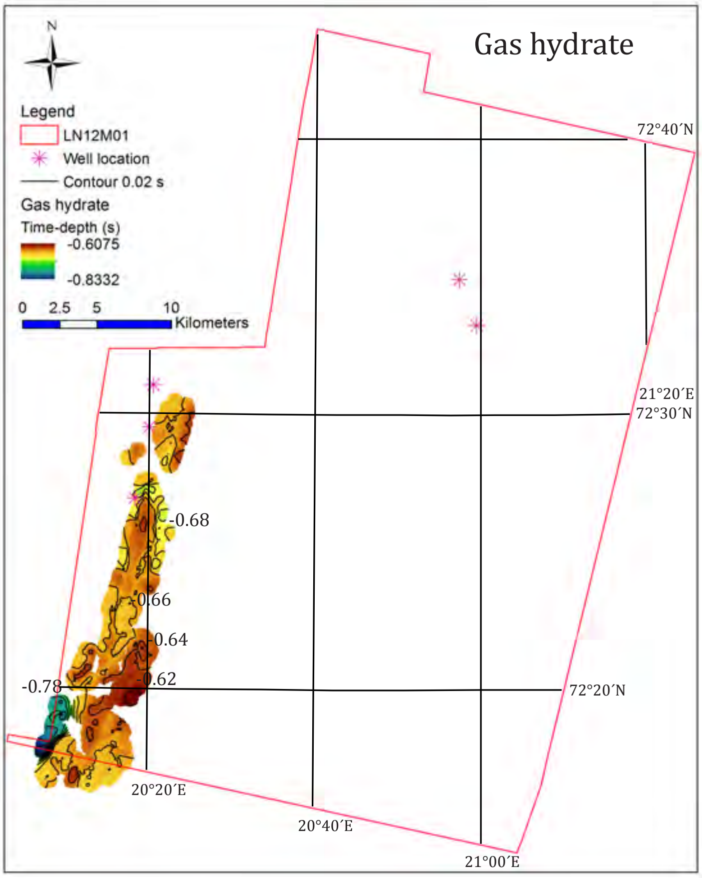

Figure A18 & A19: Paleo-bathymetry maps of the top basement and the gas hydrate, generated from the LN12M01 survey area. The depth is presented in seconds and the contour lines in each map illustrate elevation changes for every 0.2 s respective 0.02 s. Pink dots mark the location of drilled wells. The map in the upper left corner of the top basement displays an overview of the study area (Fig. A1), with the LN12M01 survey area (purple outline).

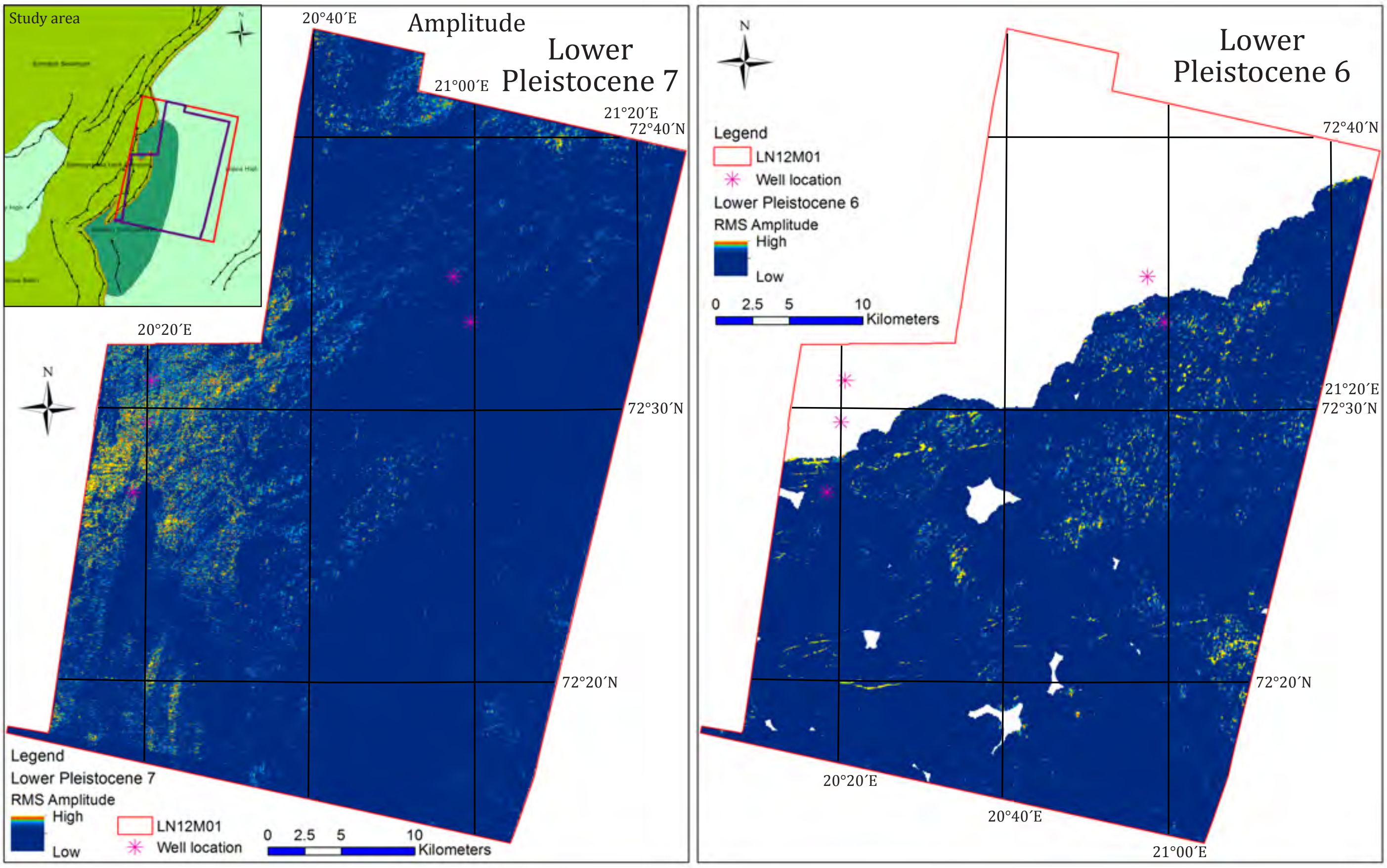

Figure A20 & A21: Amplitude maps (RMS) of the Lower Pleistocene 7 and the Lower Pleistocene 6, generated from the LN12M01 survey area. Amplitude anomalies are illustrated in red to yellow colors. Pink dots mark the location of drilled wells. The map in the upper left corner of the Lower Pleistocene 7 displays an overview of the study area (Fig. A1), with the LN12M01 survey area (purple outline).

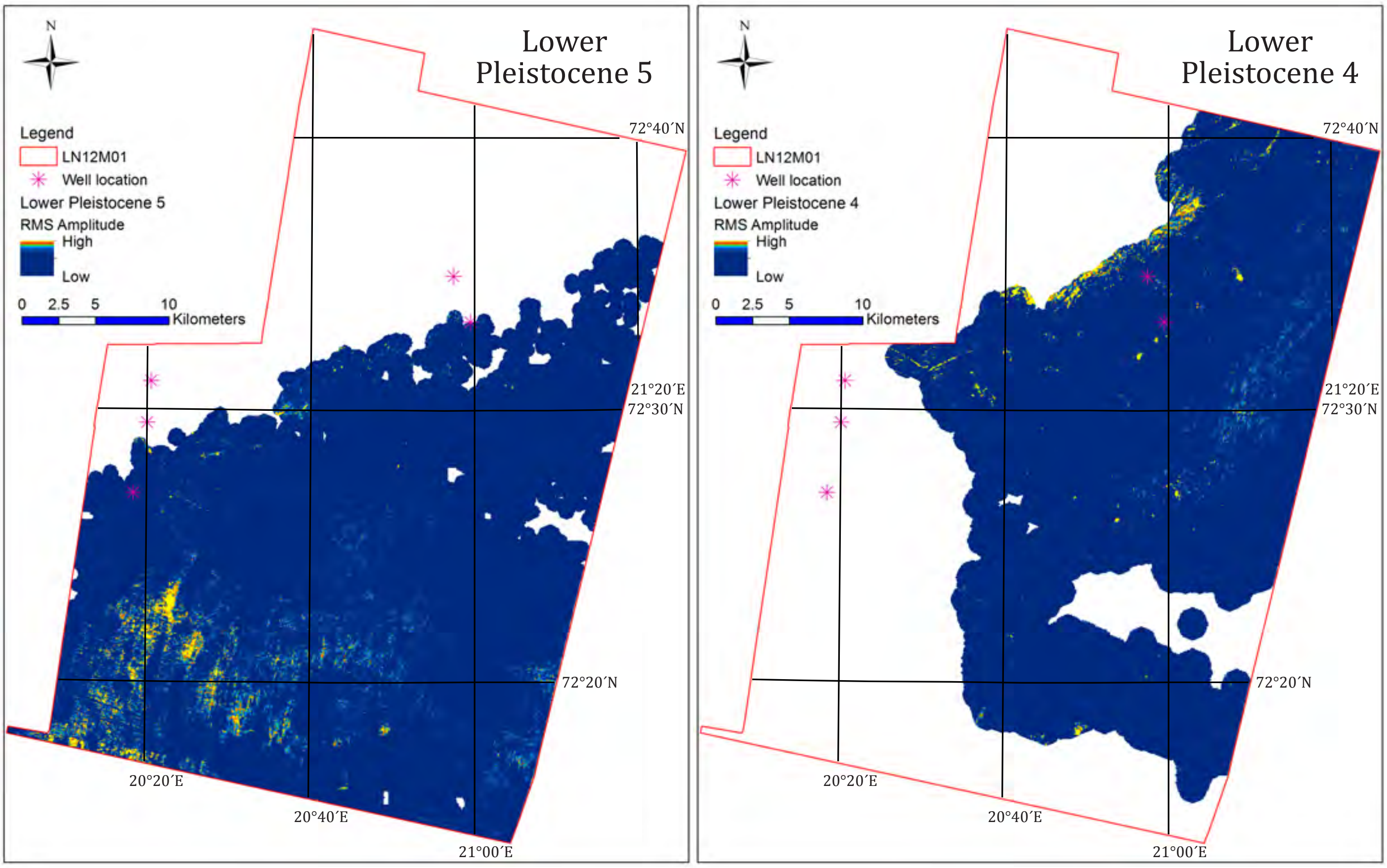

Figure A22 & A23: Amplitude maps (RMS) of the Lower Pleistocene 5 and the Lower Pleistocene 4, generated from the LN12M01 survey area. Amplitude anomalies are illustrated in red to yellow colors. Pink dots mark the location of drilled wells.

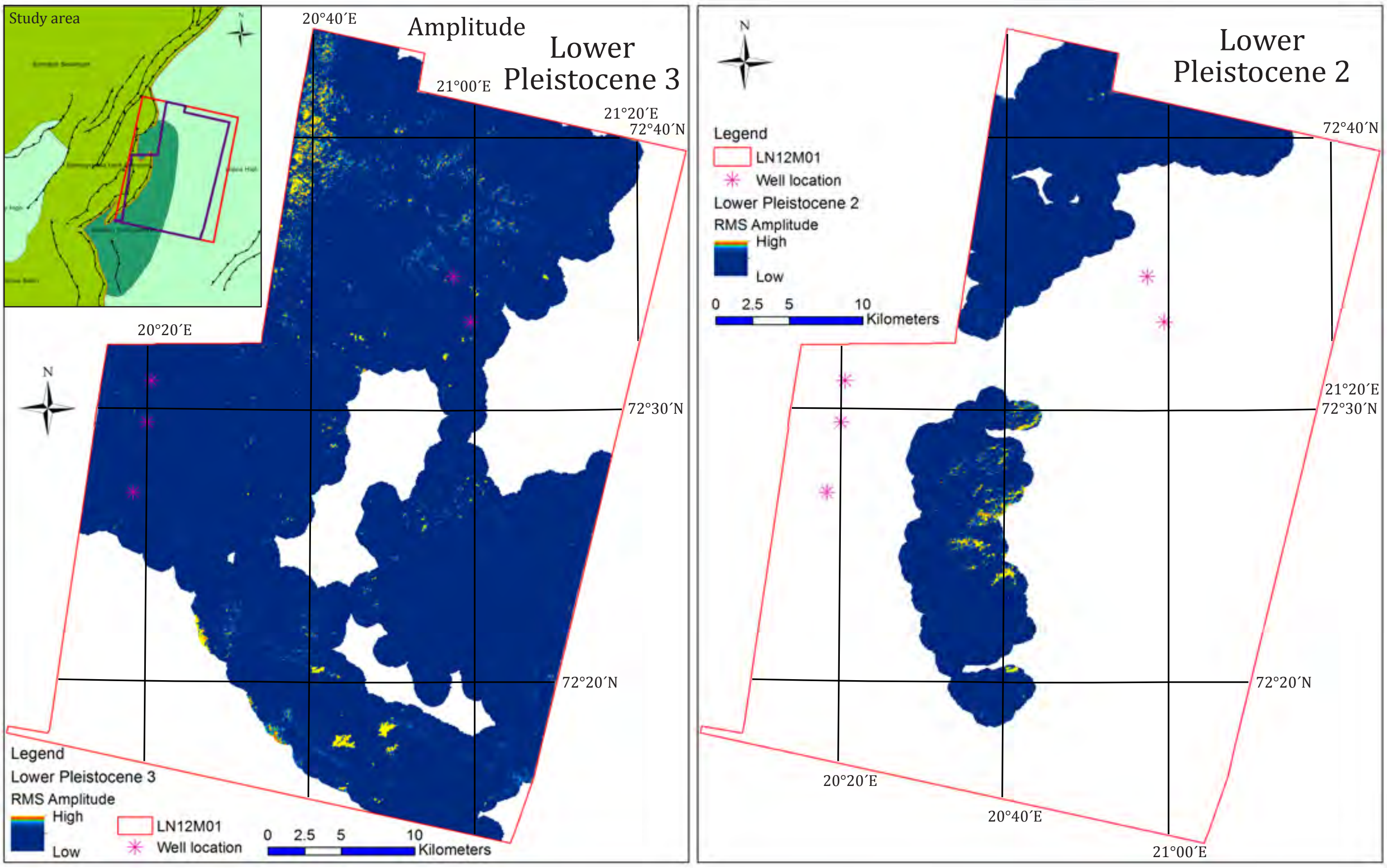

Figure A24 & A25: Amplitude maps (RMS) of the Lower Pleistocene 3 and the Lower Pleistocene 2, generated from the LN12M01 survey area. Amplitude anomalies are illustrated in red to yellow colors. Pink dots mark the location of drilled wells. The map in the upper left corner of the Lower Pleistocene 3 displays an overview of the study area (Fig. A1), with the LN12M01 survey area (purple outline).

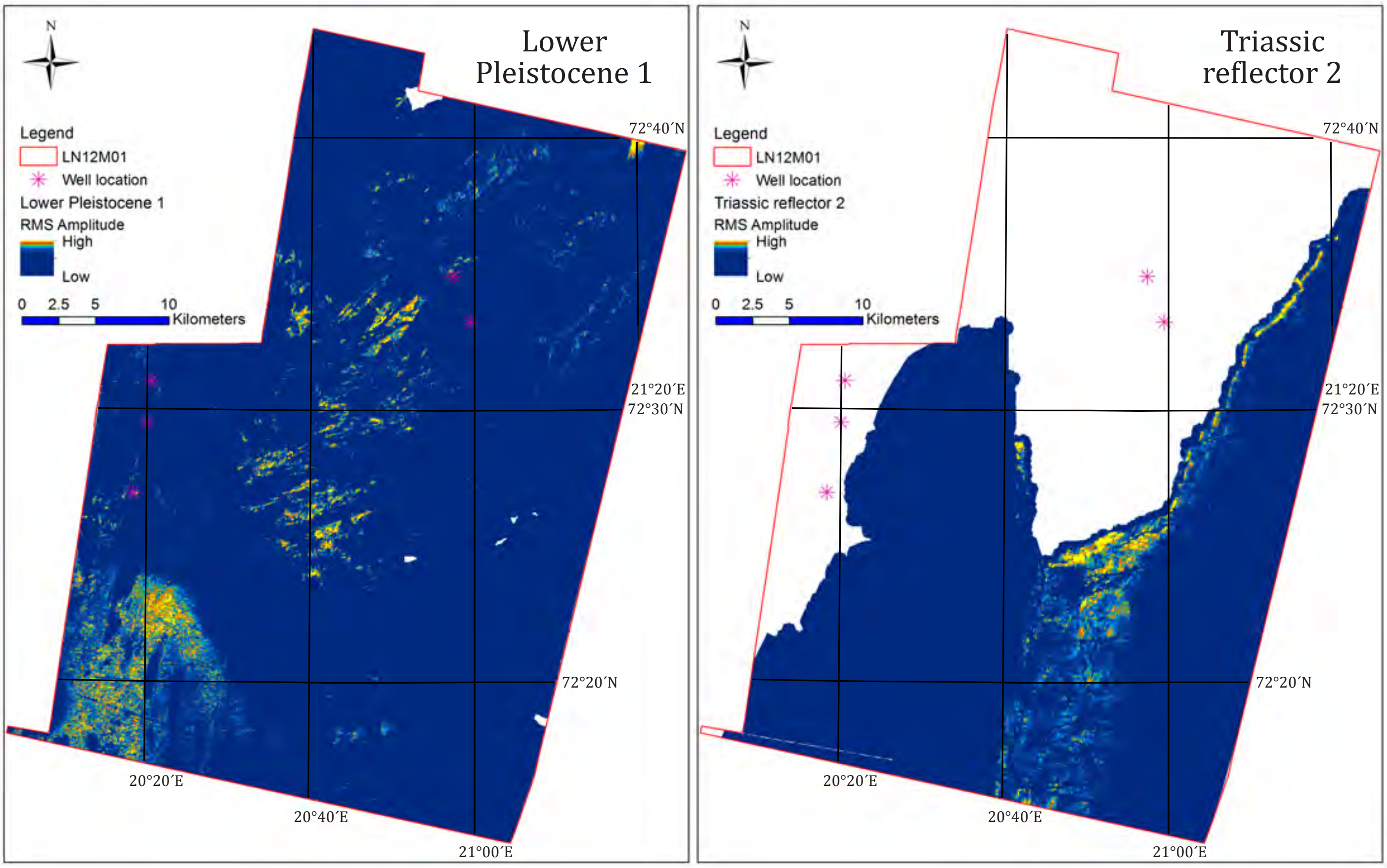

Figure A26 & A27: Amplitude maps (RMS) of the Lower Pleistocene 1 and the Triassic reflector 2, generated from the LN12M01 survey area. Amplitude anomalies are illustrated in red to yellow colors. Pink dots mark the location of drilled wells.

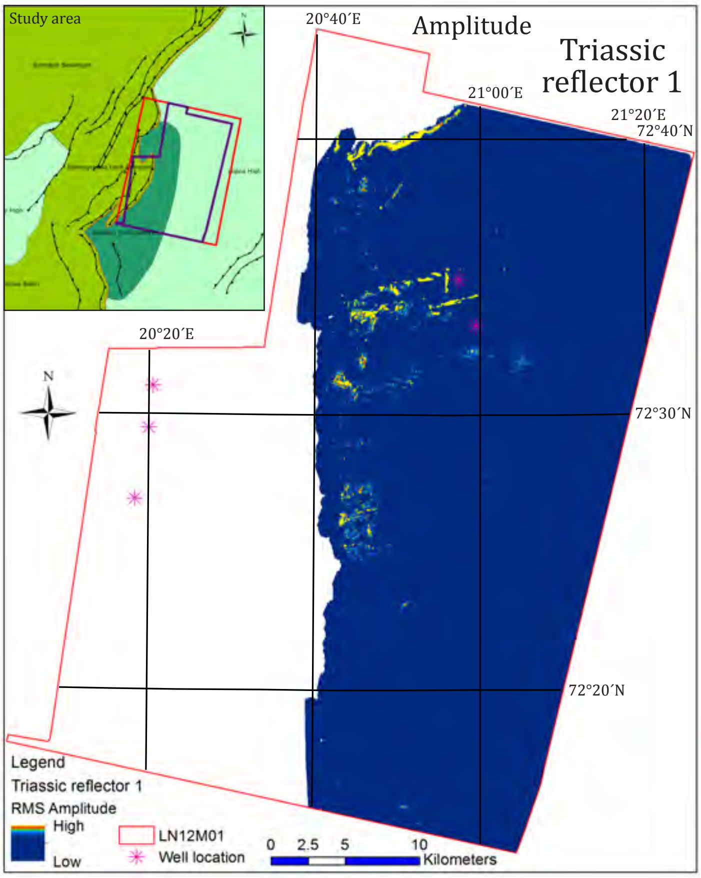

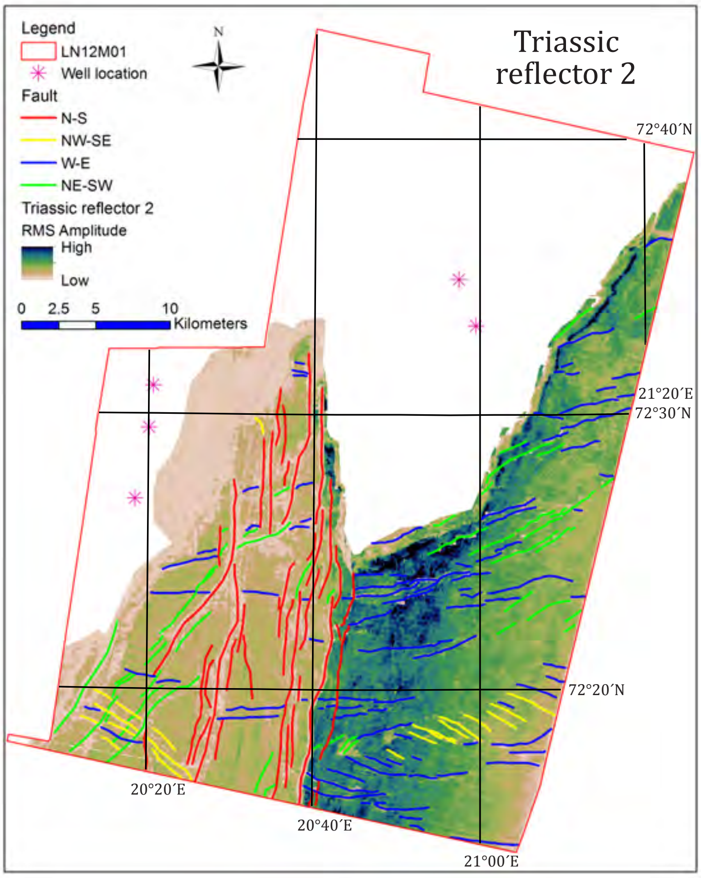

Figure A28: RMS amplitude map of the Triassic reflector 1. Amplitude anomalies are illustrated in red to yellow colors. Pink dots mark the location of drilled wells. The map in the upper left corner displays an overview of the study area (Fig. A1), with the LN12M01 survey area (purple outline). Figure A29: RMS amplitude map of the Triassic reflector 2, viewed in a different color ramp, that displays the presence of faults. The faults are highlighted using a color coded orientation. Pink dots mark the location of drilled wells.

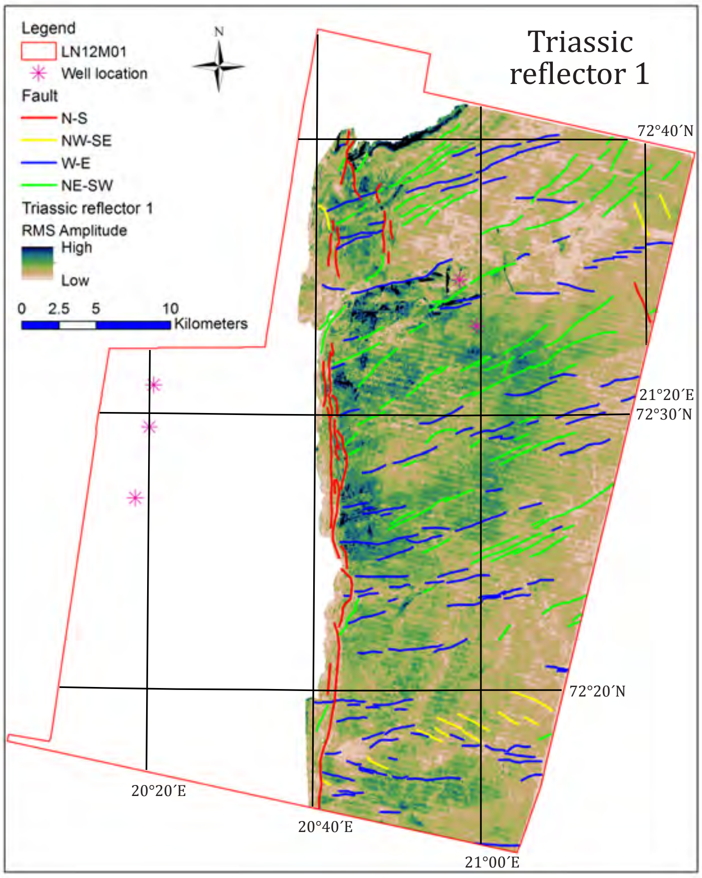

Figure A30: RMS amplitude map of the Triassic reflector 2, viewed in a different color ramp, that displays the presence of faults. Generated from the LN12M01 survey area. Amplitude anomalies are illustrated in blue to black colors. The faults are highlighted using a color coded orientation. Pink dots mark the location of wells.

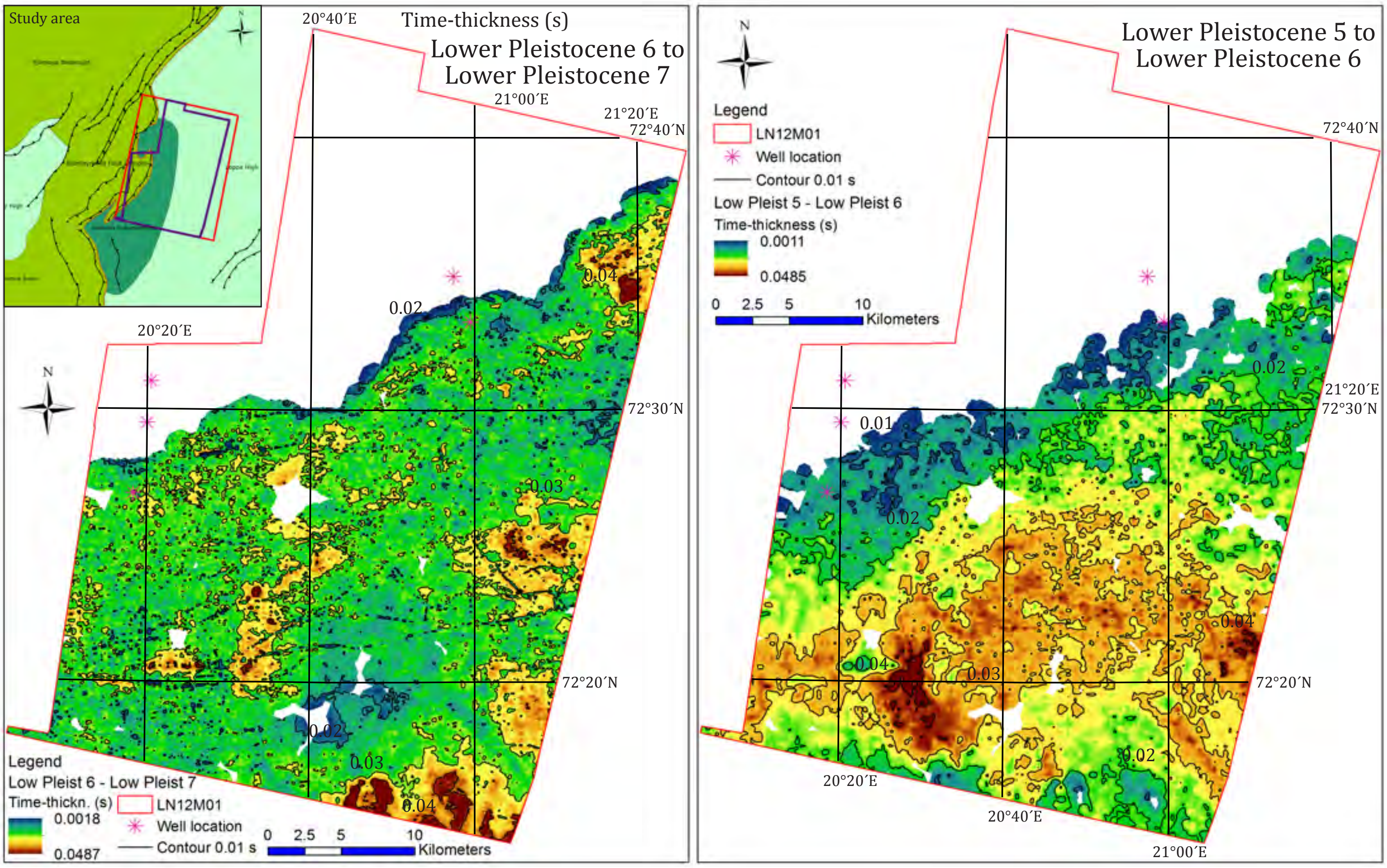

Figure A31 & A32: Isopach maps showing the time-depth differences between two layers, generated from the LN12M01 survey area. The thickness is presented in seconds and the contour lines in each map illustrate elevation changes for every 0.01 s. Pink dots mark the location of wells. The map in the upper left corner displays an overview of the study area (Fig. A1), with the LN12M01 survey area (purple).

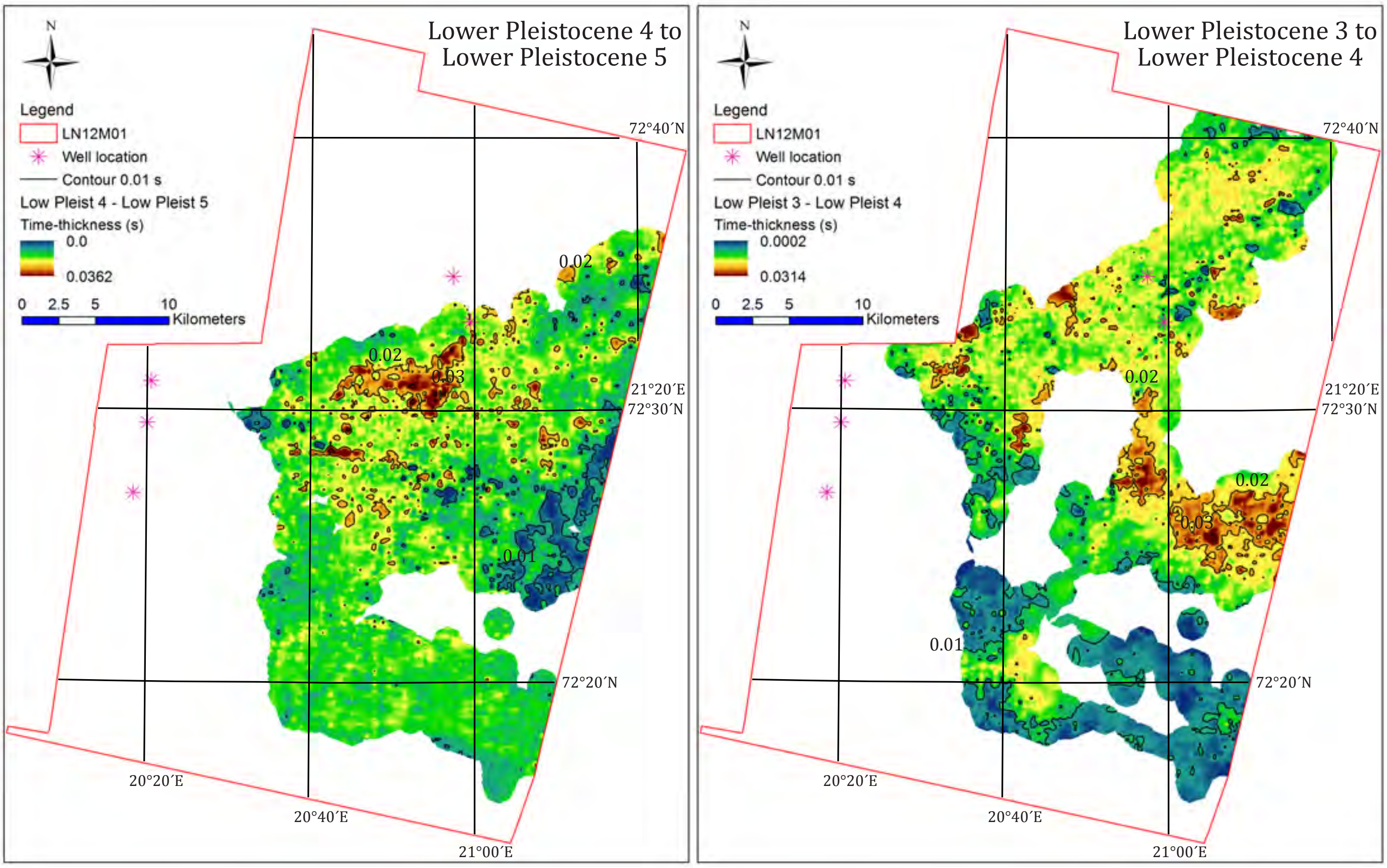

Figure A33 & A34: Isopach maps showing the time-depth differences between two layers, generated from the LN12M01 survey area. The thickness is presented in seconds and the contour lines in each map illustrate elevation changes for every 0.01 s. Pink dots mark the location of drilled wells.

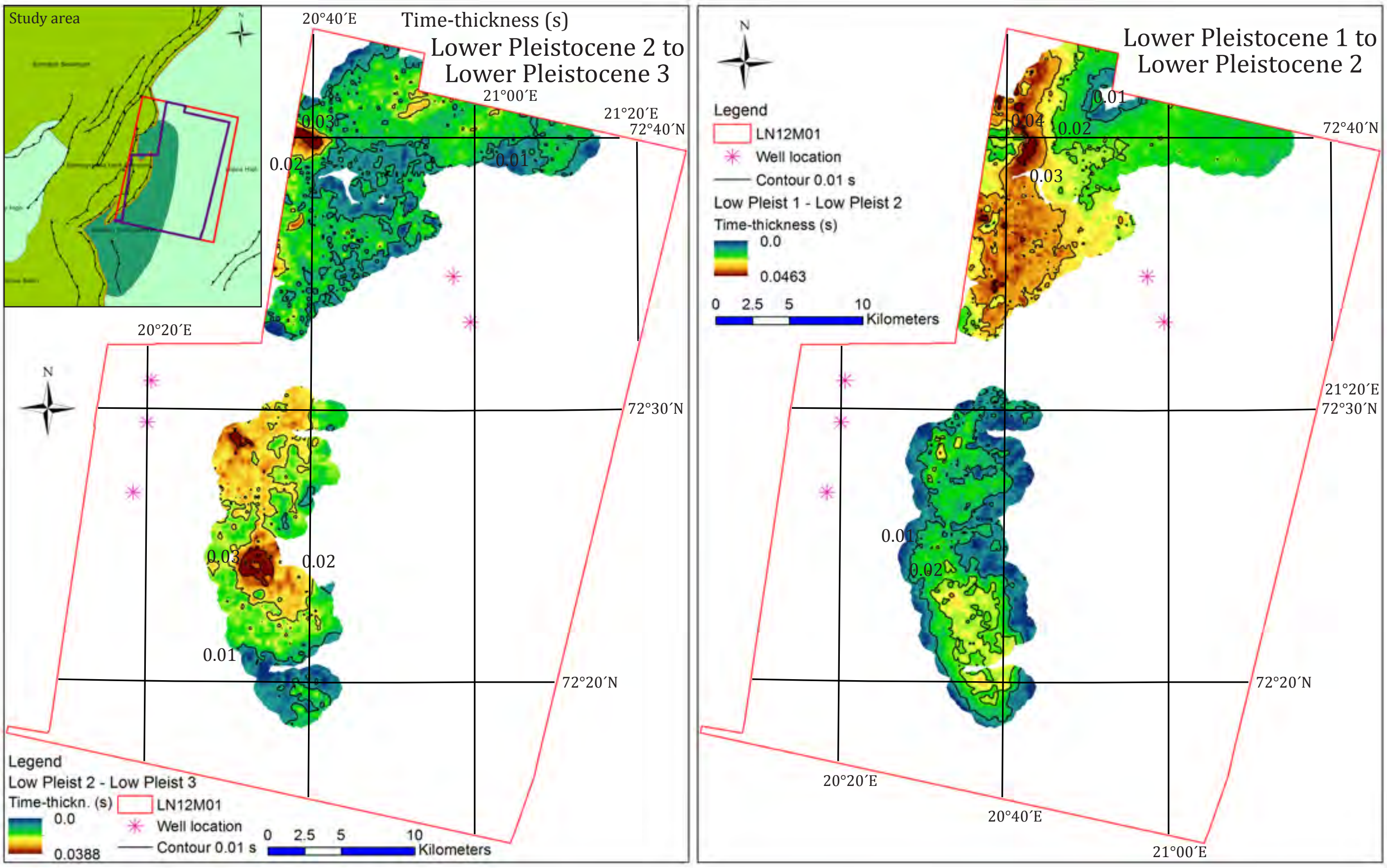

Figure A35 & A36: Isopach maps showing the time-depth differences between two layers, generated from the LN12M01 survey area. The thickness is presented in seconds and the contour lines in each map illustrate elevation changes for every 0.01 s. Pink dots mark the location of wells. The map in the upper left corner displays an overview of the study area (Fig. A1), with the LN12M01 survey area (purple).

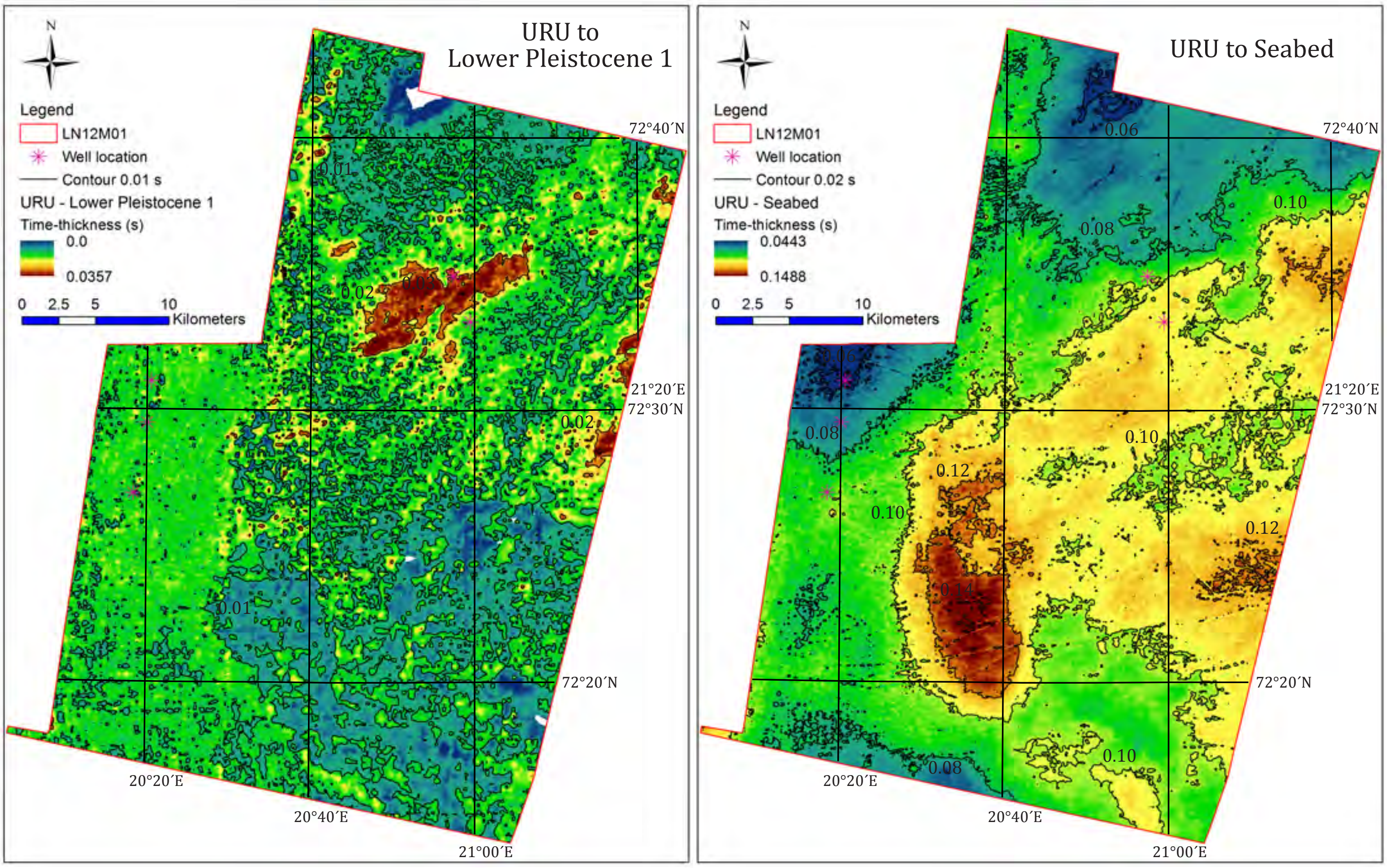

Figure A37 & A38: Isopach maps showing the time-depth differences between two layers, generated from the LN12M01 survey area. The thickness is presented in seconds and the contour lines in each map illustrate elevation changes for every 0.01 s respective 0.02 s. Pink dots mark the location of drilled wells.

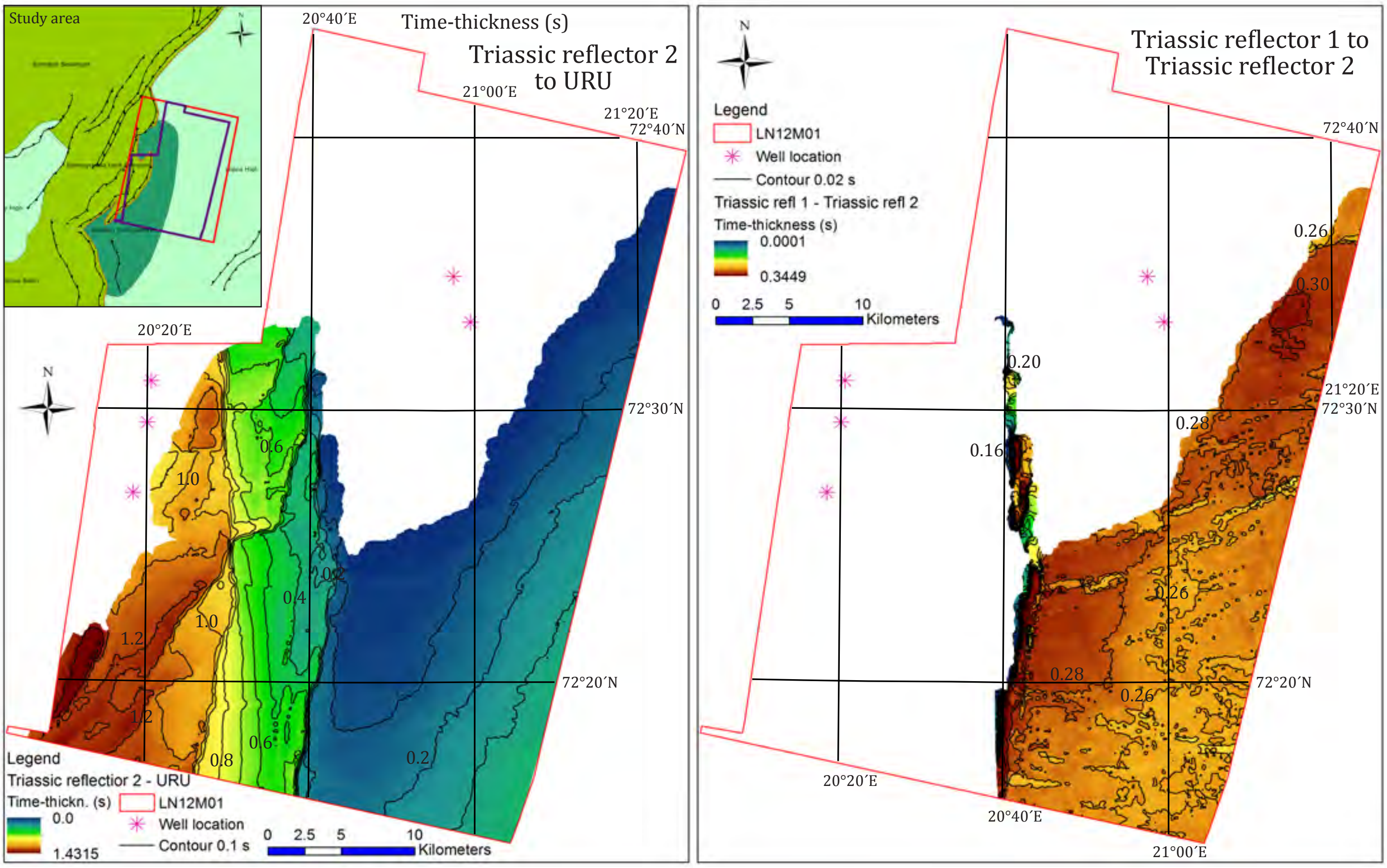

Figure A39 & A40: Isopach maps showing the time-depth differences between two layers, generated from the LN12M01 survey area. The thickness is presented in seconds and the contour lines in each map illustrate elevation changes for every 0.1 s respective 0.02 s. Pink dots mark the location of wells. The map in the upper left corner displays an overview of the study area (Fig. A1), with the LN12M01 area.

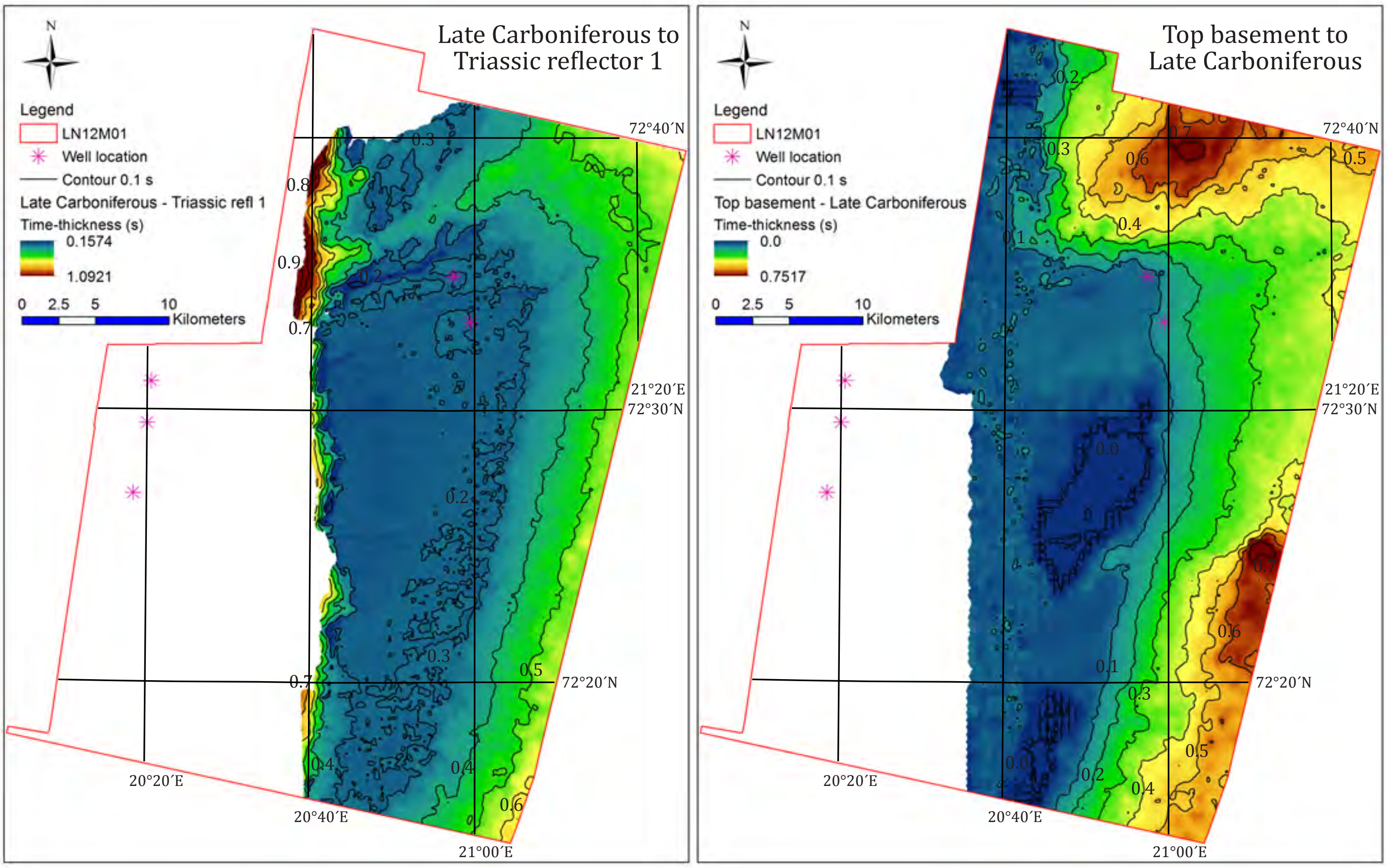

Figure A41 & A42: Isopach maps showing the time-depth differences between two layers, generated from the LN12M01 survey area. The thickness is presented in seconds and the contour lines in each map illustrate elevation changes for every 0.1 s. Pink dots mark the location of drilled wells.

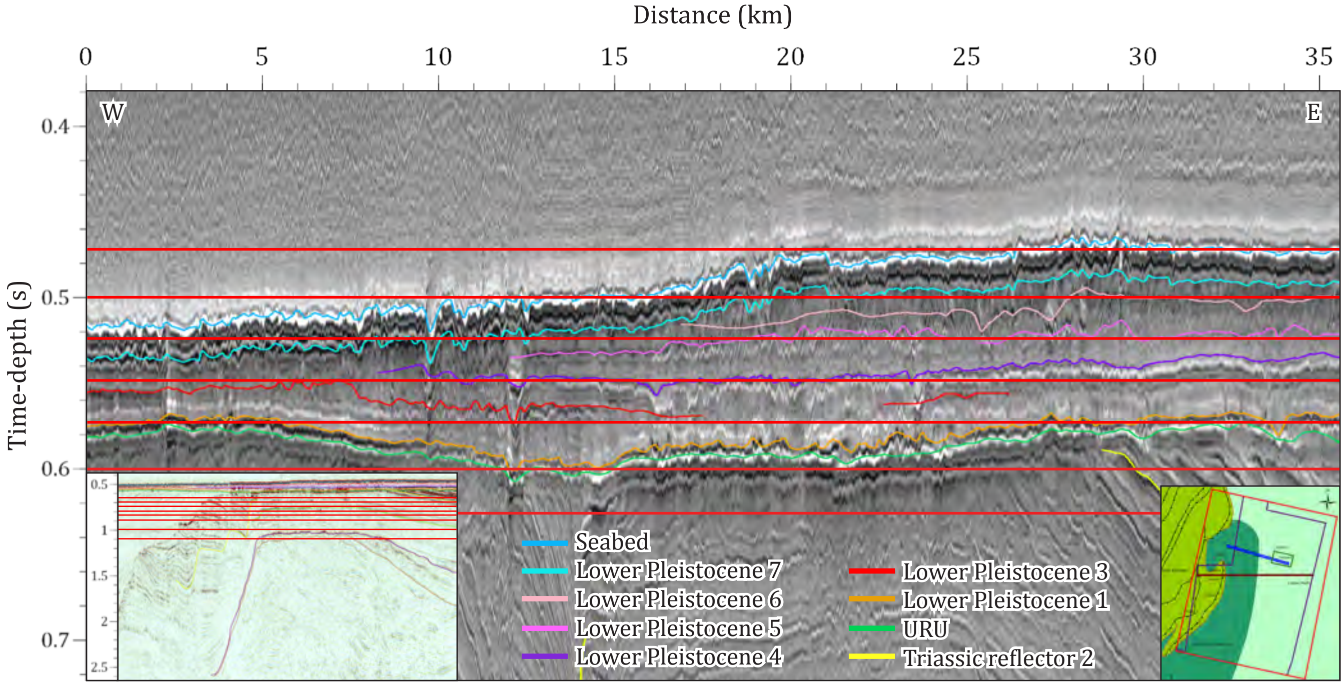

Figure A43: A seismic profile of the LN12M01 survey area, located center striking W-E. The seismic profile in the lower left corner display the full extent of the interpreted layers. Red lines mark the horizontal depth for generated time slices. The map in the lower right corner displays an overview of the study area (Fig. A1) and the LN12M01 survey areas (purple outline), with the orientation of the 2D seismic profile (dark red line).

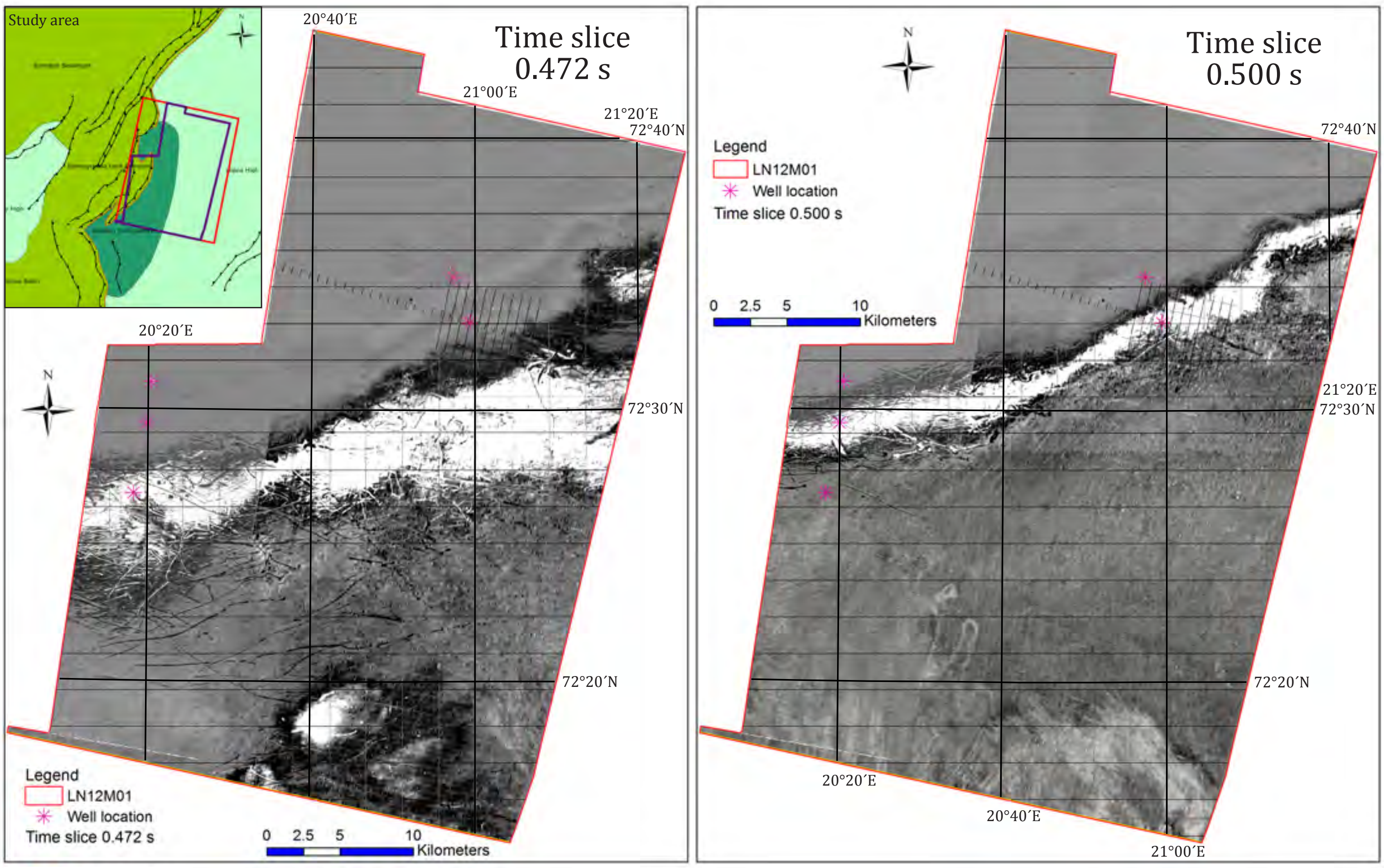

Figure A44 & A45: Time slice velocity maps cutting the LN12M01 survey area horizontally at 0.472 s and 0.500 s. The color ramp range between black and white, where black reflect areas of high permeability and white areas of low permeability. Pink dots mark the location of wells. The map in the upper left corner of the 0.472 s time slice display an overview of the study area (Fig. A1), with the LN12M01 area.

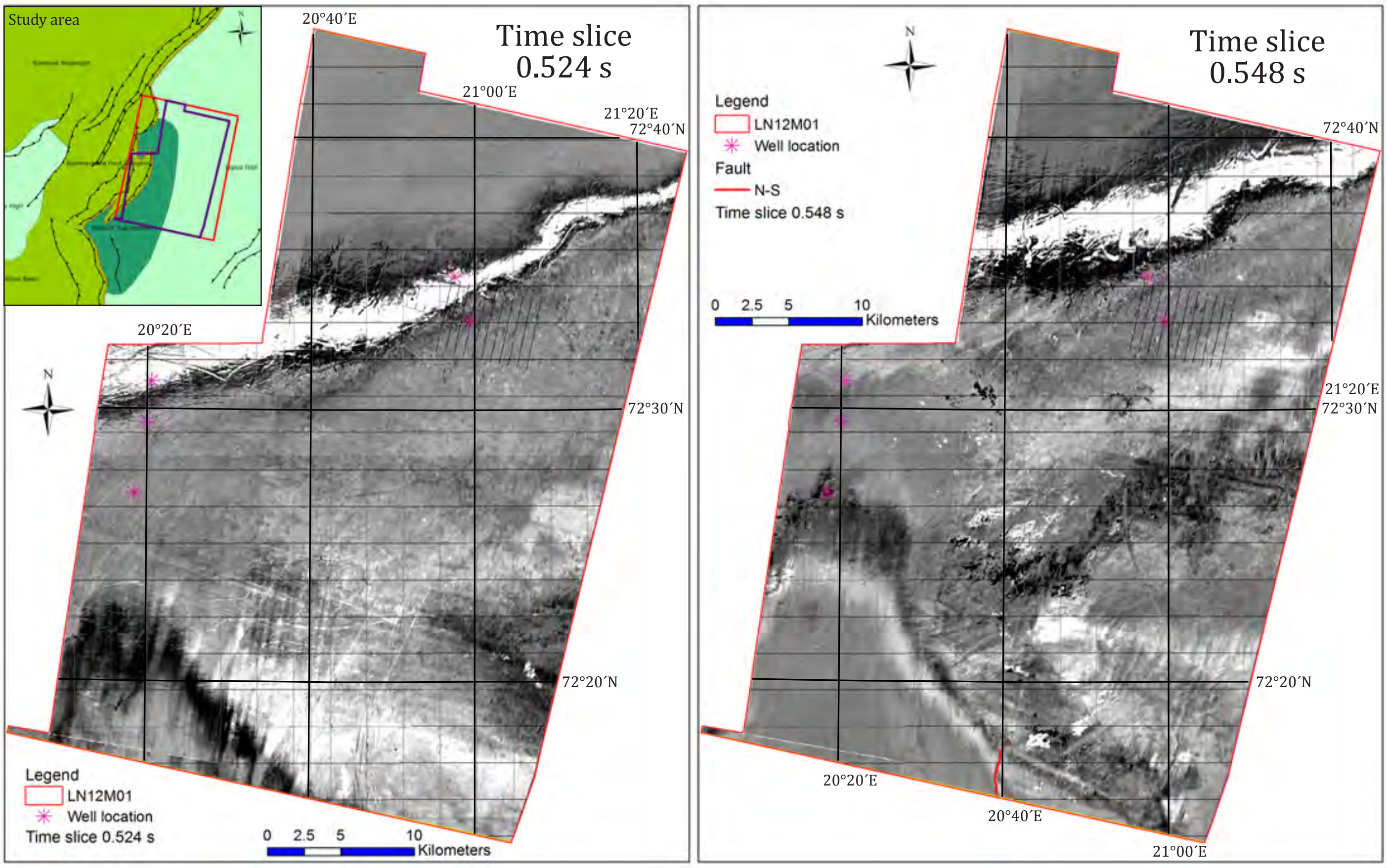

Figure A46 & A47: Time slice velocity maps cutting the LN12M01 survey area horizontally at 0.524 s and 0.548 s. Black color reflect areas of high permeability and white areas of low permeability. The fault in the 0.548 s is highlighted using a color coded orientation. Pink dots mark the location of drilled wells. The map in the upper left corner of the 0.524 s time slice displays an overview of the study area (Fig. A1).

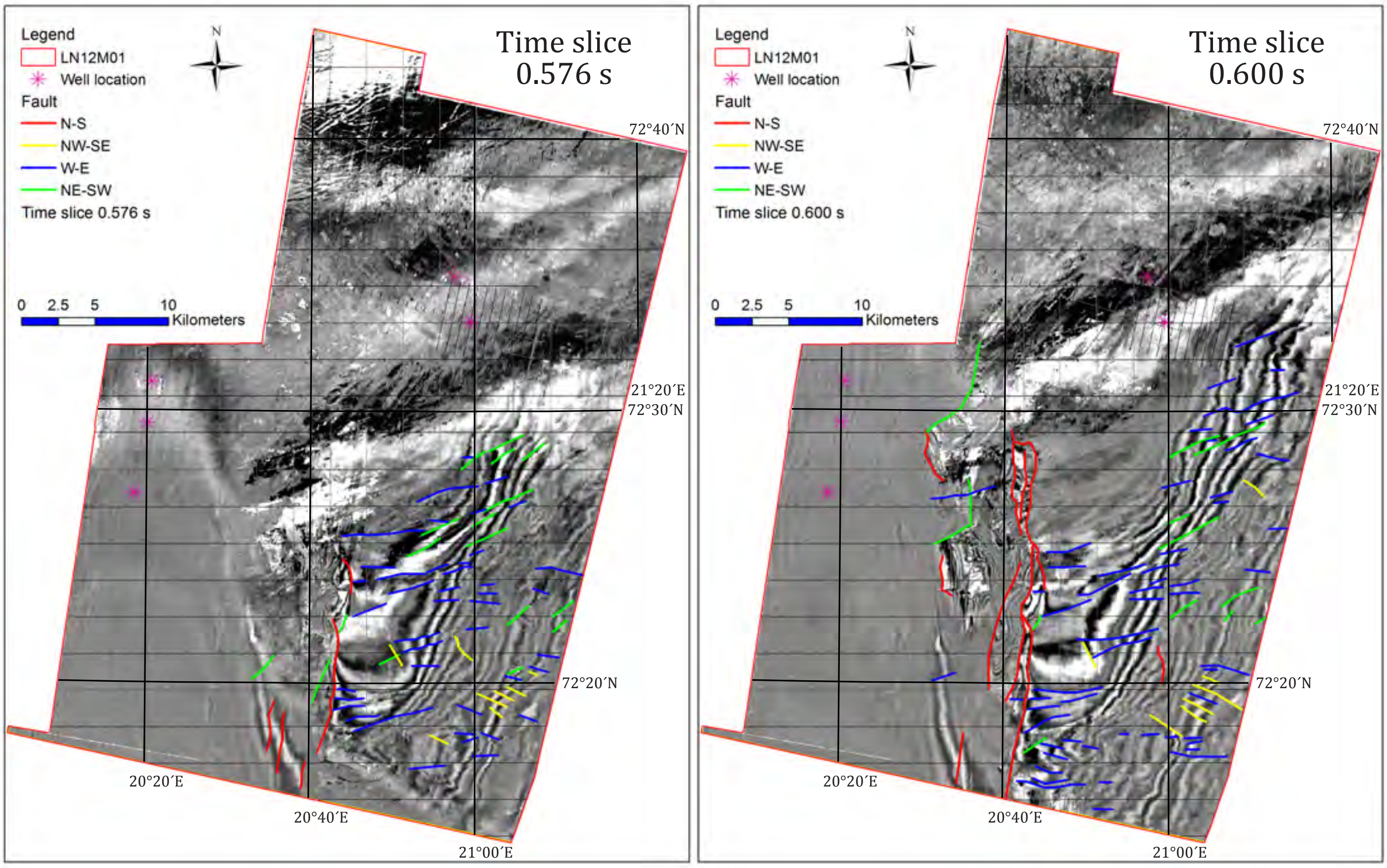

Figure A48 & A49: Time slice velocity maps cutting the LN12M01 survey area horizontally at 0.576 s and 0.600 s. Black color reflect areas of high permeability and white areas of low permeability. Faults are highlighted using color coded orientations. Pink dots mark the location of drilled wells.

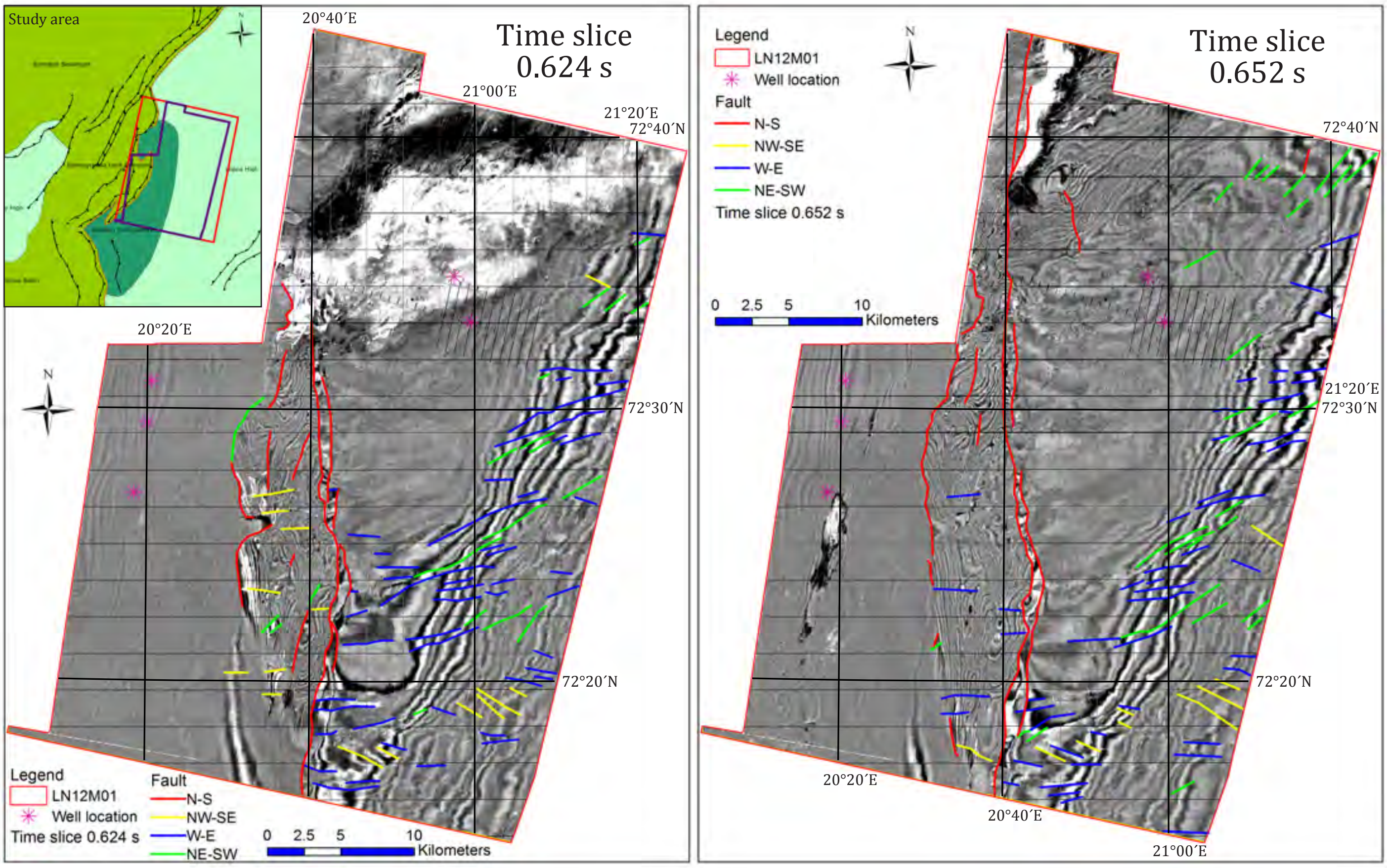

Figure A50 & A51: Time slice velocity maps cutting the LN12M01 survey area horizontally at 0.624 s and 0.652 s. Black color reflect areas of high permeability and white areas of low permeability. Faults are highlighted using color coded orientations. Pink dots mark the location of drilled wells. The map in the upper left corner of the 0.624 s time slice displays an overview of the study area (Fig. A1).

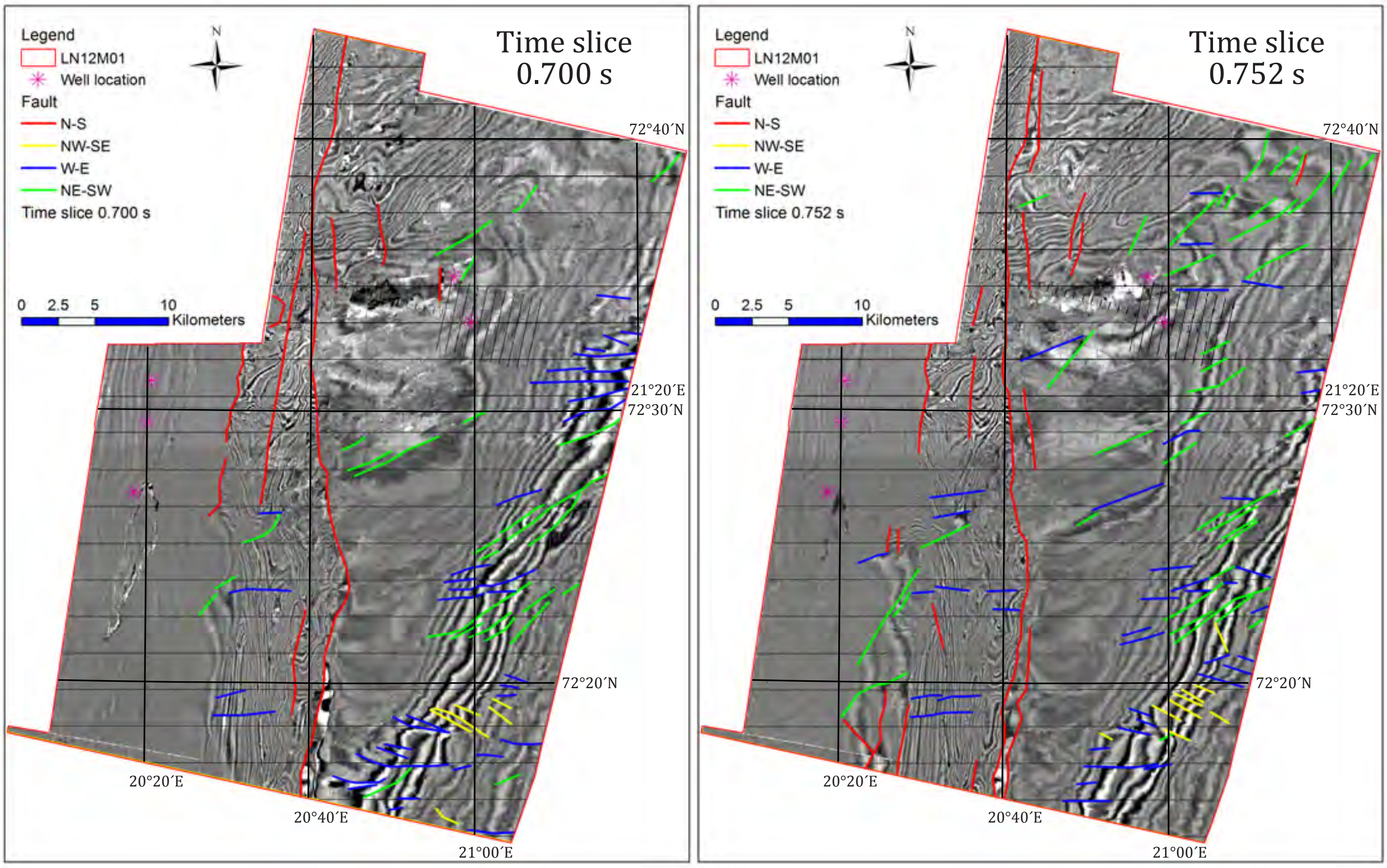

Figure A52 & A53: Time slice velocity maps cutting the LN12M01 survey area horizontally at 0.700 s and 0.752 s. Black color reflect areas of high permeability and white areas of low permeability. Faults are highlighted using color coded orientations. Pink dots mark the location of drilled wells.

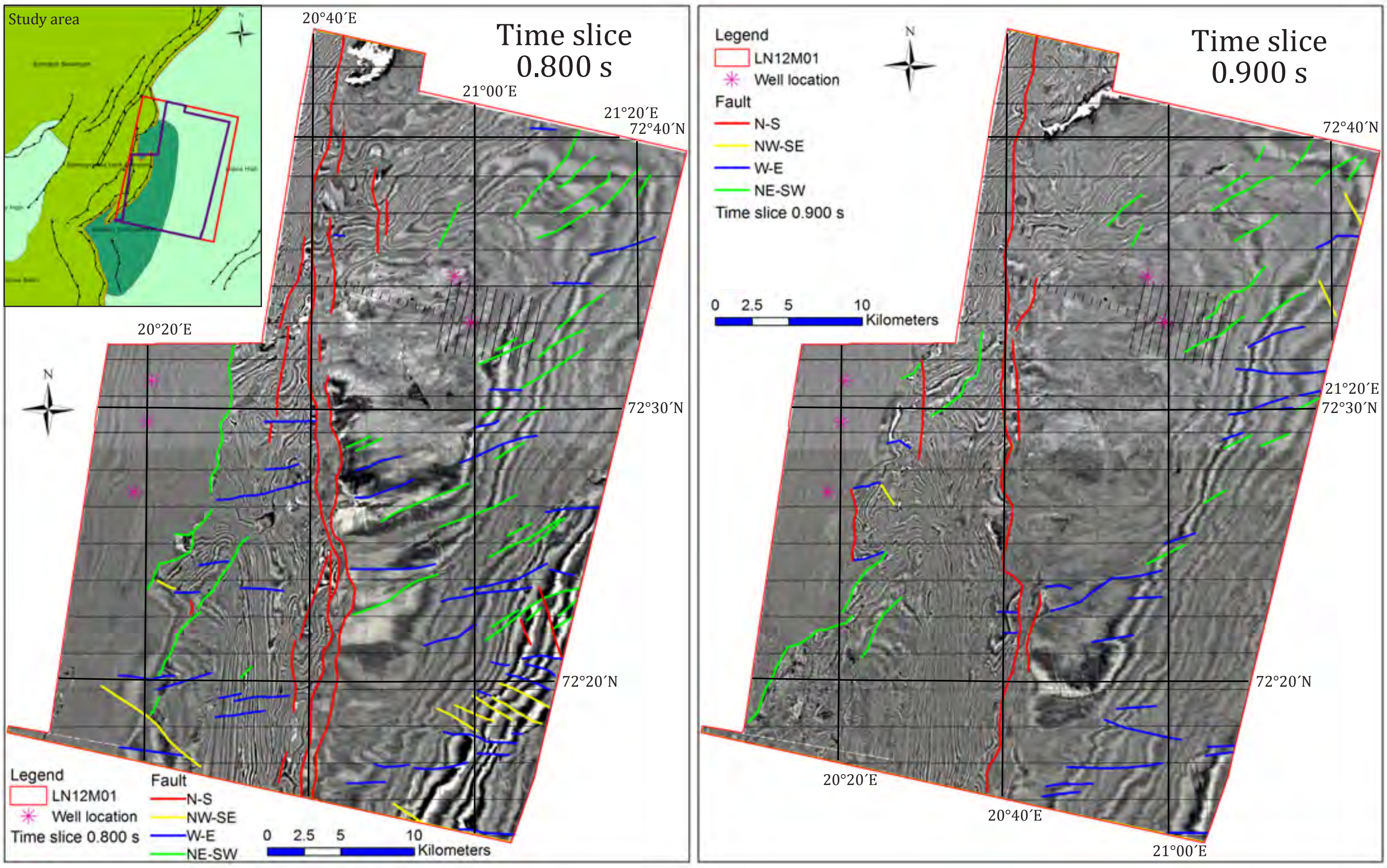

Figure A54 & A55: Time slice velocity maps cutting the LN12M01 survey area horizontally at 0.800 s and 0.900 s. Black color reflect areas of high permeability and white areas of low permeability. Faults are highlighted using color coded orientations. Pink dots mark the location of drilled wells. The map in the upper left corner of the 0.800 s time slice displays an overview of the study area (Fig. A1).

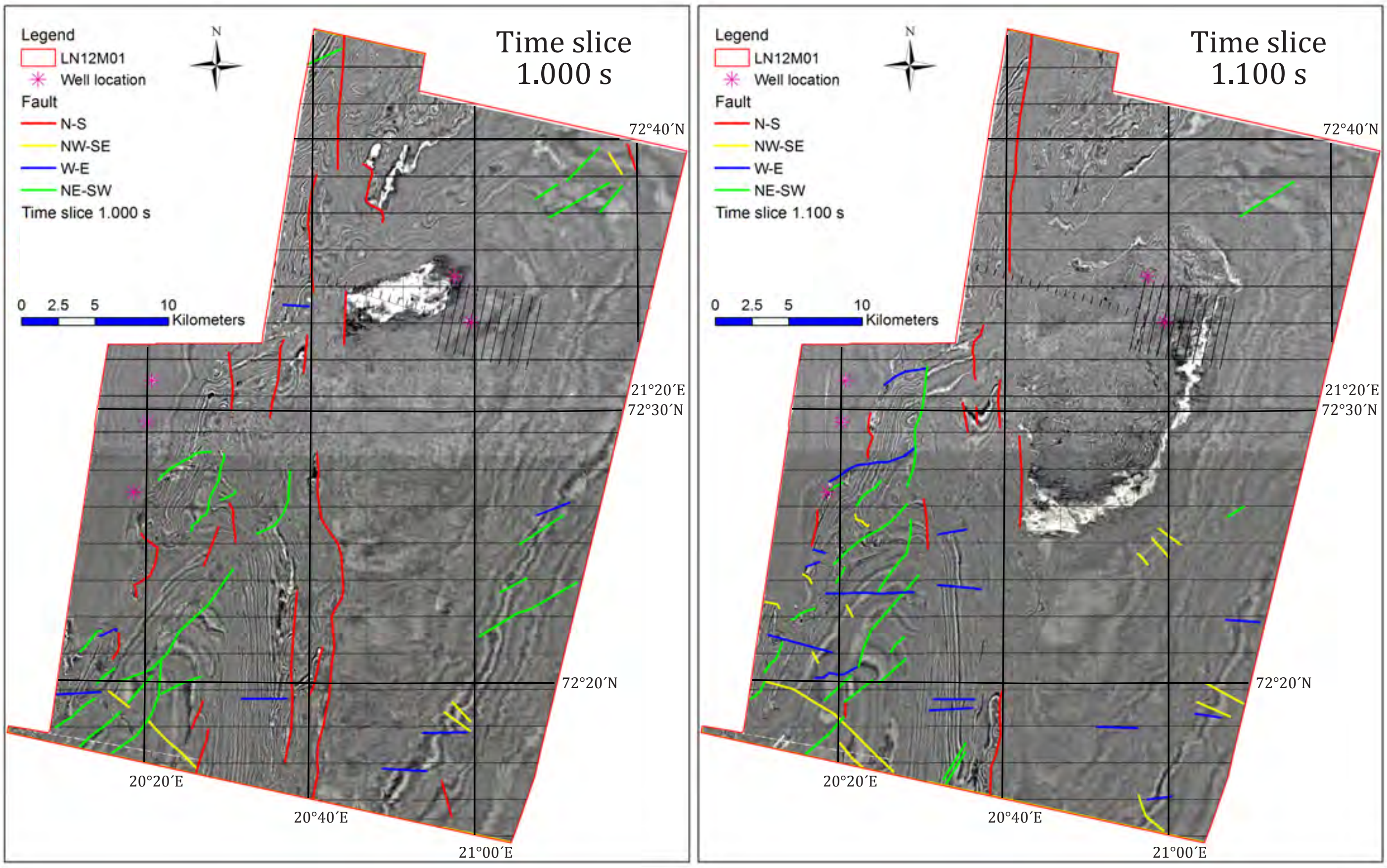

Figure A56 & A57: Time slice velocity maps cutting the LN12M01 survey area horizontally at 1.000 s and 1.100 s. Black color reflect areas of high permeability and white areas of low permeability. Faults are highlighted using color coded orientations. Pink dots mark the location of drilled wells.

Appendix B - Survey area NH0372

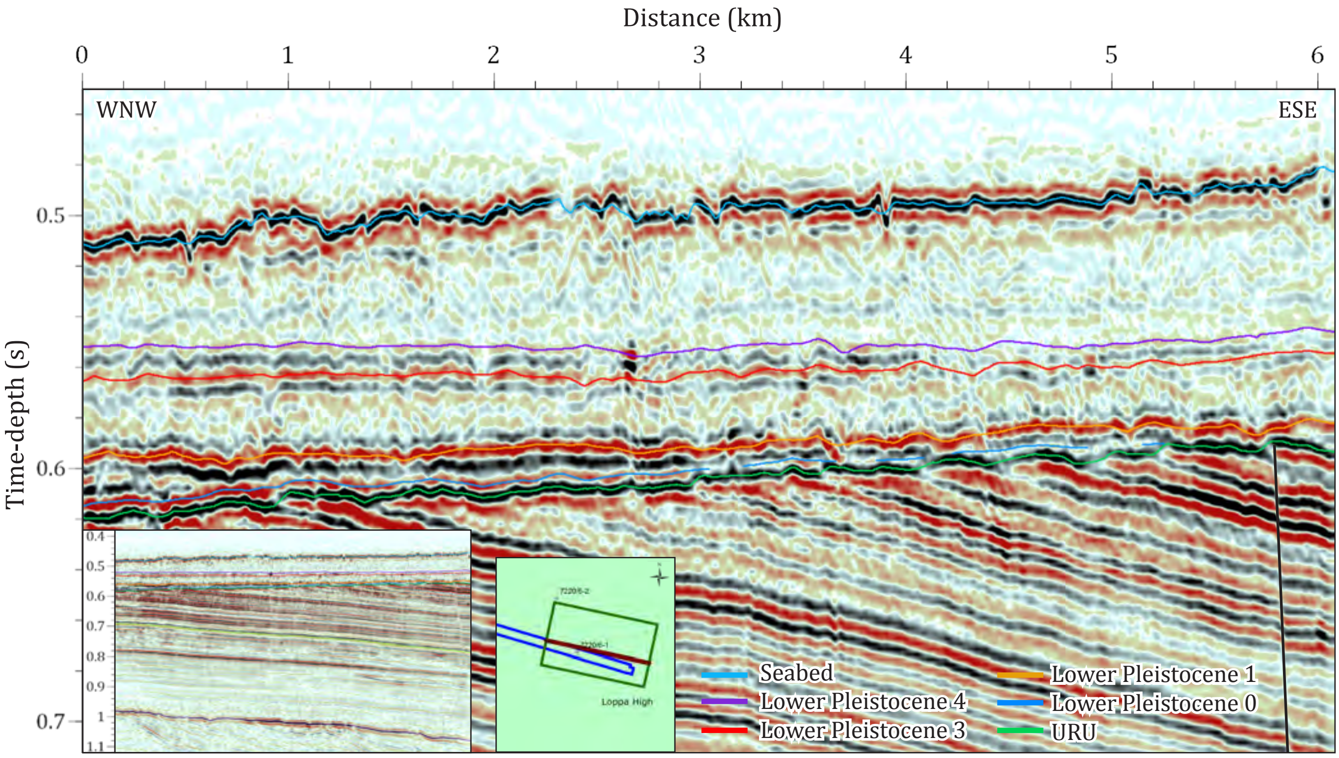

Figure B1: A seismic profile of the NH0372 survey area, located center striking WNW-ESE. Six layers are highlighted: the seabed (light blue); Lower Pleistocene 4 (violet); Lower Pleistocene 3 (red); Lower Pleistocene 1 (orange); Lower Pleistocene 0 (blue); URU (green). Two additional layer is highlighted in the deeper deposits, lower left corner: Triassic reflector 1 (neon green) and Late Carboniferous (purple). A major fault is highlighted in the ESE area by a black line. The map in the lower center displays an overview of the NH0372 survey areas (green box), with the orientation of the 2D seismic profile (dark red line). See figure A1 for the entire study area.

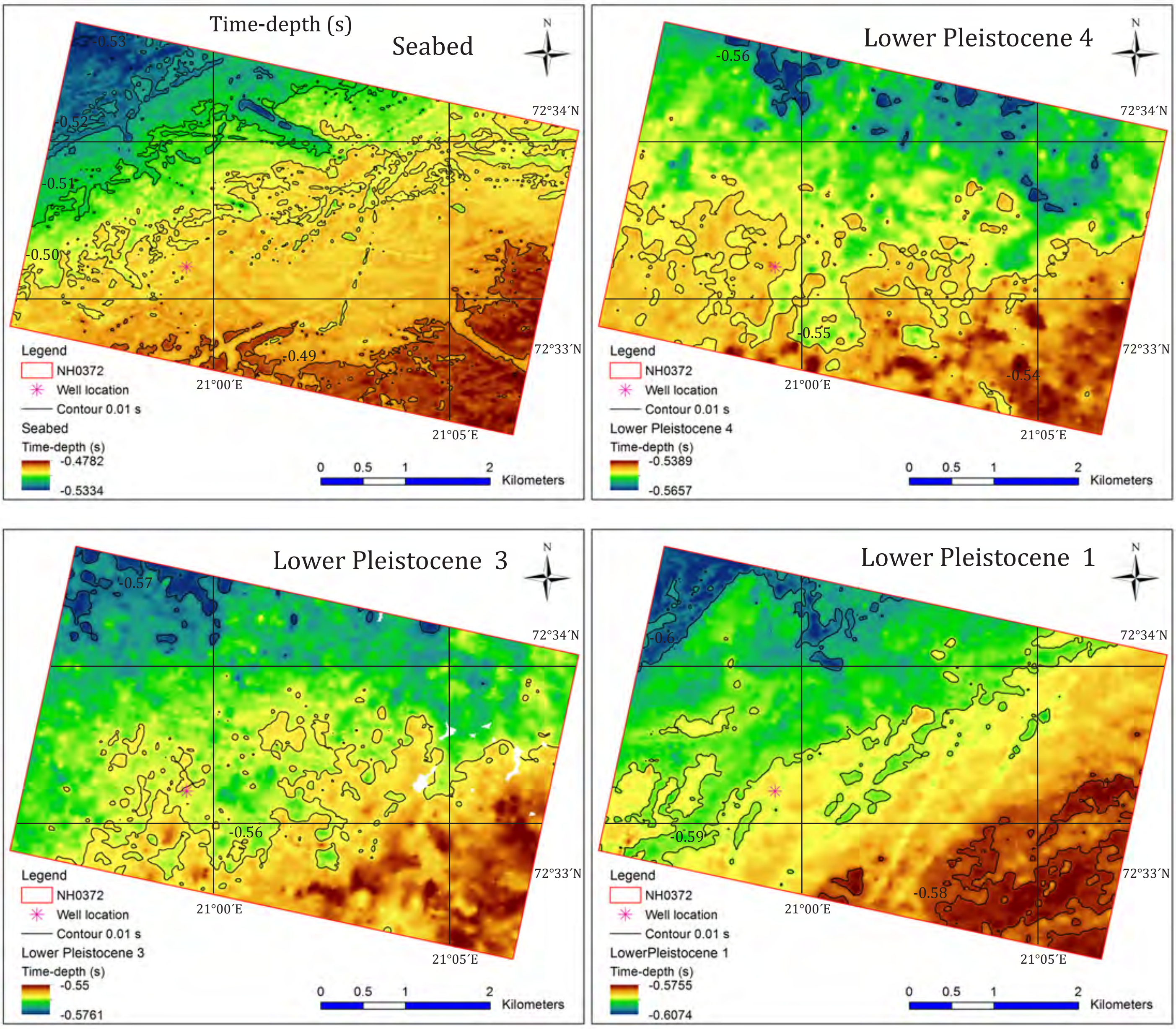

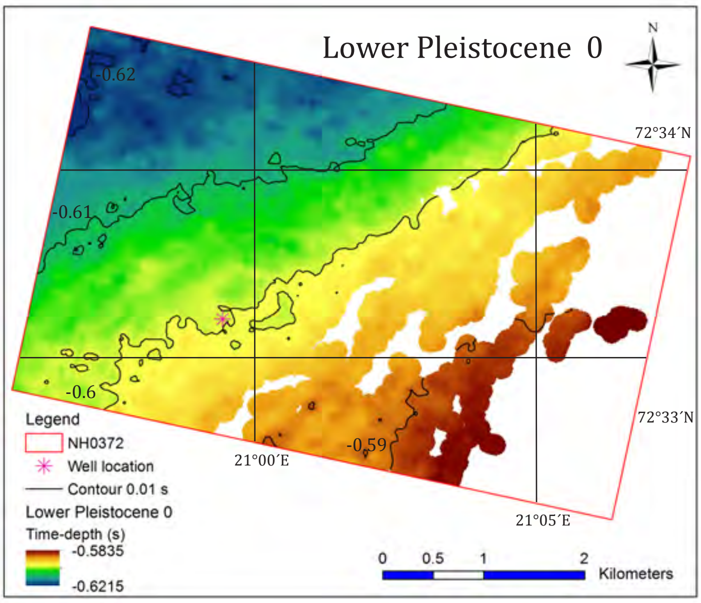

Figure B2 - B6: Paleo-bathymetry maps of the seabed, Lower Pleistocene 4, Lower Pleistocene 3, Lower Pleistocene 1 and the Lower Pleistocene 0, generated from the NH0372 survey area. The depth is presented in seconds and the contour lines in each map illustrate elevation changes for every 0.01 s. The pink dot mark the location of the well 7220/6-1. The reference map in the lower right corner displays an overview of the NH0372 survey area (green box). See figure A1 for the entire study area.

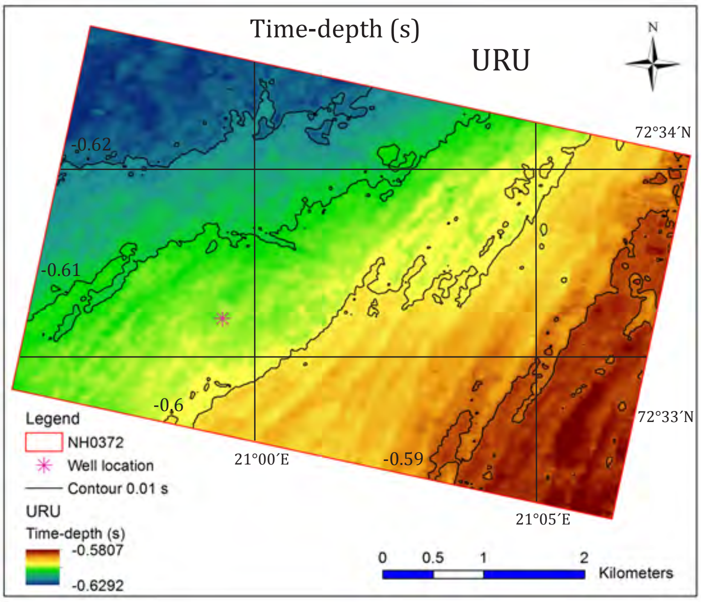

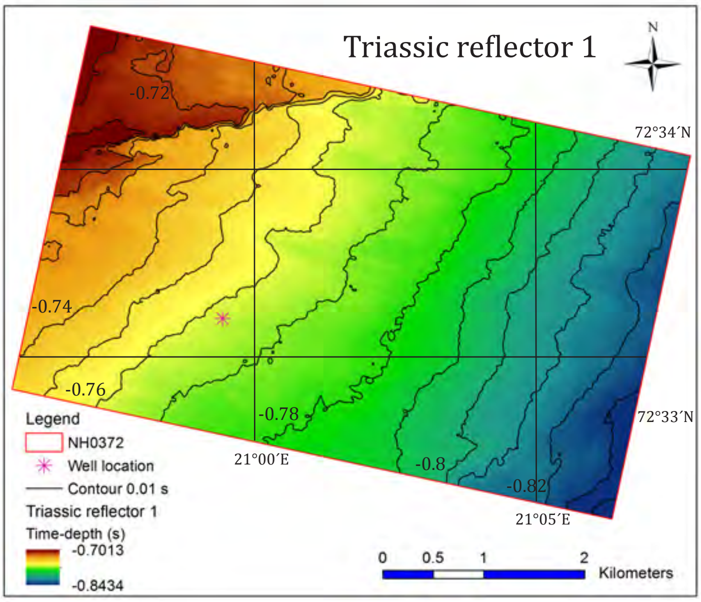

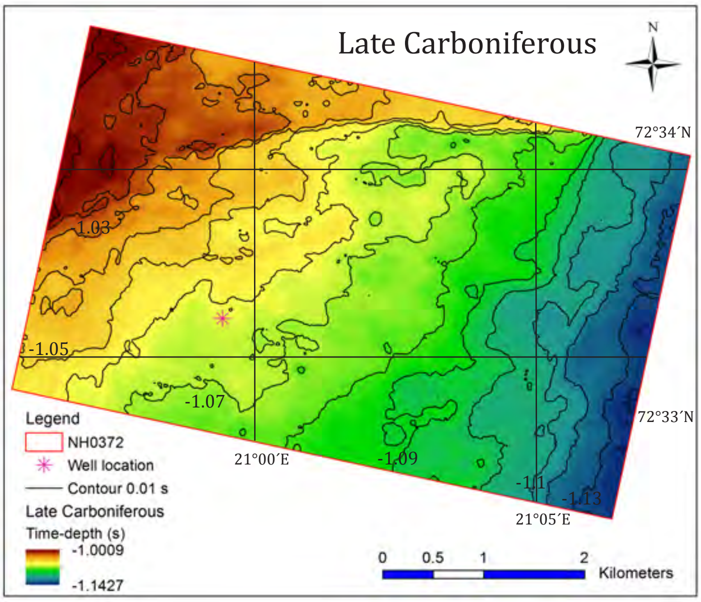

Figure B7 - B9: Paleo-bathymetry maps of the URU, Triassic reflector 1 and the Late Carboniferous, generated from the NH0372 survey area. The depth is presented in seconds and the contour lines in each map illustrate elevation changes for every 0.01 s. The pink dot mark the location of the well 7220/6-1. The reference map in the center displays an overview of the NH0372 survey area (green box). See figure A1 for the entire study area.

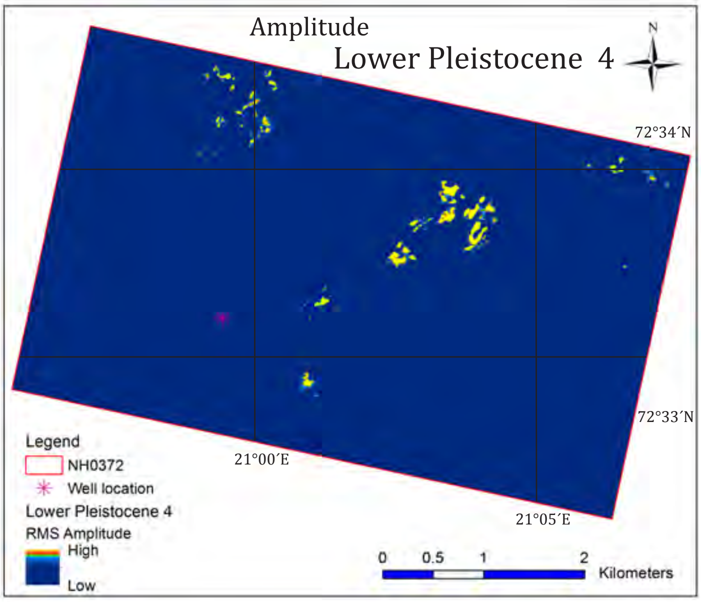

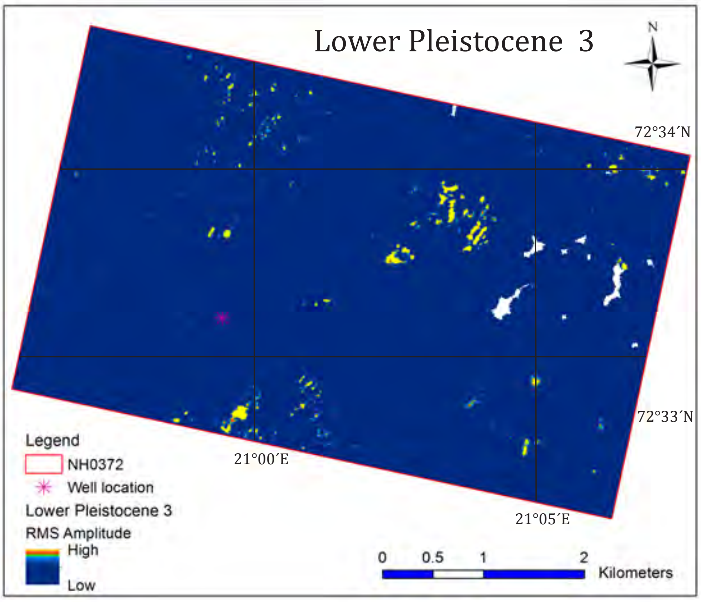

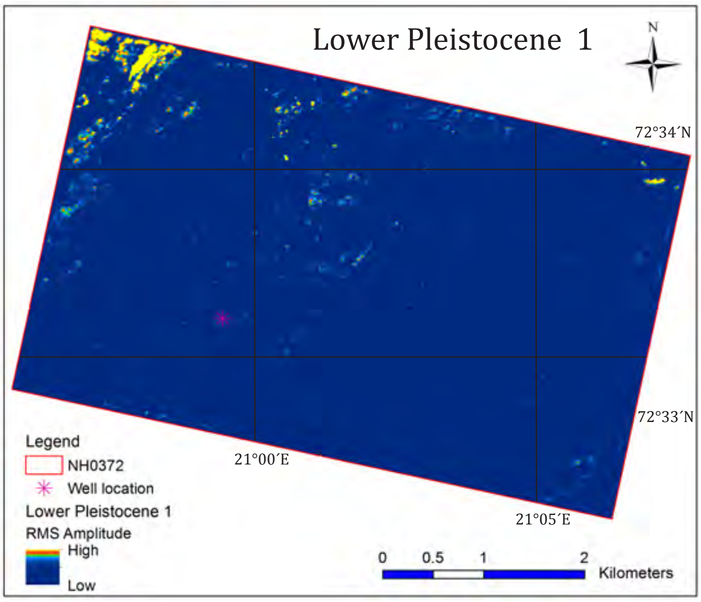

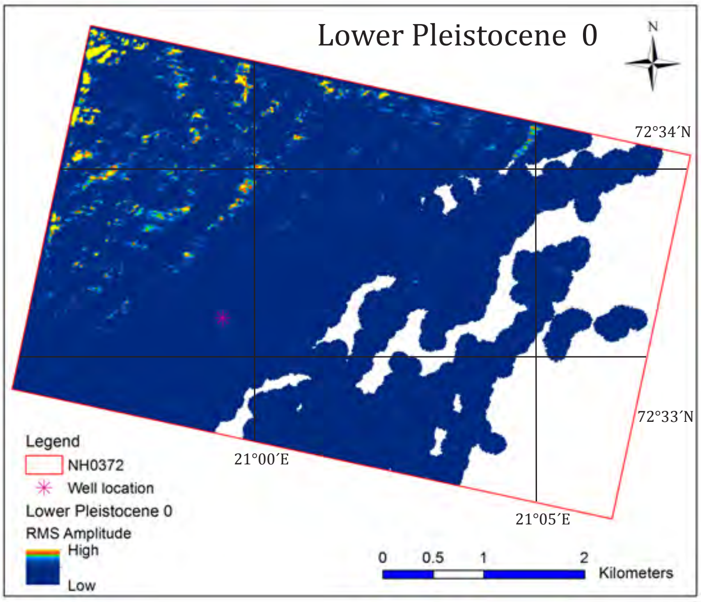

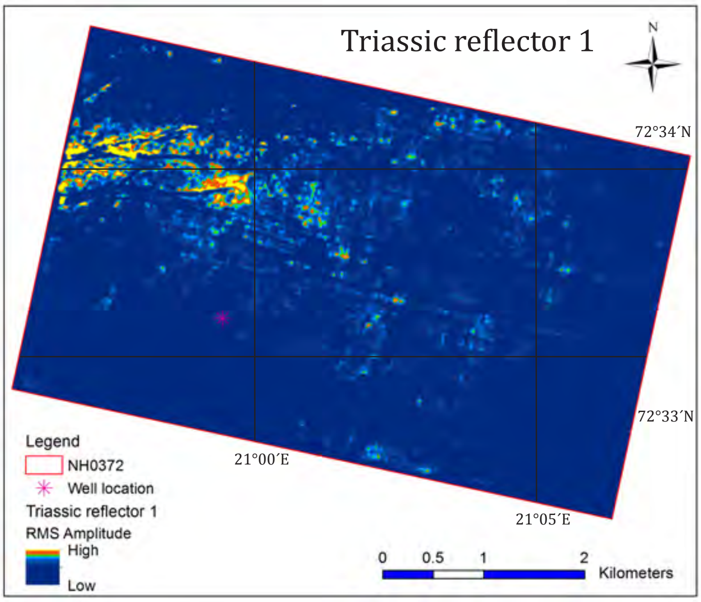

Figure B10 - B14: Amplitude maps (RMS) of the Lower Pleistocene 4, Lower Pleistocene 3, Lower Pleistocene 1, Lower Pleistocene 0 and the Triassic reflector 1, generated from the NH0372 survey area. Amplitude anomalies are illustrated in red to yellow colors. The pink dot mark the location of the well 7220/6-1. The reference map in the lower right corner displays an overview of the NH0372 survey area (green box). See figure A1 for the entire study area.

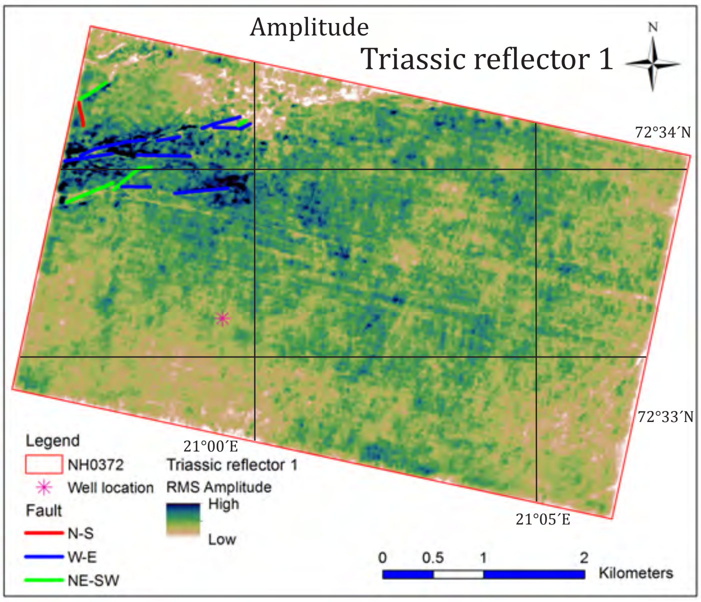

Figure B15: RMS amplitude map of the Triassic reflector 1, viewed in a different color ramp, that display the presence of faults. Generated from the NH0372 survey area. Amplitude anomalies are illustrated in blue to black colors. The faults are highlighted using a color coded orientation. The pink dot mark the location of the well 7220/6-1. The reference map in the upper right corner displays an overview of the NH0372 survey area (green box). See figure A1 for the entire study area.

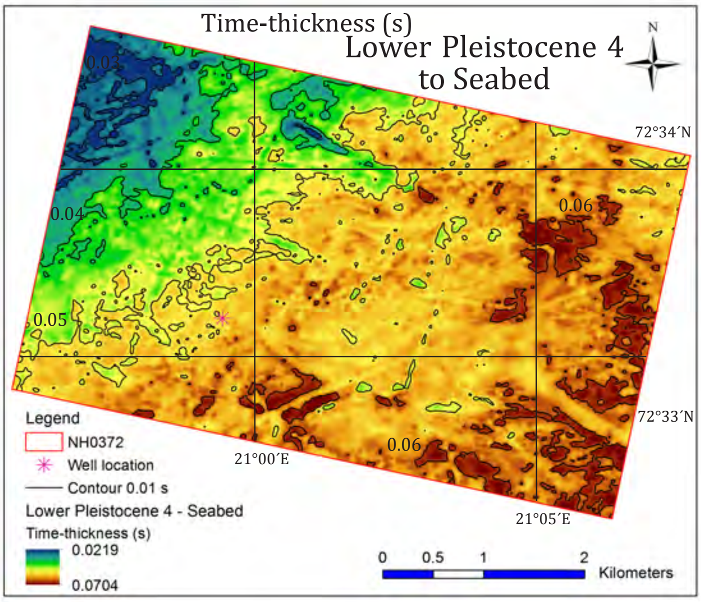

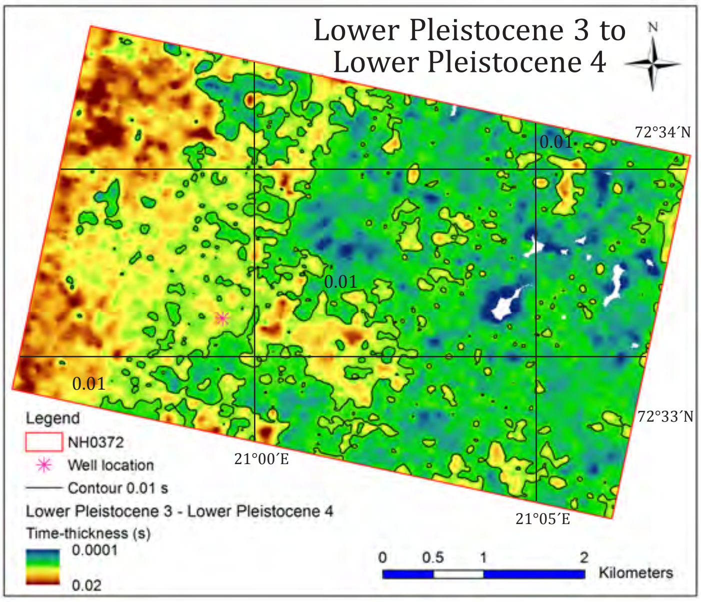

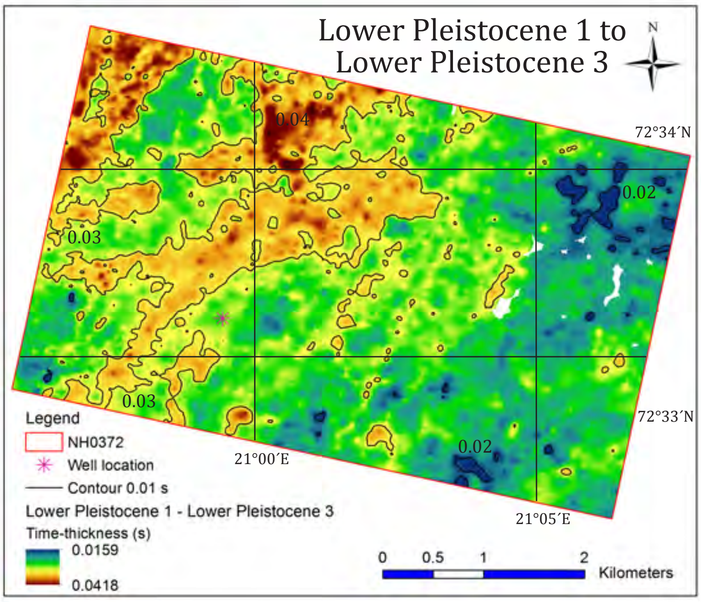

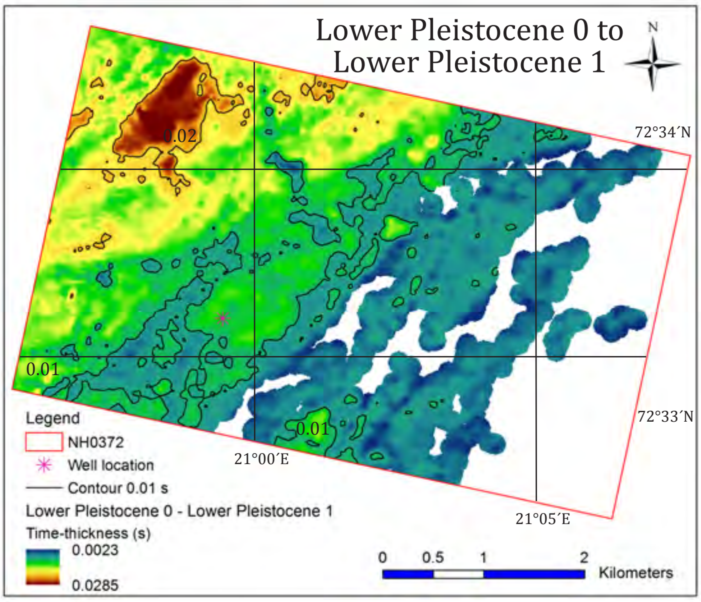

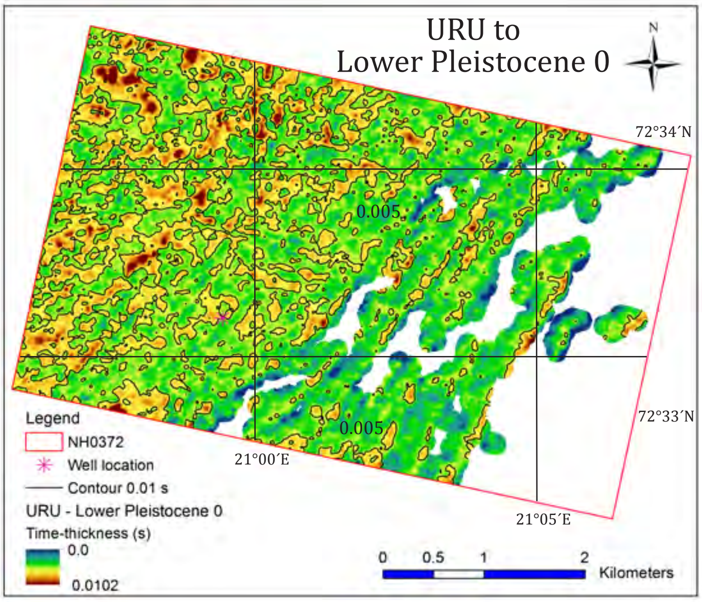

Figure B16 - B20: Isopach maps showing the time-depth differences between two layers, generated from the NH0372 survey area. The thickness is presented in seconds and the contour lines in each map illustrate elevation changes for every 0.01 s. The pink dot mark the location of the well 7220/6-1. The reference map in the lower right corner displays an overview of the NH0372 survey area (green box). See figure A1 for the entire study area.

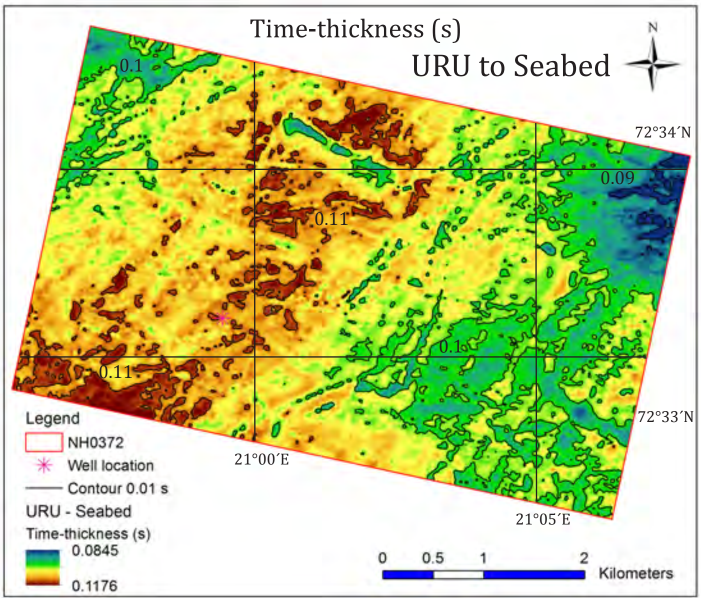

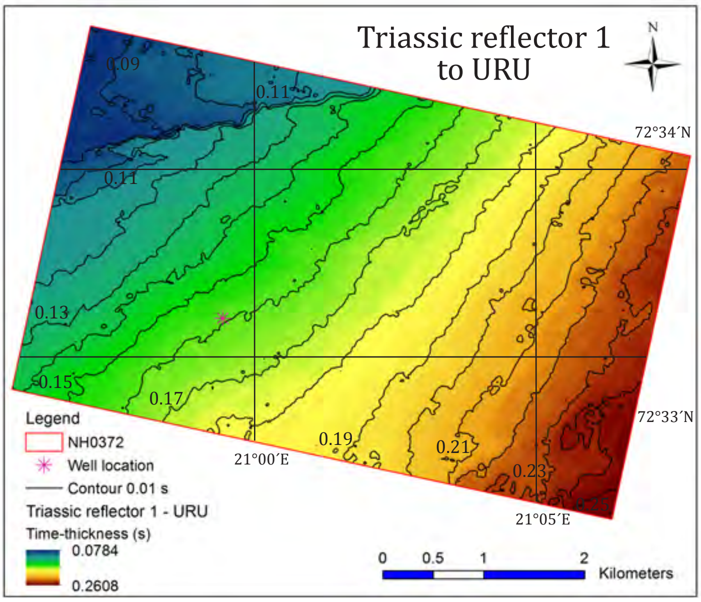

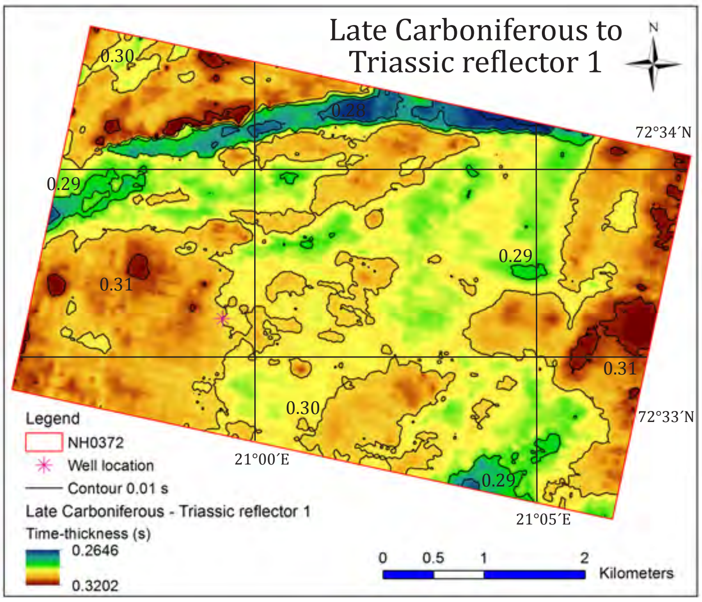

Figure B21 - B23: Isopach maps showing the time-depth differences between two layers, generated from the NH0372 survey area. The thickness is presented in seconds and the contour lines in each map illustrate elevation changes for every 0.01 s. The pink dot mark the location of the well 7220/6-1. The reference map in the center displays an overview of the NH0372 survey area (green box). See figure A1 for the entire study area.

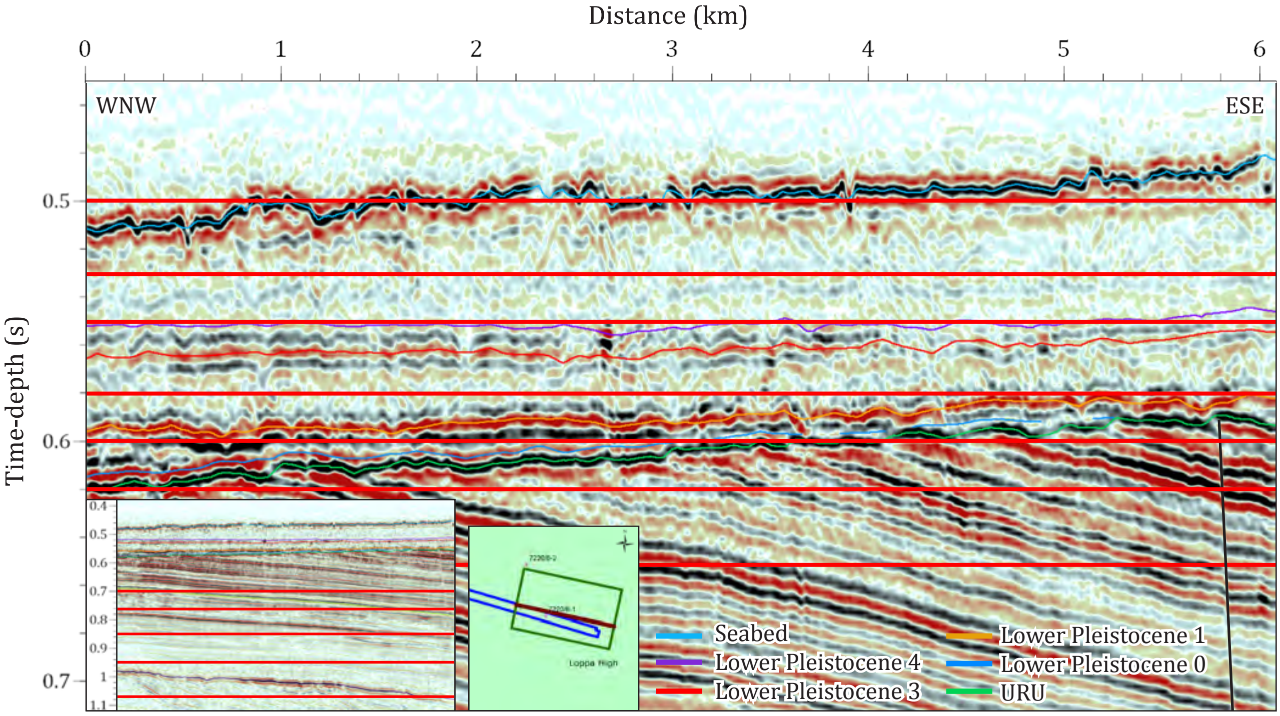

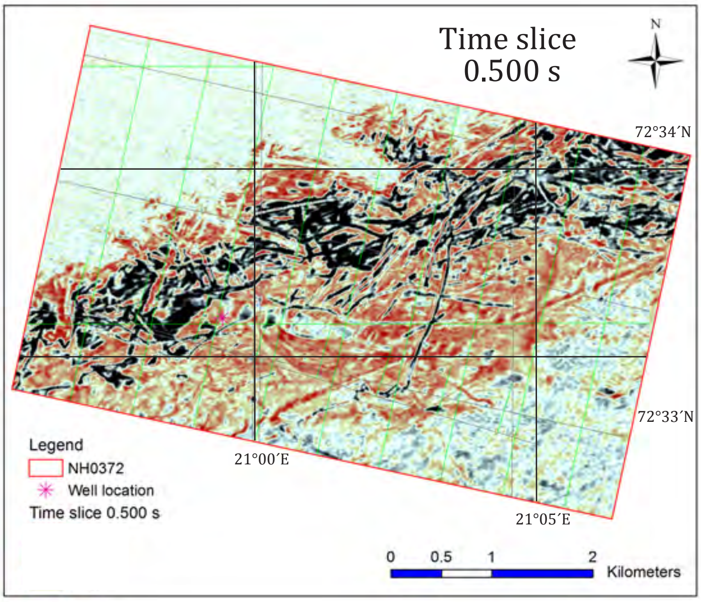

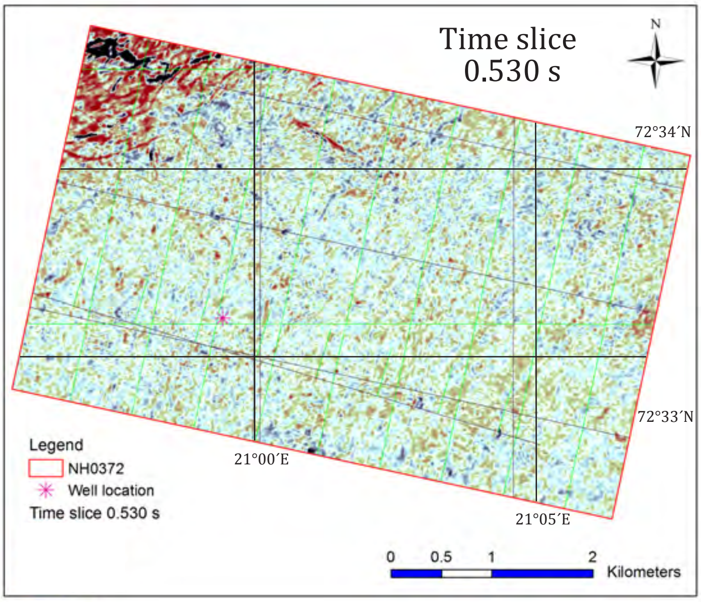

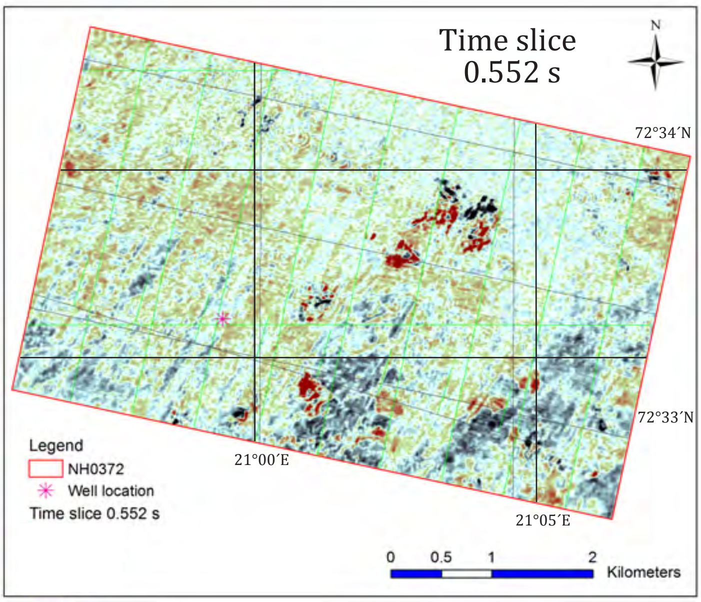

Figure B24: A seismic profile of the NH0372 survey area, located center striking WNW-ESE. The seismic profile in the lower left corner display the full extent of the interpreted layers. Red lines mark the horizontal depth for generated time slices. A major fault is highlighted in the ESE area by a black line. The map in the lower center displays an overview of the NH0372 survey areas (green box), with the orientation of the 2D seismic profile (dark red line). See figure A1 for the entire study area.

Figure B25 - B27: Time slice velocity maps cutting the NH0372 survey area horizontally at 0.500 s, 0.530 s and 0.552 s. Red color reflect areas of high permeability and black areas of low permeability. The pink dot mark the location of the well 7220/6-1. The reference map in the lower right corner displays an overview of the NH0372 survey area (green box). See figure A1 for the entire study area.

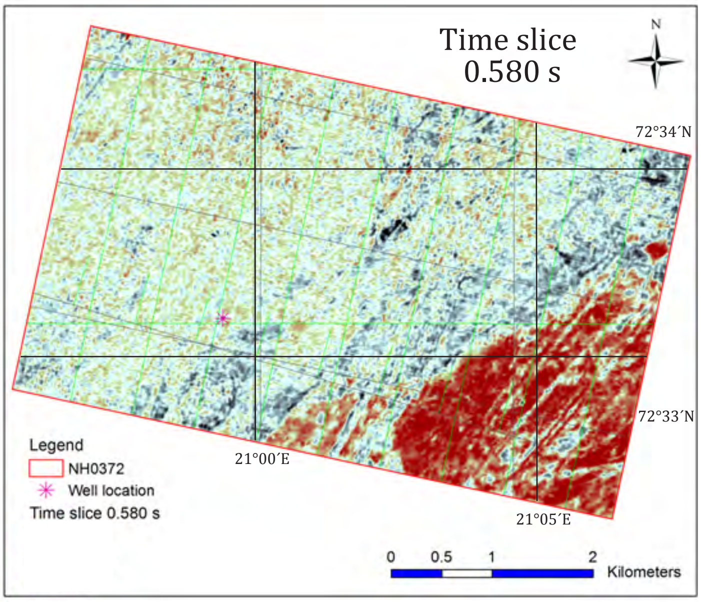

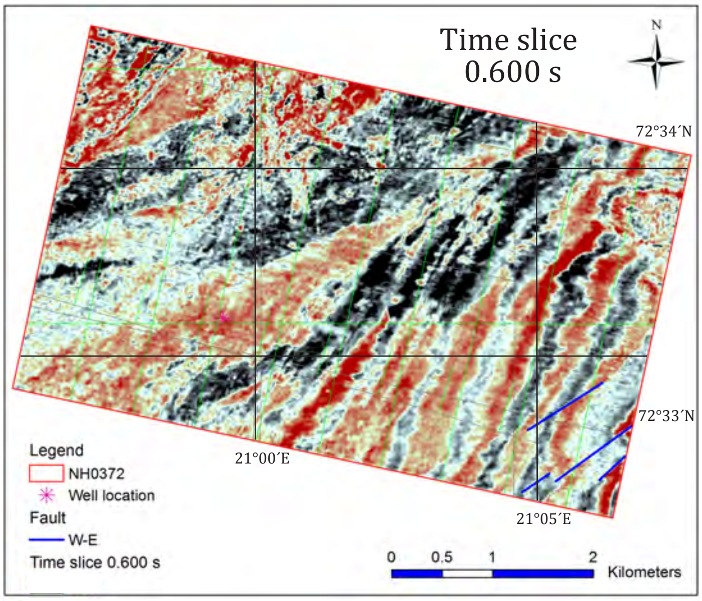

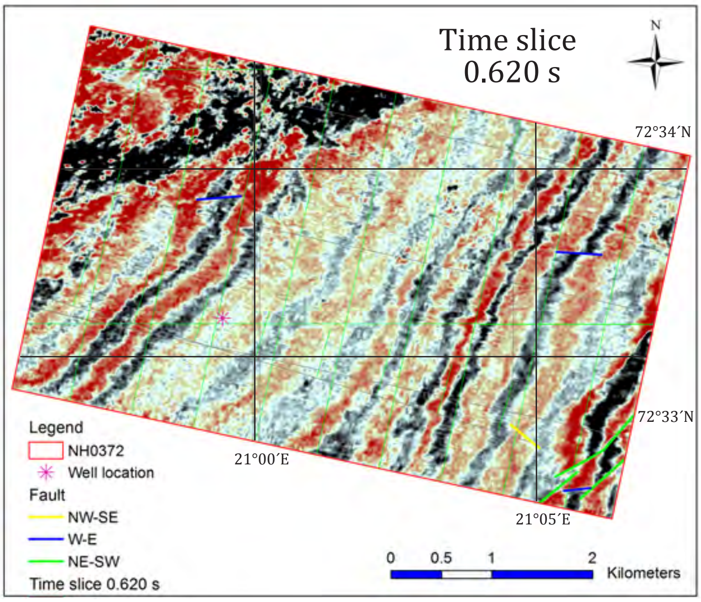

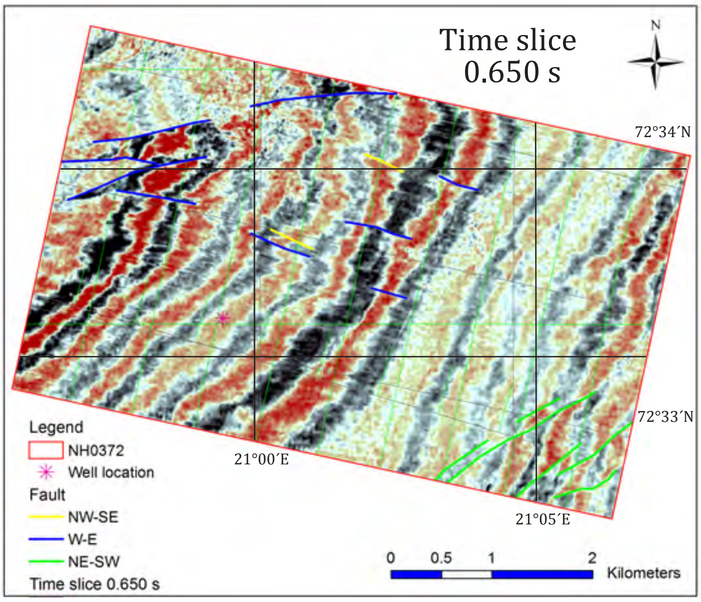

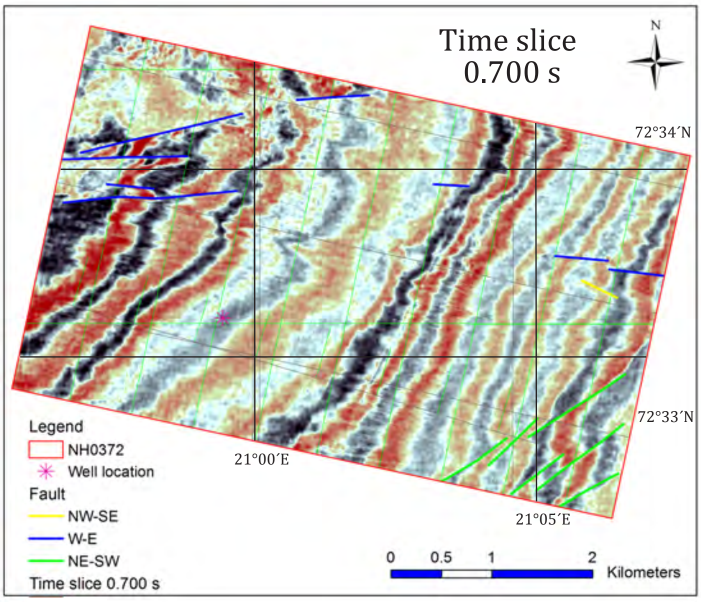

Figure B28 - B32: Time slice velocity maps cutting the NH0372 survey area horizontally at 0.580 s, 0.600 s, 0.620 s, 0.650 s and 0.700 s. Red color reflect areas of high permeability and black areas of low permeability. The pink dot mark the location of the well 7220/6-1. Faults are highlighted using color coded orientations. The reference map in the lower right corner displays an overview of the NH0372 survey area (green box). See figure A1 for the entire study area.

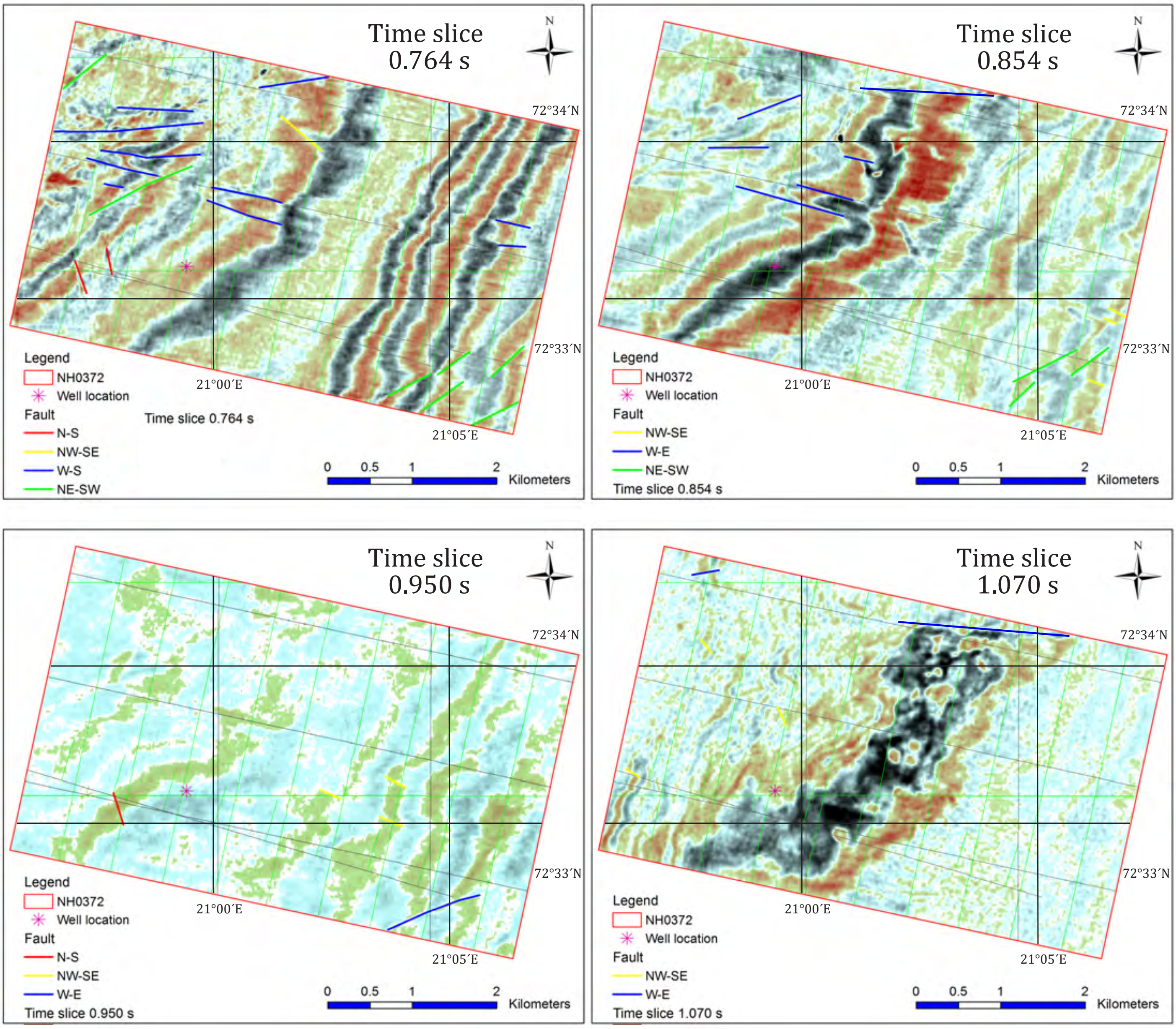

Figure B33 - B36: Time slice velocity maps cutting the NH0372 survey area horizontally at 0.764 s, 0.854 s, 0.950 s and 1.070 s. Red color reflect areas of high permeability and black areas of low permeability. The pink dot mark the location of the well 7220/6-1. Faults are highlighted using color coded orientations. The reference map in the lower right corner displays an overview of the NH0372 survey area (green box). See figure A1 for the entire study area.

Appendix C - Survey area Pcable area B PL609

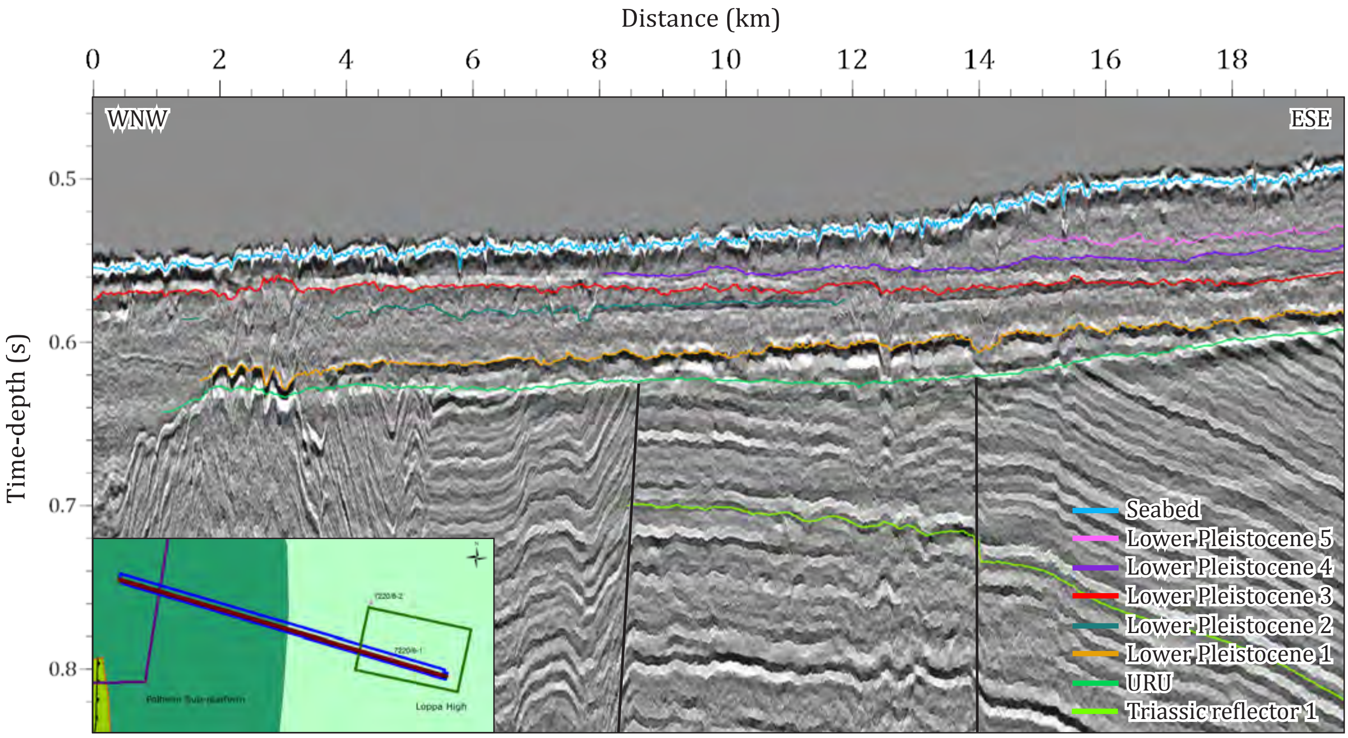

Figure C1: A seismic profile of the Pcable area B PL609 survey area, located center striking WNW-ESE. Eight layers are highlighted: the seabed (light blue); Lower Pleistocene 5 (pink); Lower Pleistocene 4 (violet); Lower Pleistocene 3 (red); Lower Pleistocene 2 (dark green); Lower Pleistocene 1 (orange); URU (green) and Triassic reflector 1 (neon green). Two major fault are highlighted in the center by black lines. The map in the lower left corner displays an overview of the Pcable area B PL609 (blue outline) and NH0372 (green box) survey areas, with the orientation of the 2D seismic profile (dark red line). See figure A1 for the entire study area.

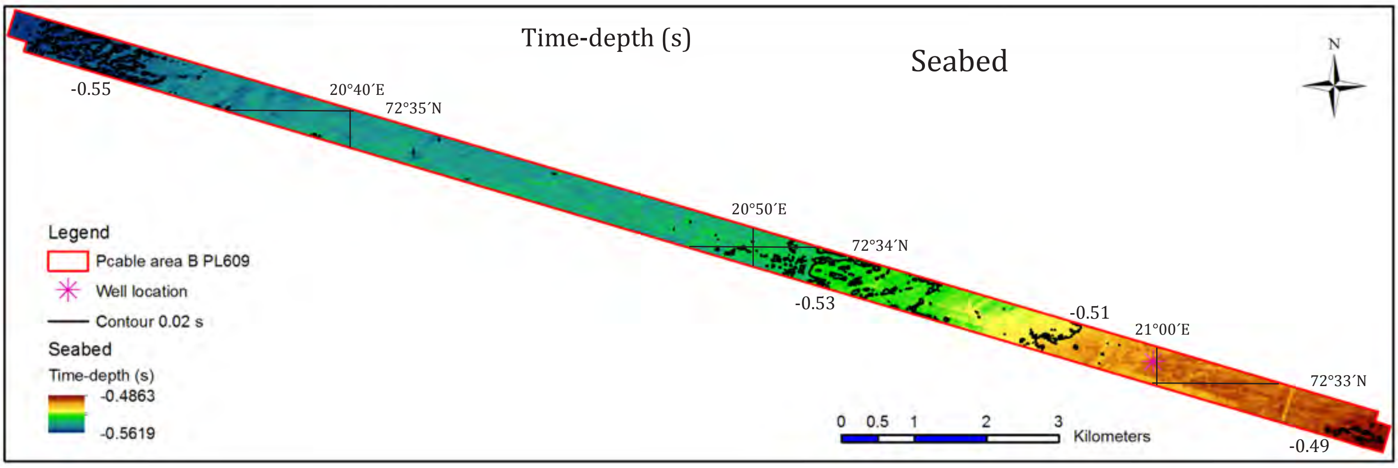

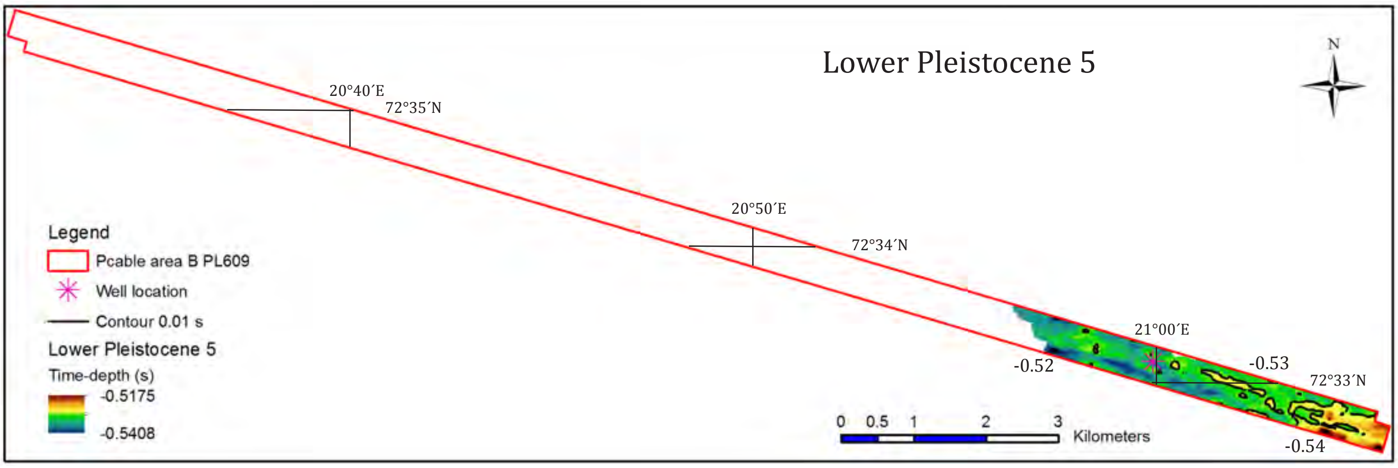

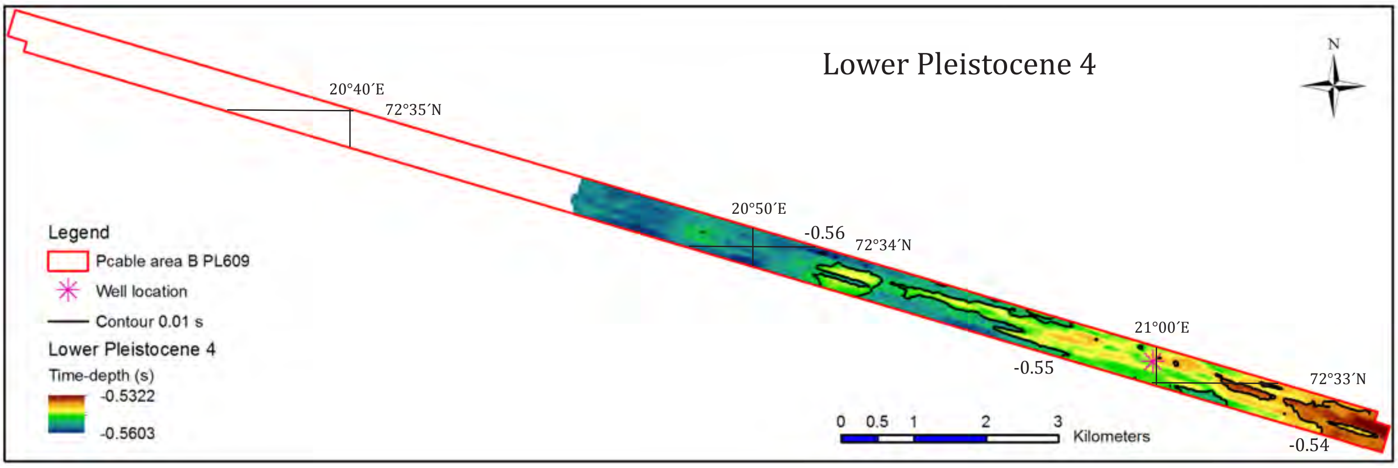

Figure C2 - C4: Paleo-bathymetry maps of the seabed, Lower Pleistocene 5 and the Lower Pleistocene 4, generated from the Pcable area B PL609 survey area. The depth is presented in seconds and the contour lines in each map illustrate elevation changes for every 0.02 s, 0.01 s and 0.01 s respectively. The pink dot mark the location of the well 7220/6-1. The reference map in the lower right corner displays an overview of the Pcable survey area (blue outline). See figure A1 for the entire study area.

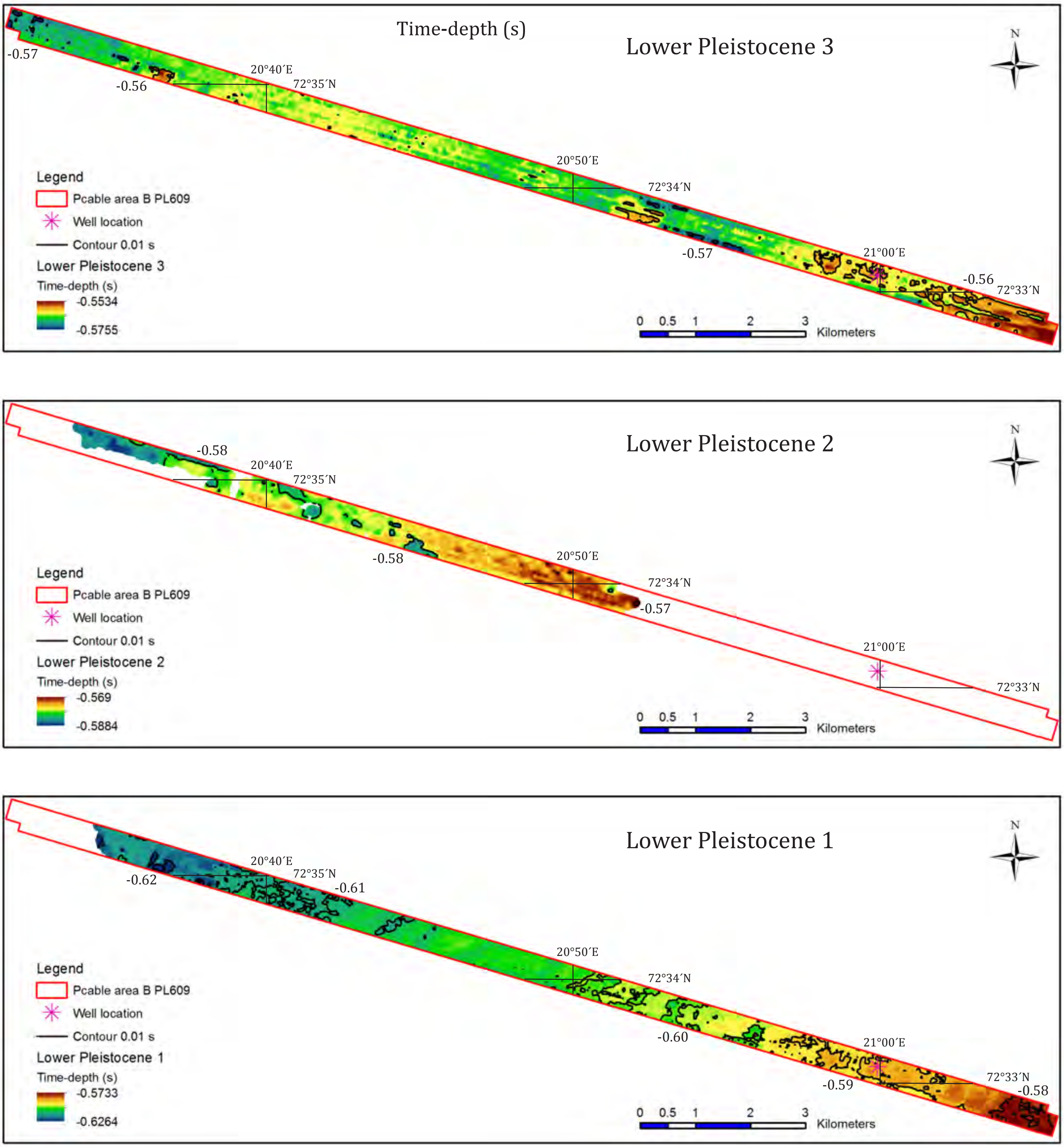

Figure C5 - C7: Paleo-bathymetry maps of the Lower Pleistocene 3, Lower Pleistocene 2 and the Lower Pleistocene 1, generated from the Pcable area B PL609 survey area. The depth is presented in seconds and the contour lines in each map illustrate elevation changes for every 0.01 s. The pink dot mark the location of the well 7220/6-1. The reference map in the lower right corner displays an overview of the Pcable survey area (blue outline). See figure A1 for the entire study area.

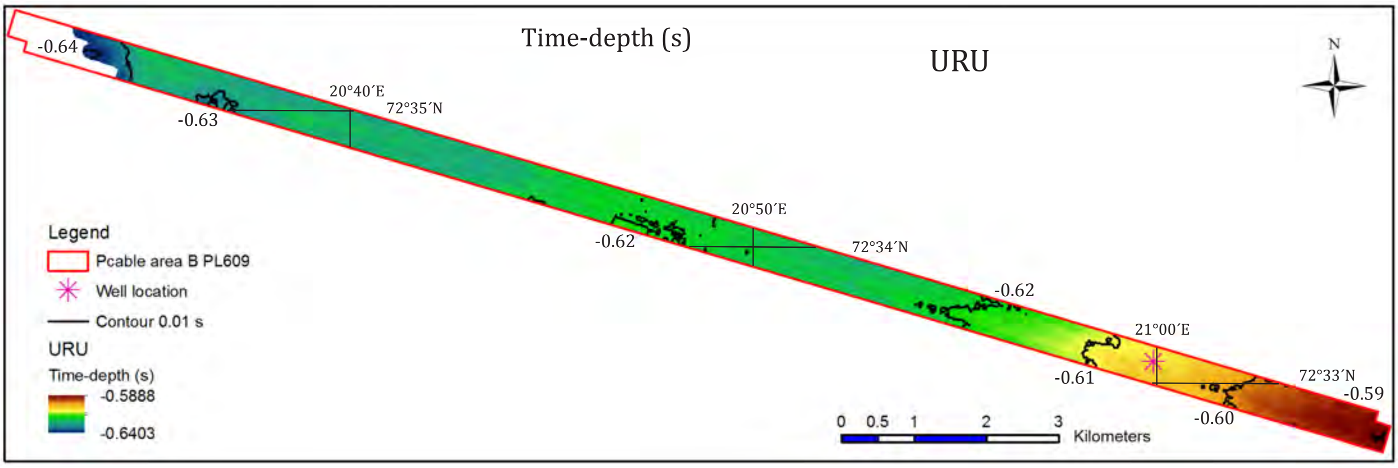

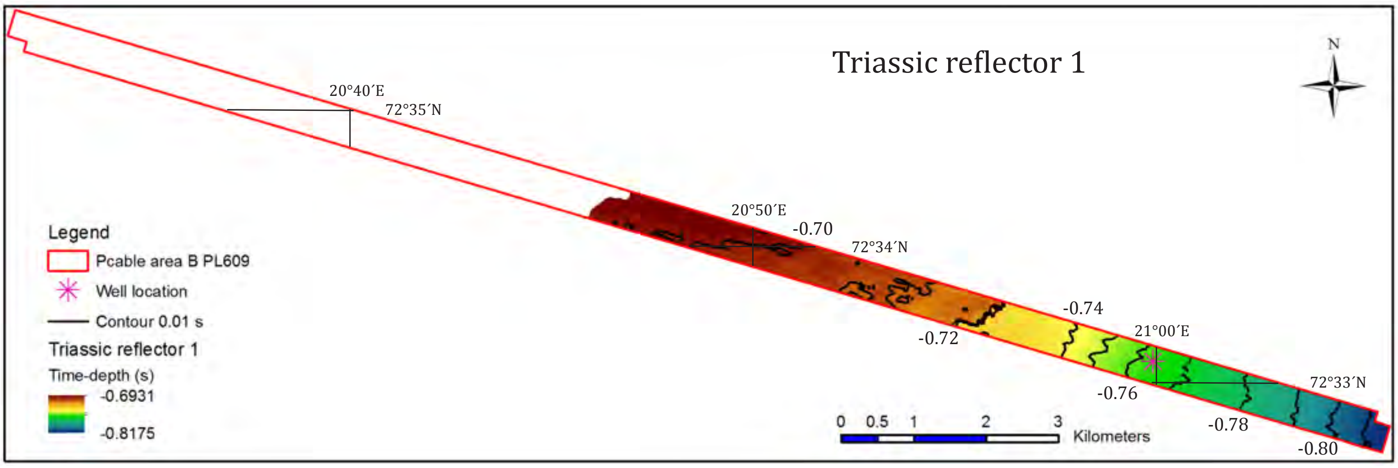

Figure C8 & C9: Paleo-bathymetry maps of the URU and the Triassic reflection 1, generated from the Pcable area B PL609 survey area. The depth is presented in seconds and the contour lines in each map illustrate elevation changes for every 0.01 s. The pink dot mark the location of the well 7220/6-1. The reference map in the lower right corner displays an overview of the Pcable survey area (blue outline). See figure A1 for the entire study area.

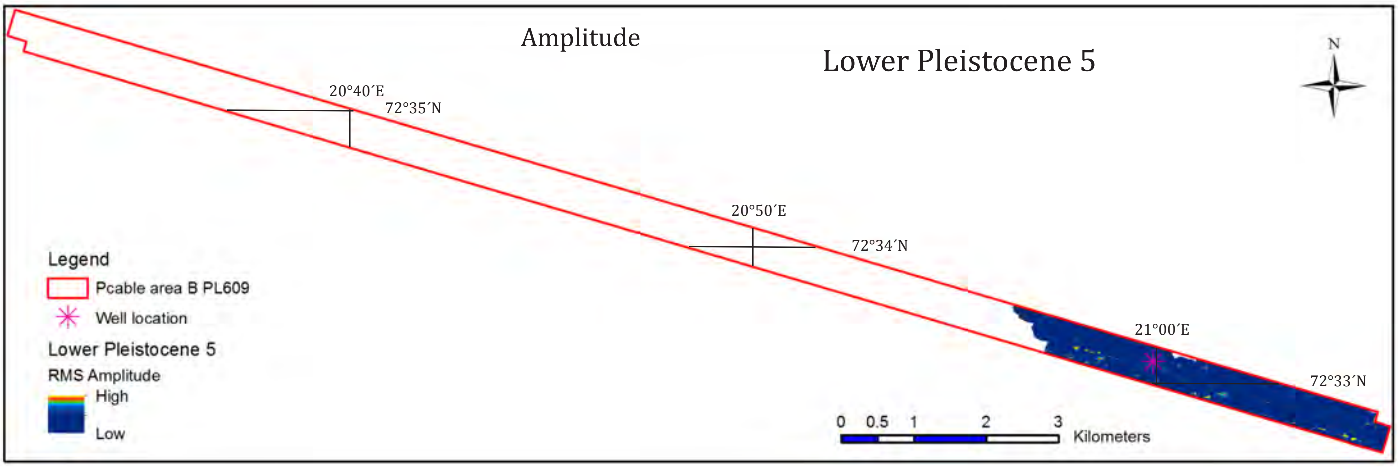

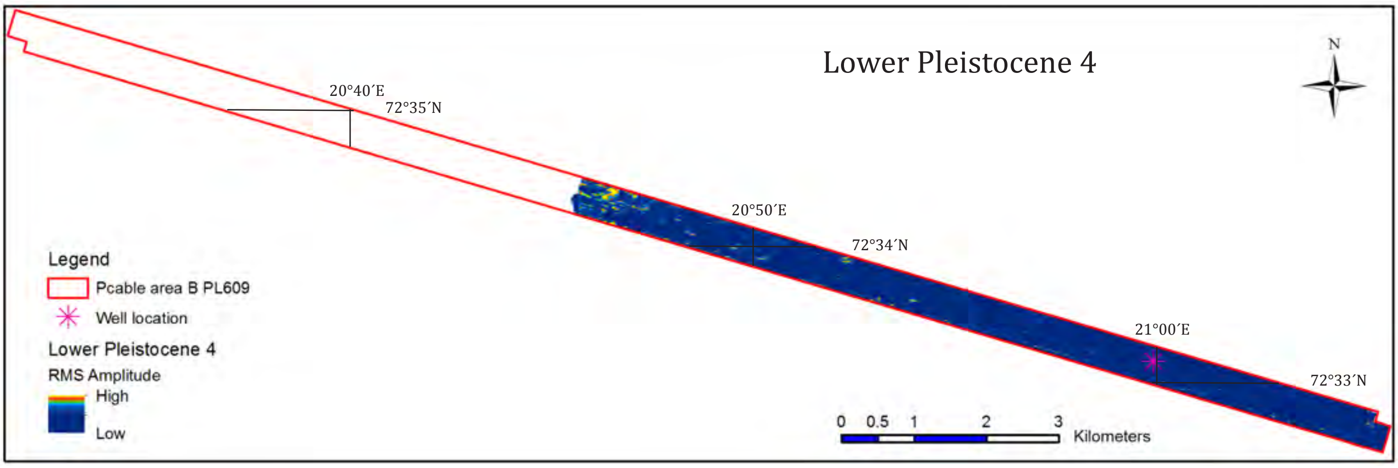

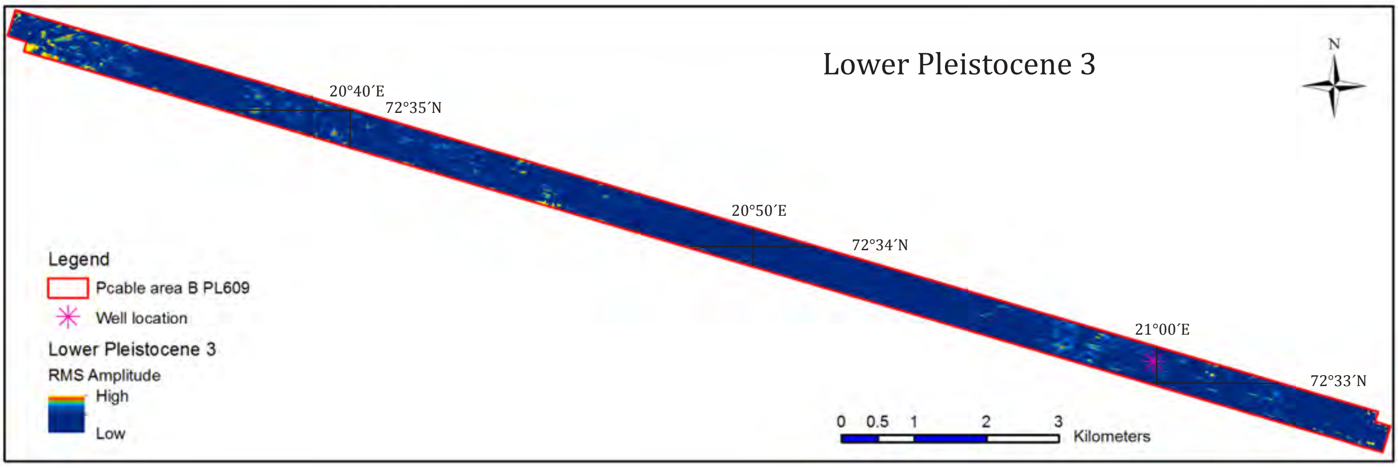

Figure C10 - C12: Amplitude maps (RMS) of the Lower Pleistocene 5, Lower Pleistocene 4 and the Lower Pleistocene 3, generated from the Pcable area B PL609 survey area. Amplitude anomalies are illustrated in red to yellow colors. The pink dot mark the location of the well 7220/6-1. The reference map in the lower right corner displays an overview of the Pcable survey area (blue outline). See figure A1 for the entire study area.

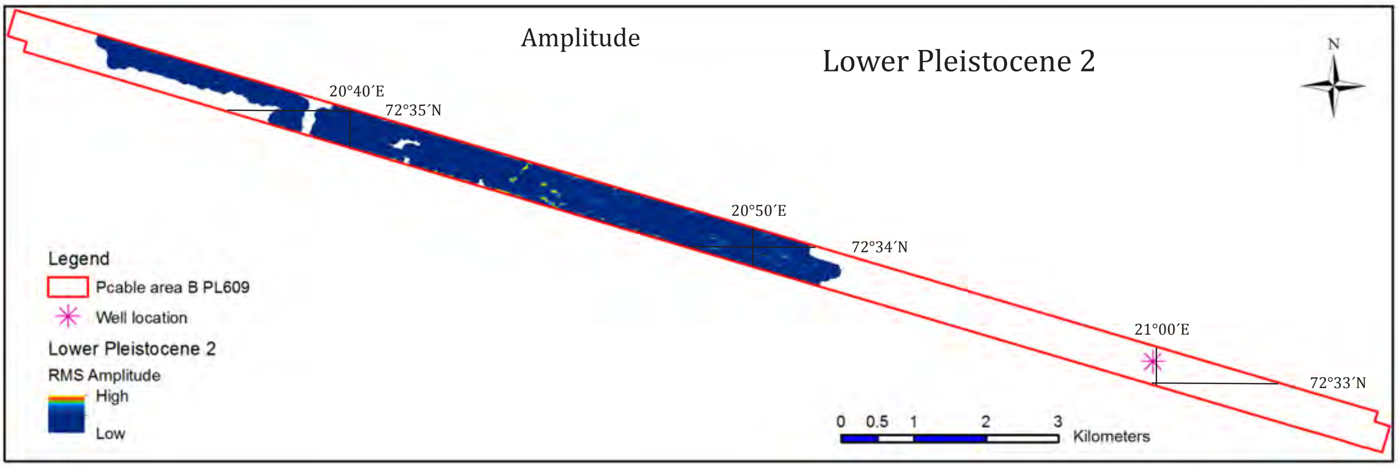

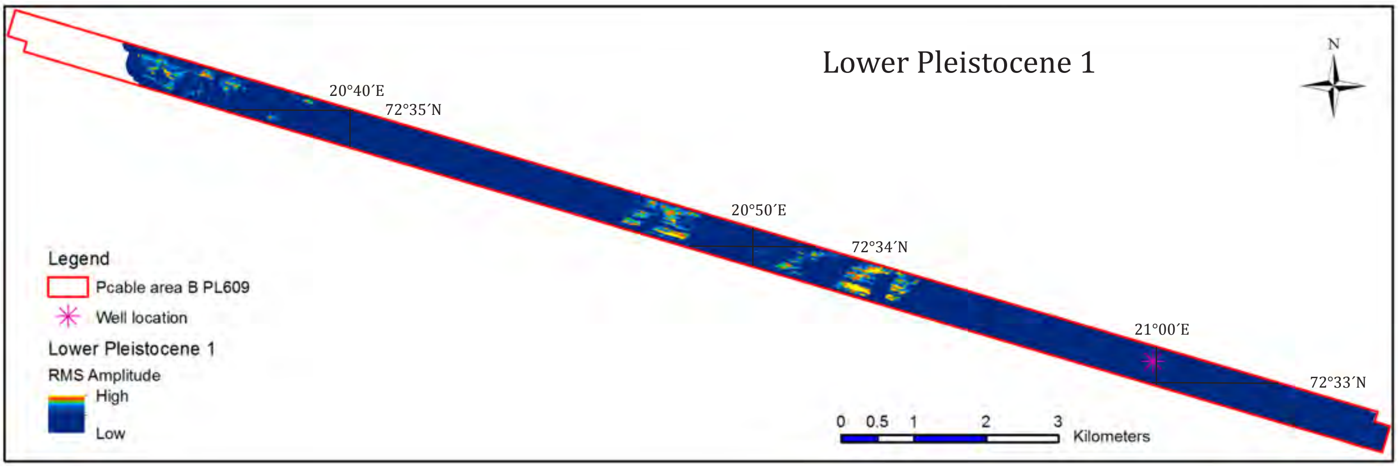

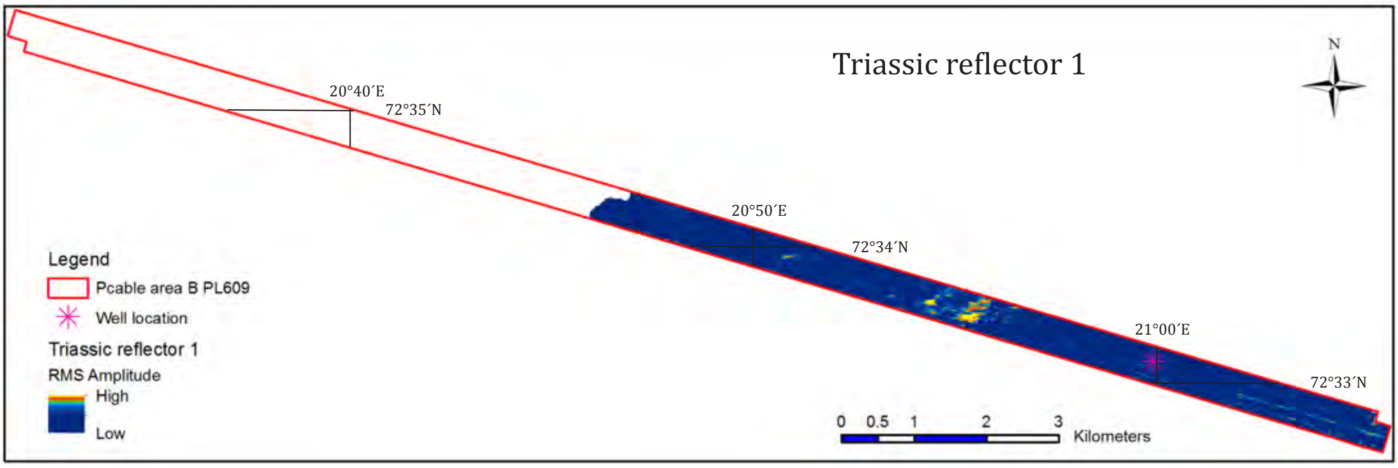

Figure C13 - C15: Amplitude maps (RMS) of the Lower Pleistocene 2, Lower Pleistocene 1 and the Triassic reflector 1, generated from the Pcable area B PL609 survey area. Amplitude anomalies are illustrated in red to yellow colors. The pink dot mark the location of the well 7220/6-1. The reference map in the lower right corner displays an overview of the Pcable survey area (blue outline). See figure A1 for the entire study area.

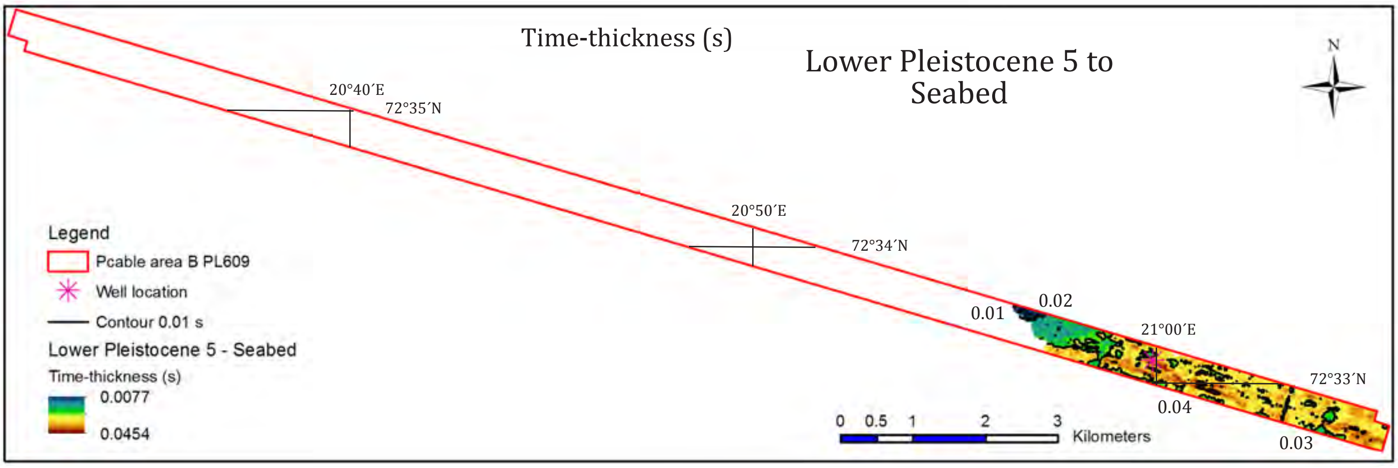

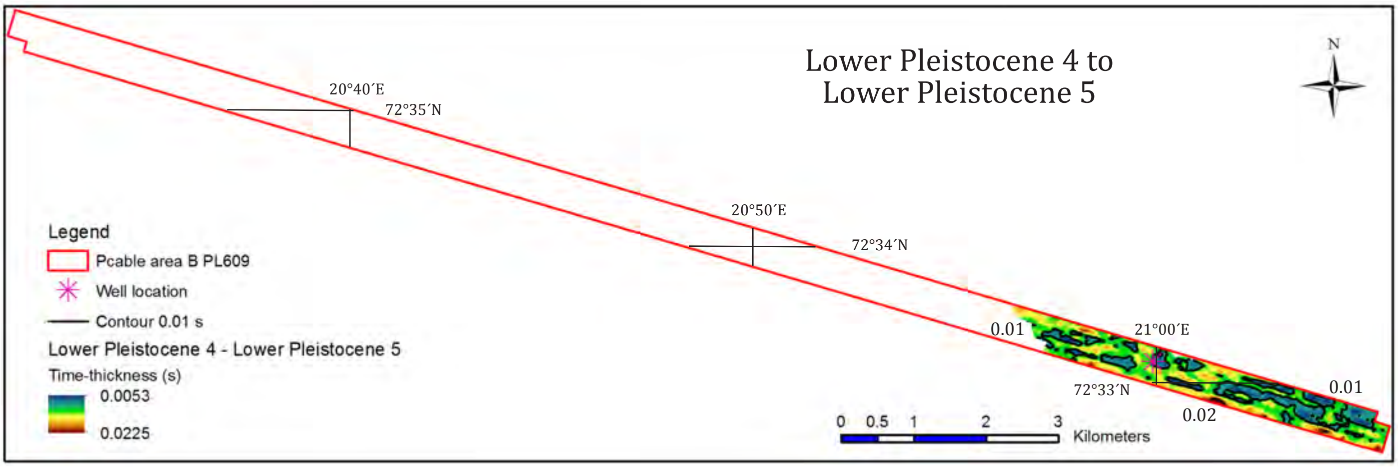

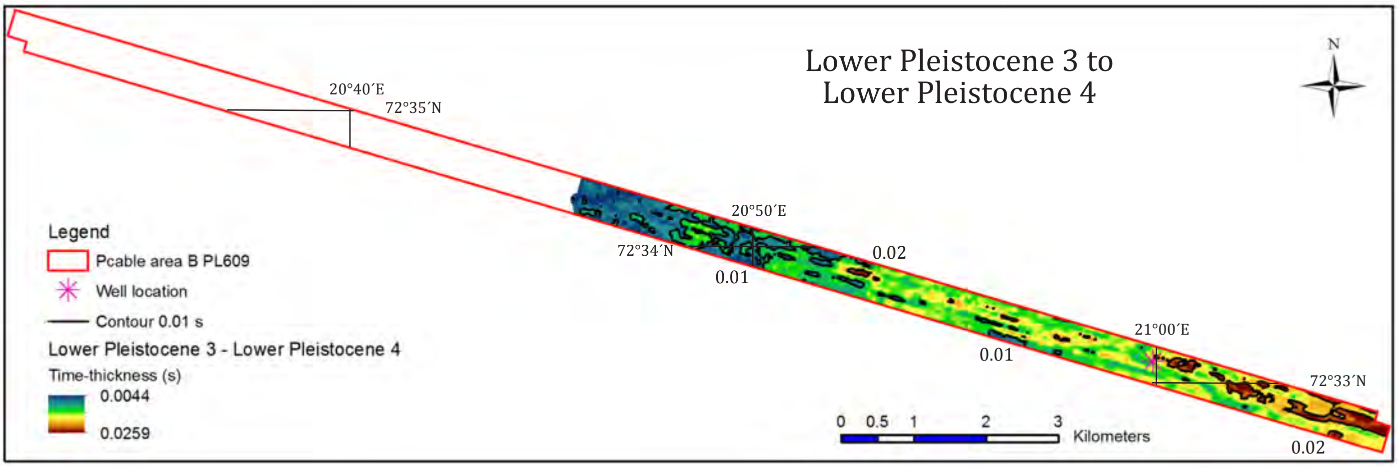

Figure C16 - C18: Isopach maps showing the time-depth differences between two layers, generated from the Pcable area B PL609 survey area. The thickness is presented in seconds and the contour lines in each map illustrate elevation changes for every 0.01 s. The pink dot mark the location of the well 7220/6-1. The reference map in the lower right corner displays an overview of the Pcable survey area (blue outline). See figure A1 for the entire study area.

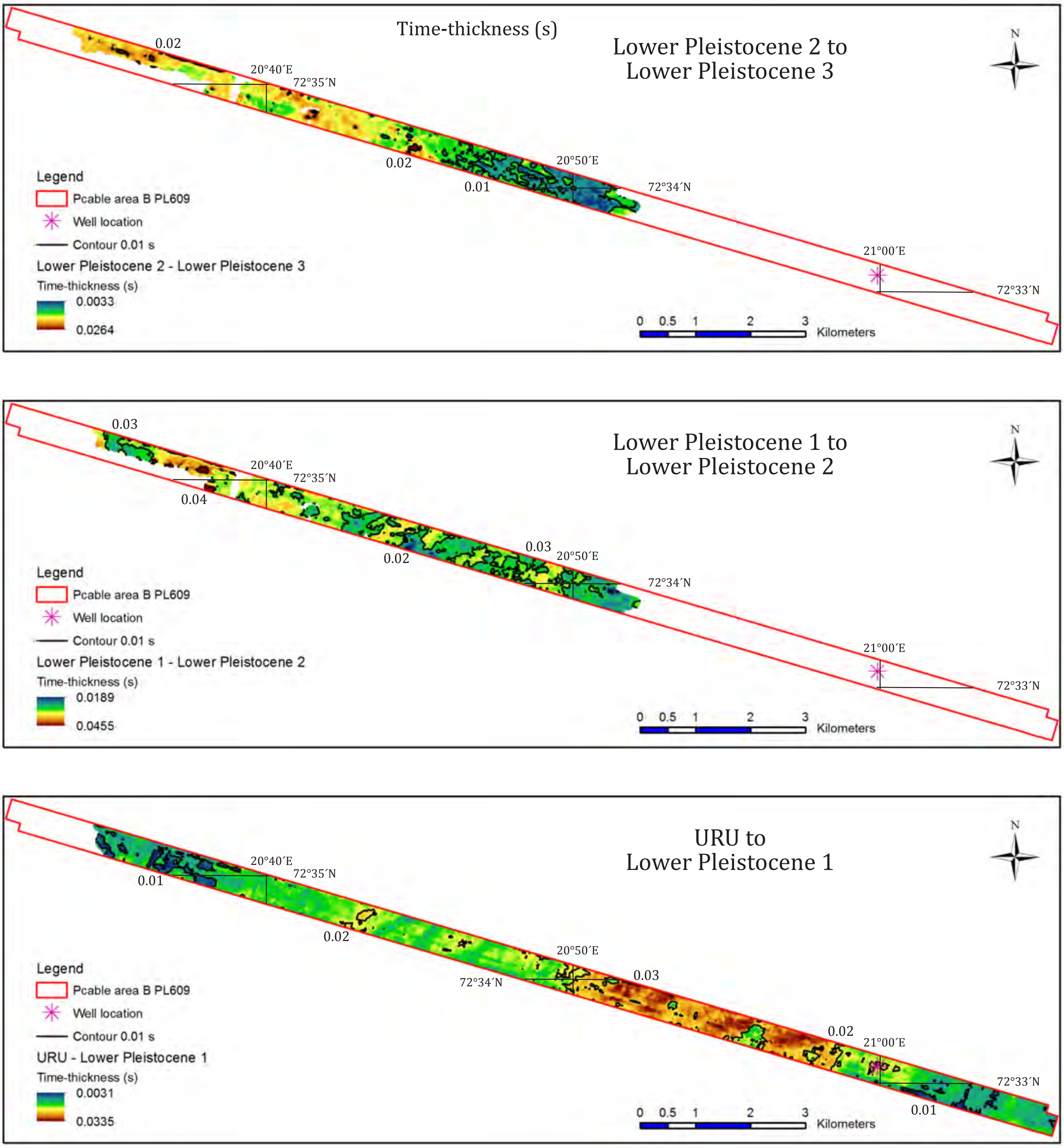

Figure C19 - C21: Isopach maps showing the time-depth differences between two layers, generated from the Pcable area B PL609 survey area. The thickness is presented in seconds and the contour lines in each map illustrate elevation changes for every 0.01 s. The pink dot mark the location of the well 7220/6-1. The reference map in the lower right corner displays an overview of the Pcable survey area (blue outline). See figure A1 for the entire study area.

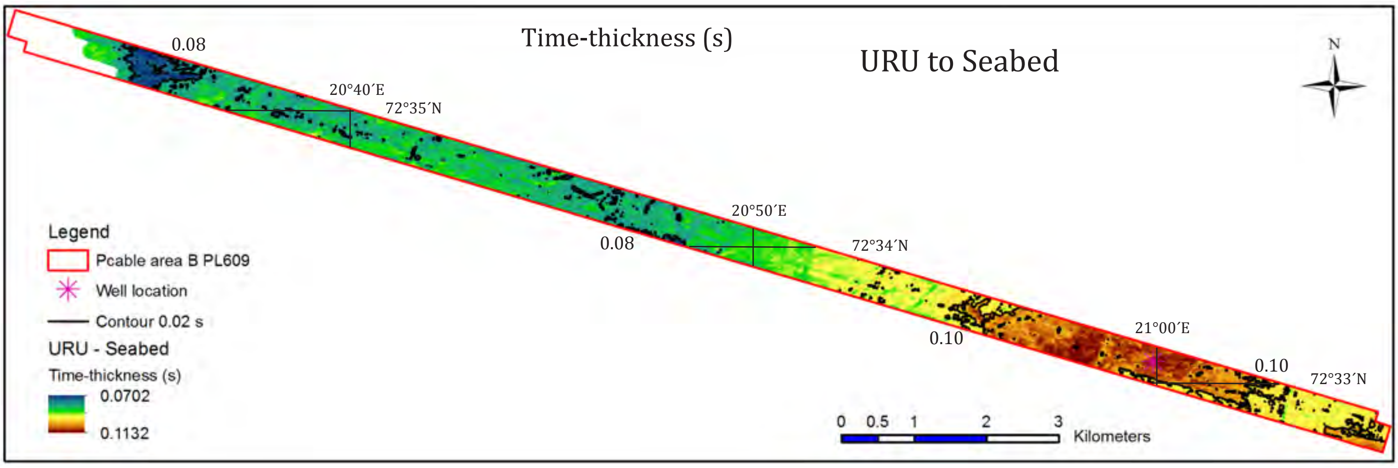

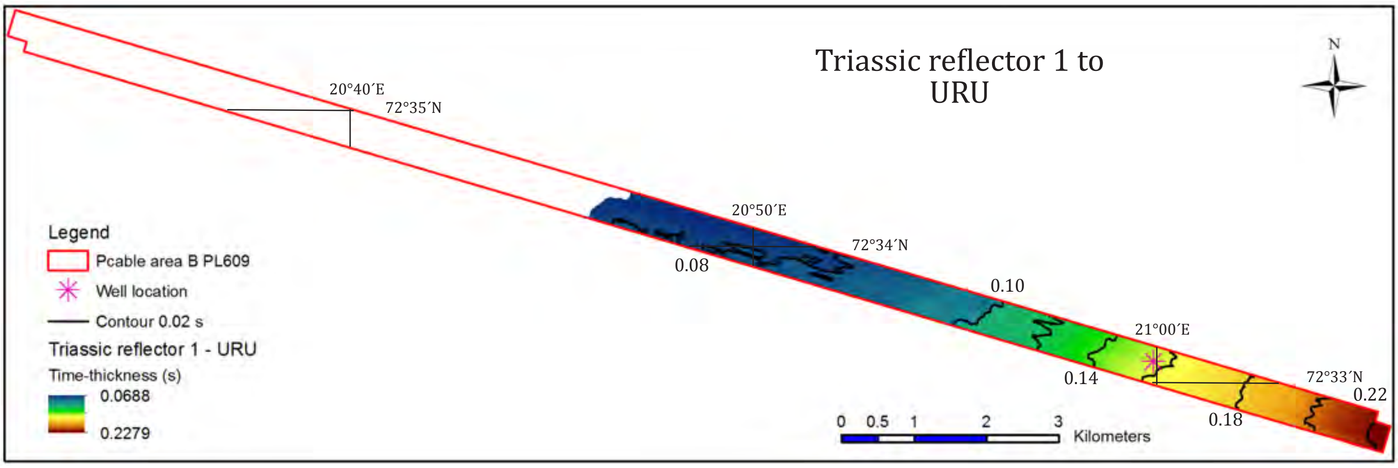

Figure C22 & C23: Isopach maps showing the time-depth differences between two layers, generated from the Pcable area B PL609 survey area. The thickness is presented in seconds and the contour lines in each map illustrate elevation changes for every 0.01 s. The pink dot mark the location of the well 7220/6-1. The reference map in the lower right corner displays an overview of the Pcable survey area (blue outline). See figure A1 for the entire study area.

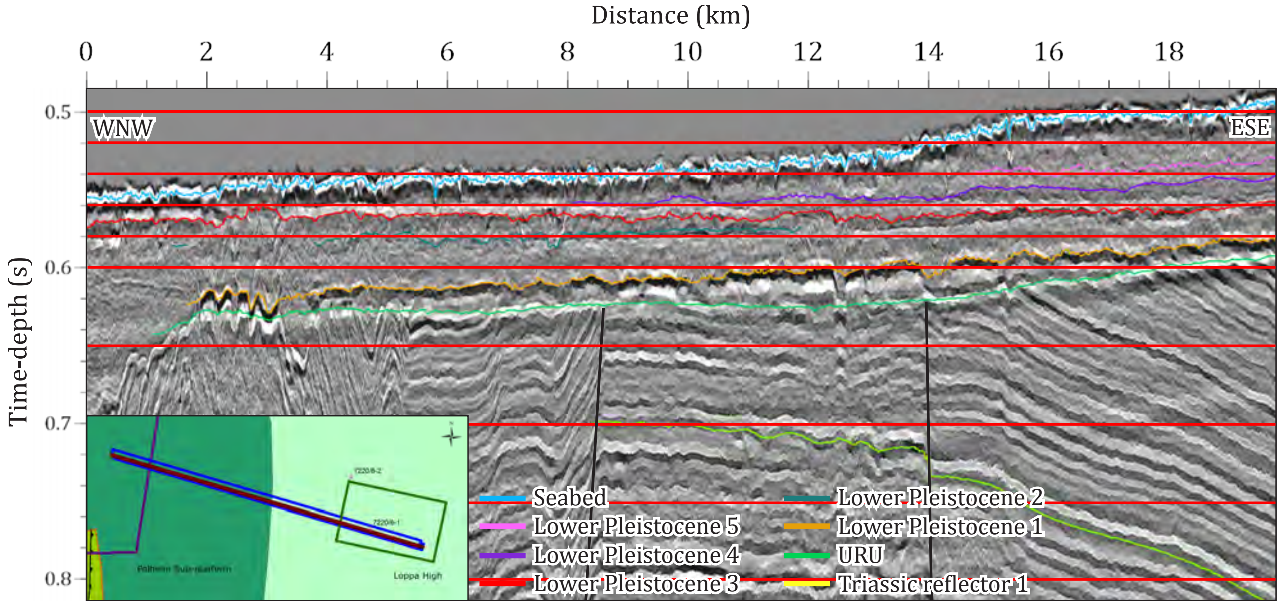

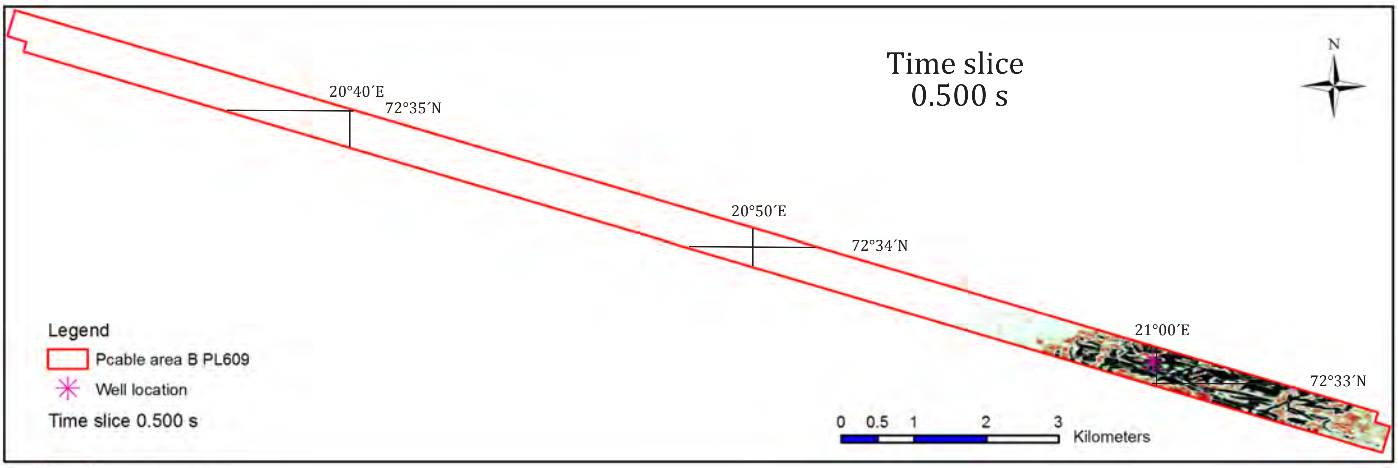

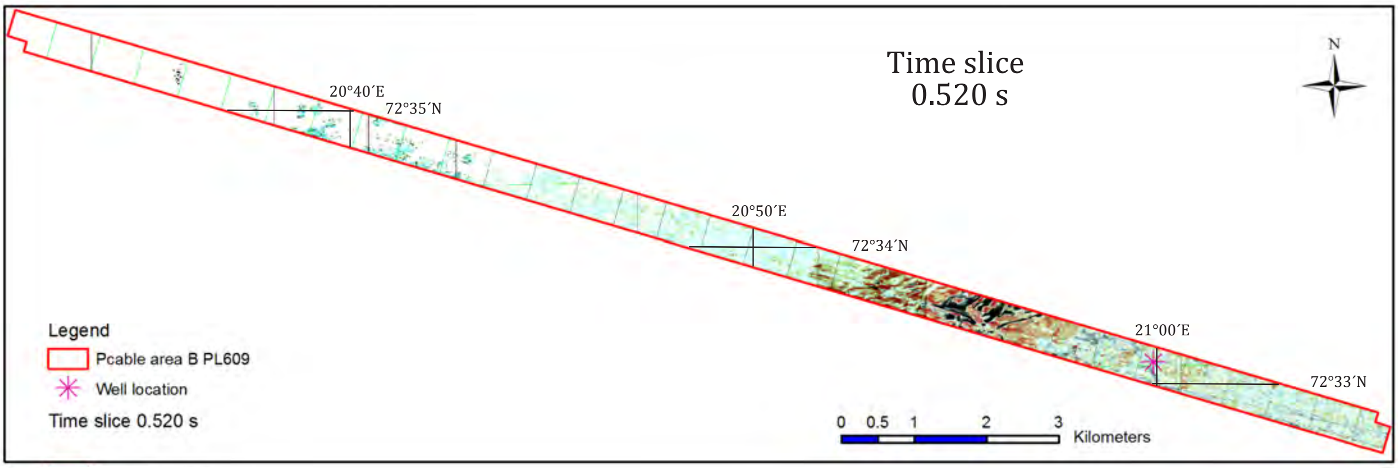

Figure C24: A seismic profile of the Pcable area B PL609 survey area, striking WNW-ESE. Red lines mark the horizontal depth for generated time slices. Two major fault are highlighted in the center by black lines. The map in the lower left corner displays an overview of the Pcable survey areas (blue outline), with the orientation of the 2D seismic profile (dark red line). See figure A1 for the entire study area.

Figure C25 & C26: Time slice velocity maps cutting the Pcable area B PL609 survey area horizontally at 0.500 s and 0.520 s. Red color reflect areas of high permeability and black areas of low permeability. The pink dot mark the location of the well 7220/6-1. The reference map in the lower right corner displays an overview of the Pcable survey area (blue outline). See figure A1 for the entire study area.

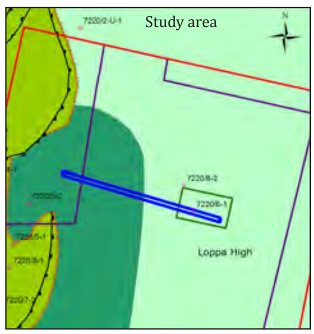

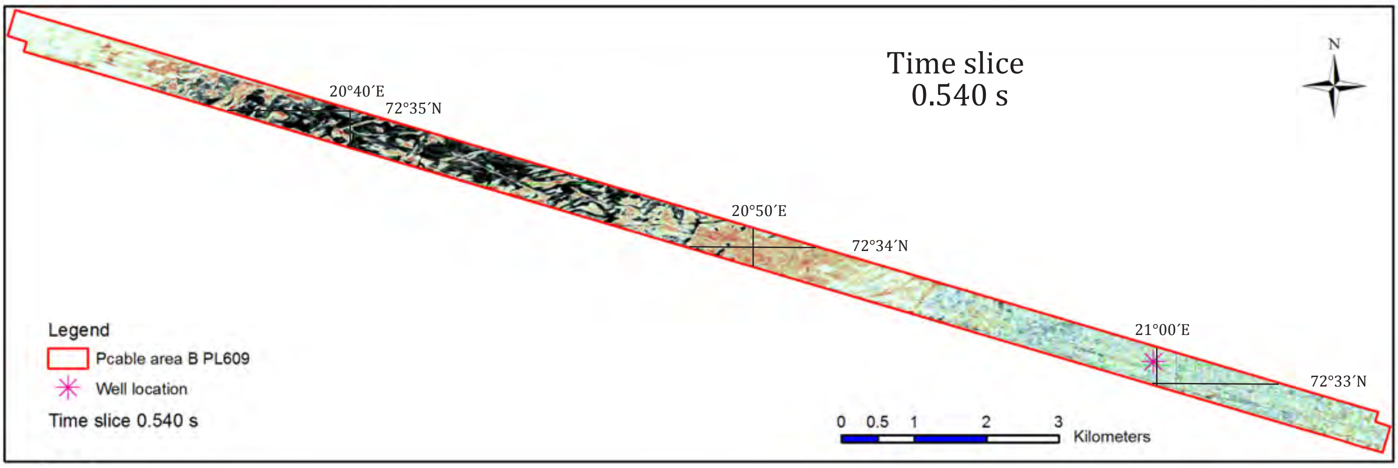

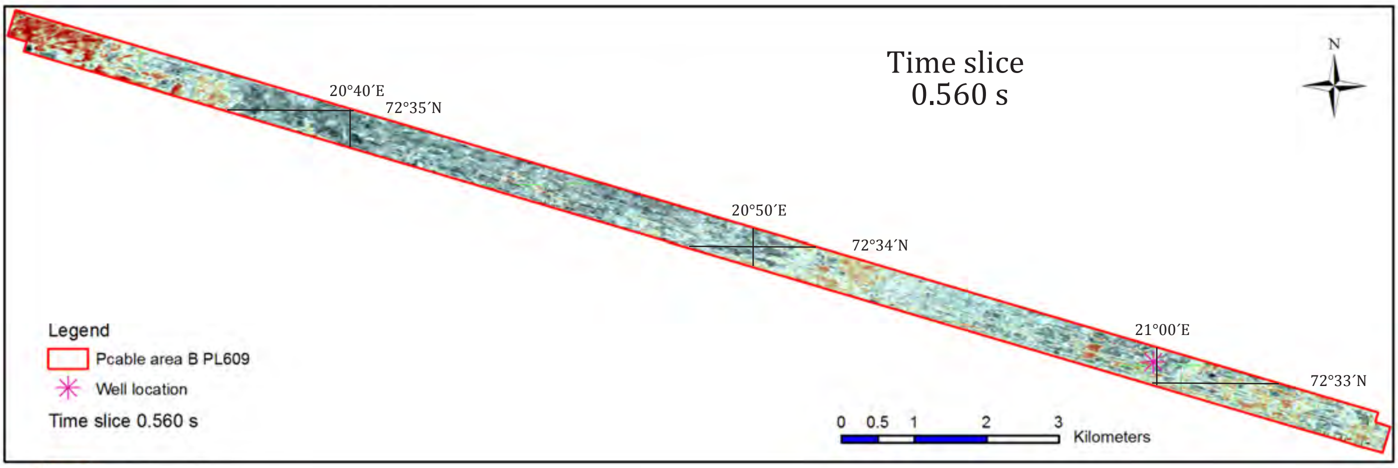

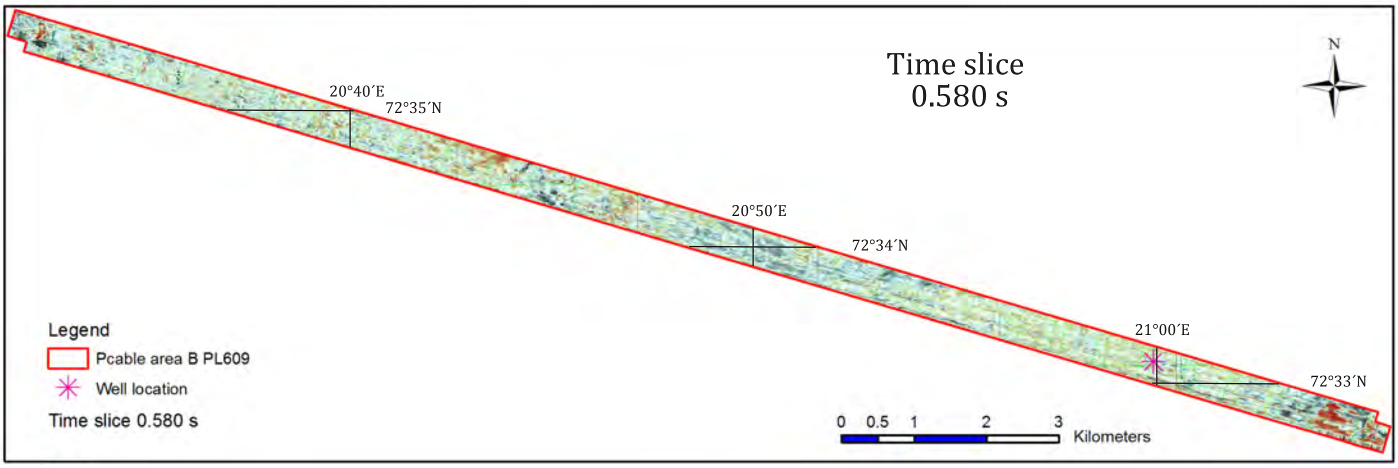

Figure C27 - C29: Time slice velocity maps cutting the Pcable area B PL609 survey area horizontally at 0.540 s, 0.560 s and 0.580 s. Red color reflect areas of high permeability and black areas of low permeability. The pink dot mark the location of the well 7220/6-1. The reference map in the lower right corner displays an overview of the Pcable survey area (blue outline). See figure A1 for the entire study area.

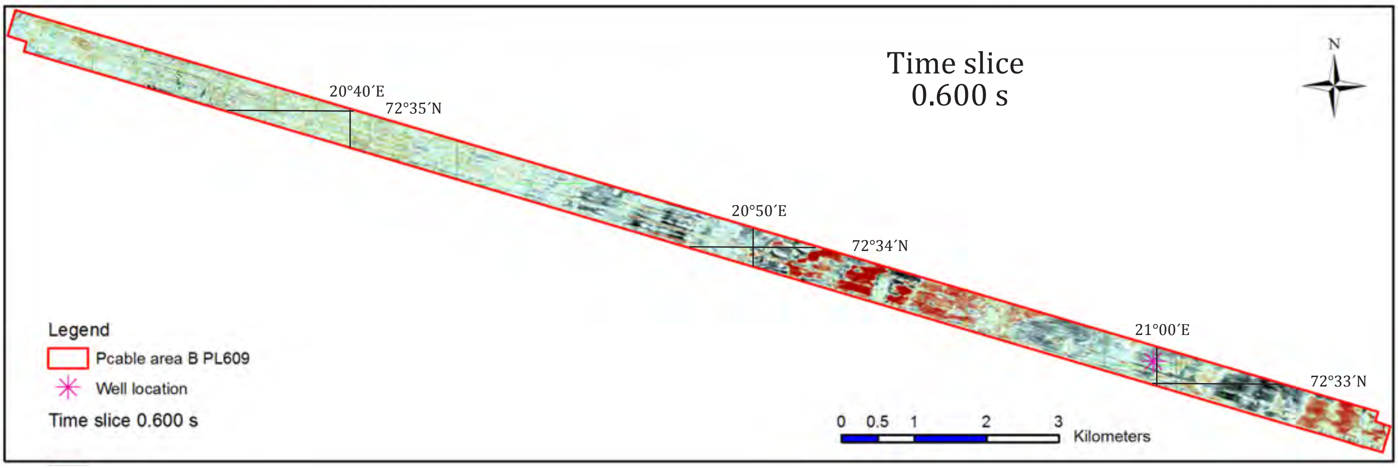

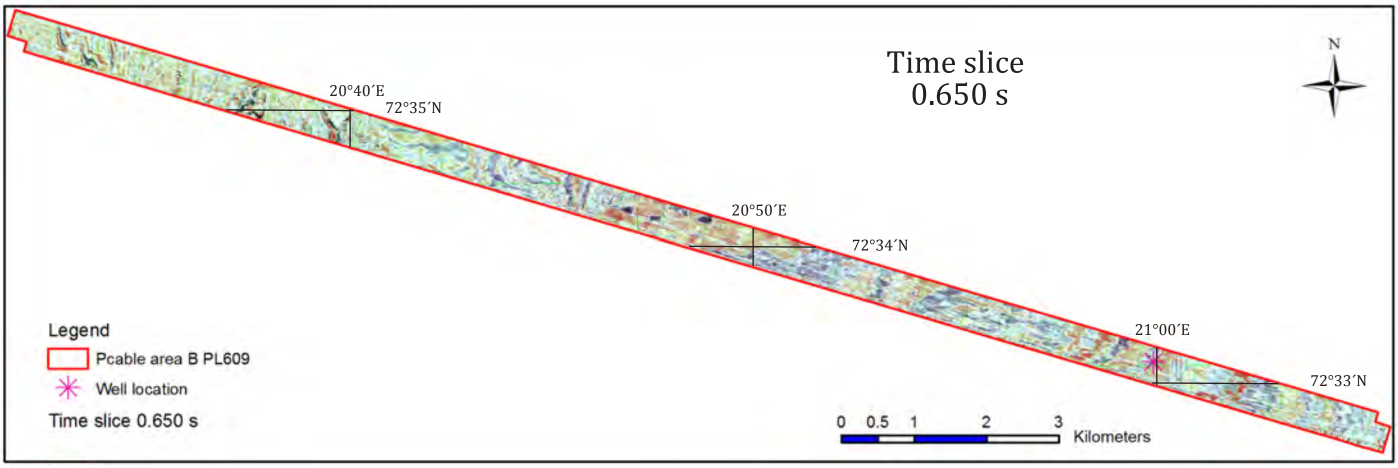

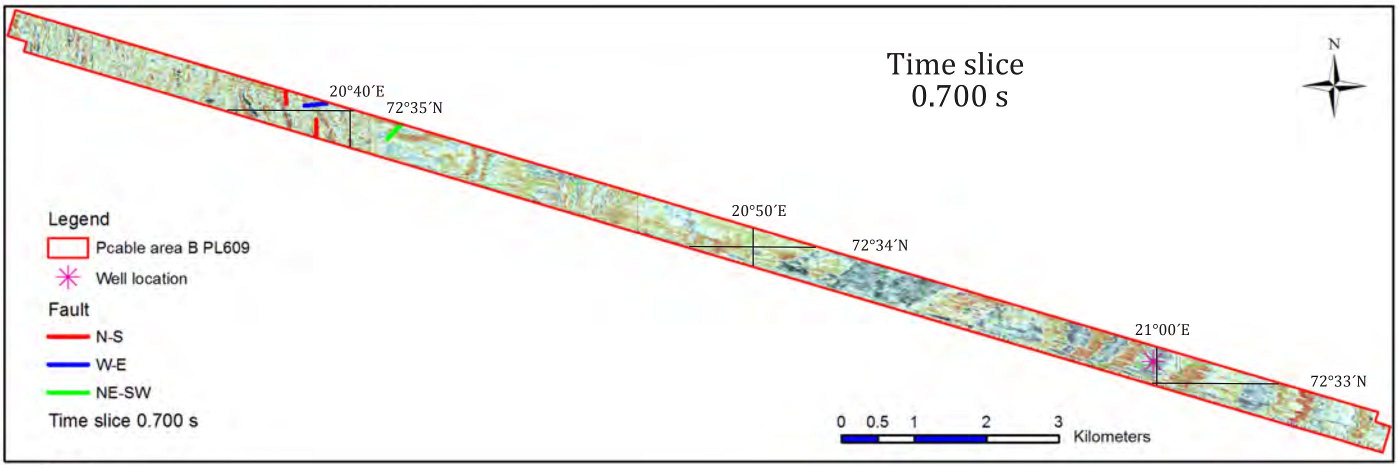

Figure C30 - C32: Time slice velocity maps cutting the Pcable area B PL609 survey area horizontally at 0.600 s, 0.650 s and 0.700 s. Red color reflect areas of high permeability and black areas of low permeability. Faults are highlighted using color coded orientations. The pink dot mark the location of the well 7220/6-1. The reference map in the lower right corner displays an overview of the Pcable survey area (blue outline). See figure A1 for the entire study area.

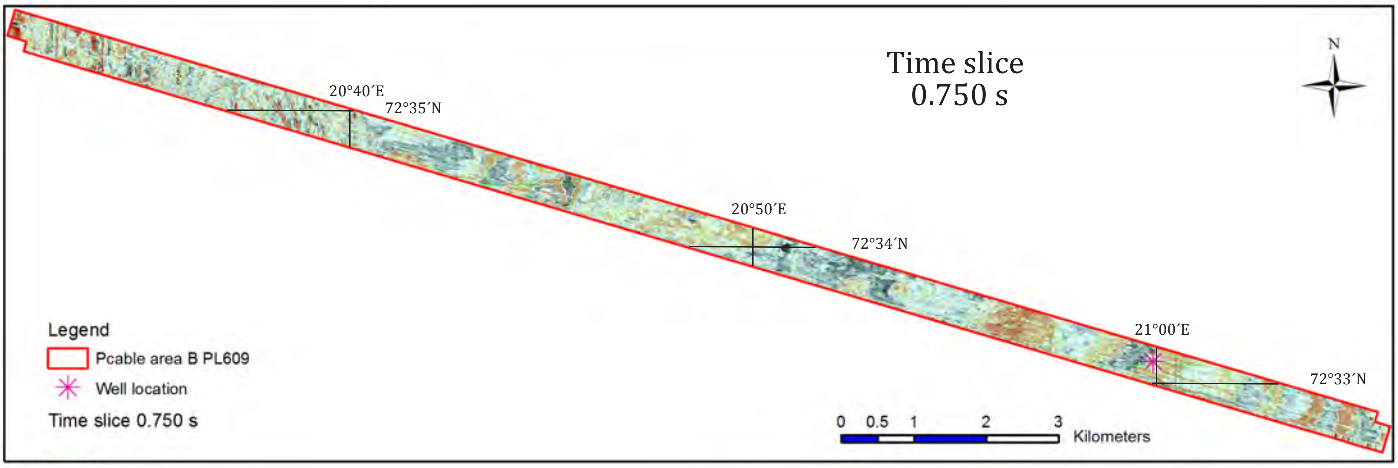

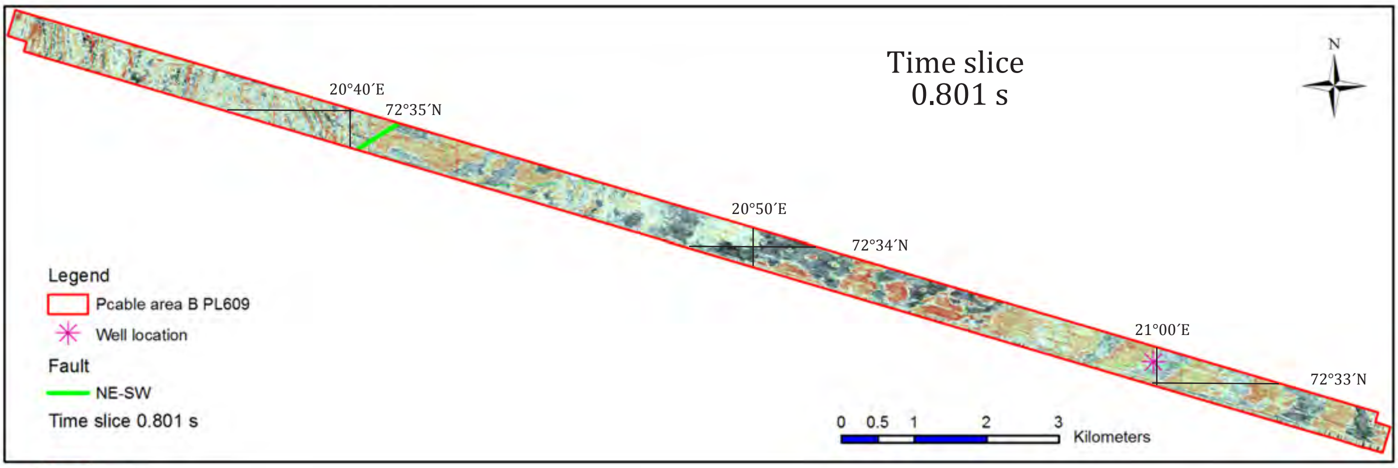

Figure C33 & C34: Time slice velocity maps cutting the Pcable area B PL609 survey area horizontally at 0.750 s and 0.801 s. Red color reflect areas of high permeability and black areas of low permeability. Faults are highlighted using color coded orientations. The pink dot mark the location of the well 7220/6-1. The reference map in the lower right corner displays an overview of the Pcable survey area (blue outline). See figure A1 for the entire study area.

Appendix D - Table 1 with the various sets of data used in this project.

Data	Filename/Survey	Source
Well data	7220/5-1	Norwegian Petroleum Directorate (NPD)
Well data	7220/6-1	Norwegian Petroleum Directorate (NPD)
Layer-file (.lyr)	structural_elements	Norwegian Petroleum Directorate (NPD)
Seismic reflection (2D)	NBRD07-234838	Lundin Norway AS
Seismic reflection (2D)	NBR10-338364	Lundin Norway AS
Seismic reflection (3D)	LN12M01	Lundin Norway AS
Seismic reflection (3D)	NH0372	Lundin Norway AS
Seismic reflection (3D)	Pcable area B PL609	Lundin Norway AS
Shape-file (.shp)	Barents_CarbonateCrust_and_BacterialMats	Lundin Norway AS
Shape-file (.shp)	Licenses_Lundin_do_not_edit	Lundin Norway AS
Shape-file (.shp)	v_geo_wlbpoint (well locations)	Lundin Norway AS
Shape-file (.shp)	COASTLINE	Lundin Norway AS
Multibeam bathymetry	Barents_Bath_Lund_North_3m	Lundin Norway AS
Multibeam bathymetry	Barents_Bath_Lund_South_2	Lundin Norway AS
Multibeam bathymetry	Barents_Bath_Lund_South_3	Lundin Norway AS
Multibeam bathymetry	Barents_Bath_Lund_South_4	Lundin Norway AS
Multibeam bathymetry	FFI_EM710_2012_1m_UTM34	Lundin Norway AS
Water column data (.wcd)	0042_20120425_112310_sverdrup	Lundin Norway AS
Water column data (.wcd)	0043_20120425_122305_sverdrup	Lundin Norway AS
Water column data (.wcd)	0044_20120425_132305_sverdrup	Lundin Norway AS
Water column data (.wcd)	0046_20120425_054005_sverdrup	Lundin Norway AS
Water column data (.wcd)	0047_20120425_064005_sverdrup	Lundin Norway AS
Water column data (.wcd)	0048_20120425_103149_sverdrup	Lundin Norway AS
Water column data (.wcd)	0049_20120425_112141_sverdrup	Lundin Norway AS
Water column data (.wcd)	0001_20120426_083212_sverdrup	Lundin Norway AS
Water column data (.wcd)	0002_20120426_093211_sverdrup	Lundin Norway AS
Water column data (.wcd)	0004_20120426_115641_sverdrup	Lundin Norway AS
Water column data (.wcd)	0005_20120426_123817_sverdrup	Lundin Norway AS
Water column data (.wcd)	0006_20120426_130522_sverdrup	Lundin Norway AS
Water column data (.wcd)	0007_20120426_132933_sverdrup	Lundin Norway AS
Water column data (.wcd)	0008_20120426_140235_sverdrup	Lundin Norway AS

Data	Filename/Survey	Source
Water column data (.wcd)	0009_20120426_150152_sverdrup	Lundin Norway AS
Water column data (.wcd)	0010_20120426_152513_sverdrup	Lundin Norway AS
Water column data (.wcd)	0011_20120426_160304_sverdrup	Lundin Norway AS
Water column data (.wcd)	0012_20120426_170305_sverdrup	Lundin Norway AS
Water column data (.wcd)	0013_20120426_170342_sverdrup	Lundin Norway AS
Water column data (.wcd)	0014_20120426_173504_sverdrup	Lundin Norway AS
Water column data (.wcd)	0016_20120426_175524_sverdrup	Lundin Norway AS
Water column data (.wcd)	0017_20120426_185525_sverdrup	Lundin Norway AS
Water column data (.wcd)	0018_20120426_191509_sverdrup	Lundin Norway AS
Water column data (.wcd)	0019_20120426_194901_sverdrup	Lundin Norway AS
Water column data (.wcd)	0020_20120426_204901_sverdrup	Lundin Norway AS
Water column data (.wcd)	0021_20120426_212318_sverdrup	Lundin Norway AS
Water column data (.wcd)	0022_20120426_215939_sverdrup	Lundin Norway AS
Water column data (.wcd)	0023_20120426_225939_sverdrup	Lundin Norway AS
Water column data (.wcd)	0024_20120426_235938_sverdrup	Lundin Norway AS